

X-Ray Timing and Spectral Observations of Galactic Black Hole Candidate XTE J1550–564 During Outburst*

K. T. Reilly

Stanford Linear Accelerator Center
Stanford University
Stanford, CA 94309

SLAC-Report-610
December 2002

Prepared for the Department of Energy
under contract number DE-AC03-76SF00515

Printed in the United States of America. Available from the National Technical Information Service, U.S. Department of Commerce, 5285 Port Royal Road, Springfield, VA 22161.

*Ph.D. thesis, Stanford University, Stanford, CA 94309.

X-RAY TIMING AND SPECTRAL OBSERVATIONS OF
GALACTIC BLACK HOLE CANDIDATE XTE J1550–564
DURING OUTBURST

A DISSERTATION
SUBMITTED TO THE DEPARTMENT OF APPLIED PHYSICS
AND THE COMMITTEE ON GRADUATE STUDIES
OF STANFORD UNIVERSITY
IN PARTIAL FULFILLMENT OF THE REQUIREMENTS
FOR THE DEGREE OF
DOCTOR OF PHILOSOPHY

Kaice Theodore Reilly
December 2002

I certify that I have read this dissertation and that in my opinion it is fully adequate, in scope and quality, as a dissertation for the degree of Doctor of Philosophy.

Elliott Bloom
(Principal Adviser)

I certify that I have read this dissertation and that in my opinion it is fully adequate, in scope and quality, as a dissertation for the degree of Doctor of Philosophy.

Vahé Petrosian
(Applied Physics Department Co-Adviser)

I certify that I have read this dissertation and that in my opinion it is fully adequate, in scope and quality, as a dissertation for the degree of Doctor of Philosophy.

Robert Wagoner
(Physics Department)

Approved for the University Committee on Graduate Studies:

Abstract

Soft X-ray transients (SXTs), a sub-class of low-mass X-ray binaries (LMXBs), provide a unique opportunity to test General Relativity and to probe fundamental physics under conditions terrestrially unattainable. SXT outbursts are of great interest because they allow the study of LMXBs under a wide range of accretion rates. The majority of known SXTs contain black holes, therefore SXT outbursts are key to understanding accretion physics around black holes and in active galactic nuclei, which are thought to contain supermassive, $M \sim 10^6 - 10^{10} M_{\odot}$, where M_{\odot} is one solar mass), central compact objects. These compact objects are most likely black holes, which exhibit, on a much larger scale, accretion physics similar to that around black holes in SXTs.

In this work, the timing and spectral properties of the SXT and microquasar XTE J1550–564 during outburst are studied. Observations made by the Unconventional Stellar Aspect (USA) Experiment on board the *Advanced Research and Global Observation Satellite* (ARGOS) are emphasized. USA data show a low-frequency quasi-periodic oscillation (LFQPO) with a centroid frequency that tends to increase with increasing USA flux and a fractional rms amplitude which is correlated with the USA hardness ratio (4–16 keV/1–4 keV). Several high-frequency quasi-periodic oscillations (HFQPOs) were detected by the *Rossi X-ray Timing Explorer* (RXTE), during periods where the LFQPO is seen to be weakening or not detectable at all. The evolution of the USA hardness ratio with time and source flux is examined. The hardness-intensity diagram shows counterclockwise cyclical evolution and possibly indicates the presence of two independent accretion flows: a geometrically thin, optically thick accretion disk and a hot sub-Keplerian flow.

A model for production of the LFQPO in XTE J1550–564 is proposed, assuming that the LFQPO is a result of acoustic oscillations in a hot sub-Keplerian transition layer (TL). Under this acoustic oscillation model (AOM), the TL is an acoustic cavity having an outer boundary at the transition layer radius, R_{TL} , where $R_{\text{TL}} \approx R_{\text{inner}}$, with

R_{inner} being the radius of the accretion disk inner edge. TL resonance is interpreted as a mechanism for the LFQPO and the eigenfrequencies are associated with the LFQPO frequencies, ν_{LFQPO} . This LFQPO mechanism requires the presence of a TL, capable of inverse-Compton scattering, with an outer boundary radius (i.e. R_{TL}) regulated by a cool Keplerian accretion disk.

Support for the AOM is provided by the correlation of the LFQPO percent rms amplitude with the USA hardness ratio, and other correlations and anti-correlations found in the USA, RXTE and Burst And Transient Source Experiment (BATSE) observations of the 1998–1999 and 2000 outbursts. An anti-correlation in the LFQPO percent rms amplitude squared with low energy photons ($\lesssim 20$ keV) from RXTE and USA data, and a correlation with higher energy photons ($\gtrsim 20$ keV) from BATSE data are observed during the XTE J1550–564 outbursts.

These trends in the LFQPO data show that the LFQPO strengthens with increasing high energy flux. The increasing ν_{LFQPO} with increasing low energy flux, during the rise to maximum in both outbursts, indicates that ν_{LFQPO} is set by the accretion disk inner edge. The spectrally inferred R_{inner} is commensurate, showing a decrease with increasing ν_{LFQPO} . Finally, RXTE spectral data indicate that the LFQPO is detectable only when the power law contribution is greater than 20% of the low energy flux, providing evidence that the LFQPO mechanism is dependent on the TL.

The AOM is consistent with all of the above observations and it has the ability to predict the approximate value of R_{inner} (i.e. $\nu_{\text{LFQPO}} \propto 1/R_{\text{TL}} \approx 1/R_{\text{inner}}$). Applying the AOM to the USA observations of the 2000 outburst rise to maximum, the inner edge of the accretion disk evolves from $68 R_{\text{Sch}}$ to $3.7 R_{\text{Sch}}$, corresponding to the observed LFQPO frequencies between 0.2 Hz and 6 Hz, respectively, where R_{Sch} is the Schwarzschild radius. For the 1998–1999 outburst rise to maximum, the accretion disk inner edge evolves from $166 R_{\text{Sch}}$ to $2.5 R_{\text{Sch}}$, corresponding to the observed LFQPO frequencies between 0.081 Hz and 13.2 Hz, respectively.

Comparison between spectrally determined R_{inner} and the AOM measurement of R_{TL} shows good agreement, but uncertainties in both measurements are dominated by systematics. These preliminary tests of the AOM indicate that it may be a useful tool in determining the location of the accretion disk inner edge and that it is a plausible model for LFQPOs observed in black hole SXTs.

To all the little critters that make it go!

Acknowledgments

To begin, I thank Elliott Bloom, my adviser, for giving me the freedom to pursue my degree in my own way. I would like to thank everyone, especially those at SLAC and NRL, who made the USA experiment possible. I am in debt to everyone in the USA Science Working Group for their consistent guidance. Without mentioning names, I want to thank everyone in Group K at SLAC for many useful discussions, where I learned much about physics and the pursuit of scientific truth.

I gratefully acknowledge Lev Titarchuk for many hours of discussion. Thanks to my reading committee, Elliott Bloom, Robert Wagoner and Vahé Petrosian, for their comments and discussion.

Thank you to Rob Hynes for the BinSim program and art work.

I would like to thank all of my friends for their support through this endeavor. Thanks to Martin O’Kane for taking a stab at reading my dissertation.

Most importantly, thanks to Klejda Bega for her patience, support and assistance over the last year. Her ability to endure the great curmudgeon was truly astonishing. I will be forever owing gratitude for all of those very late nights.

Contents

Abstract	iii
Acknowledgments	vi
1 Introduction	1
1.1 Introduction and Outline	1
1.2 History of X-Ray Astrophysics and the USA Experiment	2
2 Properties of X-Ray Binary Systems	5
2.1 X-Ray Binary Systems	5
2.2 Origin and Evolution of X-Ray Binaries	9
2.3 Overview to Accretion Processes	10
2.3.1 Sources for Accreted Matter	10
2.3.2 Accretion Mechanisms	12
2.3.3 Accretion Geometries	14
2.4 Soft X-Ray Transient (SXT) Outbursts	15
2.4.1 SXT States and Their X-Ray Spectral and Timing Properties	17
2.4.2 Properties of SXT Outbursts in Multiple Wavelengths	20
3 The USA Experiment	24
3.1 Overview of USA	24
3.2 The USA Collaboration: People and Progress	24
3.3 ARGOS and the USA Experiment	26
3.4 USA Instrument Offset Pointing	28
3.5 Schematic of USA Detectors	29
3.5.1 Proportional Counter Basics	30
3.6 Unique Characteristics of USA	33

3.7	USA Science Objectives	35
3.8	Obstacles Encountered by the USA Experiment	36
3.8.1	EDIE: The Electronics Pile-Up Problem	38
4	USA Data Selection and Analysis	68
4.1	Introduction	68
4.2	Overview of USA Data Analysis Tools	69
4.3	Obtaining and Filtering USA Data	70
4.4	Analyzing USA Data I: Light Curves	74
4.5	Analyzing USA Data II: RMS Normalized PSDs	76
4.6	Fitting Quasi-Periodic Oscillations	77
5	XTE J1550–564 Observations	81
5.1	Introduction	81
5.2	Observations and Data Analysis	83
5.2.1	Light Curves and Hardness Ratios	83
5.2.2	Power Spectra: Low-Frequency QPOs	85
5.3	Results	86
5.3.1	QPO Evolution and Correlation to State Changes	86
5.3.2	Spectral Evolution	87
5.3.3	Multi-wavelength Correlations	87
5.4	Discussion: Two-Flow Models	91
5.5	USA Analysis Checks	93
5.5.1	Upper Limit on the RMS of ‘Undetected’ LFQPOs During the XTE J1550–564 Intermediate State	100
6	The Acoustic Oscillation Model	105
6.1	Introduction	105
6.2	Transition Layer Dependence	107
6.3	RXTE Spectral Results	114
6.4	Evidence for the Existence of the Transition Layer	115
6.5	Acoustic Oscillation Model	116
6.6	AOM Suggests Kerr Black Hole	119
6.7	Derivation of the Radial Dependence in the AOM	120
6.8	Cross Checks of AOM Radii	121

6.9	HFQPOs	127
6.10	Other LFQPO Models	130
6.11	Summary of AOM and Future Work	131
7	Discussion & Conclusions	133
A	USA Data Analysis Tools	138
A.1	Introduction	138
A.2	usaview: Observation Scheduling	138
A.3	Intermediate Steps	141
A.4	dat2fits: Data Unpacking and Time Construction	143
A.4.1	Introduction to dat2fits	143
A.4.2	GPS Time Construction in dat2fits	144
A.4.3	Out of Order Events	146
A.4.4	Other Timing Anomalies in USA Data	148
A.5	usabckgnd: Calculating Background Files	148
A.6	What MkTimeUSA (mktimeusa) Does	148
A.6.1	mktimeusa: Construction of Good Time Intervals	148
A.6.2	MkTimeUSA Cutting Criteria	149
A.6.3	How to Run mktimeusa	149
A.6.4	MkTimeUSA Argument Descriptions	150
A.6.5	MkTimeUSA Output	153
A.6.6	STAT File Contents	156
A.6.7	Future Development of USA Data Cuts	157
A.7	PSDs	158
A.7.1	Description of specan	159
A.8	Fitting Tools etc.	161
B	Summary of USA Observations	162
C	Example usaview Output for XTE J1550–564	166
D	specan: Functionality and Commands	168
E	mergespec Command Line Options	172
	Bibliography	173

List of Tables

1.1	Timeline of Key Astrophysical Experiments	3
3.1	Properties of the Lorentzians	53
3.2	Noise Fit Parameters	54
4.1	XTE J1550–564 observation criteria.	70
4.2	XTE J1550–564 data cut parameters used in mktimeusa	71
4.3	Background estimates for the south pole and ascending node.	75
6.1	Energy Band Term Definitions	107
A.1	Example Table of Source Observability.	142
B.1	Summary of USA Observations	165

List of Figures

2.1	XTE J1118+226 as an example of a LMXB.	6
2.2	Cygnus X-1 as an example of a HMXB	7
2.3	Artist's conception of extreme conditions near a black hole	8
2.4	The Roche lobe.	11
2.5	RXTE/ASM light curves from several different black hole candidate outbursts	16
2.6	SXT Outburst States	18
2.7	Radio, BATSE and ASM observations of GX 339-4 during outburst. .	21
2.8	Optical/IR and X-ray light curves and ASM hardness ratio of XTE J1550- 564 during the 2000 outburst.	22
3.1	Artist's rendition of ARGOS.	26
3.2	Photograph of USA as mounted on ARGOS prior to launch.	27
3.3	Schematic diagram of the USA experiment.	29
3.4	Breakdown of USA X-ray detector modules.	30
3.5	Schematic diagram of the USA proportional chamber.	31
3.6	USA detector efficiency as a function of energy.	32
3.7	Illustration of an electron avalanche in a proportional chamber. . . .	33
3.8	Leahy normalized PSD of PHA channel 1 from a mode 2 Crab Nebula observation showing an EDIE dip.	40
3.9	Leahy normalized PSD of PHA channel 2 from a mode 2 Crab Nebula observation showing an EDIE bump.	41
3.10	Hypothetical USA count rate spectrum showing USA PHA channel boundary shifts.	42
3.11	Average of the integral count rate spectra as a function of temporal distance to the preceding photon.	45

3.12	Mean of the differential count rate spectra as a function of temporal distance to preceding photon.	46
3.13	Average of the differential count rate spectra as a function of temporal distance to preceding photon.	47
3.14	Uncorrected and corrected PSDs calculated from Fe ⁵⁵ ground data and Cassiopeia A in orbit data.	49
3.15	Corrected PSDs of Cygnus X-1 and the XTE J1859+226 during its high state.	50
3.16	Corrected PSD of XTE J1859+226 during its very high state.	51
3.17	Corrected, but not re binned, PSD of XTE J1859+226 during its very high state.	53
3.18	PSD of XTE J1859+226 VHS fit with power law and all Equation 3.3 parameters free over the 1–300 Hz range.	54
3.19	PSD of XTE J1859+226 VHS fit with power law plus three Lorentzians and all Equation 3.3 parameters free over the 1–300 Hz range.	55
3.20	PSD of XTE J1859+226 VHS fit with power law plus three Lorentzians and only c_0 of Equation 3.3 was free over the 1–300 Hz range.	56
3.21	PSD of XTE J1859+226 VHS fit with power law and only c_0 of Equation 3.3 was free over the 1–300 Hz range.	57
3.22	PSD of XTE J1859+226 VHS fit with power law and only c_0 of Equation 3.3 was free over the 1–5000 Hz range.	58
3.23	PSD of XTE J1859+226 VHS fit with power law plus three Lorentzians and only c_0 of Equation 3.3 was free over the 1–5000 Hz range.	59
3.24	PSD of XTE J1859+226 VHS fit with power law and all Equation 3.3 parameters free over the 1–5000 Hz range.	60
3.25	PSD of XTE J1859+226 VHS fit with power law plus three Lorentzians and all Equation 3.3 parameters free over the 1–5000 Hz range.	61
3.26	PSD of XTE J1859+226 VHS fit with power law and no Equation 3.3 parameters free over the 1–300 Hz range.	62
3.27	PSD of XTE J1859+226 VHS fit with power law plus three Lorentzians and no Equation 3.3 parameters free over the 1–300 Hz range.	63
3.28	PSD of XTE J1859+226 VHS fit with a power law, a power law plus three Lorentzians and Equation 3.3.	64

4.1	Difference and ratio of layers 0 and 1 of USA PHA channel 15 as a function of time during an observation of XTE J1550–564 on Day 111 2000.	72
4.2	Example XTE J1550–564 light curve before cutting.	73
4.3	Example XTE J1550–564 light curve after cutting.	74
4.4	Low-hard state PSD with LFQPO fit.	78
4.5	Intermediate state PSD with LFQPO fit.	79
5.1	Time evolution of the SB, HB, USA total range and LFQPO parameters during the 2000 outburst of XTE J1550–564.	84
5.2	Hardness Intensity Diagram	88
5.3	Time Evolution of XTE J1550–564 with Multi-wavelength Observations	89
5.4	ASM Hardness Intensity Diagram	93
5.5	HB and SB versus Total Range	94
5.6	SB and HB versus Total Range with Ascending and South Pole Node Identifiers	95
5.7	ASM and USA Hardness Ratios	96
5.8	Anomalous LFQPO in USA Hard Band	97
5.9	Day 121 2000: LFQPO non-detection example.	98
5.10	Day 123 2000: LFQPO non-detection example.	99
5.11	Day 125 2000: LFQPO non-detection example.	100
5.12	Day 128 2000: LFQPO non-detection example.	101
5.13	Day 130 2000: LFQPO non-detection example.	102
5.14	Day 132 2000: LFQPO detection example.	103
6.1	LFQPO percent rms as a function of the USA hardness ratio	108
6.2	ASM and BATSE fluxes, LFQPO percent rms and LFQPO frequency as a function of time during the 1998–1999 outburst.	109
6.3	USA and BATSE fluxes, LFQPO percent rms and LFQPO frequency as a function of time during the 2000 outburst.	110
6.4	LFQPO rms squared as a function of the ASM flux, the BATSE flux, the BATSE/ASM hardness ratio and the BATSE/USA hardness ratio.	111
6.5	General accretion geometry for the acoustic oscillation model.	117
6.6	LFQPO frequency as a function of the AOM radii and the spectrally determined radii.	123

6.7	LFQPO frequency as a function of the AOM radii and the spectrally determined radii plus $2.0 R_{\text{Sch}}$	124
6.8	Plot of AOM radii versus the spectral radii for the 1998–1999 outburst.	125
6.9	The ratio of the AOM radii to the spectral radii as a function of LFQPO frequency for the 1998–1999 outburst.	126
6.10	The ratio of the AOM radii to the spectral radii plus $2.0 R_{\text{Sch}}$ as a function of LFQPO frequency for the 1998–1999 outburst.	127
6.11	HFQPO frequency as a function of AOM radius plotted with theoretical HFQPO models	128

Chapter 1

Introduction

1.1 Introduction and Outline

Soft X-ray transients (SXTs) serve as the primary subject of this dissertation. The greatest focus is given to SXTs where the compact object is a black hole candidate. Observations made by the Unconventional Stellar Aspect (USA) Experiment of XTE J1550–564 during its 2000 outburst are discussed in detail. The outline of topics is as follows. In the next section a brief overview of the history of X-ray astrophysics is given. Chapter 2 discusses the properties of SXTs in outburst and sets the context for studying such systems. Some terminology is defined for the reader in Chapter 2. Chapter 3 provides an overview of the USA experiment and acts as a guide to more detailed USA reference sources. Chapter 4 makes use of XTE J1550–564 data to identify how these tools are used in the selection and analysis of USA event mode data. The tools referred to in Chapter 4 are described in detail in Appendix A, which also describes the complete USA data stream. Chapter 5 gives a detailed discussion of the USA data collected during the 2000 outburst of XTE J1550–564. Interpretation of the data is also given in a broader context as determined by the current understanding of SXT outbursts. The data and interpretation presented in Chapter 5 supports the existence of two active accretion flows during the outbursts of XTE J1550–564. In Chapter 6 a phenomenological model of low-frequency quasi periodic oscillations (LFQPOs) observed during the 2000 outburst of XTE J1550–564, is discussed. Data from the 1998-1999 outburst of XTE J1550–564 are also used to support the model presented in Chapter 6. The model proposes that the LFQPOs occur via modulations due to a transition layer, corona, surrounding the compact object. The model is used

to estimate the distance from the center of the compact object to the inner edge of the accretion disk. Chapter 7 provides a discussion and conclusions.

1.2 History of X-Ray Astrophysics and the USA Experiment

As a field of physics, X-ray astrophysics is relatively new.¹ Its origins date to 1949 when researchers at the Naval Research Laboratory (NRL) in Washington DC discovered, using captured German V2 rockets, that the Sun emits copious X-rays. Over a decade later other cosmic X-ray sources were discovered. The first extra-solar X-ray source to be observed was Scorpius X-1, which was discovered in 1962 June 18 by an American Science and Engineering Experiment (ASEE). ASEE was led by Riccardo Giacconi who received the 2002 Nobel Prize for his vast contributions to the field of X-ray astrophysics, including the discovery of Scorpius X-1 and the diffuse X-ray background. The ASEE was the beginning of rapid growth in the field of X-ray astrophysics. In 1963 the Crab Nebula was discovered as a strong X-ray source and shortly thereafter it was found that radio galaxies, such as Centaurus A and Virgo A, and Seyfert galaxies were also X-ray sources. Since this early period in X-ray astrophysics, the birth of ever improved X-ray observing missions has been steady. With each new mission exciting discoveries have been made, adding to both the understanding and the unexplained within the field. Historically speaking, confusion has always been the result of physicists' explorations in newly available wavelengths, energies, and sensitivities.

X-ray astrophysics has been fueled by international scientific interests. Discoveries have been made by individual countries launching missions as well as through international collaborations. Some of the key agencies involved in X-ray missions over the years have been the United States Air Force (USAF) and Department of Defense (DOD), the National Aeronautics and Space Administration (NASA) in the USA, the European Space Agency (ESA) and the Japanese Space Agency (JSA). Some of the missions flown by these agencies and their highlights are listed in Table 1.1. These agencies have often worked on collaborative projects.

¹The contents of this section are extensively based on Charles and Seward 1995, Encyclopedia.com 2002 and Tucker 2002.

Dates	Instrument Name	Mission Highlights
1949	V-2 Rockets	Solar X-rays
1963 to 1970	Various Rocket and Balloon Flights	X-ray binaries, Pulsars, Galaxies, Solar X-ray images (Nobel Prize 2002)
December 1970 to March 1973	Uhuru X-ray Satellite	All sky survey, 400 X-ray sources discovered, X-ray production fueled by accretion
May 1969 to June 1979	Vela Satellites	Discovery of Gamma-ray bursts, Observation of X-ray bursters
August 1974 to July 1976	Astronomy Netherlands Satellite	Discovery of X-ray bursters, more X-ray binaries
October 1974 to March 1980	Ariel V	Soft X-ray Transient (SXT) A0620-00
May 1975 to April 1980	Small Astronomy Satellite-3	X-ray emission from white dwarf SS Cygni, a variable star; further research on X-ray bursters
August 1977 to January 1979	High Energy Astronomy Observatory-1 (HEAO-1) HEAO A-1 survey	Discovery of the Cygnus superbubble, Active galactic nuclei spectra, all sky survey (Wood et al. 1984)
November 1978 to April 1981	Einstein X-ray Observatory	First X-ray images of shock waves in supernova remnants, 7000 X-ray sources catalogued, development of new ways to study dark matter
May 1983 to April 1986	EXOSAT	Discovery of quasi-periodic oscillations in neutron stars and black holes
June 1990 to February 1999	Roentgen satellite (ROSAT)	Number of X-ray sources expanded to 125,000; X-rays are observed from the surface of neutron stars; 70% of soft X-ray background get resolved
1993 to July 2000	Advanced Satellite for Cosmology and Astrophysics (ASCA)	First evidence of gravitational redshift due to strong gravity around black hole!
December 1995 to present	Rossi X-ray Timing Explorer (RXTE)	Added significantly to the understanding of processes in the vicinity of black holes and neutron stars (tremendous progress), burst oscillations, kHz QPOs, X-ray millisecond pulsars
April 1996 to April 2002	BeppoSAX	Wide band spectra for active galactic nuclei, positions of gamma-ray bursts and their X-ray afterglow
April 29, 1999 to November 16, 2000	Unconventional Stellar Aspect (USA)	See Chapter 3
July 1999 to present	Chandra X-ray Observatory	Number and nature of black holes in the universe
December 1999 to present	XMM-Newton	Energy budget of radiation from a black hole accretion disk; detailed spectra of active galactic nuclei
October 2000 to present	High Energy Transient Explorer (HETE-2)	Localization of gamma-ray bursts

Table 1.1: Timeline of key X-ray astrophysics missions with some of the highlights. The contents of this table are largely based upon Tucker 2002.

Recently, collaborations have developed, not just between groups of astrophysicists, but among the different fields of physics. Astrophysicists have often specialized in observing a particular wavelength. However, there has been cooperation between

groups and multi-wavelength studies of astrophysical phenomena are common. New partnerships are developing between the fields of high-energy astrophysics² and particle physics. The USA experiment, although primarily an X-ray astrophysics mission, was a cooperative effort between the X-Ray/UV Astrophysics and Applications Section at NRL and the Particle Astrophysics group at the Stanford Linear Accelerator Center (SLAC). A similar collaboration is underway with the Gamma-ray Large Area Space Telescope (GLAST), both an inter-disciplinary and international collaboration.

These new inter-disciplinary collaborations are a result of the progress in particle physics and astrophysics toward a deeper understanding of Quantum Physics and General Relativity. In their current formulation, these contradictory theories comprise the most significant problem in physics—the unification of Quantum Physics and classical gravitational physics—being addressed by physicists at this time. In order to understand the unification of these theories, it is widely believed that probes of matter will have to be made under the most extreme conditions. The primary X-ray sources studied by the USA experiment may be thought of as laboratories (less than ideal as they may be) providing the most extreme conditions known to be obtainable. The ability of USA to observe X-ray sources using a large effective area and high timing resolution ($2 \mu\text{s}$) makes it ideal for studying extreme gravity and matter at extreme energies. As astrophysicists gain concrete understanding of accretion processes and geometries of systems which are the sources of the X-rays observed, it may be possible to understand more fundamental problems at energies that cannot now be observed terrestrially. The study of the X-ray binary system XTE J1550–564, presented in this work, is a small step toward this understanding.

²High energy astrophysics is a term often used to include the various branches of astrophysics, such as the branches which study X-rays, gamma-rays, neutrino physics, etc.

Chapter 2

Properties of X-Ray Binary Systems

2.1 X-Ray Binary Systems

An X-ray binary system is composed of two stellar objects locked in a close orbit. These two objects are referred to as a primary and companion, and a close orbit is defined to be small enough for each of the stars to have an influence on the other's evolution. The primary object is a compact object, which is a white dwarf, a neutron star, some other proposed state of matter (e.g. q-star), or a black hole candidate. The companion, secondary star, is either a white dwarf or a 'normal' star (where gravitational pressure is balanced by thermal pressure). The primary star accretes matter from its companion. The X-ray binary will have varying luminosity depending on the type of primary, companion, overall accretion geometry, etc. (White et al. 1995). Accretion processes will be described in Section 2.3, see Figures 2.1 and 2.2 for a representation of how these systems might appear.

X-ray binaries are broken down into two classes: low-mass X-ray binaries (LMXBs) (companion mass $\lesssim 1M_{\odot}$, late type star, Figure 2.1) and high-mass X-ray binaries (HMXBs) (companion mass $\gtrsim 10M_{\odot}$, early type star, Figure 2.2). These two classes are defined by the type of companion star in the system. In HMXBs the companion star is a B or O type star. In LMXBs the companion is a star later than type A. (Star types are defined by their position on a Hertzsprung-Russel or Color-Magnitude Diagram, see Binney and Merrifield 1998 and references therein for a complete explanation of star types.) The companion is the supplier of material for accretion, which

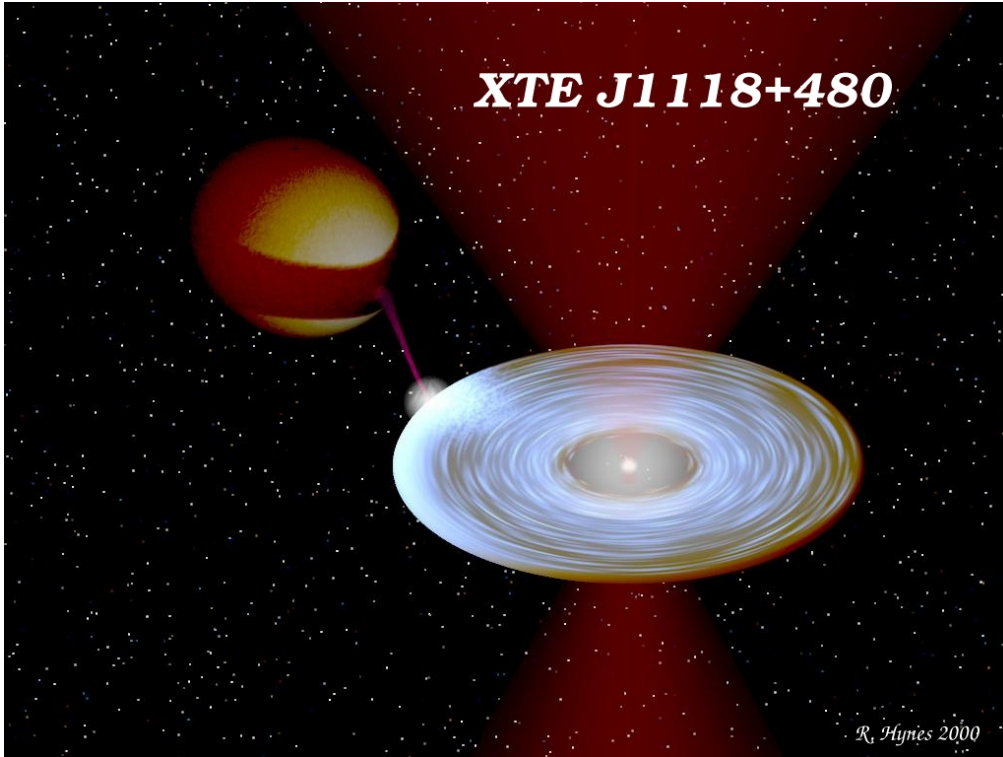


Figure 2.1: Approximate scale image of the system XTE J1118+226 as an example of an LMXB. Several points are highlighted with this figure. First, the accretion disk does not continue all the way in to the compact object. There is a wide swath of red/burgundy which represents jets or ejections coming from the sources. There is a very thin stream taking matter through the inner Lagrangian point onto the compact object via the large accretion disk. The point at which this thin accretion stream originates (at the surface of the normal type star) is the inner Lagrangian point. Notice that the accretion disk of the compact object is not completely filling its Roche lobe. The accretion disk extends out to approximately the circularization radius, which is about 65% of the Roche lobe radius. This figure is not to scale with Figure 2.2. Image courtesy of R. Hynes.

is the main source of X-ray production in these systems.

The interest of this work is directed toward a class of LMXBs known as soft X-ray transients (SXTs).¹ SXTs are characterized by long periods of quiescence interrupted by intense outbursts where their luminosity can increase by > 100 times. These outbursts can be observed throughout the entire electro-magnetic spectrum, including the radio, optical and X-ray wavelengths (van Paradijs and McClintock 1995). SXTs

¹These systems are also referred to as X-Ray Novae (XRN) or dwarf novae. Perhaps the most appropriate term for these systems is low-mass X-ray binary transients (LMXBTs) (Lasota 2001). For this work the term SXT will be used.

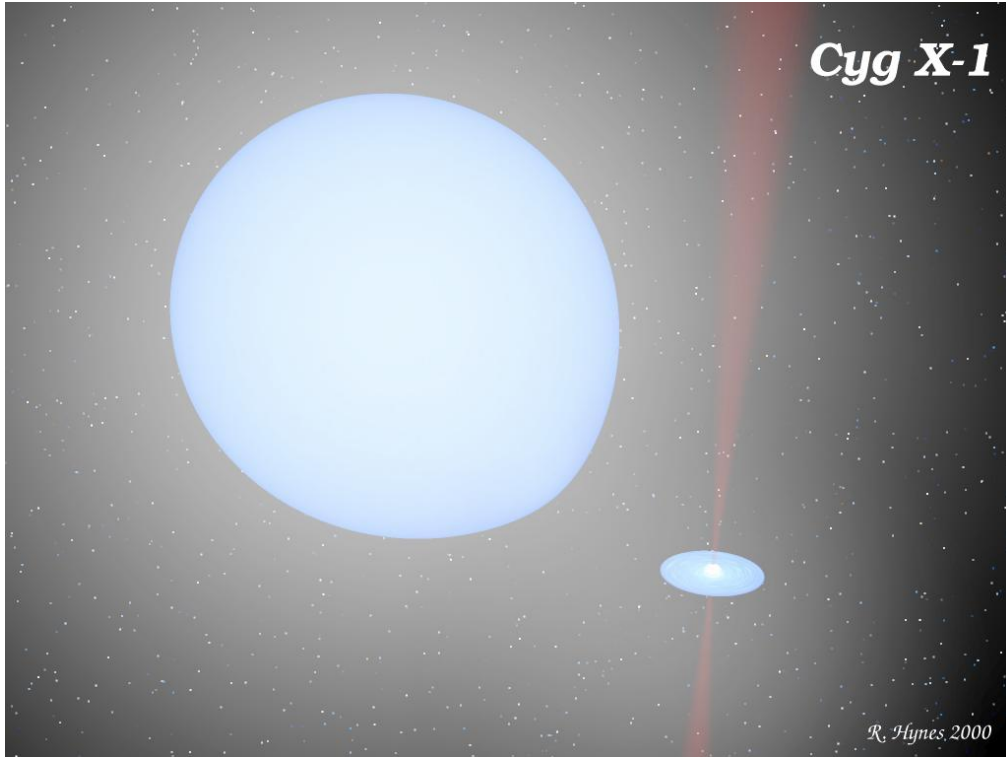


Figure 2.2: Approximate scale image of the Cygnus X–1 system as an example of a HMXB. Note that in comparison to Figure 2.1 the accretion disk of this system is relatively much smaller than the companion star. However, in this case there is a significant stellar wind. There is also an indication of highly collimated jets in this source which is not always present. This figure is not to scale with Figure 2.1. Image courtesy of R. Hynes.

containing primary objects of mass $> 3M_{\odot}$, a majority of all SXTs, are of particular interest because they are most likely black holes. The interest in black hole systems is derived from the desire to test General Relativity under extreme conditions and to find direct confirmation for the existence of an event horizon. The event horizon, defined as the point at which nothing traveling less than or equal to the speed of light can escape the gravitational field of the black hole, is located at $1 R_{\text{Sch}}$, the Schwarzschild radius,

$$R_{\text{Sch}} = \frac{2GM}{c^2} \approx (3 \text{ km})(m M_{\odot}) \quad (2.1)$$

where G is the gravitational constant, c is the speed of light and M is the mass of the black hole, M_{\odot} is the mass of the Sun (1.99×10^{30} kg) and m is the mass of the black hole in solar masses. Confirmation of the existence of an event horizon would provide further validation of General Relativity and possibly support the divide

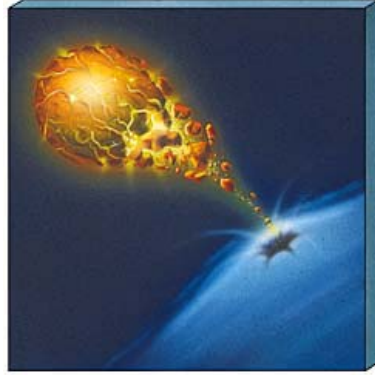


Figure 2.3: Artist's conception of extreme conditions near a black hole (Chaisson and McMillan 2002).

between Quantum Mechanics and General Relativity.

Proof of the existence of an event horizon may provide definitive proof of an object being a black hole as predicted by General Relativity. This is very difficult because it requires confirmation of the absence of something (i.e. a surface). Very interesting work is being done to prove that the currently known black hole candidates have event horizons. Work has been done by Narayan and Heyl 2002 to show that the absence of Type I X-ray bursts (bursts occurring as a result of thermonuclear explosions on the surface of many neutron stars) in black hole candidate systems is proof for the absence of a surface. Additional work, comparing neutron star SXTs and black hole candidates SXTs in quiescence makes use of the low luminosities in the black hole systems as proof in favor of the existence of event horizons (Garcia et al. 2001).

SXTs containing a black hole candidate provide potential laboratories for the study of physics at densities of $\rho \sim 10^{15} \text{ g cm}^{-3}$, temperatures of $T \gtrsim 10^7 \text{ K}$ and gravitational fields of $g \sim 10^{11} g_{\text{Earth}}$. These conditions cannot be physically reproduced on Earth. It is amusing to think about what might happen to matter under the duress of the conditions very near a black hole, see Figure 2.3 for an artist's interpretation of these circumstances. The figure shows an ordinary star approaching the event horizon of a super-massive black hole.

From an astrophysical point of view, SXTs are particularly interesting sources to observe because they provide the opportunity to study accretion physics at variety of rates over a relatively short period of time (weeks to months). Accretion rates and processes can vary dramatically during the evolution of an SXT outburst. See

Figure 2.5 for some black hole candidate SXT outburst light curves.²

Examples of black hole candidate SXTs observed by USA during outburst are XTE J1118+480 (see Wood et al. 2000 for the details of USA observations), XTE J1859+226 and XTE J1550-564. XTE J1859+226 and especially XTE J1550-564 are central to work in later chapters. USA data on XTE J1859+226 will be studied in Section 3.8.1 and XTE J1550-564 is the subject of Chapters 5 and 6. It is interesting to note that both of these sources have been shown to be microquasars (i.e. they have both been shown to produce relativistic jets and ejections). microquasars take their name from certain AGN, quasars, known to produce extremely intense collimated radio jets. Jet production in SXTs may be very important in understanding the overall accretion process, because there may be links between jets and quasi-periodic oscillations and other phenomena present in SXTs. Building evidence seems to indicate that most if not all SXTs are capable of producing jets or ejections, detectable through their radio emission, during the low-hard state of their outbursts (Fender 2001). An extensive discussion of SXT outbursts and their states is given in Section 2.4.

2.2 Origin and Evolution of X-Ray Binaries

Based on terrestrial experience, Earth orbiting a single stellar object, the existence of binary star systems may seem peculiar to the casual observer. However, current theories of star formation, which indicate that stars form in groups, explain why the majority ($\sim 60\%$ of stars *are* contained in binary systems. It is assumed that gravitationally bound gas collapses to form multi-star systems which are also gravitationally bound. ‘Exceptional’ stars are individual stars (e.g. the Sun) that are thought to be a result of disrupted binary or triple star systems. As is evinced by the majority of stars being contained in binary or other multi-star systems, the Sun and other individual stars are the exception. For more detail on the processes governing star formation see Larson 1995, and references therein.

Once a multi-star system is formed, natural stellar evolution, as governed by the initial and environmental conditions, will proceed. Some of these group systems will then form, by a process which is not well understood, LMXBs. Current theories

²A light curve is simply a plot of the source intensity (flux or luminosity or count rate, etc.) as a function of time.

suggest that LMXBs form from triple star systems or from extremely fortuitous conditions in binary star systems, which allow the two stars to remain in a close orbit after one of the objects goes supernova and forms a black hole or neutron star. The system must be the proper distance with the proper mass ratio to insure that the lighter star does not merge with the heavier star or is not blown away during the supernova explosion. See Verbunt and van den Heuvel 1995 and references therein for a more complete description of LMXB formation.

2.3 Overview to Accretion Processes

It has been well established that the main source of power, in X-ray luminous astronomical sources, is the release of gravitational potential energy as matter is accreted onto a compact object. There are many forms by which accretion may occur and several possibilities for the origin of accreted matter. Since a complete discussion of accretion may be found in many books, here only a brief summary of accretion is given. For a more detailed discussion of accretion, see Frank et al. 2002.

2.3.1 Sources for Accreted Matter

There are two possible sources from which matter may be accreted onto a compact object. The first is the interstellar medium. The second is from a nearby object, such as a star, giving off material. This latter source, the companion star in SXTs, is the most relevant to accretion processes involved in the work to be presented here. In an SXT, or more generally an X-ray binary system, there are a variety of means by which matter may be accreted. The two most common possibilities are accretion through Roche lobe overflow and through a wind from the companion. It is possible for both processes to occur simultaneously.

Wind fed accretion typically occurs in HMXBs, when the massive companion does not fill its Roche lobe but instead emits a nearly isotropic stellar wind, see Figure 2.2. As the compact object passes through the stellar wind, gas is captured by the compact object's gravitational field and subsequently accreted. SXTs, generally LMXBs, accrete matter from the companion through Roche lobe overflow. For a definition of the Roche lobe see Figure 2.4. Roche lobe overflow occurs when the companion star is large enough to contact and spill out of the equipotential surface which defines its Roche lobe. The gas then naturally falls into the potential well of

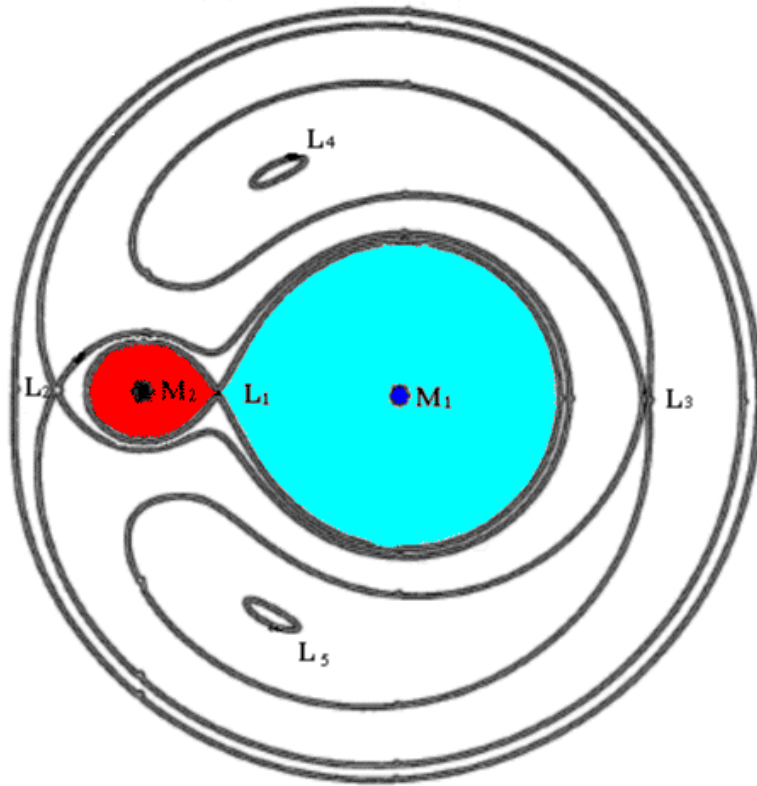


Figure 2.4: Equipotential surfaces in a binary system showing the Roche lobe. In this figure, M_1 is the mass of the companion star and M_2 is the mass of the compact object. Lagrangian points are labeled L_{1-5} and equipotential surfaces are shown with the solid lines. The equipotential which is filled in red about M_2 and aqua about M_1 makes up the Roche lobe for each of the stars in the binary system. Notice that these two Roche lobes meet at the L_1 Lagrangian point. The L_1 Lagrangian point, often referred to as the inner Lagrangian point, is a saddle point and is where matter is transferred to the compact object when the companion star fills its Roche lobe. Figure courtesy of Zac 2002.

the compact object.

Once the material leaves the companion and becomes trapped in the gravitational well of the compact object, there are many (not yet fully understood) processes which ultimately decide the fate of that matter. A great deal of theoretical and observational work is being done to understand the accretion physics around compact objects. Debate is most intense concerning accretion processes very near to the compact object, especially in black hole candidate systems.

2.3.2 Accretion Mechanisms

Bondi Accretion

The simplest possible accretion scenario involves a spherically symmetric and steady flow onto the compact object. Spherically symmetric implies that the relative (non-radial) motion between the compact object and the radial accretion flow is negligible. In this case the angular momentum and magnetic fields of the accreted medium may be neglected (Bondi 1952; Frank et al. 2002). It is further assumed that viscosity plays no role in the accreting gas. In nature, Bondi accretion may be used to approximate accretion of gas from the interstellar medium onto a star. Bondi accretion is not well suited to describing accretion in binary systems.

Angular Momentum Dissipation

Bondi accretion is not an adequate description of most accretion processes. After other Bondi accretion scenarios, such as accretion from the interstellar medium onto a star having relative motion, the next most simplistic view of accretion is the Shakura-Sunyaev α -disk model (Shakura and Sunyaev 1973 and see also Frank et al. 2002 for an in depth discussion of accretion). The α -disk parameterizes turbulent viscosity in order to simply describe the most typical accretion scenarios. In general any matter accreted onto a compact object will have angular momentum. As the matter accretes the angular momentum must be transported outward. The properties of angular momentum transport, including the timescale, are governed by viscosity. The model uses α , as defined by

$$\nu = \alpha c_s H$$

where ν is the kinematic viscosity, c_s is the sound speed in the disk and H is the disk half thickness, to parameterize the effective viscosity. Whether accretion occurs via Roche Lobe overflow or is wind fed, the most natural way for angular momentum to be transported is through the formation of an accretion disk via viscous forces in the accreting gas. Viscosity flattens out the accreting matter, by transferring angular momentum out and matter in. During this process frictional forces cause the inner regions of the disk to heat to temperatures of order 10^7 K (1 keV).

The α -disk formalism is a phenomenological model which allows one to avoid the details of hydrodynamic, magnetohydrodynamic and turbulent processes by which the frictional forces in the disks are created. These forces are extremely important

as they provide the means for the transport of angular momentum outward and ultimately the accretion of matter onto the compact object. More recent work has attempted to explain the mechanism of the previously *assumed* viscosity in accretion disks. Balbus and Hawley 2002; Balbus et al. 1996 and references therein discuss a magneto-rotational instability (MRI) as the source of viscosity allowing outward angular momentum transport in accretion disks. The key point of the MRI is that shear instabilities may form in weakly magnetized plasmas which are differentially rotating. These instabilities provide a natural means of generating turbulent viscosity. The MRI can be scaled in terms of the ‘standard’ α -disk formalism to make predictions about the effective viscosity (Balbus et al. 1996).

Very near to the compact object the accretion flow is not likely to be a thin disk and the process becomes much more complicated. Accretion physics in these inner regions is the most interesting, because these regions are precisely where the effects of strong gravity and new physics are expected to be observable. There are many theoretical models which purport to describe accretion very near to the event horizon of black holes. There are many reasons why the α -disk model is insufficient. In its most basic form the α -disk model assumes a thin disk which extends down to the last stable orbit, material from the disk then free falls onto the compact object. In black hole systems the last stable circular orbit is outside of the event horizon, within a few R_{Sch} . At this point, circular orbits around the black hole become unstable. The α -disk model cannot account for accretion in the region between the inner edge of the accretion disk and the compact object. Further, there is a growing body of observational evidence indicating that the accretion disk is often truncated much farther out (up to several hundred R_{Sch} , depending on the state of the system) than the last stable orbit. Additionally, within the accretion disk there are many factors other than the viscosity, which must be considered. There is turbulence, there are magnetic fields and there are most likely multiple accretion flows present.

Aside from an accretion disk which extends down to the last stable orbit, there are many other possible models to describe accretion in the areas near to the black hole. Here models of advection-dominated accretion flows (ADAFs) and their derivatives models are briefly discussed. ADAFs are geometrically similar to Bondi accretion, because they are quasi-spherical and the radial velocity of the accreted gas is near to the free-fall velocity. ADAFs are much more complex than pure Bondi accretion. They account for viscosity and rotational velocities within the accreted gas. These

effects make ADAFs a much more realistic description of accretion, at radii smaller than that of the accretion disk inner edge, onto black holes. One of the interesting points about ADAFs is that they are not very luminous. This is because the time scale for thermal energy, created by viscosity and adiabatic compression, to escape the accreting gas is longer than the time scale for the gas to be accreted. Because the flow is an inefficient radiator, the trapped energy is advected into the central black hole instead of contributing to the luminosity (see Narayan et al. 1998 for a review of ADAFs).

The validity of simple ADAF models has been questioned and other models have been proposed (e.g. ADAF plus jet) (Yuan et al. 2002). Following the introduction of ADAF models, derivative models, which accounted for convection and the possibility of outward and inward flows of material, were proposed. Models accounting for convection are often referred to as convection-dominated accretion flows (CDAFs), see Quataert and Gruzinov 2000 for example. Generalizations of the ADAF include the possibility of inflows and outflows are known as advection-dominated inflow outflow solutions (ADIOS), see Blandford and Begelman 1999 for example. More work is still needed in connecting these accretion flows with jet formation in LMXBs and an α -like accretion disk (i.e. a thin disk which also includes effects such as the MRI, dependence of the viscosity on radius and disk height, etc.).

2.3.3 Accretion Geometries

The actual accretion flows present in black hole SXT systems are not likely to be made of only an α -disk or only an ADAF. Many geometries with two or more accretion flows are possible. The term geometry is used to refer to several questions surrounding the accretion flow: Is the system wind fed or fed through the Roche lobe? How large is the accretion disk? Does the disk extend to the last stable orbit? Does the disk fill the entire Roche lobe? Is there a corona?³ Where is the corona? etc.

Spectral observations of LMXBs have shown that the model of a thin accretion disk extending down to the last stable orbit and then dumping into the black hole is too simplistic. The energy spectra show a power law feature extending, in some cases, to gamma ray energies, which cannot be accounted for by an accretion disk alone. This observational evidence indicates that accretion around black hole SXTs

³A ‘corona’ or transition layer is a geometrically thick accretion flow which, through inverse Comptonization, is the most likely source for the power law tail seen in X-ray binary energy spectra.

is made of an optically thick and geometrically thin accretion disk (α -type disk) plus an optically thin Comptonizing medium (which could be an ADAF or generalized ADAF model). Several theoretical two-component accretion geometries have been proposed and analyzed in order to account for these observations.

Some of the results from this analysis have been summarized by Poutanen 1998 and are recounted here. There have been four basic geometries proposed in order to explain the energy spectra in seen in X-ray binary systems: sandwich, magnetic flares, cloudlets and sombrero. In the sandwich model a standard thin disk with a slab corona covering most of the disk is assumed. By contrast, the magnetic flares model assumes a patchy corona covering the accretion disk. These patches are considered to be active regions capable of inverse Comptonization. The cloudlet model assumes a cold disk disrupted, within a hot corona near the compact object, into optically thick dense cool clouds. Finally, the sombrero models assumes an accretion disk which extends only a short distance into the corona. In this case the corona surrounds the compact object and is quasi-spherical. The accretion disk may be truncated at tens to hundreds of R_{Sch} from the compact object. Spectral analysis has shown that the cloudlet and sombrero models give the best description of the accretion geometry in black hole LMXBs. It is very difficult for spectral observations to distinguish between these two models.⁴ These models are very similar because they both involve a cold, optically thick and geometrically thin accretion disk which surrounds a central hot corona. For the purposes of the following sections and chapters, this geometry is assumed for black hole SXTs.

2.4 Soft X-Ray Transient (SXT) Outbursts

The properties of SXTs are dependent upon the mass and type of the companion star and the nature of the compact object: white dwarf, neutron star or black hole candidate. Additionally the initial conditions of the outburst are relevant. This can be seen from Figure 2.5, which shows the light curves of several black hole candidate

⁴The cloudlet model provides an interesting and plausible mechanism for generation of high-frequency QPOs (HFQPOs), see Section 2.4.1 for a definition of QPOs. As the accretion disk moves toward the compact object, the cool cloudlets, within the hot corona, will orbit more closely to the compact object. This will cause these ‘blobs’ to heat and their orbit period could define the frequency of the observed HFQPOs. Because the orbits of the cloudlets are somewhat randomly distributed, it is expected that the HFQPOs will occur at different frequencies. This could be consistent with the observed variability of HFQPO frequencies.

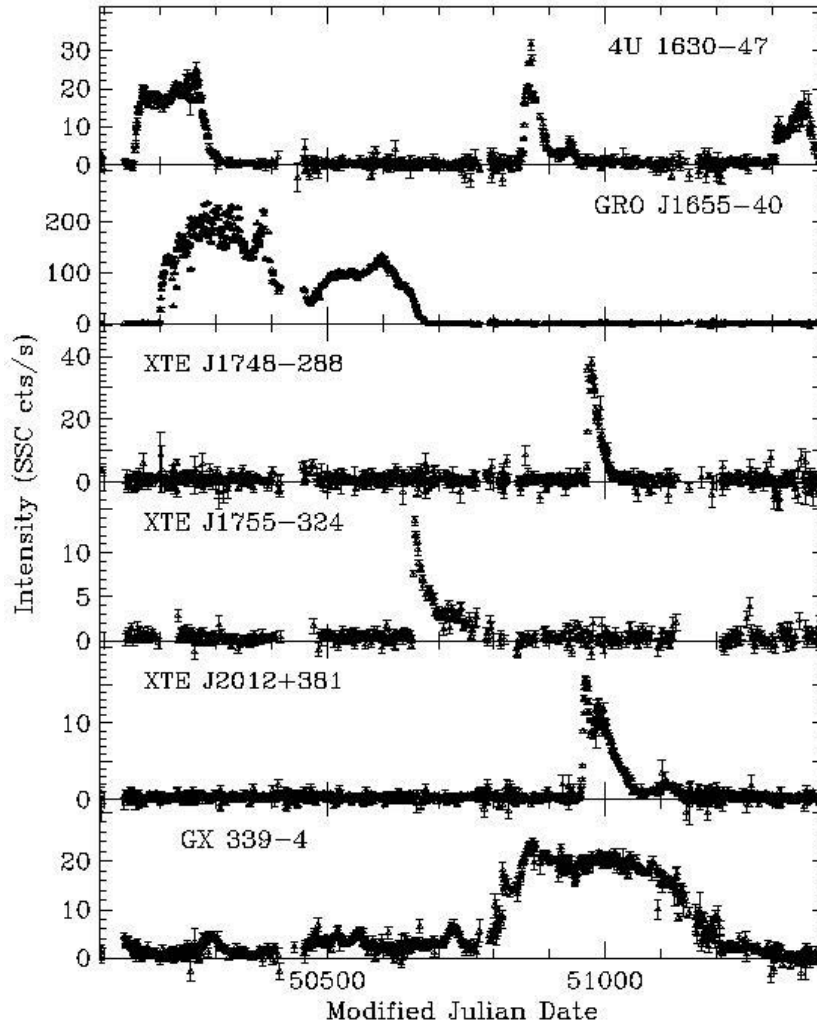


Figure 2.5: RXTE/ASM light curves from several different black hole candidate outbursts, figure from Bradt et al. 2000.

SXTs. The source, 4U 1630-472, in the top panel of the figure, shows multiple outbursts each having widely different profiles. Although they are not shown in the figure, several other black hole SXTs have had multiple outbursts each having very different profiles from the others. Aside from 4U 1630-472, XTE J1550-564 is another source in which multiple outbursts have been seen (three to date). The outbursts of XTE J1550-564 are discussed in greater detail in later chapters. Although Figure 2.5 shows that the light curve profiles may vary significantly from source to source and outburst to outburst, when looked at more closely these systems and their outbursts are actually very similar. When the energy spectral properties and timing properties

of these sources were studied in detail, it was shown that outbursts transition among some qualitatively well defined states.

2.4.1 SXT States and Their X-Ray Spectral and Timing Properties

In general, an SXT outburst can be described by its evolution through spectral and timing states. Figure 2.6 gives the generic timing and spectral features of the outburst states and shows the possible accretion geometry during each of the states. It is assumed that changes in timing and spectral properties during the outburst are a result of changes in accretion.

The spectral qualities of a state are determined by the energy distribution of the emitted photons and the timing properties are determined by small changes in flux on short timescales. SXT energy spectra are made of two primary components, a black body,

$$f_{bb}(\lambda, T) = \frac{2hc^2/\lambda^5}{\exp(\frac{hc}{\lambda kT}) - 1}, \quad (2.2)$$

and a power law, $f_{pl} \propto E^{-\Gamma}$, where h is the Planck constant, k is the Boltzmann constant, λ is the wavelength, ν is the frequency, c is the speed of light, T is the black body temperature, E is the photon energy, and Γ is the power law index. Changes in the SXT state are accompanied by changes in the relative strength of these two components in the X-ray spectrum.

The timing features are revealed as low Q and high Q quasi-periodic signals in the power spectral density (PSD) function.⁵ The low Q features are often referred to as broad band variability, these features can span several decades of frequency. High Q features are quasi-periodic oscillations, comparably narrow, but not sharp by standards of pulsar peaks, and come at both low and high frequencies. They are often referred to as low-frequency quasi-periodic oscillations (LFQPOs) and high-frequency quasi-periodic oscillations (HFQPOs). As shown in Figure 2.6, specific states are identifiable by the strength, absence, or presence of specific timing and spectral features.

Generally, there are thought to be five states which an SXT may occupy (Done

⁵High Q may be somewhat misleading as used here. The Q is in fact not very high at all, these timing features are only quasi-periodic and thus have significant width. In general QPOs have $Q \equiv f/\Delta f > 2$, where f is the centroid frequency and Δf is the full width at half maximum (van der Klis 1989b).

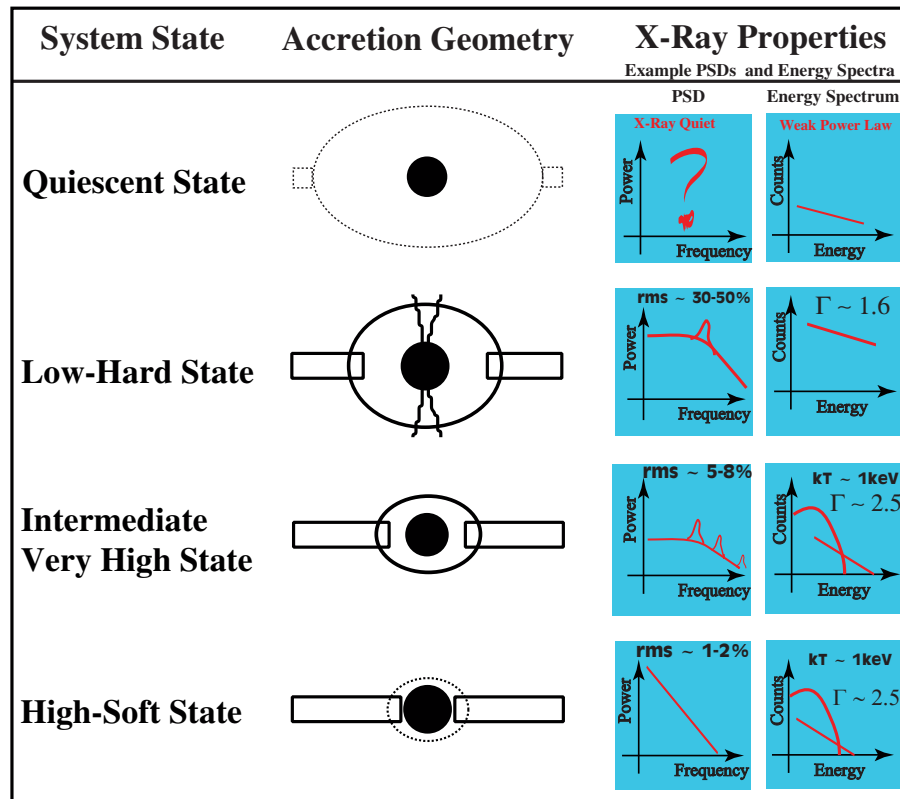


Figure 2.6: The geometry, and spectral and timing properties are shown for each of the five SXT outburst states. Under **System State** the common name for each state is given. The **Accretion Geometry** shows the outburst geometry for each state, approximately a sombrero geometry. The filled black circles represent the compact object. The oval shapes represent the quasi-spherical Comptonizing medium and the rectangular shapes are the optically thick accretion disk. In the quiescent state very little material is being accreted and the disk is thought to be unstable, this is why the accretion disk and corona are represented with dashed lines. The lines leaving the corona in the low-hard state represent jets. There are two panels under **X-Ray Properties**. These are examples of the timing (as seen in a PSD) and energy spectral properties during each state. The example PSDs show both the broad band variability, the very low Q features, and the quasi-periodic phenomena, the higher Q features sitting on top of the broad band variability. The quiescent state has a question mark for its PSD, because the timing properties of that state are not well studied. The example energy spectra show the black body component as a large hump and the power law as a straight line. Several variables are shown: kT represents the accretion disk black body temperature, Γ is the power law index and rms is the total percent root mean square variability.

2002):

- The quiescent state (QS) is the state most frequently occupied by SXTs. It is

thought to be characterized by an unstable α -accretion disk surrounding some form of a quasi-spherical optically thin and geometrically thick accretion flow. This quasi-spherical flow is often referred to as a corona or transition layer, for the remainder of this work it will be referred to as TL. Observations have shown the energy spectra to be dominated by a power law with a weak flux (Done 2002). The timing properties are not well studied because of the paucity of X-ray photons from a quiescent source.

- The low-hard state (LS) is characterized by low luminosity in the soft X-ray band and a strong high energy flux as shown by a power law in the energy spectrum. Here the α -disk is stable, but truncated at many R_{Sch} . The disk surrounds the TL, which acts as the source of the high energy power law. The power law is a result of inverse Comptonization in the TL of seed photons from the α -disk. PSDs calculated during the LS indicate broad band variability of 30–50% root mean square (rms) which is accompanied by low-frequency quasi-periodic oscillations (LFQPOs). Typically, a source moves through the LS at the beginning and end of an outburst. Relativistic jets and ejections are commonly observed during the LS.
- The high-soft state (HS) has a very high luminosity which comes almost entirely from an α -disk, which shows as a nearly pure black body in the energy spectra. There is often an extremely weak power law component. The PSDs generally show 1–2% rms as a simple power law (i.e. the noise in the HS PSD is not band limited as it is in the LS, IS and VHS). In the HS the inner edge of the α -disk, based on energy spectral work, seems to be the closest it comes to the compact object.
- The intermediate state (IS) and very high state (VHS) have nearly identical timing and spectral properties, but occur at different luminosities. The VHS has a much greater X-ray intensity than the IS and the HS. The IS and VHS energy spectra are dominated by a black body spectrum and a weak power law tail (stronger than in the HS). The PSDs show 5–8% rms variation and may show both LFQPOs and HFQPOs.

In this interpretation of the SXT states a sombrero geometry, see Figure 2.6 has been assumed. It is important to note that geometries which include magnetic flares in the truncated α -disk may be relevant to the spectral character of certain

outburst states. In the HS and IS/VHS there are weak power law components in the energy spectra which may be a result of magnetic reconnection in the disk (Done 2002). Further, because the accretion disk extends much closer to the compact object during the IS/VHS and HS, magnetic flaring may become more important. See Balbus and Hawley 1991 and Hawley and Balbus 1991 for a discussion of magnetic flares in accretion disks. Observations taken during the QS of SXTs indicate an α -disk that is unstable and highly truncated. The interpretation SXT states described above assume that the disk is truncated during the QS and when an outburst begins, accretion through the disk increases, pushing the inner edge closer to the compact object. However, observational evidence seems to support that in the QS the α -disk is unstable and highly truncated and that when an outburst begins, accretion through the disk increases. As this occurs the disk become more luminous and the TL shrinks. In the IS/VHS and HS it is possible that the inner TL completely collapses into an α -disk configuration and magnetic flaring becomes a more important contributor to the power law tail in the energy spectrum. It is also possible, and perhaps more likely, that the TL remains during those states, but has a dramatically weakened flux. In this case, magnetic flaring may still be important.

The underlying geometry is still assumed to be sombrero. The necessity for a sombrero geometry is further supported by the best candidate model for SXT outbursts: the disk instability model (DIM). The DIM relies on a thermal-viscous instability in the α -disk as a trigger for the outburst. In order for the DIM to give a qualitatively accurate reproduction of SXT outburst observations, it requires that the α -disk be irradiated by X-rays near the central compact object and be truncated at $> 100 R_{\text{Sch}}$ during the QS. The accretion disk will remain truncated and material will accumulate until the temperature and viscosity reach a point of instability, causing a sudden dramatic increase in the accretion rate through the disk. For a complete review of the DIM see Lasota 2001 and references therein.

2.4.2 Properties of SXT Outbursts in Multiple Wavelengths

Simultaneous observations of SXTs in multiple wavelengths are imperative to gaining a complete understanding of accretion physics. This is because there are limited physical means of producing photons in different wavelengths and energy distributions. These types of simultaneous observations are often referred to as multi-wavelength campaigns. Recent radio observations of LMXBs during outburst indicate that most,

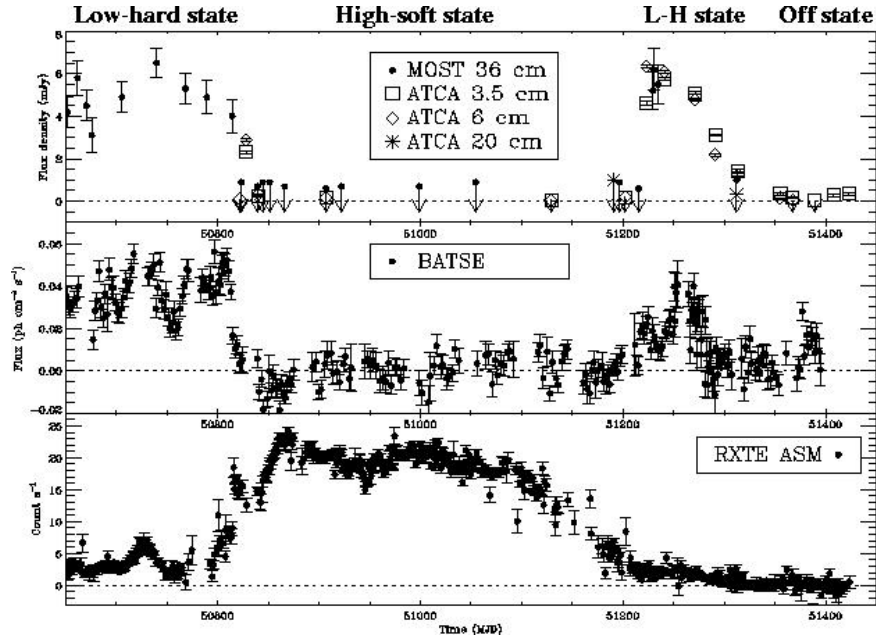


Figure 2.7: Radio, BATSE and ASM observations of GX 339-4 during outburst, figure from Corbel et al. 2000. This figure is given as an example of how different wavelengths offer new insights into the physical processes causing the outburst. This figure shows several wavelengths as a function of time over the outburst; The top panel shows radio emission, the middle panel shows BATSE flux (20–100 keV) and the bottom panel shows the ASM flux (1.5–12 keV). The outburst states are labeled at the top of the figure.

if not all, LMXBs are capable of producing collimated jets and relativistic ejections (Fender 2002). These recent findings serve as an example of how critical aspects of an SXT outburst might be missed if only observing in a single wavelength. Until these radio observations were performed on multiple LMXBs and SXTs, it was thought that only a special class of galactic sources, known as microquasars, were able to produce relativistic jets.

Figure 2.7 emphasizes the importance of multi-wavelength campaigns in the study of SXT outbursts. The figure shows an outburst of GX 339-4 in three different wavelengths. GX 339-4 is known to be a microquasar as a result of the strong radio emission (top panel) during the initial and final low-hard state. During both LSs, the BATSE flux (20–100 keV) (middle panel) is strong and the ASM is weak or absent. During the high-soft state, BATSE is absent and the ASM flux is strong. Further, note that the RXTE all-sky monitor (ASM) flux (1.5–12 keV) (bottom panel) increases as the BASTE and radio flux become undetectable and then the opposite occurs as

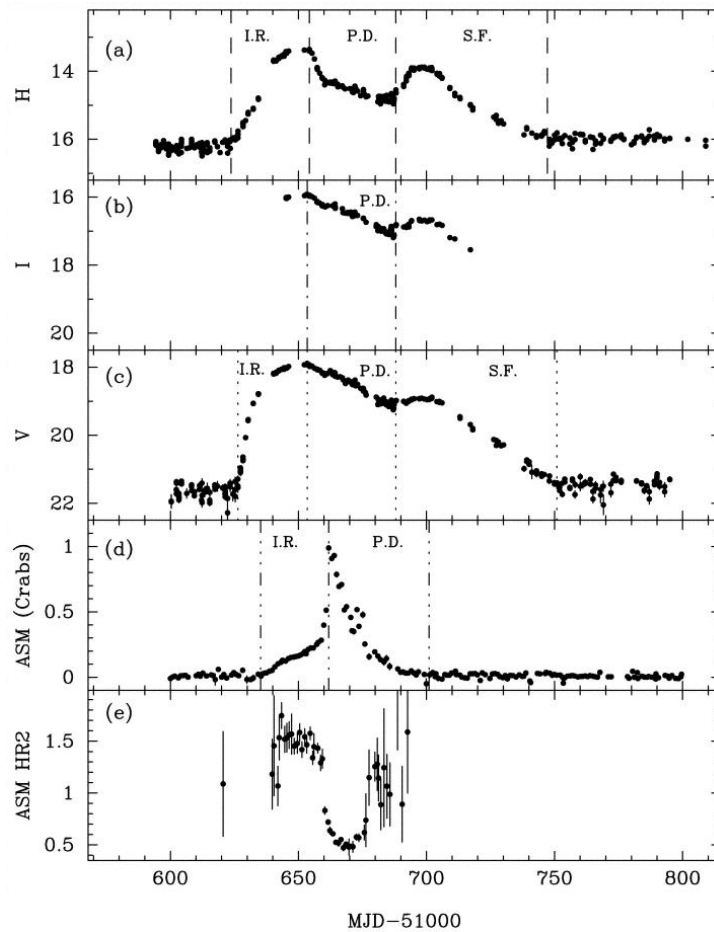


Figure 2.8: Optical/IR and X-ray light curves and ASM hardness ratio of XTE J1550–564 during the 2000 outburst, figure from Jain et al. 2001. Panel a shows the near infrared (IR) (H-band) behavior of XTE J1550–564 during the 2000 outburst. Panels b and c show the optical I-band and V-band behavior, respectively. Panel d shows the crab normalized ASM light curve. Panel e shows the ASM HR2 hardness ratio (5–12 keV/3–5 keV). The initials I.R., P.D., and S.F. stand for initial rise, primary decay and secondary flare, respectively.

the system moves back into the final low-hard state (Corbel et al. 2000). This is a very typical outburst scenario for SXTs. From these multi-wavelength observations several things are immediately apparent. First, there is a strong high energy flux, the BATSE light curve (middle panel), before and after the much softer ASM shows that an outburst has occurred. Contemporaneous with the BATSE flux is a strong radio component. Together these two observations indicate that there is a relativistic jet (radio data) and a highly luminous TL (BATSE data) during the low-hard state of the

outburst.⁶ Adding in the ASM observations (bottom panel), there is an indication that a strong flux from the accretion disk acts to quench the jet and the corona. This implies a link between the existence of a strong corona and a relativistic jet, a common characteristic of SXT outbursts.

Figure 2.8 shows optical, infrared (IR) and X-ray light curves for the XTE J1550–564 outburst to be discussed in Chapters 5 and 6. The optical light curves shown indicate features in XTE J1550–564 which are similar to those observed in GX 339-4. BATSE data is shown for XTE J1550–564 in Chapter 6 which demonstrates almost identical behavior to that seen in GX 339–4 as depicted by Figure 2.7. Here, the results of optical and infrared observations, Figure 2.8, of the XTE J1550–564 outburst are discussed. There is an optical/IR peak during the initial low-hard state and the final low-hard state. These peaks, although not simultaneous, correspond to peaks in the BATSE data. Radio observations during this outburst indicate that the initial optical/IR maximum are related to a discrete relativistic ejection during the transition from the initial low-hard state to the intermediate state. Further, radio observations indicate that a jet is possibly reforming as XTE J1550–564 moves back into the final low-hard state. This jet formation is accompanied by an optical/IR maximum, the second observed maximum (Jain et al. 2001; Corbel et al. 2001). Additional information is gained by the temporal separation of the optical/IR maximum and the X-ray maximum. This separation is of order days, the same order as the viscous timescale, the natural timescale for movement of the accretion disk. This supports the assumption of an accretion disk which is truncated at several hundred R_{Sch} at the beginning of the outburst and moves in very close to the compact object throughout the rise of the outburst, as shown by the ASM light curve in Figure 2.8 (Jain et al. 2001). Last it is worth noting that this type of optical/IR behavior has also been seen in Aquila X-1 and GRO J1655-40 (see Jain et al. 2001 and references therein).

Based on the results presented in this section, the value of multi-wavelength observations is made clear. In later chapters, the relationship between phenomena, such as quasi-periodic oscillations, and light curves in different wavelengths is used to explain the mechanism behind timing features in SXT outbursts.

⁶Radio observations of LMXBs often show flat or inverted spectrum. Under the interpretation of jet models (Hjellming and Johnston 1988), this indicates that the radio flux is emitted as synchrotron radiation from a collimated optically thin medium (plasma outflow from the compact object).

Chapter 3

The Unconventional Stellar Aspect (USA) Experiment

3.1 Overview of USA

In this chapter an overview of the USA experiment is given. The summary given here is not intended to be complete. For more detailed discussions of the USA experiment see Shabad 2000 and Ray et al. 2001. There are other USA science working group documents which give detailed accounts USA specific issues. As this chapter goes on and it becomes appropriate, the reader will be referred to these documents. In this chapter, the topics to be discussed are the USA collaboration, current and past science from USA, the USA and ARGOS missions, specifications and unique attributes of USA, scientific objectives and obstacles encountered.

3.2 The USA Collaboration: People and Progress

Unlike most recent X-ray astronomy missions, the USA experiment is a relatively small collaboration between, primarily, the Stanford Linear Accelerator Center (SLAC), funded by the Department of Energy (DOE), and the Naval Research Laboratory (NRL), funded by the Department of Defense (DOD). While the USA experiment was operational, the small size of the collaboration gave great freedom in scheduling observations and allowed for everyone to share significant experimental and scientific responsibilities. The following people from SLAC and NRL were the primary contributors to the USA science working group. From SLAC: E. Bloom, D. Engovatov,

W. Focke, B. Giebels, G. Godfrey, P. Saz Parkinson, G. Shabad, D. Tournear and myself. Aside from one professor (E. Bloom) and SLAC staff scientists, this group is made of two post-doctoral researchers and five graduate students.¹ From NRL: R. Bandyopadhyay, G. Fewtrell, G. Fritz, P. Hertz, M. Kowalski, M. Lovellette, P. S. Ray, M. Wolff, D. Wood, K. Wood. Kent Wood is the principal investigator for the USA experiment. There were also lesser and more sporadic contributors from the following institutions: NASA Ames, U. Calgary, GMU, MIT, U. Oregon, Saddleback College, and Sonoma State University. Among these, the most notable is Jeff Scargle from NASA Ames, as he worked closely with our group. It is significant to note that very few of the people on this list were working solely on the USA experiment. Many were spread between several projects. However, everyone in the collaboration played a key role in the USA experiment and its scientific accomplishments so far.

To this date USA data has been used in the following publications:

- “USA Experiment Observation of Spectral and Timing Evolution During the 2000 Outburst of XTE J1550-564,” 2001, *The Astrophysical Journal*, Volume 561, Issue 2, pp. L183-L186, (This *Letter* provides the primary content of Chapter 5.),
- “Observation of X-ray variability in the BL Lac object 1ES1959+65,” 2002, *The Astrophysical Journal*, Volume 571, Issue 2, pp. 763-770,
- “USA Experiment and RXTE Observations of a Variable Low-Frequency Quasi-periodic Oscillation in XTE J1118+480,” 2000, *The Astrophysical Journal*, Volume 544, Issue 1, pp. L45-L48,
- A follow-up of the preceding paper, written by the group at NRL, “Disk Diffusion Propagation Model for the Outburst of XTE J1118+480,” 2001, *The Astrophysical Journal*, Volume 563, Issue 1, pp. 246-254,
- A paper in which USA data contributed 7 eclipsing observations to 122 RXTE eclipsing observations, “Eclipse Timings of the Low-Mass X-Ray Binary EXO 0748-676. III. Orbital Period Jitter Observed with the Unconventional Stellar Aspect Experiment and the Rossi X-Ray Timing Explorer,” 2002, *The Astrophysical Journal*, Volume 575, Issue 1, pp. 384-396,

¹Other contributors from SLAC and the Stanford community were a post-doc, Chris Chaput; graduate students, Han Wen and Mallory Roberts; and the SLAC Group EK data aid, Mark Yashar.



Figure 3.1: An Artist’s rendition of ARGOS. The rectangular object on the side of the satellite facing out of the page is the USA experiment.

- “Observations of GRS 1915+105 from the USA Experiment on ARGOS”, *Astrophysics and Space Science Supplement*, 2001, Volume 276, pp. 23-24,
- Many conference talks and posters
- Several other projects using USA data are now in the works, some of which are close to publication.

The work toward and consisting of the first paper in the list, relating to USA observations of XTE J1550–564, makes up the bulk of science in later chapters. Currently, there are several other projects in the works that make use of USA data. These other projects include theoretical work related to the first paper above, the results are presented in Chapter 6.

3.3 ARGOS and the USA Experiment

The USA experiment is mounted onboard of the *Advanced Research and Global Observation Satellite* (ARGOS), see Figure 3.1. In this section some of the key specifications of ARGOS and, in particular, the USA experiment are discussed. ARGOS

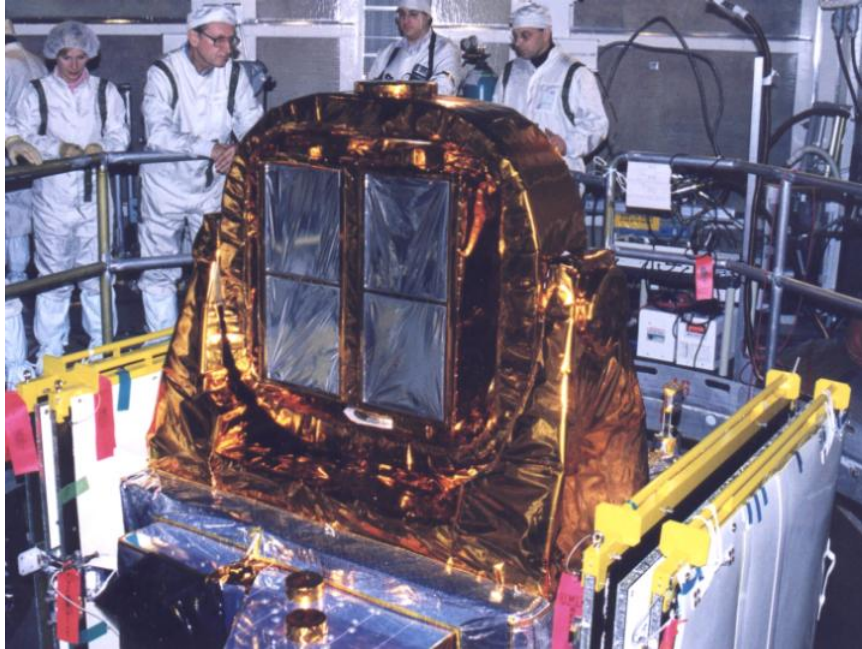


Figure 3.2: A photograph shows USA, as mounted on ARGOS, prior to launch. Some of the members of the USA team are seen in the background.

was built by Boeing as part of the Air Force Space Test Program. The mission was launched from Vandenberg Air Force Base, via Delta-II Rocket, after 10 attempts (a record number of attempts for the Delta-II at that time), on February 23, 1999. The launch delays were mainly due to poor weather. After successful launch ARGOS was put into an 800 km altitude, Sun-synchronous orbit at 98.8° inclination, as measured from the equator. With this orbit ARGOS passes over the Earth's equator at roughly the same local time each day. ARGOS was host to 9 experiments (several of these experiments, USA and others, are no longer operational).

USA science data collection began 1999 April 29. Detector 1 (detectors were labeled 0 and 1) was lost almost immediately after, in the beginning of 1999 June 8. The USA mission ended on 2000 November 16 when the second detector ran out of gas due to a slow leak. In contrast to the first detector which lost pressure very quickly, the second detector lasted several weeks after its leak was detected. Although the exact cause of the leaks in the proportional chambers can never be known, it is speculated that a micro-meteor or some other space debris, which pierced the detector pressure window (described below), was the culprit.

Figure 3.2 shows USA mounted on ARGOS prior to launch. The USA proportional

chambers are clearly outlined by the two silver rectangles, which are the aluminized mylar Sun shields, see Figure 3.4. These chambers were originally used in the NASA SPARTAN 1 mission and were extensively refurbished for use in the USA mission. The original USA design specifications began with these dual proportional chambers, each having $\sim 1000 \text{ cm}^2$ of effective area in the 3.5–7 keV energy range, see Figure 3.6. A copper collimator designed and built at SLAC gave USA a field of view of 1.3° FWHM with a 0.1° flat top. USA pointing control was designed to have an accuracy of 0.1° with a 0.03° jitter. The approximate energy range was 1–16 keV. While the USA experiment was running it was possible to collect science data in five different modes of operation, modes 1 to 5. These modes were characterized by different energy and time resolutions as well as different telemetry rates. The primary modes used to collect data during USA’s orbit lifetime were 1, 2 and 5. Event data discussed in later chapters were collected in modes 1 and 2. Data collected in these two modes have $32\mu\text{s}$ time resolution in 16 pulse height analyzer (PHA) channels, or energy channels, which have an approximate width of 1 keV. Data from modes 3 and 4 have $2\mu\text{s}$ time resolution in 8 PHA channels. Mode 5 was USA’s spectral mode, giving data with 10 ms time resolution in 48 PHA channels. These five modes fall into two different telemetry rates: low rate and high rate. In the low rate are modes 1, 3 and 5. The low telemetry rates for these modes implies a maximum count rate of 3070 cnts/sec and 2456 cnts/sec for modes 1 and 3, respectively. Although mode 5 is a low rate mode, because of its diminished timing resolution, it could handle an unlimited (for all practical purposes, the detector would have shut off long before mode 5 would fill) flux of X-rays before filling its memory buffers. Mode 2 and 4 are high telemetry rate modes having maximum count rates of 9950 cnts/sec and 7960 cnts/sec, respectively. Ideally high telemetry rate modes would have always been used, but due to limited space on the shared ARGOS data recorder USA was not allowed to run continuously at those modes.

3.4 USA Instrument Offset Pointing

The USA experiment was unique among X-ray astronomy experiments because it used an offset pointing mechanism and not an inertial pointing mechanism. Offset pointing implies that the USA experiment moves relative to ARGOS in order to point at a source and then continuously tracks that source as ARGOS moves through

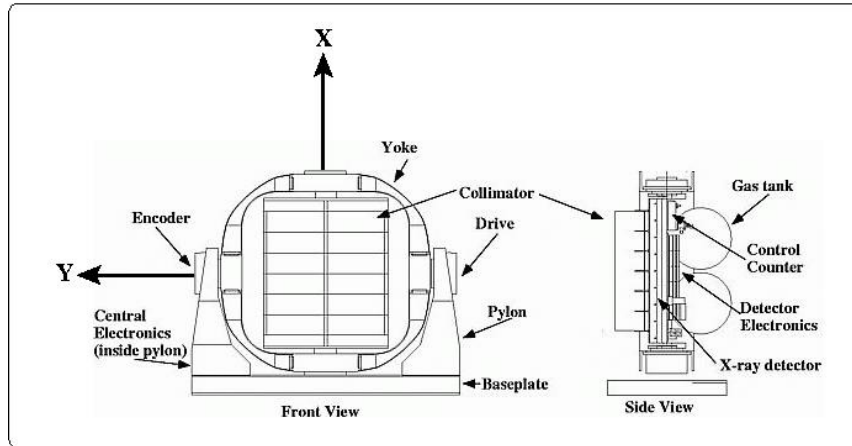


Figure 3.3: Schematic diagram of the USA experiment. Various features of USA are labeled. This diagram is shown to illustrate the USA offset pointing mechanism. The pitch encoder is labeled encoder by the Y -axis label. The yaw encoder is in a similar location at the X -axis.

its orbit (the pitch, see below, is continuously adjusted as USA tracks a source). For experiments using inertial pointing, the orientation of the satellite in its orbit is changed in order to observe a source. USA's use of offset pointing resulted from the requirement of nadir pointing for the Earth observing experiments onboard. A simple schematic of the USA pointing system is shown in Figure 3.3. Pointing was done by rotating the detector about the X -axis and Y -axis as shown in the figure. The amount of rotation about the X -axis is determined from the yaw encoder value and the amount of rotation about the Y -axis is determined by the pitch encoder value. Yaw and pitch values are given in the experiment housekeeping data. In the USA polar Sun synchronous orbit, negative yaw values pointed the detector toward the Sun and positive yaw values pointed the detector away from the Sun.

3.5 Schematic of USA Detectors

Figure 3.4 shows the individual components of the two identical USA detector modules. The detector components are from front to back: An aluminized mylar Sun shield to protect the detector from excessive temperature cycling; copper collimator, giving a limited field of view, allowing observations of single point sources; the collimator support mesh, which protected the very thin pressure window from the collimator; the $5.01\mu\text{m}$, $5.00\mu\text{m}$ of mylar and $0.01\mu\text{m}$ of nichrome, thick detector

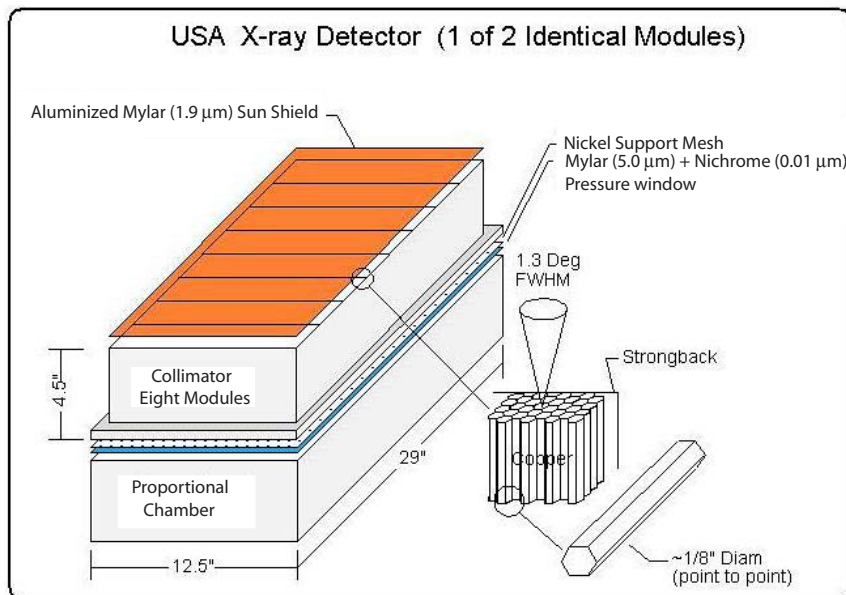


Figure 3.4: A breakdown of the components in each of the USA X-ray detector modules is shown.

pressure window which extended the USA energy acceptance down to 1 keV; finally, the base of the proportional counter chamber. The detector components are held in place by the copper collimator which is bolted down to the to the gold-plated aluminum base of the proportional chamber, thus holding the mesh and pressure window in place. See Figures 3.4 and 3.5 for the detector dimensions.

The USA detectors were multi-wire constant flow proportional chambers containing $P - 10$ gas, 90% Argon and 10% Methane, at slightly greater than 1 atm of pressure. See Figure 3.5 for the USA detector wiring. Each detector was made of two layers containing two interlaced anodes. There is a single perimeter veto wire for both layers (This prevents false detections due to charged particles entering through the sides of the detector). There is also a anti-coincident veto, which eliminates any event creating a signal on two wires. There are a total of five anodes.

3.5.1 Proportional Counter Basics

This section briefly describes the process by which photons are detected in proportional chambers. In the case of the USA detector, about 10–20% of photons with energies $\gtrsim 1$ keV can enter the proportional chamber by passing through the collimator and mylar/nichrome pressure window. All photons having energies $\gtrsim 2$ –3 keV

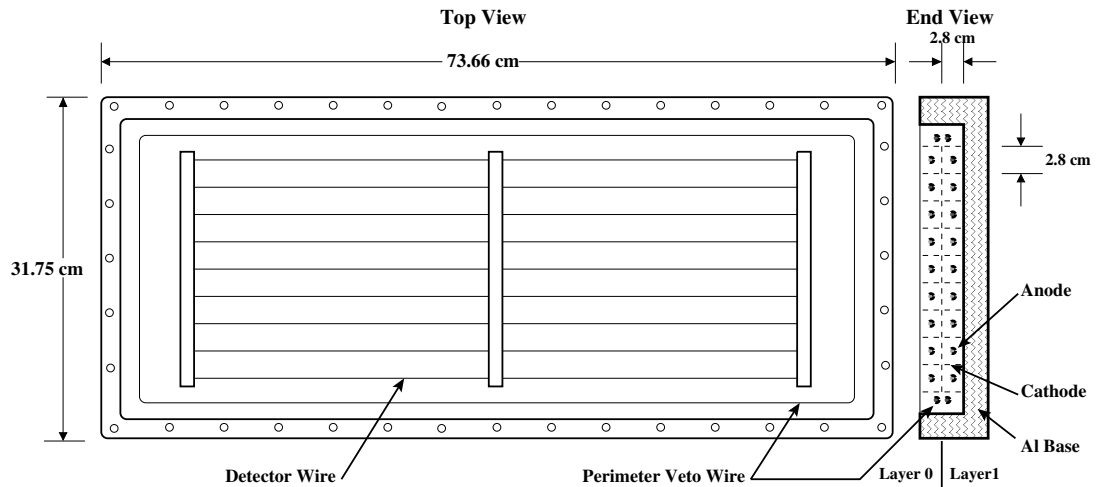


Figure 3.5: A schematic diagram of the USA proportional chamber is shown. Top and side views of the chamber are given. The side view illustrates that each chamber has two layers. Each layer has two anode wires. The chamber has a gold-plated aluminum base for which the dimensions are shown.

will pass through the pressure window. Once a photon has entered the chamber the likelihood of its detection is dependent upon its energy. Photons in the energy range $\sim 1\text{--}16$ keV will be detected according to the overall energy dependent efficiency of the chamber. Figure 3.6 shows the USA detector efficiency as a function of energy, for the complete details of the USA energy calibration see Saz Parkinson 2003. Photons with energies much greater than ~ 16 keV have a very small probability of being stopped in the chamber and, thus, go undetected.

In order for a photon to be detected after entering the chamber, that photon must collide with a molecule of the Argon gas (which is 90% of the chamber gas) and produce a photo-electron. This free electron will be accelerated in the strong electric field around the thin anode wire and subsequently collide with other gas molecules. These collisions will create more free electrons and the process will continue. The end result is an ‘electron avalanche’ in a small vicinity around the anode wire, which then causes a current to flow, see Figure 3.7.

If the incident photon is energetic enough, then enough electrons will be converted, in the avalanche, to produce a large enough current for the detector electronics to register a valid event. The specific size of this current is dependent upon the properties of the chamber and the energy of the incident photon. Generally, all proportional

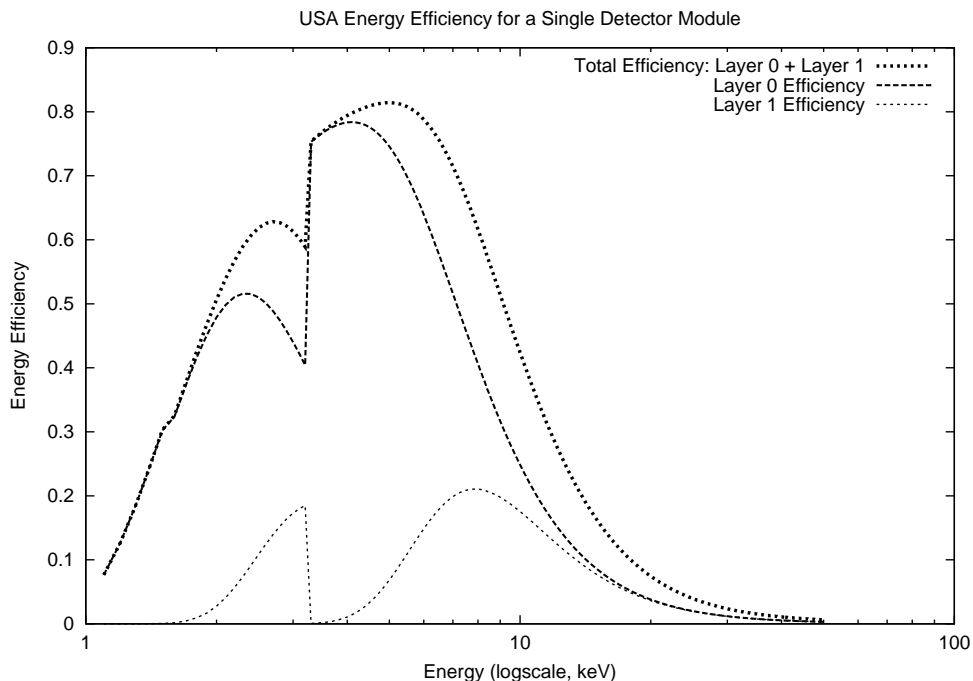


Figure 3.6: USA detector efficiency as a function of energy. The lines in the figure are as defined in the top right corner. Layer 0 is the top layer and layer 1 is the bottom layer. The abscissa is on a logarithmic scale. Efficiency is the fraction of photons incident upon the detector which are actually detected. The efficiencies shown account for transmission through the pressure window, gas efficiency and loss of detector area due to the copper collimator and the support mesh. It is easily seen that most photons with energies < 10 keV are detected in the top layer.

chambers have slightly different energy responses, but all have the property that the number of electrons freed will depend on the energy of the incident photon (for USA on order of 10^5 electrons are freed per event (Godfrey 2002)). This dependence is linear to a very good approximation (i.e. the number of electrons released is *proportional* to the incident photon energy).

The USA detector electronics pick up the current as a pulse which is then amplified, converted by the analogue to digital converter (ADC), the detector electronics then determine the photon pulse height analyzer (PHA) channel and a layer identification, this information is handed off to the detector interface board (DIB) where the

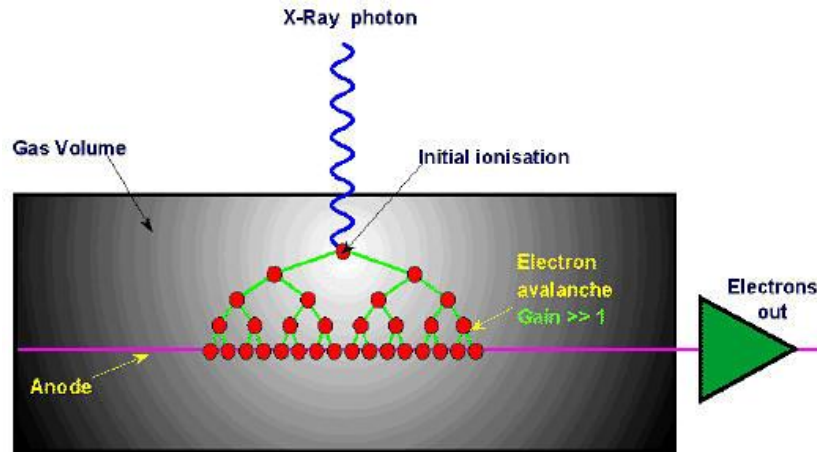


Figure 3.7: Illustration of an electron avalanche in a proportional chamber.

raw bits are packed for telemetry.² The PHA channel to which a photon is assigned is dependent on the gain, which is dependent on a variety of things—including the gas, temperature and chamber voltage (quantum uncertainties in the photon energy also affect the PHA channel assignment). During the USA energy calibration it was discovered that the gain varied in a predictable way throughout the orbit—these gain variations were found to be due to a ~ 3 K temperature variation. Thus, it was necessary to have a separate energy calibration for the ascending and descending nodes³ of the USA orbit. Because of these gain variations, an energy calibration for the polar regions of the USA orbit should also be made.⁴

3.6 Unique Characteristics of USA

As an X-ray astronomy mission the USA experiment had a variety of characteristics which distinguished it from other similar missions. The fact that it was built and operated by a small collaboration has already been mentioned. This type of collaboration has been beneficial to the USA science working group for many reasons, one being that all USA data are entirely proprietary and there is a high data to scientist ratio.

²A complete description of the USA electronics may be found in Shabad 2000 and USA SWG 1996.

³The USA orbit may be broken into a day side and night side which corresponds to the ascending node and descending node, respectively.

⁴The details of the USA energy calibration can be found in Saz Parkinson 2003

USA's use of offset pointing has also been mentioned. The reason for using offset pointing was to meet the needs of other experiments on ARGOS. These other experiments had a wide variety of objectives, including remote Earth sensing. The two remote sensing experiments required that ARGOS have constant nadir pointing and that USA use offset pointing.⁵ As with other experiments onboard ARGOS, USA had applied objectives in addition to its astronomy objectives. The applied objectives included navigation based on the use of known bright and constant X-ray sources of known position (e.g. the Crab nebula).

As an X-ray astronomy mission, USA had several other properties which set it apart. Most notable among these was its polar orbit. Astronomy missions do not usually use polar orbits, because of energetic particles in Earth's radiation belts and at the poles. Equatorial orbits are preferable for Astronomy missions. In fact, USA's polar orbit did add some extra challenges to the mission. The primary consequence of the orbit was a significant reduction in continuous USA observing time. Each 90 minute orbit was split into four observation segments: two polar which were less than 10 minutes in length and two equatorial: which were approximately 20 minutes in length. These segments were divided by Earth's radiation belts and by the South Atlantic Anomaly, because it was necessary to prevent damage to the USA detectors, to shut down the high voltage as USA passed through. Each Radiation belt interrupted observations twice per revolution. Low backgrounds in the equatorial regions made these the most desirable orbital segments for observations, however, observations made at the poles were useful for bright sources.

Two other notable features of USA are its energy acceptance and its use of GPS timing. The USA energy acceptance begins at ~ 1 keV, in contrast to the RXTE experiment which begins at ~ 2 keV. The ~ 1 – 2 keV energy range is very interesting for many of the soft X-ray sources studied, because a high fraction over their flux is in this band. ARGOS/USA was one of the first science satellites to use GPS timing, allowing absolute times, over extended periods, to be known to a few microseconds. GPS also allows for very accurate knowledge of the satellite position and velocity.

⁵For a description of the other experiments onboard ARGOS see Ray et al. 2001.

3.7 USA Science Objectives

The USA experiment planned to meet its applied and scientific objectives through a unique observing strategy. The underlying idea was the creation of a data base of high exposures (defined by effective area of the instrument times the time an object is observed) to a relatively small number of X-ray objects. One month exposures were planned for 30 objects over a three year period. The scientific objectives to be met by this strategy included the possible discovery of millisecond pulsars and timing studies of X-ray sources having a high flux in the range of 1–2 keV.⁶ Applied objectives included navigation and the use of X-ray pulsations as independent clocks, atmospheric studies and space computing. For a complete and detailed description of the USA science and applied objectives see Wood et al. 1994. For a final tally of observations made by USA see Table B.1.

High frequency variability, millisecond timescales, is among the most important and interesting phenomena to be studied by any X-ray mission, because it is thought to be a result of modulations of X-rays produced within a few Schwarzschild radii of the compact objects contained in the systems observed. USA's microsecond timing resolution is ideally suited to probing high frequencies and, thus, regions close to compact objects. These close-in regions are interesting because they are expected to provide insight into the effects of strong gravity and serve to test the limits of the current understanding of General Relativity and Quantum Mechanics.

One of the most significant obstacles encountered by USA was discovered as the group attempted to study high frequency variability in Cygnus X–1. Shortly after launch it was discovered that the USA electronics had an anomaly that has hindered the ability to detect quasi-periodic oscillations and broad band power at frequencies greater than about 50 Hz. In the next section some of the experimental obstacles will be discussed. An extensive discussion of the problems relating to the study of high frequency variability is given in Section 3.8.1.

⁶The 1–2 keV energy range is important because other experiments had an acceptance down to only 2 or so keV.

3.8 Obstacles Encountered by the USA Experiment

This chapter has primarily discussed the design specifications of USA. After the launch of ARGOS/USA, just as with any experiment, a variety of unforeseen obstacles were encountered. In this section an overview of some of these obstacles is given. Many of the problems discussed here have been solved or otherwise accounted for and have detailed reports to which the reader is referred. In other cases work is still in progress. A complete accounting of the significant events occurring during the USA mission can be found at USA SWG 2001c.

Within 24 hours of the ARGOS/USA launch, the first difficulties arose. Failure of the GPS receiver to remain locked after initialization sporadically caused ARGOS to enter the Sun safe mode. After the ARGOS GPS receiver was initialized, the lock to the GPS signal was lost. Sun safe mode was entered when the GPS lock was lost and the last (prior to loss of lock) position solution was incorrect. When lock was lost the last solution was propagated in order to determine the position of ARGOS until the receiver could be reinitialized. In cases in which the last solution was incorrect, then this faulty solution would be propagated and cause ARGOS to move out of position and become 'disoriented' with respect to the Sun (the solar panels would face away from the Sun causing ARGOS to lose power). This would then result in a Sun safe mode.

A few days after the Sun safes, caused by the failure of the GPS to remain locked, several thermal anomalies were observed in the USA detectors. These anomalies came in the form of extreme heat cycling. Prior to the point of the first thermal event, the heat cycle was approximately 1 degree throughout the orbit. The first thermal event was marked by a 10 degree fluctuation in temperature. These thermal events were the eventual cause of the more stringent USA yaw value restrictions. It is not possible to know exactly why the detector began to heat up, however several theories were put forth. Most speculation on the cause of the thermal events is related to the loss or damage of the USA detector heat shields. The mylar heat shields could have been damaged in launch, torn, partially or fully removed or coated with a non-reflective debris from one of the other experiments aboard ARGOS. Any of these scenarios good cause heating to occur when USA was at small angles to the Sun.

About nine weeks after the launch of ARGOS the formal initialization of USA

began. It was quickly discovered that there was a problem with USA pointing. There was a sign error in the software aboard ARGOS and additional offsets were needed. Within three weeks from this time one USA detector was lost due to a rapid leak, of unknown origin, in its proportional chamber. After the loss of the detector, pointing problems persisted. A variety of pointing epochs ensued, see USA SWG 2001a for a full accounting of these epochs. Pointing problems during the mission arose from a variety of different factors (beginning with the sign error), again, see USA SWG 2001a for the full details.

Other more minor issues surfaced during the mission, including a problem with ‘missing events’ and some spurious X-ray burst detections. Missing events were manifest as a lower count rate in the actual event data as compared to the housekeeping data. The discrepancy was found to be caused in part by differing deadtimes in the detector electronics. A full explanation of the missing events problem can be found in (Saz Parkinson 2003) (see also Shabad 2000 for a discussion of the two deadtimes in the USA electronics). There is no write up concerning the spurious burst detections, but they were found to be spurious because they occurred when ARGOS was in a particular longitude and latitude range. These ‘bursts’ were detected in many sources in this range and they were consequently deemed spurious. Later work by Warren Focke showed that the spectral characteristics of the ‘burst’ are well fit by bremsstrahlung with no column absorption and not well fit when absorption is included.⁷ The lack of absorption indicates that the X-rays in the ‘burst’ were most likely created terrestrially.

The next section addresses the final obstacle to be discussed. This is the problem mentioned at the end of Section 3.7, which has limited USA’s ability to detect timing properties above the 50–100 Hz range. The discussion in the following section makes use of USA data, from XTE J1859+226 during its 1999 outburst, as a context for explaining the problems at high frequencies in USA timing analysis.

⁷See USA SWG telecon minutes from 2002 August 21.

3.8.1 The Energy Dependent Instrumental Effect (EDIE): The Electronics Pile-Up Problem – Detection of High-Frequency Variability in XTE J1859+226 as a Case Study

Introduction

Shortly after the launch of USA, a distortion in the power spectral density (PSD)⁸ functions was detected. In this section the known attributes of this distortion are given. A simple model of the cause and a discussion of correcting the distortion is presented. The deadtime correction for USA PSDs having this distortion is the most critical problem to be addressed. Extensive work on the USA deadtime correction is presented in Shabad 2000. The work presented therein develops an extremely accurate deadtime correction which is only suitable for PSDs calculated from X-ray sources having a symmetrical PHA count rate spectrum (i.e. counts per second as a function of USA PHA channel; see below and Figure 3.10 for a further description), hereafter count rate spectrum. Shabad 2000 also presents a phenomenologically based recipe for deadtime correction in sources having non-symmetrical count rate spectra. The recipe presented is reviewed in this section. First a discussion is given on the problems encountered when PSDs were calculated for sources having non-symmetrical count rate spectra.

A symmetrical count rate spectrum is an “energy spectrum” of sorts. Specifically, a symmetrical count rate spectrum is an energy spectrum (or in the case of USA, a USA PHA count rate spectrum) in which the actual numbers of photons detected by USA are mirrored about an axis in a plot of counts as function of USA PHA channel. The simplest example of such a spectrum is obtained from an Fe⁵⁵ source. This was the spectrum used for the USA deadtime calibration (Shabad 2000). It is important to note that a non-symmetrical count rate spectrum can be created in almost *any* source if appropriate energy channel selections are made. Also, the symmetry of the *actual* source energy spectrum is not the issue, only the symmetry of the spectrum as seen in the USA PHA channels is relevant. The use of PHA channel selection is how the problem first showed itself. Prior to the launch of USA, all PSDs were made using all, 0–15, PHA channels. The primary calibration source was Fe⁵⁵, which has

⁸Calculation of PSDs using USA data is described in Section A.7 and rms normalized PSDs are discussed in Section 4.5. See also van der Klis 1989a.

a very symmetric count rate spectrum. This is why the distortion was not seen prior to launch.

Because the anomalous feature or distortion in USA PSDs is energy dependent (i.e. it is affected by shape of the energy spectrum), the feature has been labeled the Energy Dependent Instrumental Effect (EDIE). In this section, a limited empirical account of EDIE will be given; then the technique for correcting EDIE developed in (Shabad 2000) will be studied. This technique is applied to PSDs of XTE J1859+226⁹ in order to extract the significance of high-frequency variability, which is purported to be observed by USA in that source. It is found that the claims of Shabad 2000, that there is high-frequency variability in XTE J1859+226, are not unfounded. However, the statistics are poor and it seems that the work concerning high-frequency variability in any USA observations should not be pursued until a better method of correction for EDIE can be developed. Finally, a method to gain a greater empirical understanding, so that EDIE can be corrected, is suggested but not pursued, as it would take several months to complete and others are currently working toward a solution.

Finding EDIE

When the USA experiment first began collecting in flight data the Crab Nebula and Cygnus X-1 were sources of significant interest to the group. Both Cygnus X-1 and the Crab Nebula are persistent X-Ray sources. Cygnus X-1 is interesting because it is a black hole candidate, which has been and still is studied extensively, and the Crab Nebula is interesting because it has a constant Poisson flux and is a pulsar, making it an ideal calibration source. Naturally, these two sources were the first used to test out USA data analysis tools and procedures. Some of the first data analysis tools being developed were for time series analysis. At the time the most sophisticated code was **GUfft**. **GUfft** was the first tool that could make energy selections before calculating a PSD, see Chapter A for a description of **GUfft** and other USA data analysis tools.

Prior to the launch of USA, PSDs were calculated using all PHA channels. After launch people wanted to use energy selected time series for PSDs. This was a primary motivation for making a code like **GUfft**. One effect of selecting certain PHA channels can be the creation of a highly asymmetric count rate spectrum and a consequent distortion of the PSD. The first example of this distortion, EDIE, was seen

⁹XTE J1859+226 is another microquasar, like XTE J1550-564 observed by USA during an outburst. For some background information on XTE J1859+226 see Chapter 2 and, for additional work done on USA observations of XTE J1859+226, see Shabad 2000.

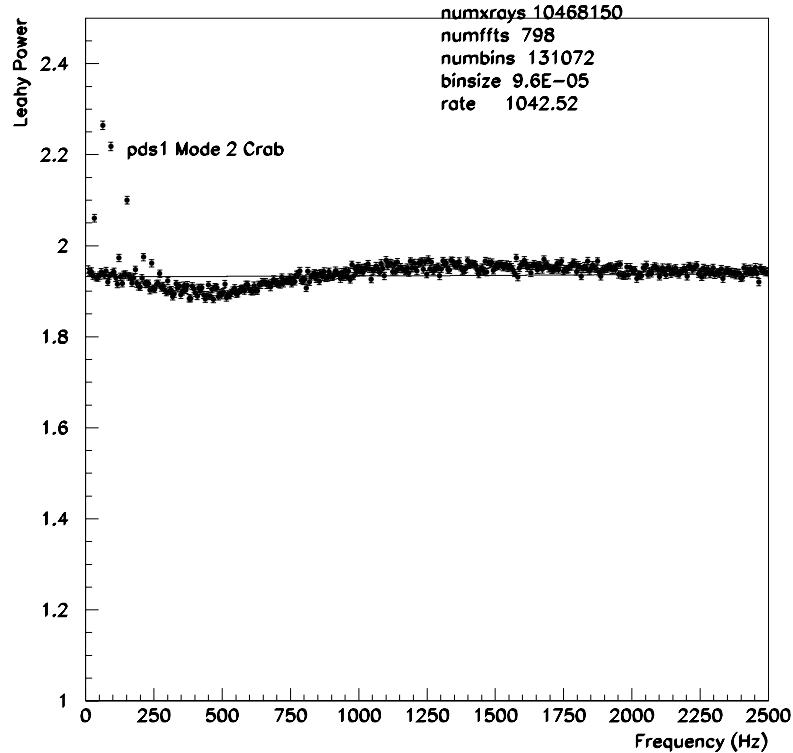


Figure 3.8: Leahy normalized PSD of PHA channel 1 from a mode 2 Crab Nebula observation showing an EDIE dip. The statistics in the upper right are total number of X-rays used in the PSD, number of individual PSDs averaged, the time series bin size in seconds and the average count rate in counts per second. The filled circles with error bars are the calculated PSD and the thin solid line is the deadtime as given in Shabad 2000 for a source having a symmetrical count rate spectrum. Bins showing spikes of Leahy Power are due to the Crab Pulsar.

in Cygnus X-1, when a PSD was calculated after cutting out a few of the low PHA channels.¹⁰ A very large feature was seen in the power spectrum at approximately 400 Hz. Initially it was thought that the 400 Hz bump, or distortion, was a possible signature of a black hole. These thoughts were quickly dispelled when the same distortion was seen in the Crab Nebula, a known neutron star. With the observation of this distortion in two sources at the same location in the PSD, around 400 Hz, it was clear that a problem was present in the USA data stream or electronics. Figure 3.8 and 3.9 show the distortion due to EDIE in two Crab Nebula PSDs. The figures represent EDIE in its two most distinguishing manifestations, a “dip” and “bump,” respectively. The difference in these two PSDs is only in what energy channels have

¹⁰The first observation of EDIE was made by Pablo Saz Parkinson while doing preliminary analysis of Cygnus X-1 data and helping to test the **Gufft** program.

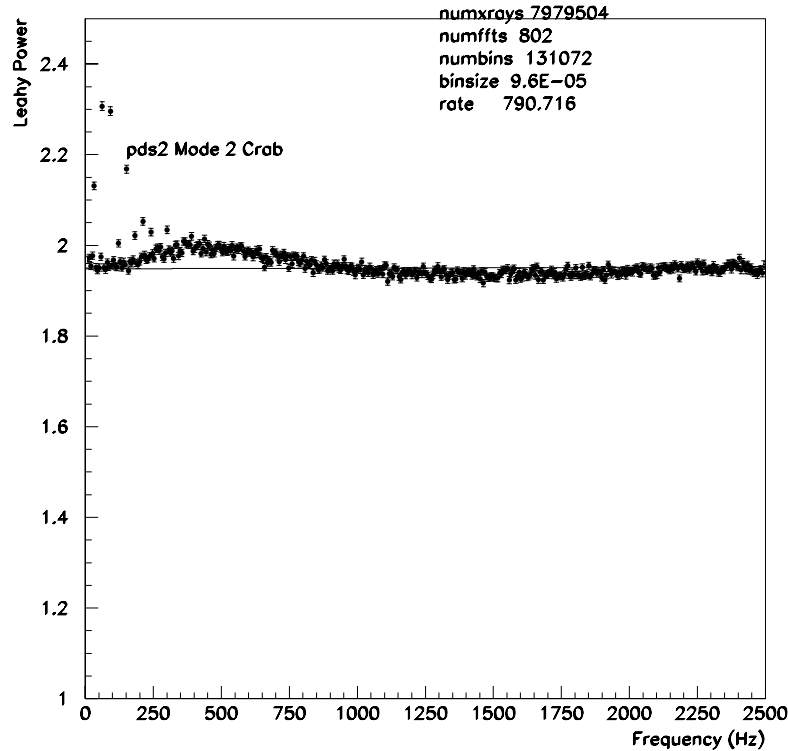


Figure 3.9: Leahy normalized PSD of PHA channel 2 from a mode 2 Crab Nebula observation showing an EDIE bump. The statistics in the upper right are total number of X-rays used in the PSD, number of individual PSDs averaged, the time series bin size in seconds and the average count rate in counts per second. The filled circles with error bars are the calculated PSD and the thin solid line is the deadtime as given in Shabad 2000 for a source having a symmetrical count rate spectrum. Bins showing spikes of Leahy Power are due to the Crab Pulsar.

been excluded from the time series. For simplicity this distortion, whether a dip or bump, or the effect formerly known at the 400 Hz bump, will be referred to as EDIE or the PSD distortion.

In addition to Cygnus X-1 and the Crab Nebula, EDIE has been seen in Fe^{55} on ground calibration data, XTE J1859+226, and any other object in which PHA channel cuts were made prior to PSD calculation. EDIE is seen in the data for modes 1, 2 and 3. It is supposed that they would be also seen in mode 4. PSDs in which energy selections were made for mode 4 data have not been done, but there is no reason to believe that the effect would be any different than that seen in the other event modes. Additionally, the point is somewhat moot, because no in orbit science data were collected in mode 4.

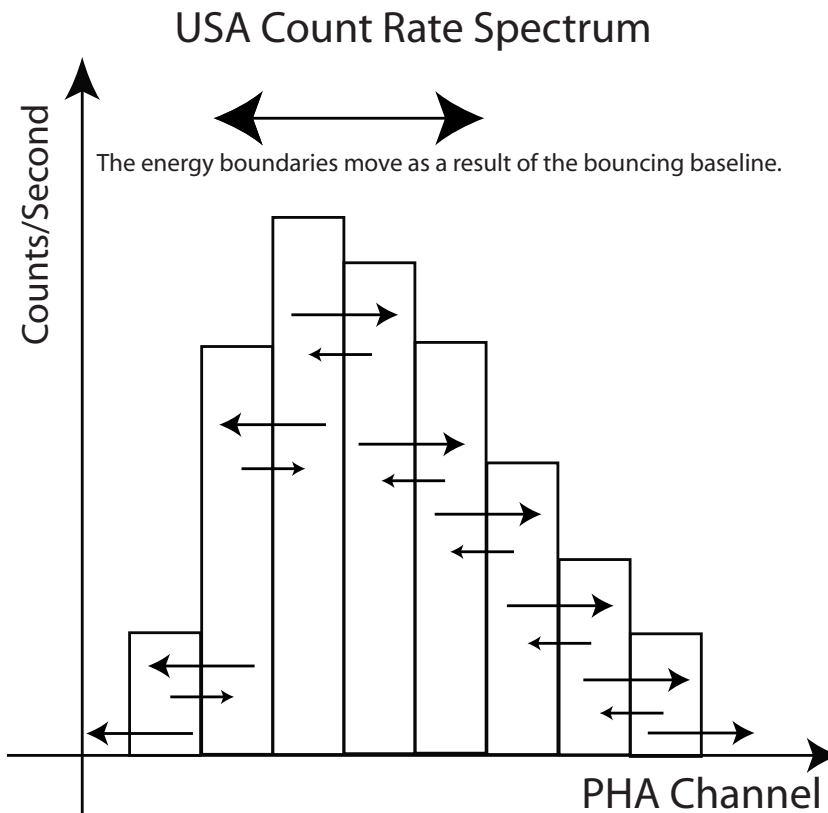


Figure 3.10: Hypothetical USA count rate spectrum, counts as a function of PHA channel for an observation, showing USA PHA channel boundary shifts. This figure gives an example of how the USA PHA channel boundaries might shift as a result of “baseline bounce” from previous events. The large two-sided arrow at the top of the count rate spectrum indicates that the location of all channel boundaries oscillate as an event enters the USA detector. The one-sided arrows indicate events moving from one PHA channel to the adjacent channel as the energy boundaries oscillate. Large arrows indicate the direction of a net positive flow of events across a particular boundary. The small arrows show that events will move in both directions. The net positive flow will always be from the PHA channel of higher rate than its neighboring channel. Notice that events are lost from the lowest and highest channel. This last point should be qualified, because an energy shift of a few eV (as is EDIE) will shift very few events out of the highest energy channel, which has a tail to high energies. There is no arrow indicating a shift of events into the lowest PHA channel. The USA electronics set a lower energy threshold for an event to be considered real, thus a slight increase in the baseline may cause an event to rise above this threshold and appear in the lowest PHA channel. Again this will be a very small number of events.

What is the Cause of EDIE?

The exact cause of EDIE is not yet understood, however a hypothesis has been given. There is no evidence to suggest that this hypothesis is not correct. The problem is

that it has not been possible to model the USA electronics well enough to simulate EDIE nor has it been possible to make accurate enough measurements to isolate the effect within the USA electronics.¹¹ Without an exact understanding of EDIE an empirical model is the best that can now be done. Empirical work is the only basis for the hypothesis to be presented. The hypothesis is that EDIE is due to a bouncing baseline in the USA electronics. This is an effect of pile-up. If two or more photons arrive closer together in time than the time required for the electronics baseline to return to “zero” after the initial photon detection, then these subsequent photons will have their energy slightly displaced by the “non-zero” in the bouncing baseline (Godfrey 2001).

This hypothesis is based on work done to assess the features of EDIE. Several USA sources, having generally understood PSDs, were selected for some simple tests. **GUfit** was used to calculate PSDs for the sources while placing a variety of energy cuts on the data. A PSD was calculated separately for each of the 16 USA PHA channels for each source. All data available for these sources in modes 1, 2, and 3 was used for the tests. In total, hundreds of PSDs were calculated. The specific sources used were Fe⁵⁵ ground calibration data, Cassiopeia A, XTE 1859+226, the Crab Nebula and Cygnus X-1. Generally, it was found that the behavior of EDIE is determined by the count rate spectral character and rate of energy selected photons used to calculate the PSD.

Because the Fe⁵⁵ ground calibration was taken under controlled circumstances, it was the logical starting point for characterizing the nature of EDIE, while the other sources were used for comparison. By calculating PSDs, in each of USA’s 16 energy channels for modes 1 and 2, it was possible to understand the qualitative behavior of EDIE. Perhaps the most significant piece of information acquired about EDIE in this work was that: A count rate spectrum with a positive slope¹² will cause a “dip” in the PSD around 400 Hz, a count rate spectrum with a negative slope will cause a “bump” around 400 Hz and a count rate spectrum having zero slope will follow the standard deadtime as given in Shabad 2000 (i.e. there should be no distortion of the PSD). Further the amplitude of EDIE is proportional to the magnitude of the count rate spectral slope. It also appears that the magnitude of EDIE is proportional to the

¹¹There is an on ground brass board replica of the USA electronics which people have used to try to isolate the cause of EDIE.

¹²Here slope refers to the average slope over the count rate spectrum of selected PHA channels.

count rate, but this possibility has not been specifically addressed.¹³ Additionally it was found that EDIE has a particular and well defined shape which should be predictable based on the count rate spectrum.¹⁴

In sum these results led to the pile-up hypothesis as a cause of EDIE. Although not fully confirmed, this hypothesis is the only widely accepted explanation for EDIE so far. Evidence for this hypothesis will be presented below. Here it is worth noting that all PSDs have so far agreed with this qualitative discussion on the nature of EDIE. Now the pile-up hypothesis is explained in greater detail.

The reason why pile-up or the bouncing baseline can cause an effect in the PSD is best explained pictorially. Figure 3.10. shows an example count rate spectrum. The arrows indicate the inflow and outflow of events from their correct PHA channel into an incorrect PHA channel due to a slight energy shift in the USA detector electronics. The larger arrows indicate a greater outflow than the smaller arrows. The PHA channel having a higher rate will have a greater absolute number of events moving into an adjacent PHA channel. This is the same as saying the amplitude of EDIE is dependent upon the slope of the count rate spectrum. The net effect is a periodic shift in the location of the PHA channel boundaries. The size of this shift is estimated to be a few eV (Godfrey 2001).

An empirical correction for EDIE may be based on the pile-up hypothesis using the following equation as a model for the distortion in the PSD,

$$\Pi(f) = \Psi \times \mathcal{W} \left[f, \left(\frac{\rho_2 - \rho_1}{\epsilon_2 - \epsilon_1} \right) \right], \quad (3.1)$$

where Π is the PSD function for Poisson subtracted deadtime, f is the frequency, Ψ is a positive constant used to adjust the amplitude, ρ_2 and ρ_1 are the number of events in the PHA channels corresponding to the energies ϵ_2 and ϵ_1 , respectively. These PHA channels mark the boundaries of the energy selected time series. The function \mathcal{W} is an empirically determined “standard form” of the EDIE distortion. Determining the exact form of \mathcal{W} is the main problem preventing the easy correction of EDIE. In future work, it may be possible to fit a few hundred USA PSDs to a function and then correlate the parameters of that function to the spectral characteristics of the time series used in the FFTs. If a function having good correlations could be found

¹³To know for sure if the amplitude was rate dependent it would be necessary to find two separate count rate spectra having the same average slope but different rates.

¹⁴This will be the basis of a proposed method of correcting for EDIE in this section.

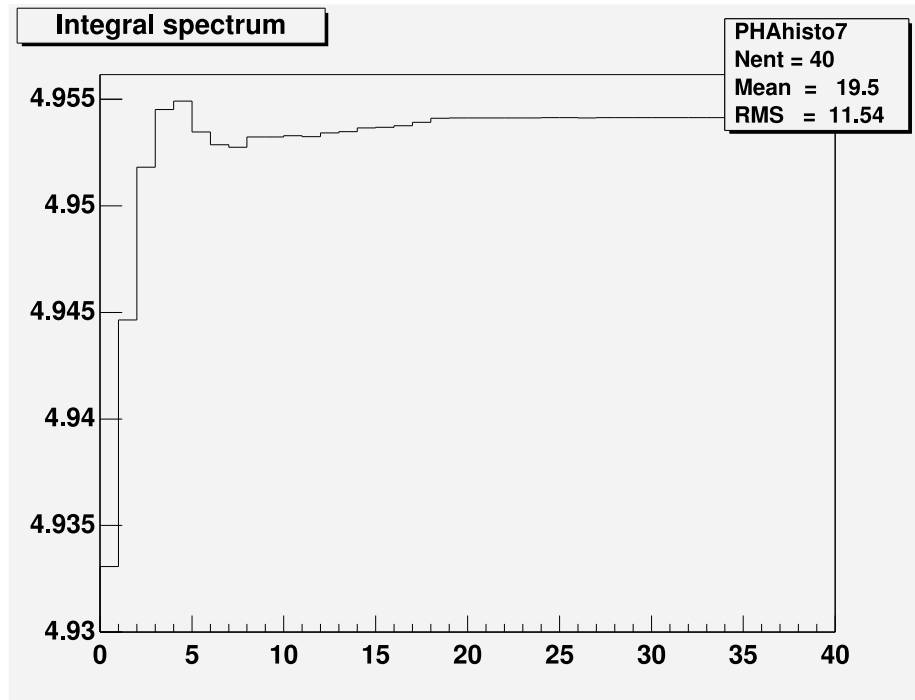


Figure 3.11: Average of the integral count rate spectra as a function of temporal distance to the preceding photon. Ticks on the x-axis represent multiples of $96 \mu\text{s}$. The values on the y-axis are in units of USA PHA channel. The Fe^{55} count rate spectra are sharply peaked in PHA channel 5. The y values of each point in the plot were determined by calculating the average PHA channel in each integral count rate spectra. See text for details on calculating the average of the count rate energy spectra.

then it would be possible to extrapolate the form of \mathcal{W} for any given PSD.

This is not the ideal way to handle EDIE, but a complete understanding, with data to match, has been elusive. The USA group has made attempts at measuring and simulating the baseline using the on ground USA electronics brass board and simple Montecarlo codes, respectively. Measurement of the baseline on the brass board would be ideal, however this measurement has proven to be very difficult. Simulations of the detector electronics continue. So far simulations have been unsuccessful. At this point the use of an empirical correction for EDIE seems to be the most promising possibility. For an additional discussion of EDIE see Shabad 2000 and Godfrey 2001.

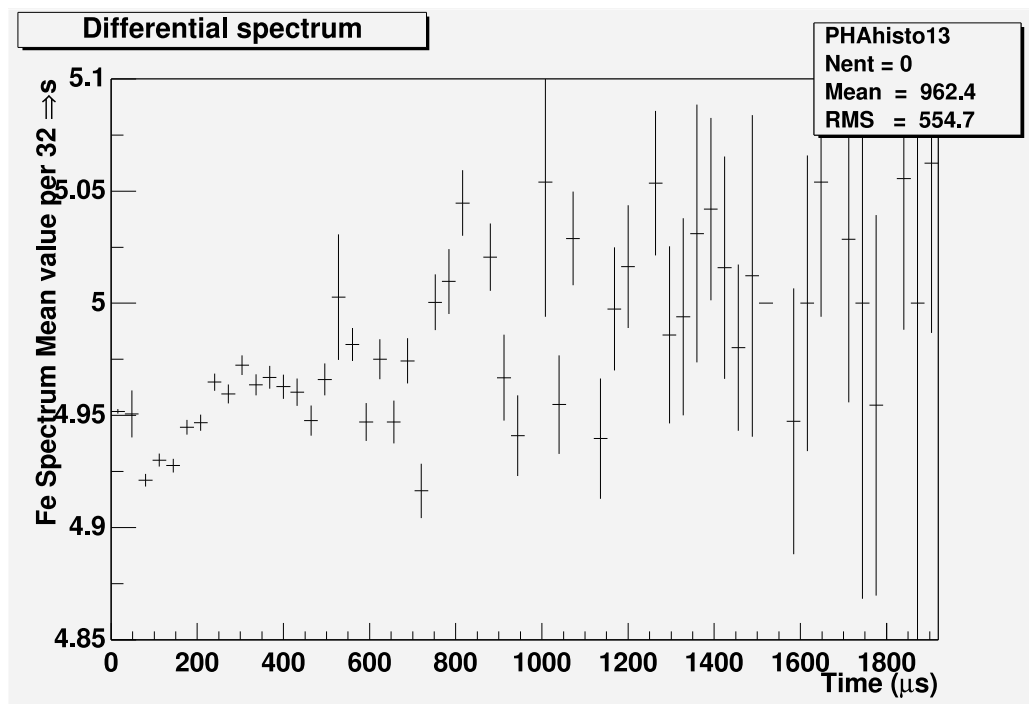


Figure 3.12: Mean of the differential count rate spectra as a function of temporal distance to preceding photon. The values on the y-axis are in units of USA PHA channel. See text for details.

Is EDIE Due to Pile-Up?

In the previous section some evidence was given that EDIE is due to pile-up. This evidence was based on PSD features alone. It is reasonable to wonder if the effects of EDIE are observable in another way which will confirm the pile-up hypothesis. Two tests have been suggested for such a confirmation. The first test was to create several count rate spectra, according to a photon to be used and its temporal proximity to the preceding photon (e.g. a count rate spectra of all photons which were separated by $96 \mu\text{s}$ from the preceding photon). Count rate spectra made with different time intervals should have slightly different average energies. When comparing only a few of the count rate spectra, there were slight shifts in the average, but they were not significantly different. A shift was seen but it was within the uncertainty of the peak of the count rate spectrum. In the end the result was inconclusive but it led to another

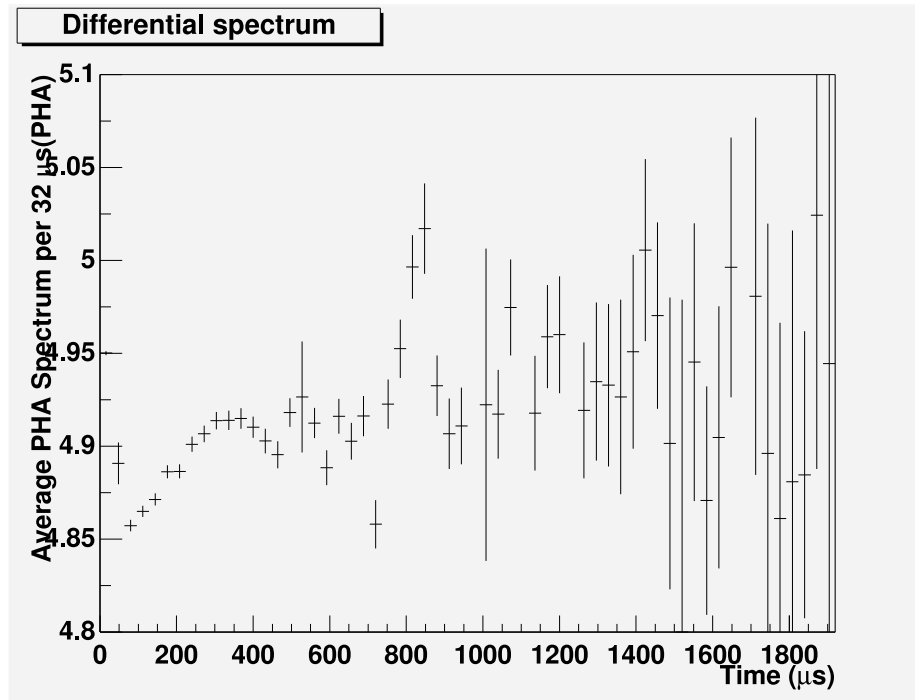


Figure 3.13: Average of the differential count rate spectra as a function of temporal distance to preceding photon. The values on the y-axis are in units of USA PHA channel. See text for details.

test which will now be discussed.

Originally, this test was done by Berrie Giebels using Fe^{55} ground calibration data. Three different time dependent count rate spectral plots were made, Figures 3.11, 3.12 and 3.13. The basic result of these plots and more recent work being to done by Pablo Saz Parkinson, is that EDIE has been shown to be a result of a baseline bounce. An explanation of the figures is now given.

Figure 3.11 was generated by calculating average integral count rate spectra for different separation distances. These separation distances were defined to be an integral number of $96 \mu\text{s}$ intervals between a current photon and some initial photon. The process for this calculation is most easily described by moving along each tick on the x-axis. For the first tick, the average value, of the count rate spectrum made from all photons within $1 \times 96 \mu\text{s}$, is calculated. For the second tick all photons falling within $2 \times 96 \mu\text{s}$ are used in the average, for the third tick all photons within $3 \times 96 \mu\text{s}$ are used and for the n th tick all photons within $n \times 96 \mu\text{s}$ are used. This procedure is repeated until all photons are used as the initial photon. All of these separation

interval dependent count rate spectra were combined to generate Figure 3.11. From the figure it is clear that the average PHA channel has dependence on the time from a preceding photon. Note that Figure 3.11 matches almost identically the shape of the autocorrelation function in Shabad 2000 Figure 5.33.

Figures 3.12 and 3.13 give a nearly identical result using the mean and average of the differential count rate spectra. The differential count rate spectra were calculated by choosing all photons that were preceded by another photon in less than $32 \mu\text{s}$ making a count rate spectrum of those photons, then choosing all photons that were preceded by another photon in less than $2 \times 32 \mu\text{s}$ and greater than $32 \mu\text{s}$ making a count rate spectrum of those, until n . In the end there is a count rate spectrum for all multiples of the $32 \mu\text{s}$ separation distance between adjacent photons. A further requirement, that no preceding photon be preceded by another photon by less than $400 \mu\text{s}$, was imposed on all preceding photons. This requirement was made in order to look for the baseline bounce due to only a single photon. Figure 3.12 plots the mean PHA channel and Figure 3.13 the average PHA channel for each count rate spectrum just described.

The results of Figures 3.11, 3.12 and 3.13 provide compelling evidence in support of EDIE being a pile-up effect. If EDIE were not a result of pile up, the figures would show only a flat line at the value of the Fe^{55} source (i.e. PHA channel 5).

A Recipe for Accounting for USA Energy Dependent Instrumental Effect

The preceding study of EDIE has made it possible to develop a preliminary, but general, recipe for the correction of the PSD distortion. This recipe is now given. In the next section a discussion of how this recipe was used and slightly refined with XTE J1859+226 data is given. The following recipe makes use of a phenomenologically determined function in order to fit the unknown instrumental effect. There is, according to Shabad 2000, precedent for fitting the tail of a power spectrum and then using that model as a noise subtraction for the unfitted part of the power spectrum. See Shabad 2000 for its original development with USA data and Wen 1997 for usage of a similar technique with High Energy Astrophysical Observatory (HEAO) A-1 data and Jernigan et al. 2000 for usage of a similar technique with RXTE data.

A sketch of the procedure for characterizing the energy-dependent effect in USA power spectra is as follows: Using Fe^{55} ground calibration data the general functional

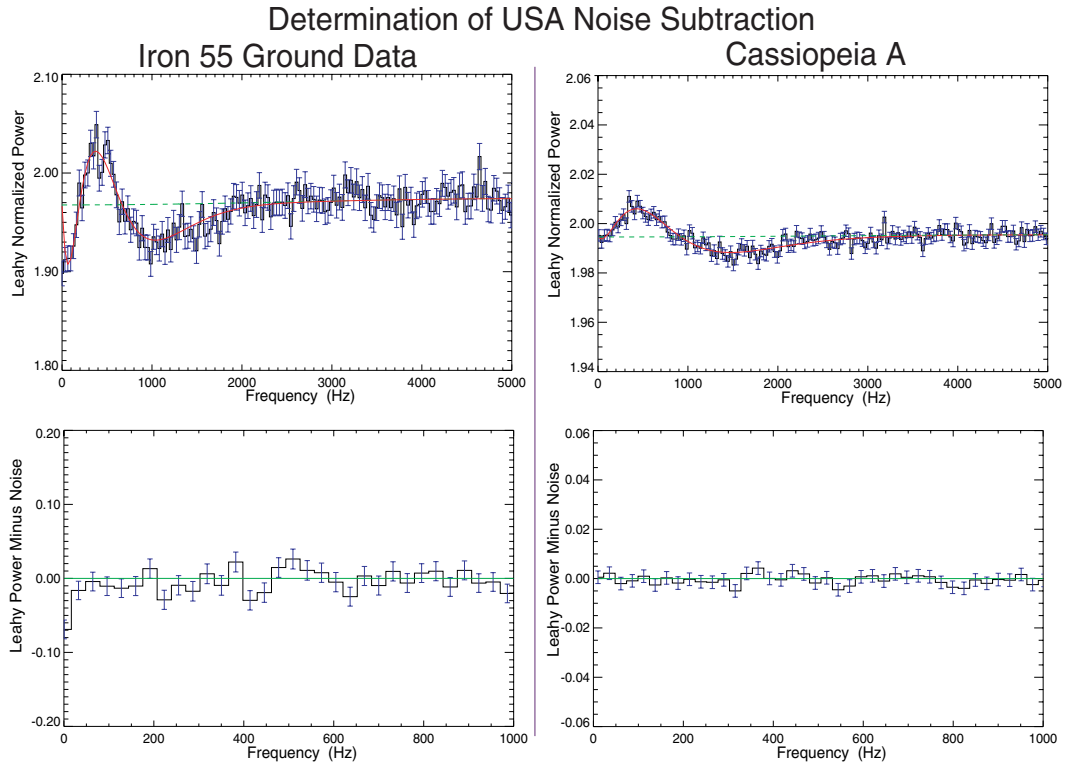


Figure 3.14: Uncorrected and corrected PSDs calculated from Fe^{55} ground data and Cassiopeia A in orbit data. Top Left: Uncorrected Leahy normalized PSD of the USA mode 2, detector 0, channel 6 ground data. The average rate during this observation was 523 cnts/sec, the time series bin size was $96\mu\text{s}$ and the total exposure time was 0.7 ks. This PSD was fit over the range of 0–5000 Hz to Equation 3.2. The solid red line is the fit and the dashed green line is the simple Poisson noise floor with dead time effects, as given by Equation 3.4, for a symmetrical count rate spectrum. Bottom Left: The residuals after subtracting the Equation 3.2 fit from the Fe^{55} ground data PSD. The residuals are consistent with zero in the ≈ 30 –5000 Hz region. Top Right: Uncorrected Leahy normalized PSD of the mode 1, channel 2 Cassiopeia A data. The average rate during this observation was 106 cnts/sec, the time series bin size was $96\mu\text{s}$ and the total exposure time was 22.7 ks. The PSD was fit over the range of 300–5000 Hz to Equation 3.2. The solid red line is the fit and the dashed green line is the simple Poisson noise floor with dead time effects, as given by Equation 3.4, for a symmetrical count rate spectrum. Bottom Right: The residuals after subtracting the Equation 3.2 fit from the Cassiopeia A PSD. The residuals are consistent with zero in the ≈ 0 –5000 Hz region. Figure adapted from Shabad 2000.

form and qualitative energy dependence of the effect was determined. Many different equations were attempted before finding a functional form which described EDIE in several sources. Making a fit to mode 2 channel 6 ground data, Figure 3.14, in the

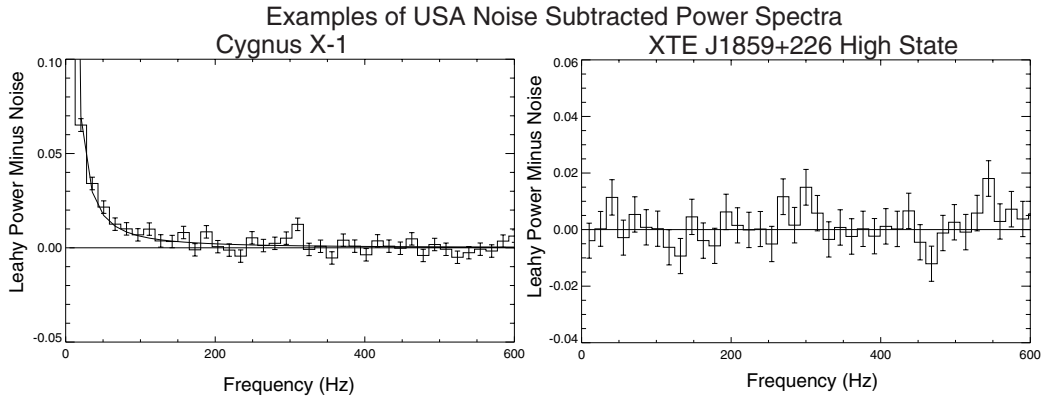


Figure 3.15: Corrected PSDs of Cygnus X–1 and the XTE J1859+226 during its high state. PSDs were corrected by fitting Equation 3.2 in the 320–5000 Hz and then subtracting over the 0–5000 Hz range. Left plot: Corrected PSD of the mode 1 Cygnus X–1 data. The PSD was calculated in the energy range 4.2–19.8 keV, with an average rate of 377 cnts/sec, a time series bin size of $96 \mu\text{s}$ and total exposure time of 23.6 ks. The solid line is a best fit power law with index of -1.53 . Right plot: Corrected PSD calculated from mode 1 XTE J1859+226 high state observations. The PSD was calculated in the energy range 4.2–19.8 keV, with an average observed rate 274 cnts/sec, a time series bin size of $96 \mu\text{s}$ and total exposure time 6.6 ks. As expected, high-frequency variability is observed to be weak or absent in the high state. Figure adapted from Shabad 2000.

frequency range of 0–5000 Hz the functional form of the instrumental effect was found to be: (Shabad 2000)

$$P^{noise}(f) = P^{instrumental}(f) + bP^{other}(f) \quad (3.2)$$

where

$$P^{instrumental}(f) = c_0 e^{-0.0048f'} f'(f' - c_1)(f' - c_2), \quad (3.3)$$

$$P^{other}(f) = P_1 + P_2 \cos(2\pi f t_b) \quad (3.4)$$

and

$$f' = c_3 f \quad (3.5)$$

Note P^{other} is the simple Poisson noise floor as modeled in Shabad 2000, f is the frequency, t_b is the FFT bin size, P_1 and P_2 are parameters generated by a Monte Carlo simulation of the USA deadtime and its idiosyncrasies (e.g. same time events).

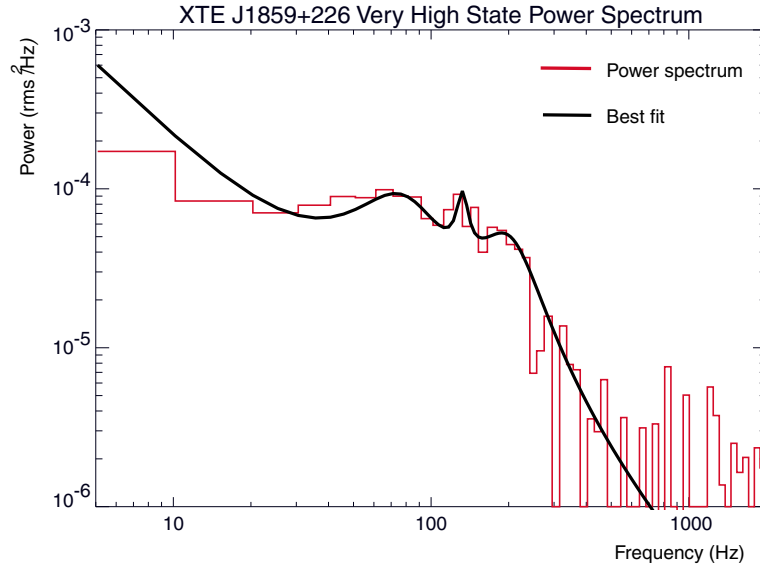


Figure 3.16: Corrected PSD of XTE J1859+226 during its very high state. The bins represent the corrected PSD and the curve is the best fit to a power law plus three Lorentzians. The PSD was calculated from mode 1 data in the energy range 4.2–19.8 keV, with an average rate of 465 cnts/sec, bin size of 96 μ s and total exposure time 13.4 ks. The PSD was corrected by fitting Equation 3.2 in the 300–5000 Hz and then subtracting over the 0–5000 Hz range.

$P^{instrumental}(f)$ is the phenomenological equation obtained from the Fe^{55} data, $c_{0,1,2,3}$ and b are free parameters used in fitting $P^{instrumental}(f)$ to an unknown power spectrum. The parameter b is approximately one in all cases so far studied. The value of -0.0048 in the exponential was found through fitting the Fe^{55} data and may be a time constant related to electronics problem which is causing EDIE.

The final outcome of fitting Equation 3.2 to the ground data was an excellent fit in the region from a 30–5000 Hz, see 3.14. The fit only varies from the power spectrum in the region below 30 Hz. This is completely adequate when looking for signals at higher frequencies. However, it should be noted that for Cassiopeia A, Cygnus X–1 and the XTE J1859+226 high state the expected results are obtained, even from 0–30 Hz when using Equation 3.2 to subtract the noise and instrumental effects. Refer to Figures 3.14 and 3.15 for examples of how the distortion can be subtracted using a fit to Equation 3.2. in all cases results are as expected. Specifically, the expected power law in the PSD remains for Cygnus X–1 and there is no power in the Cassiopeia A, XTE J1859+226 high state, or Fe^{55} ground data.

Once Equation 3.3 was obtained and modeled with several sources it was then

possible to make a recipe for subtracting the EDIE distortion, based on the technique used on the above sources. The procedure is to first subtract Equation 3.4 from the PSD, fix b at one, and then fit Equation 3.3 to the power spectrum in the range from 300–5000 Hz.¹⁵ Doing so determines the parameters of Equation 3.3 in the range of 0–5000 Hz, with possible over-subtraction of power in the range of 0–30 Hz as in the Fe⁵⁵ data. As is shown with Cassiopeia A, Cygnus X–1 and the Fe⁵⁵ ground data, this will give an accurate description of the noise at all frequencies.

Once the PSD tail is fit, the parameters, $c_{0,1,2,3}$, of Equation 3.3 are held fixed and a fit, with the addition of any “structure,” is made over the non-tail range. This fit is made to structure (QPOs, continuum power, etc.) plus Equation 3.3, however only the structure parameters are allowed to vary. Finally, a fit is made to the entire range with all parameters, including those in Equation 3.3, varying. This is done in order to obtain the most accurate parameter uncertainties. Using $c_{0,1,2,3}$ from this fit Equation 3.3 is subtracted from the power spectrum.

For XTE J1859+226 in its very high state (VHS), the power spectrum was handled in the manner described above. Specifically, the power spectrum was fit with Equation 3.3 in the range from 300–5000 Hz. This was done after subtracting off the dead time corrected Poisson noise floor, Equation 3.4, with $b = 1$. The resulting spectrum was then fit, in the range 0–300 Hz, with a power law and three Lorentzians added to Equation 3.3, holding $c_{0,1,2,3}$ fixed. Lastly, a fit was made where all parameters were allowed to vary over the 0–5000 Hz frequency range. For the results of this fit see Tables 3.1 and 3.2. Table 3.1 shows the final values for the three Lorentzians and Table 3.2 shows the final values for the parameters in Equation 3.3 and the power law which fits the PSD continuum.

Tests of Different EDIE Fitting Scenarios and Determination of the Significance of the QPO-like Structure Observed by USA in XTE J1859+226

In this section the XTE J1859+226 VHS PSD will be looked at in greater detail. In doing so several issues regarding the recipe given in the previous section will be addressed. The recipe given above is not unique. There are many possibilities for how a PSD with a distortion might be fit to Equation 3.3 and then corrected for

¹⁵The range of the fit depends on the ranges of interest. In the following discussion it will be shown that it is possible to get a very accurate model of the noise floor by fitting at higher frequencies, for example 500–5000 Hz

Lorentzian	Centroid Frequency (Hz)	FWHM (Hz)	Amplitude (fractional rms)
1	73_{-4}^{+4}	56_{-26}^{+29}	$0.035_{-0.015}^{+0.031}$
2	132_{-2}^{+2}	14_{-6}^{+12}	$0.025_{-0.007}^{+0.008}$
3	193_{-35}^{+16}	115_{-55}^{+10190}	$0.021_{-0.011}^{+0.054}$

Table 3.1: Results of final fit to XTE J1859+226 VHS. See text for details. Errors are given at 1σ .

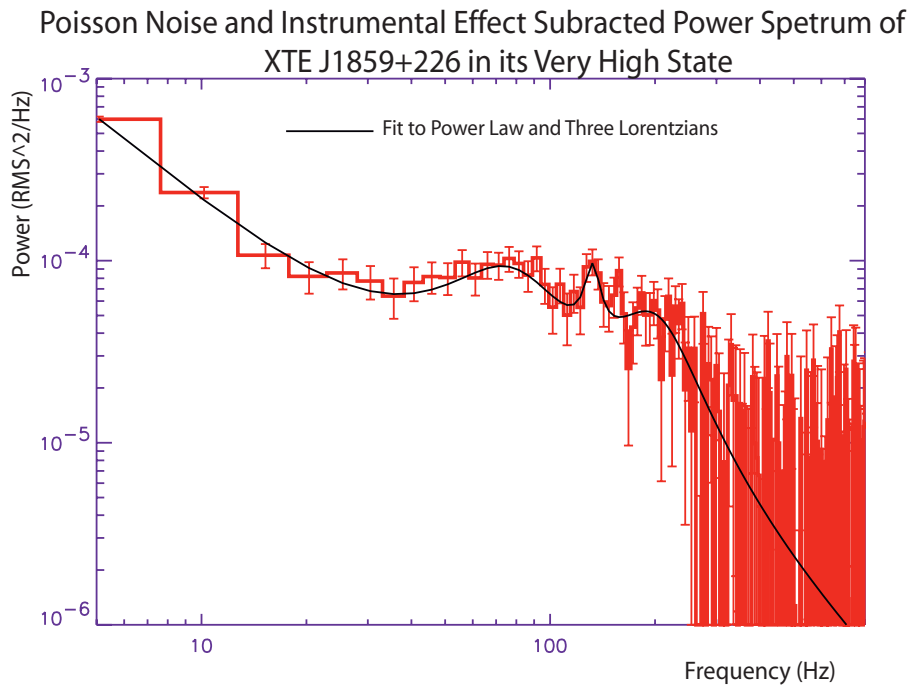


Figure 3.17: This is same as Figure 3.16 except that the data is not re-binned. All fitting was done using the original bins used in the FFTs. This plot represents an average of 2^{11} bins $96 \mu\text{s}$ in width over 13.4 kiloseconds of data. Data was only used from the energy range 4–16 keV. The average observed count rate in this energy range is 465 cnts/sec. The EDIE correction was made as outlined in the text.

the distortion. Several of these fitting scenarios are discussed. The choice of fitting scenario is extremely important, because different scenarios can dramatically alter the statistical significance of structure, and features (e.g. QPOs) within that structure, above the Poisson noise and EDIE distortion. In XTE J1859+226, for example, depending on the scenario used for subtracting EDIE, the probability that the three

Parameter	$c_0 \times 10^9$	c_1	c_2	c_3	b	Normalization	Index
Best Fit	$(-4.32^{+1.04}_{-2.02})$	$261.08^{+186}_{-74.4}$	$949.48^{+53.1}_{-53.1}$	$1.140^{+0.1}_{-0.08}$	1.0	$3.7526^{+0.927}_{-0.600}$	$-1.579^{+0.107}_{-0.251}$

Table 3.2: Results of final fit to XTE J1859+226 VHS. See text for details. Normalization is the power law normalization and index is the power law index. Errors are given at 1σ . The parameter b was fixed at 1.0.

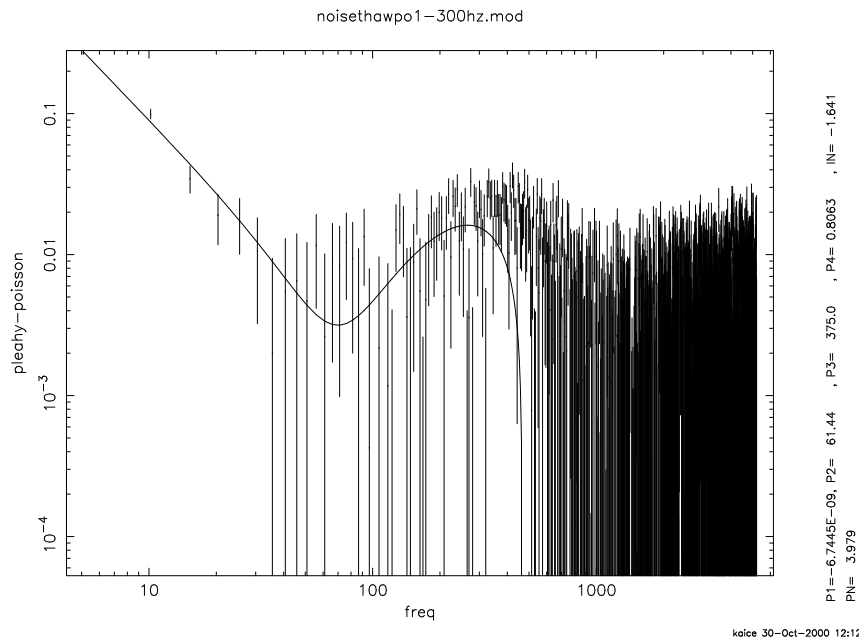


Figure 3.18: PSD of XTE J1859+226 VHS fit with power law and all Equation 3.3 parameters free over the 1–300 Hz range. Equation 3.4 was first subtracted and then the PSD was fit to Equation 3.3 in the range 300–5000 Hz with no parameters frozen. A power law was then added to Equation 3.3 and a fit was made from 1–300 Hz allowing all parameters to vary.

Lorentzians shown in Figure 3.16 are a required part of the fitting model may change between the 68% and the 93% confidence levels. It will be argued that the previously given recipe is the best way (without having a theoretical model of the detector electronics or an empirical model from on ground and in orbit data) to correct for the PSD distortion due to EDIE. This argument will be made by showing the results of the other fitting scenarios. Using the recipe/scenario from the previous section, the three Lorentzians in Figure 3.16 should be included as structure above the power law

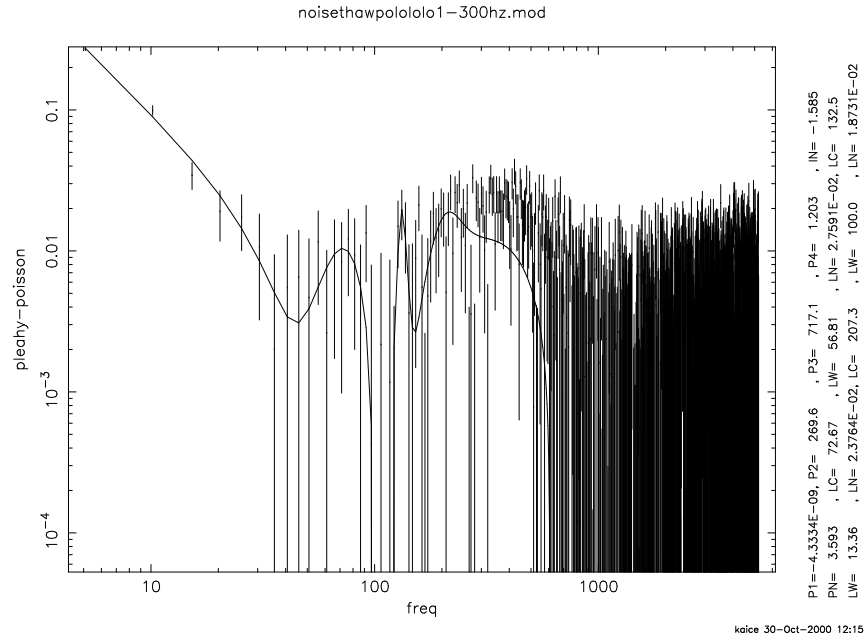


Figure 3.19: PSD of XTE J1859+226 VHS fit with power law plus three Lorentzians and all Equation 3.3 parameters free over the 1–300 Hz range. Equation 3.4 was first subtracted and then the PSD was fit to Equation 3.3 in the range 300–5000 Hz with no parameters frozen. A power law and three Lorentzians were then added to Equation 3.3 and a fit was made from 1–300 Hz allowing all parameters to vary.

at the 93% confidence level.

Ultimately the reason for trying various fitting scenarios is to determine whether or not a method other than that described in the previous section (fitting the tail of the PSD) can better fit the PSD or provides a more accurate or fundamental means of accounting for EDIE. The other fitting possibilities described are variations on what should be done after the PSD tail is fit at very high frequencies (i.e. > 300). Although there is precedent based on previous work, see Wen 1997 and Jernigan et al. 2000, that the the phenomenological function should only be fit the the PSD tail, it is also helpful to see this explicitly. An additional strike against most of the following fitting scenarios is that, by fitting a phenomenological function to an unknown PSD distortion, there is an inherent assumption that anywhere the parameters of that function are allowed to vary there is no power. Further it was shown by Shabad 2000 and in the previous section, that when Equation 3.3 is fit only to the PSD tail it accounts for EDIE at all frequencies. Some of the other possible fitting scenarios will

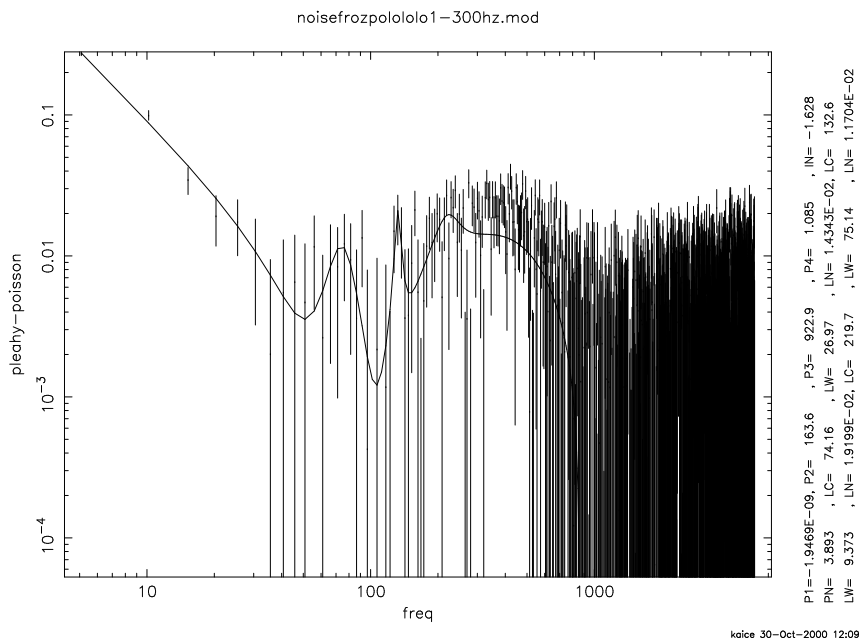


Figure 3.20: PSD of XTE J1859+226 VHS fit with power law plus three Lorentzians and only c_0 of Equation 3.3 was free over the 1–300 Hz range. Equation 3.4 was first subtracted and then the PSD was fit to Equation 3.3 in the range 300–5000 Hz with no parameters frozen. A power law and three Lorentzians were then added to Equation 3.3 and a fit was made from 1–300 Hz allowing only c_0 to vary.

be discussed while presenting a discussion on the significance of the high frequency power reported by Shabad 2000 and shown in Figure 3.16.

A description of tests for this QPO-like structure will be discussed. Specifically, the problem to be addressed is whether or not the three Lorentzian structures shown in Figure 3.16 are real or would it be possible to adequately describe the power, above the noise and EDIE, using a simple power law void of any structure. The answer to this question hinges on understanding how to fit EDIE. It is shown that the claim, by Shabad 2000, that there is excess power, above the power law in the 50–300 Hz range, is valid at the 93% confidence level. However, the structure of this power is in question. Tests for determining if the structure is three Lorentzians or something else are outlined in the conclusions portion of this section.

From the previous description of the correction scenario it is clear that many steps are involved in the process of fitting EDIE and accounting for structure in USA PSDs. The first step in any fitting scenario is to fit the PSD tail in order to

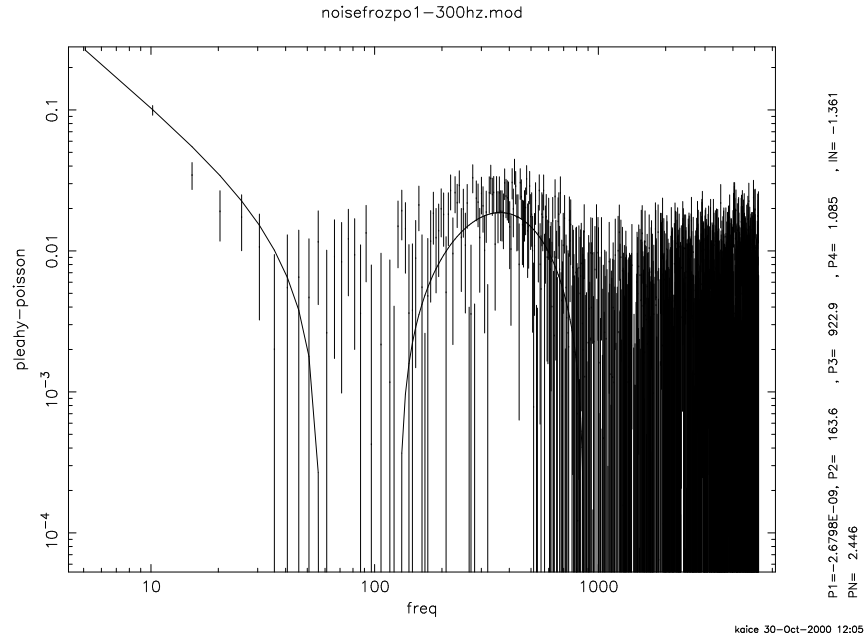


Figure 3.21: PSD of XTE J1859+226 VHS fit with power law and only c_0 of Equation 3.3 was free over the 1–300 Hz range. Equation 3.4 was first subtracted and then the PSD was fit to Equation 3.3 in the range 300–5000 Hz with no parameters frozen. A power law was then added to Equation 3.3 and a fit was made from 1–300 Hz allowing only c_0 to vary.

reasonably constrain the functional form of EDIE.¹⁶ The subsequent steps may be not as obvious. The uncertainty comes down to a question of whether or not some or all of the parameters in Equation 3.3 should be allowed to vary while making fits to the PSD structure at lower frequencies (those frequencies not included in the tail).

The different fitting scenarios to be discussed make use of the the original and not re-binned PSD from Shabad 2000. A re-binned version of this PSD is shown in Figure 3.16 and the not re-binned PSD is shown in Figure 3.17. Both of these figures have EDIE subtracted and show the best fit, using the recipe in the previous section, to a power law and three Lorentzians. The results of fitting the not re-binned PSD using both a pure power law and a power law plus three Lorentzians along with various scenarios of fitting Equation 3.3 are shown in Figures 3.26–3.25. A discussion of these results and fitting scenarios is now given.

¹⁶The frequency range of the tail fit depends on the ranges of interest. It appears that it is possible to get a very accurate model of the noise floor by fitting at higher frequencies, for example 500–5000 Hz instead of 300–5000 Hz.

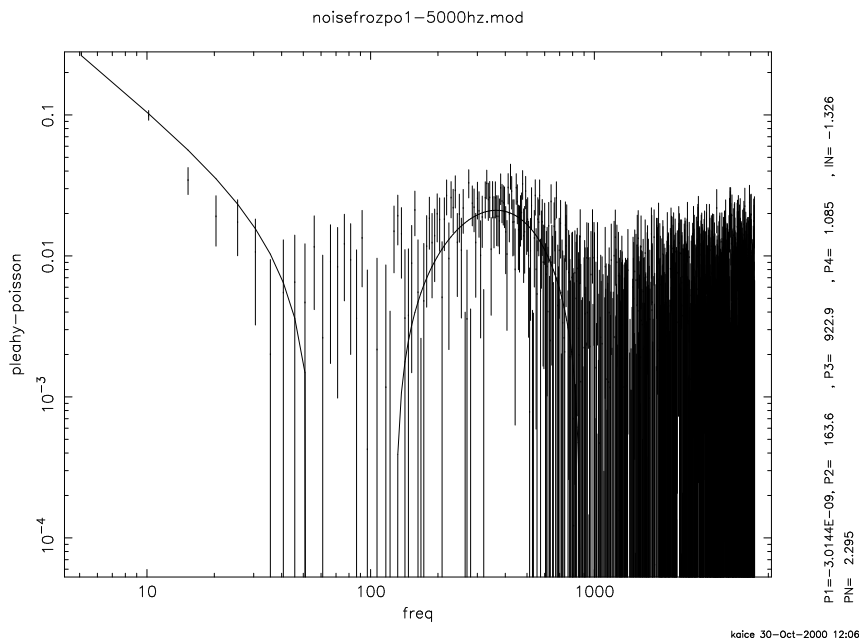


Figure 3.22: PSD of XTE J1859+226 VHS fit with power law and only c_0 of Equation 3.3 was free over the 1–5000 Hz range. Equation 3.4 was first subtracted and then the PSD was fit to Equation 3.3 in the range 300–5000 Hz with no parameters frozen. A power law was then added to Equation 3.3 and a fit was made from 1–5000 Hz allowing only c_0 to vary.

In all fitting scenarios to now be discussed the first two steps were the same. First, Equation 3.4 was subtracted from the PSD and then Equation 3.3 was fit to the tail of the resulting PSD. For all cases the tail was taken to be 300–5000 Hz. Following the tail fit, noise and structure at frequencies less than 300 Hz were accounted for in different ways. The specific details of each fit are described in the figure captions. In general, the PSD was fit with either a power law or a power law plus three Lorentzians added to Equation 3.3. The fits were either in the range 1–300 Hz or 1–5000 Hz. In these fits, following the tail fit, different restrictions were placed on the parameters in Equation 3.3. Either all Equation 3.3 parameters were frozen, or the normalization c_0 was thawed, or all parameters were allowed to vary. We now try to exclude some of these fitting scenarios based on the results shown in Figures 3.26–3.25.

Given even incomplete knowledge EDIE, the fitting scenarios used to characterize the combined instrumental effect and source variability, used in Figures 3.18, 3.19 and 3.20 may be excluded by eye. These plots are excluded simply because it is clear

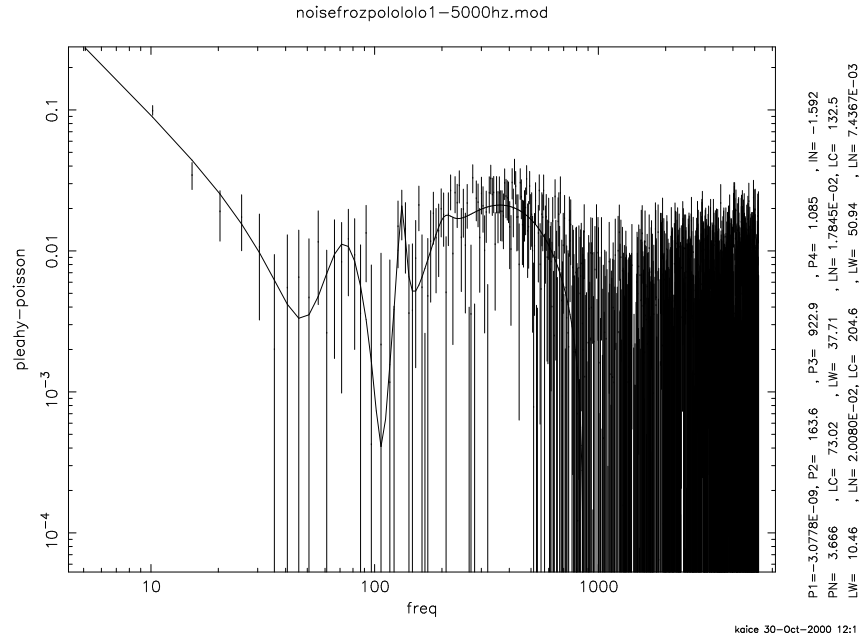


Figure 3.23: PSD of XTE J1859+226 VHS fit with power law plus three Lorentzians and only c_0 of Equation 3.3 was free over the 1–5000 Hz range. Equation 3.4 was first subtracted and then the PSD was fit to Equation 3.3 in the range 300–5000 Hz with no parameters frozen. A power law and three Lorentzians were then added to Equation 3.3 and a fit was made from 1–5000 Hz allowing only c_0 to vary.

that the parameters which were allowed to vary in the low-frequency range should not have been. Their variation pulled the fit of Equation 3.3 away from the actual shape of EDIE. The same effect is present but not quite as obvious in Figure 3.21. However upon comparison of Figure 3.21 and Figure 3.22, the effect is more easily seen. Based on these results, it is possible to exclude any fitting scenario in which (after fitting the PSD tail) any parameters of Equation 3.3 are allowed to vary only over the non-tail frequency range. Figure 3.22 poses the possibility that, once the tail has been fit, it may be correct to allow some or all of the Equation 3.3 parameters to vary along with structure over the entire PSD frequency range.

Figures 3.22 and 3.23 were both fit in the same manner and both fits support the above possibility. It may be possible that, after the tail fit, a fit can be made to Equation 3.3 plus some structure in which the amplitude, c_0 , is allowed to vary, if the fit is done over the entire frequency range. The scenario used in obtaining the fits shown in Figures 3.24 and 3.25 go one step further, they allow all parameters in

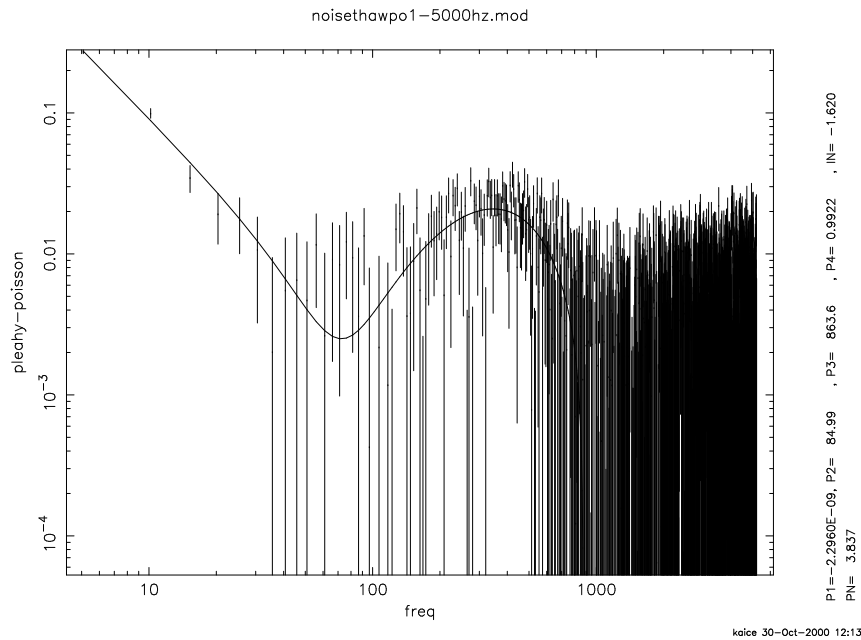


Figure 3.24: PSD of XTE J1859+226 VHS fit with power law and all Equation 3.3 parameters free over the 1–5000 Hz range. Equation 3.4 was first subtracted and then the PSD was fit to Equation 3.3 in the range 300–5000 Hz with no parameters frozen. A power law was then added to Equation 3.3 and a fit was made from 1–5000 Hz allowing all parameters to vary.

Equation 3.3 to vary over the entire frequency range. In doing so, the χ^2 values, 1.12 and 1.13, respectively, for the fits in Figures 3.24 and 3.25 are very good. They are better than in any other fitting scenario. However, there are several problems with allowing all parameters to vary. The first is that a function having many parameters can be made to fit almost anything. The second is that χ^2 values obtained from such a fit, 1–5000 Hz, will be artificially low, because of large error bars at high frequencies in the PSDs shown here. The good χ^2 values are possibly more a testament to the knowledge of EDIE than they are useful in deciding the nature and significance of any structure in the PSD in the non-tail region. Structure in the PSD is the main driving force behind doing this. The last and possibly most compelling reason why the fit scenario used for figures 3.24 and 3.25 should be excluded, as a reasonable means of accounting for EDIE, is based on the concept of fitting a PSD tail to a phenomenologically determined function. If all parameters in Equation 3.3 are allowed to vary after the tail has been fit then one of two assumptions must be made: Either

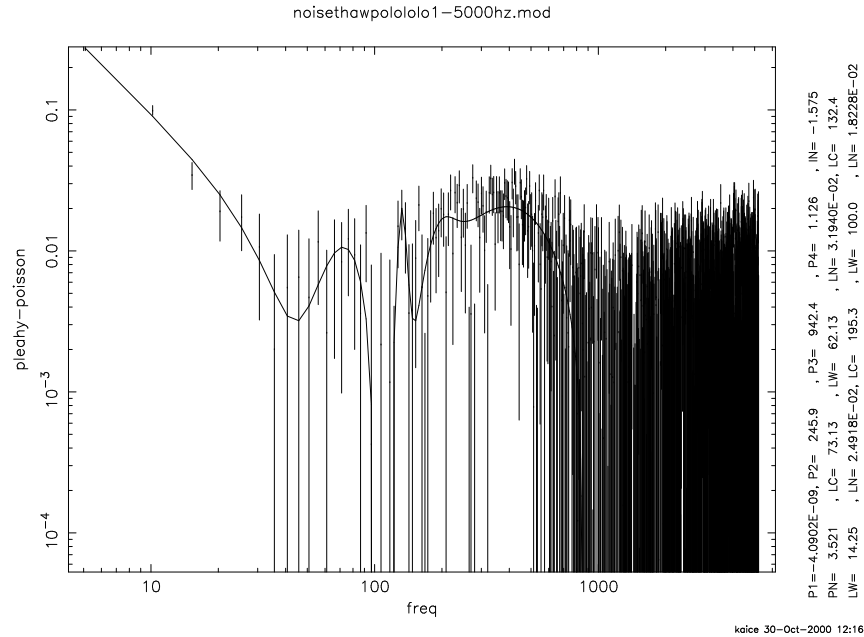


Figure 3.25: PSD of XTE J1859+226 VHS fit with power law plus three Lorentzians and all Equation 3.3 parameters free over the 1–5000 Hz range. Equation 3.4 was first subtracted and then the PSD was fit to Equation 3.3 in the range 300–5000 Hz with no parameters frozen. A power law and three Lorentzians were then added to Equation 3.3 and a fit was made from 1–5000 Hz allowing all parameters to vary.

it has to be assumed that the structure, above EDIE, is known exactly or that any discrepancy between the PSD and the structure will be accounted for by Equation 3.3 and is a part of EDIE. The first assumption is not correct because there is no way of knowing *a priori* the PSD structure. The second assumption is counter to the idea behind using a fit of a phenomenologically determined function to a PSD tail in order to account for an effect such as EDIE. The basic assumption is that by fitting the tail, the non-tail noise, distortions and all, are fully accounted for and the generic shape of the noise should not change much. This was shown to be the case for four different sources in the previous section. Thus, the scenario in which all Equation 3.3 parameters are allowed to vary over the entire frequency range is excluded.

The arguments given above do not necessarily exclude the possibility of allowing only the amplitude, c_0 , to vary. However, if the amplitude is allowed to vary only over the non-tail frequencies then, from Figures 3.21 and 3.20, it has been shown to give inadequate fits to EDIE. If the entire frequency range is used as in Figures 3.22

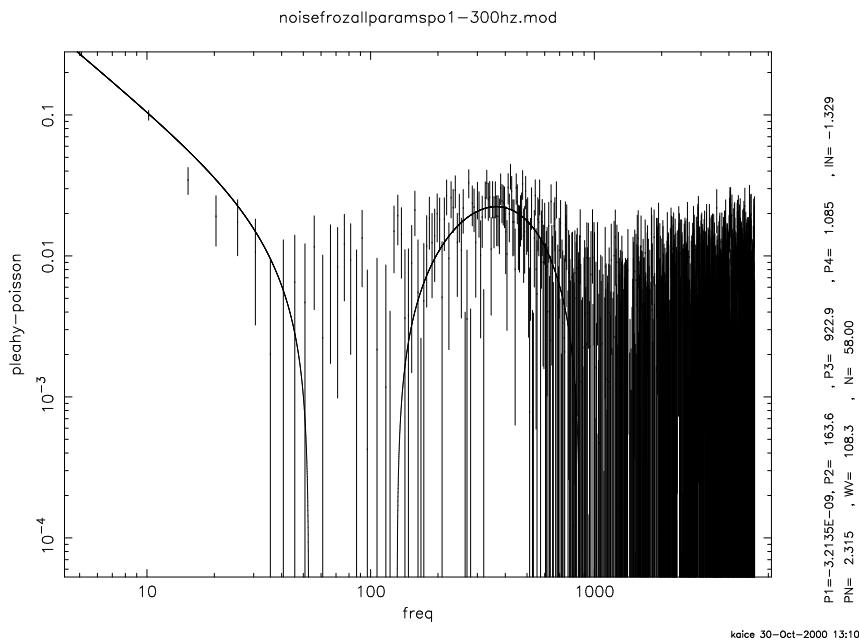


Figure 3.26: PSD of XTE J1859+226 VHS fit with power law and no Equation 3.3 parameters free over the 1–300 Hz range. Equation 3.4 was first subtracted and then the PSD was fit to Equation 3.3 in the range 300–5000 Hz with no parameters frozen. A power law was then added to Equation 3.3 and a fit was made from 1–300 Hz allowing no Equation 3.3 parameters to vary.

and 3.23, then it is more difficult to argue against allowing the amplitude to vary, because both the structure and EDIE seem to be accurately modeled. An argument should be made against allowing any parameters of Equation 3.3 vary while also trying to find a fit to unknown structure in the PSD. This goes against the principle of using the tail as a reference for the entire PSD *known* noise floor. Also, by the same reasoning used to exclude Figures 3.24 and 3.25, Figures 3.22 and 3.23 are excluded based on their χ^2 values. Anytime a fit is made to a region with such large error bars, it is expected to fit well. Admittedly the arguments against allowing the amplitude to vary in the way shown in Figures 3.22 and 3.23 are not as strong as possible. It may be argued that there is some uncertainty in the amplitude especially given the large errors in the tail. This scenario stands out as the second best and only other reasonable scenario, presented here, for accounting for EDIE. The best scenario is that presented in the previous section and used to obtain the fits in Figures 3.26 and 3.27.

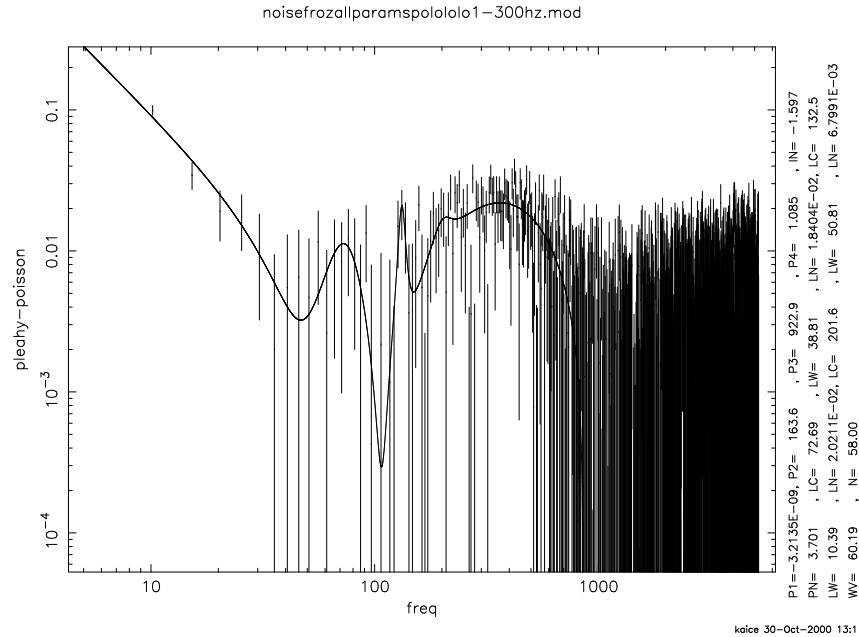


Figure 3.27: PSD of XTE J1859+226 VHS fit with power law plus three Lorentzians and no Equation 3.3 parameters free over the 1–300 Hz range. Equation 3.4 was first subtracted and then the PSD was fit to Equation 3.3 in the range 300–5000 Hz with no parameters frozen. A power law and three Lorentzians were then added to Equation 3.3 and a fit was made from 1–300 Hz allowing no Equation 3.3 parameters to vary.

Although the scenario used for the fits shown in Figures 3.22 and 3.23 is considered to be the most accurate means of accounting for EDIE, it is informative to have a worst case scenario with which to compare. The scenario of Figures 3.22 and 3.23 will be used as the worst (but reasonable) case in the ultimate goal of this section. This goal is to determine if there is structure above EDIE and a power law in the VHS PSD of XTE J1859+226. Allowing c_0 to vary over the entire frequency range acts a worst case because all such fits made using that scenario give low χ^2 values regardless of the model of structure on top of EDIE. They have artificially low χ^2 values because of the very good fit of EDIE at high frequencies (i.e. the goodness of the fit at high frequencies is outweighing the badness of the fit a low frequencies). Taking the worst case scenario method, fitting a power law plus three Lorentzians, Figure 3.23, gives $\chi^2 = 1.117$ and fitting a power law only, Figure 3.22, gives $\chi^2 = 1.153$. Using an

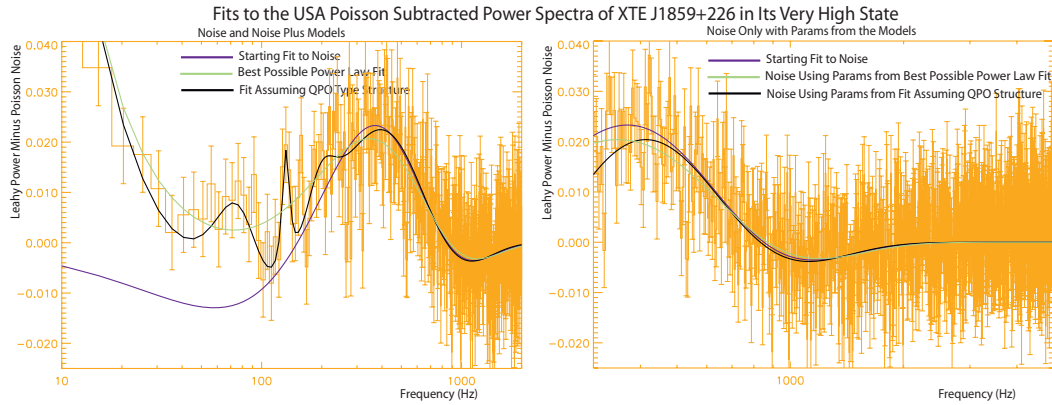


Figure 3.28: PSD of XTE J1859+226 VHS fit with a power law, a power law plus three Lorentzians and Equation 3.3. The starting fit to the noise was made by first subtracting Equation 3.4 and then fitting to Equation 3.3 in the range 300–5000 Hz with no parameters frozen. The best possible power law fit was made as described in Figure 3.26 and the fit assuming QPO type structure was made as described in Figure 3.27. Once these three fits were made the best possible power law fit and the fit assuming QPO type structure were then independently fit again allowing all parameters to vary including those in Equation 3.3 over the range 1–5000 Hz. These two fits are shown in the above PSDs and the starting fit to noise is plotted for comparison. It is clear that the final best possible power law fit, in the 300–5000 Hz pulls away from the starting fit to noise much more than does the fit assuming QPO type structure. This is more easily seen from the PSD on the right which a close up, in the relevant range, of the PSD plot on the left. It is expected that a perfect model to the structure under 300 Hz would not pull the fit away from the starting fit to the noise in any significant way during the fitting process just described. These two plots seem to show that this assumption is true. Based on the f-test the QPO type structure is a more accurate model of the structure than the power law. The original fit to the noise floor is distorted by adding an incorrect model, in this case a pure power law. The more correct model, the power law with Lorentzians shows very little distortion. From the f-test the pure power law was excluded at the 93% level. The consequence of fitting an incorrect model to the entire frequency range is that the Equation 3.3 parameters were distorted and they no longer accurately described EDIE. The objective of fitting over the entire frequency range is to obtain an estimation of the errors on the parameters in Equation 3.3 and the model for structure above EDIE.

f-test to compare these models gives:

$$\frac{1.153}{1.117} = 1.032 > 1.030 \quad (3.6)$$

for 1021 degrees of freedom in the numerator and 1012 degrees of freedom in the denominator. The value 1.030 is the 68% confidence level. Thus, in the worst case scenario a model of a pure power law may be excluded at 68% confidence.

Now looking at the best case scenario and what seems to be the correct method to make the fits. In this case all Equation 3.3 parameters are frozen, including c_0 , after fitting to the high frequency region. This result indicates that it is possible to exclude the pure power law at a 93% confidence level. This is done using Figures 3.26 and 3.27. The χ^2 values for the fits shown in Figures 3.26 and 3.27 are 1.934 and 1.281, respectively. Here fits were first made at high frequencies, all noise parameters were then frozen and a fit was made to any structure at low frequencies. This is just as in Section 3.8.1. Finally an f-test is used to compare the fits to the two models:

$$\frac{1.934}{1.281} = 1.510 > 1.509 \quad (3.7)$$

for 56 degrees of freedom in the numerator and 47 degrees of freedom in the denominator. The value 1.509 is the value at which a 93% confidence level exclusion of a pure power law may be made.

There is one last detail to be addressed regarding the correct fitting scenario described above. This detail involves the process of finding the errors on the fit parameters. This should be done after the best model for the non-tail structure has been determined. Once this has been done, one should fit over the entire 1–5000 Hz range allowing all parameters to vary so that error bars may be obtained for all parameters in the model and Equation 3.3. The χ^2 value will become artificially low. It was found by trial and error that, assuming a correct model for structure above Equation 3.3 has been found, doing this last fit to estimate the error bars does not significantly distort the properties of Equation 3.3. In Figure 3.28 an example comparing the power law and the power law with three Lorentzians is given. In the figure it can be seen that the incorrect model, the lone power law, distorts the noise approximation much more than does the correct model.

The method arrived at in this section is almost the exact method described in Shabad 2000. It was used to obtain the corrected PSDs shown for Cassiopeia A, the XTE J1859+226 high state, Cygnus X–1, and the Fe⁵⁵ ground data, Figures 3.14 and 3.15. There is one significant addition made by the work presented in this chapter. Here it has been shown that systematic uncertainties due to the lack of knowledge of EDIE may be estimated by allowing all parameters to vary in non-tail frequency

range ¹⁷ once the PSD structure has been fitted. That is the best way to obtain proper error bars on the fit parameters is to make one final fit varying all parameters, noise and structure. As shown in Figure 3.28 this will not change the goodness of the fit to EDIE in the tail, unless the model for structure at frequencies lower than the tail frequency range is incorrect.

Conclusions

EDIE was initially observed in Cygnus X–1 data and then shown to be in all USA data subjected to energy cuts (and some data not subjected to energy cuts). A description of EDIE as a problem of pile-up in the USA detector electronics was developed based on the study of hundreds of PSDs in multiple sources. An accurate simulation of EDIE as a pile-up problem has been difficult to obtain. Empirical evidence has been more promising.

The integral and differential spectra, see figures in Section 3.8.1, confirm the idea that EDIE is due to electronics pile-up. This confirmation was made using Fe⁵⁵ on ground calibration data. Recently, plots similar to those shown in Section 3.8.1 have been made using in flight data for multiple sources showing a nearly identical result (Saz Parkinson 2003).

A phenomenological recipe to correct USA PSDs for the distortion caused by EDIE was presented and tested. The tests were performed on sources having well know PSD structure. This afforded a check of the recipe. The original form of the the recipe as used in USA data was presented by Shabad 2000.

The recipe presented, for the correction of unknown distortions in PSDs of other experiments, was applied to distortions, caused by EDIE, in USA PSDs. The recipe makes use of a fit to the PSD tail as an indicator of the noise floor at all frequencies. This type of PSD correction is common (Wen 1997; Jernigan et al. 2000). However, the recipe is not without problems. The most significant issue is the determination of the uncertainty in the noise floor subtraction. A method to estimate the error bars on the parameters in Equation 3.3 was discussed. Work needs to be done to confirm the validity of this uncertainty estimation.

Original high-frequency variability work done by Shabad 2000 using USA observations of XTE J1859+226 was scrutinized. The original data set was used throughout

¹⁷As mentioned before, allowing the parameters to vary all the way out to the highest frequencies gives artificially low χ^2 .

this process. The claim of excess power, beyond a simple power law, in the range 30–300 Hz, is found to be valid. Three Lorentzians added to the power law are a necessary feature in the model at the 93% confidence level. There is a need for further checks. The USA observations of XTE J1859+226 should be re-analyzed from scratch. New FITS files should be created, the data should be freshly cut and PSDs recalculated. Re-cutting the data is required because the USA data analysis tools have improved significantly since the original XTE J1859+226 analysis was performed. Assuming the recipe presented here is to be used to search for high-frequency variability, it is suggested that instead of fitting the PSD to either a power law or a power law plus three Lorentzians, there should some intermediate fits made. These intermediate fits would be to fit one Lorentzian at a time to all of the initial locations of the original three and comparing all possible combinations of one, two and three Lorentzians to find what fits the data best.

Even with a complete re-analysis of the XTE J1859+226 data there may still be considerable concerns over the validity of the recipe for PSD noise floor subtraction presented in this section. In order to ease these concerns, one or more of three things must be accomplished. Most likely the quickest means is to find a method of predicting the uncertainty in the noise floor as determined by the recipe presented in this section. (What is the validity of the final step, allowing all parameters to vary over the entire frequency range to get the parameter error bars? Seems like a reasonable idea.) The next most expeditious avenue would be to make use of the concepts put forward in Section 3.8.1 as a means for defining a parameter space based on spectral shape and rate to predict the shape of EDIE in any generic PSD. The final and apparently most difficult, is to create a full scale model of the USA detector electronics which accurately generates time series which reproduce EDIE in their phony PSDs. Work relevant to all of these possibilities is on-going.

Chapter 4

USA Data Selection and Analysis

4.1 Introduction

The USA system of data selection and analysis is reviewed in this chapter by making use of USA observations from the 2000 outburst of XTE J1550–564 as an example. Discussion of the analysis of mode 5 data, the USA spectral mode, will not be given here. For an explanation of how to analyze mode 5 ping data refer to Giebels et al. 2002.¹ Here the analysis of USA event modes (modes 1-4), which provide time tagged photon data, is discussed. See Section 3.3 for a more detailed description of the USA event modes. This chapter describes the process of going from raw USA data to background subtracted light curves and fitted power spectra. Where appropriate, specific details about the XTE J1550–564 observations are given.

Processing raw USA data required the development of a variety of software tools. The details of software tools for the USA data analysis are given in Appendix A. The next section provides a brief overview of these tools and defines their role in USA data analysis. Beginning with Section 4.3, the remainder of this chapter outlines a general recipe for the analysis of USA event mode data.

¹A ‘ping’ observation is one in which the total observation time is split between short periods of on source and off source. Ping observations were done in order to have near simultaneous and direct observations of backgrounds. A system for analyzing mode 5 data which were not collected as ping observations has not been fully developed.

4.2 Overview of USA Data Analysis Tools

Before data could be analyzed the USA science working group had to decide what X-ray sources would be observed. The group made these decisions during weekly teleconferences (while the instrument was operational). As discussed in Section 3.7 the general philosophy for observations was to obtain large data sets on a small number of sources. In implementation of this philosophy, the USA team met several obstacles, see Section 3.8, in creating an ideal observing strategy.

The consequence of these obstacles, in particular the likely loss or damage of heat shields, was a limit to the range possible yaw values which caused an effective decrease in the observable sky area and number of days each year for observations of individual sources. The absence of heat shields prevented the observation of sources for which the detector might become ‘stuck,’ for a prolonged period, in a position vulnerable to the Sun. The satellite scheduling software accounted for this possibility and would never allow an unsafe observation to be scheduled. However, the satellite scheduling software did not allow the group to quickly establish of the observational availability of a source. Substantial modifications of the **usaview** code were for this purpose. Ultimately, **usaview** allowed long term planning for the mission.

Once sources were decided upon and data were collected, downloads from ARGOS were made and the data were eventually stored in the USA level 1 database. This database, located at NRL and mirrored at SLAC, is accessed via a series of C programs and a TCL/TK interface. The TCL/TK code is known as **picktelemII**. **picktelemII** may be used to select data based on a variety of criteria. Once all observations meeting said criteria have been found **PicktelemII** calls **dat2fits** to dump that data from the level 1 archive into a more familiar and widely know, in the astrophysical community, format–FITS files. FITS is an acronym for Flexible Image Transport System (Hanisch et al. 2001).

PicktelemII allows the user to select/cut data based on a variety of criteria and manipulate those data in different ways. Although, **picktelemII** is a very powerful tool it does not yet have a method for automated data selection. Data selection done by **picktelemII** is subject to human error and is not repeatable. If a user wishes to make data cuts, that might be repeated by others in the future, they will need to use the **mktimeusa** code. First, the user can select a set of whole observations in **picktelemII** and then generate the corresponding FITS files. Once this is done **mktimeusa** can be used to cut or filter the data according to various criteria. A full

Criteria	Condition
Source Name	XTE J1550–564
Observation Length	> 2 minutes
Average Count Rate	> 50 counts/second
Observation Type	Pointed Observations Only
Percentage Archived	> 50%
Orbital Node	All
USA Science Mode	1 and 2

Table 4.1: XTE J1550–564 observation criteria.

discussion of **mktimeusa** is given in Section A.6.

Once a set of filtered (cut) data has been generated, the science analysis may begin. Usually, the first steps are to generate power spectra, light curves and PHA files (count rate spectra).² When it is desirable to do spectral fitting with the data, the user must account for background X-rays. This is handled with the code **usabckgnd** (Saz Parkinson 2003). The current version of **mktimeusa** requires that background files be present. **Usabckgnd** estimates the background in the appropriate region for an observation and generates background files usable by the common X-ray spectral manipulation tool (developed at HEASARC)–**Xspec** (Dorman and Arnaud 2001). A complete description of **Xspec** is available on the web at

[http : //heasarc.gsfc.nasa.gov/docs/xanadu/xspec/manual/manual.html](http://heasarc.gsfc.nasa.gov/docs/xanadu/xspec/manual/manual.html).

PSDs are generated by a code written with particular consideration for USA data–**specan**. A full description of **specan** is given in Section A.7. PSD fitting presented in this work was done using the Quick and Dandy Plotter (QDP).

4.3 Obtaining and Filtering USA Data

Now that a general description of the USA data stream has been given, it is possible to present a general recipe for USA data analysis. Whether or not a user has a particular source in mind or a particular kind of observation, the starting point is downloading the data from the USA database in the form of FITS files. This is done most easily using **pickleII**, which allows the user to download any number of observations meeting a wide range of criteria. Some of the criteria include source

²These data products are defined in the following sections.

Parameter	Value
MinimumHV	2600
PoleRatioMultiplier	3
MaximumOffset	0.5
MinimumOffset	0
MinimumLimbAngle	4
RatioMultiplier	25
FracAboveBckgnd	1.5
MaximumCh15Diff	15
TimeBeforeOnSource	32
NbinsAVG	16
MinDataLength	16
TimeBeforeOffSource	8
MinimumYawAngle	-35
MinPVtoTCVRatio	0.55
RateMultiplier	5
PoleMaxCh15DiffMultiplier	7

Table 4.2: XTE J1550–564 data cut parameters used in **mktimeusa**. For a complete description of the parameters in this table see Section A.6.

name, percentage of data from an observation archived, orbital node, length of observation, USA science mode, type of observation, etc. For the XTE J1550–564 data observations were selected based on the criteria given in Table 4.1.

Once all possible USA observations have been narrowed down to the few desired, **picktelemII** can be used to dump the observations into FITS files. Once in FITS files the data is ready to be filtered or cut. Data filtering is the process by which data is systematically selected for properties making it appropriate for the desired analysis. Currently, the most straightforward and repeatable way to filter USA data is by using **mktimeusa**, described in Appendix A. **Mktimeusa** has multiple parameters which must be set. It has often been necessary to go through a process of trial and error to find the proper criteria for individual sources. The parameter values used to filter the XTE J1550–564 data are shown in Table 4.2.

Soft electron backgrounds are one of the most useful criteria which **mktimeusa** uses for cuts. Soft electron backgrounds are easily detected because they deposit large amounts of energy in only the top layer of the detector (the degree of ionization energy loss of charged particles is given by the Bethe-Bloch equation). Electrons are highly ionizing particles, thus after they have moved only a short distance through the detector gas they will be detected. This causes soft electrons to be detected

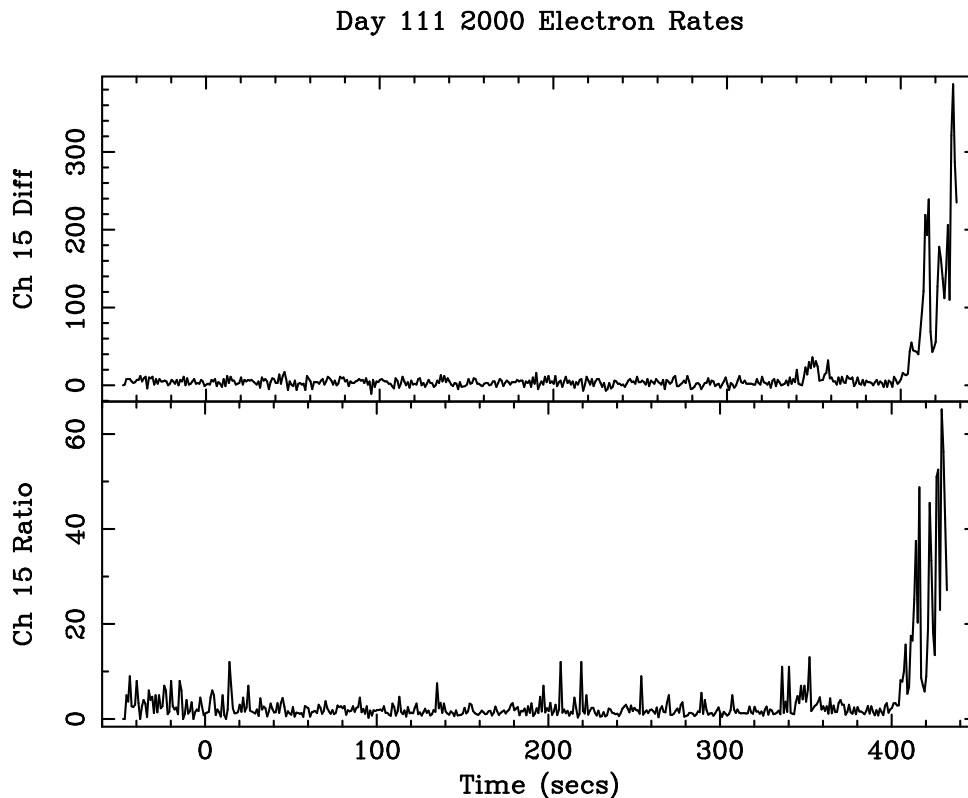


Figure 4.1: Difference and ratio of layers 0 and 1 of USA PHA channel 15 as a function of time during an observation of XTE J1550–564 on Day 111 2000. The top panel shows the difference in channel 15 (layer 0 minus layer 1) and the bottom panel shows the ratio (layer 0/ layer 1). The plots shown in this figure are representative of those used to filter out data, in high background regions, based on soft electron rates. Notice that at around 400 seconds the difference and ratio begin to dramatically increase. The smaller peaks before the 400 second mark are just noise. The use of soft electron rates is only one way, used by **mktimeusa**, to determine that backgrounds are unfavorable.

shortly after entering the detector, in the top layer. In general the electrons will deposit their energy in USA’s highest PHA channel. This allows **mktimeusa** to make background cuts based on the difference and ratio, between the top and bottom layer, of PHA channel 15, for modes 1 and 2. The efficiencies for channel 15 in each of the layers is known to be 0.022 and 0.026, for the top and bottom layer, respectively (Saz Parkinson 2003). **Mktimeusa** calculates rates for the top and bottom layer in channel 15 and then calculates a channel 15 difference and ratio for the detector, see

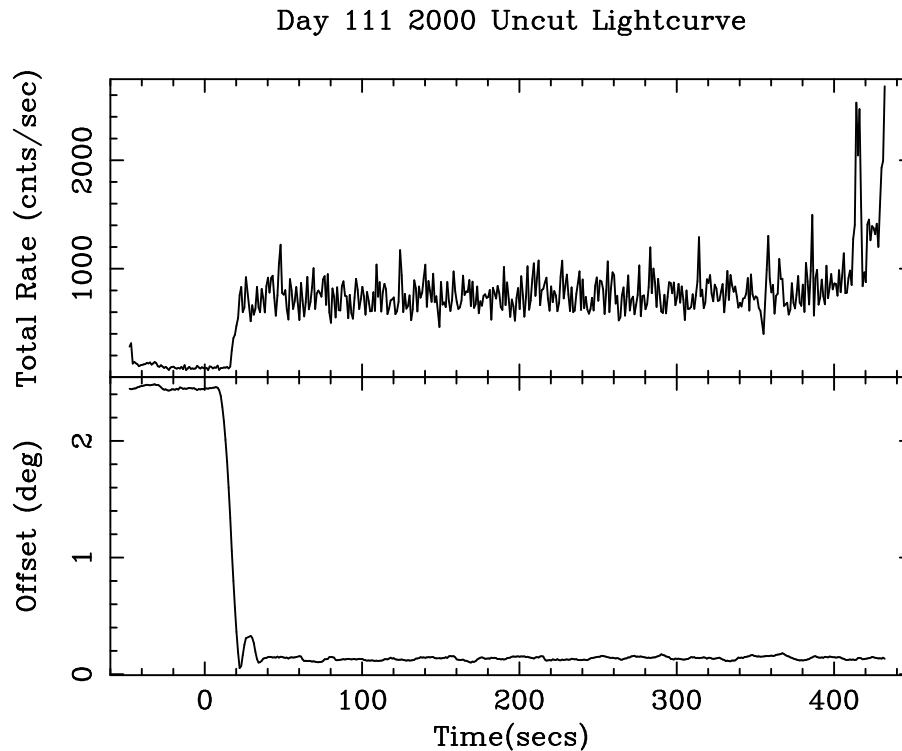


Figure 4.2: Example XTE J1550–564 light curve before cutting. The top panel is the light curve and the bottom panel is the pointing offset. It is informative to see the pointing offset to decrease and USA goes on source. This short off source period is typical of USA observations and acts as a resource for additional background information.

Figure 4.1. When the difference or ratio is too far outside of what it should be, based on the known layer efficiencies, those data are cut from the light curve. Comparing Figure 4.1 to Figures 4.2 and 4.3 it is clear how the rising electron rates were used to cut the data.

After running `mktimeusa` it is always necessary to look at the light curves in order to insure that the data is being cut in the desired way. Figures 4.2 and 4.3 give an example of before and after light curves for XTE J1550–564. Once the data has been adequately cut, the next two most obvious data products to be obtained are background corrected light curves and power spectral density functions (PSDs). Light curves for different energy ranges can be useful to make a variety of other data products such as: color-color diagrams, hardness-intensity diagrams (HIDs) or hardness ratios. The next sections will discuss how PSDs and background subtracted

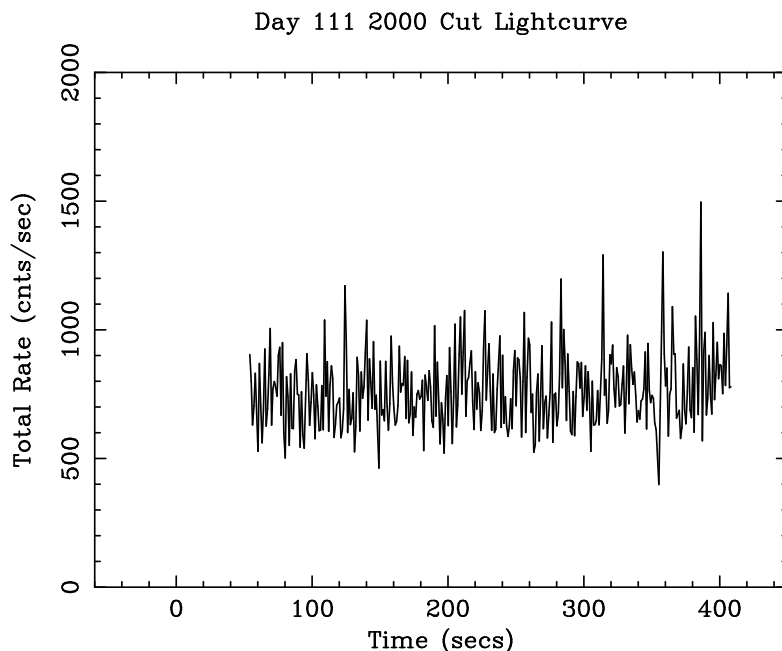


Figure 4.3: Example XTE J1550–564 light curve after cutting.

light curves were created for the XTE J1550–564 USA data.³

4.4 Analyzing USA Data I: Light Curves

Light curves are a plot of the intensity, represented by count rate or flux, as a function of time, in a specific energy range. Light curves are often normalized to counts per second. Figure 5.1 show three light curves in the top three panels. The USA data used to make those light curves is background subtracted and has been selected according to the procedure given above. After cuts the USA observations of XTE J1550–564 consisted of 193 individual observations. Each pointing occurred in groups of 2–8 times per day between 2000 April 14 and 2000 June 18. The total data used was ~ 49 ks out of ~ 94.3 ks of observation time.⁴

Light curves are made from energy selected USA data. Because the lowest (channel

³The method presented in the following sections for calculating background subtracted light curves will be made obsolete once the background files generated by `usabckgnd` are more reliable.

⁴There are several reasons for the nearly 50% loss of data due to cutting. The primary two causes for are that the first 10–20% (80–100 seconds) of scheduled observations is taken up by off-source pointing. The last part of observations are almost always performed in very high background regions and, thus, are cut out. Together these make up almost all of the data loss.

Node	USA Total Range	USA Hard Band (HB)	USA Soft Band (SB)
Ascending Node	66.07 ± 24.98	35.83 ± 16.28	30.24 ± 12.55
South Pole	96.31 ± 21.81	59.80 ± 15.44	36.50 ± 9.23

Table 4.3: **Background Estimates.** Background estimates (in counts/second) for the south pole and ascending node as determined by USA blank sky observations.

0) and highest (channel 15) PHA channels are noisy, potentially having false events in addition to somewhat indeterminate energy acceptances, they are always disregarded (assumed as the under-flow and over-flow channels). For the purposes of studying the XTE J1550–564 outburst, three energy bands from the USA data were used. These bands are the USA total range, corresponding to PHA channels 1–14 (~ 1 –16 keV), the USA soft band (SB), corresponding to PHA channels 1–3 (1–4 keV), and the USA hard band (HB), corresponding to PHA channels 4–14 (4–16 keV). For the remainder of this work, including all subsequent chapters, the total range always refers to USA data in the ~ 1 –16 keV energy range, SB always refers to USA data in the 1–4 keV energy range and HB always refers to USA data in the 4–16 keV energy range. The reasons for choosing the particular energy ranges to study XTE J1550–564 are clarified in the following chapters. For now these light curves serve only as examples.

Each point of USA data shown in the light curves of Figure 5.1 is made of an average of several individual observations. All points are background subtracted using the following technique. All observations were sorted by their orbital node, because backgrounds in different nodes can be dramatically different. In the case of XTE J1550–564 observations were taken in only two orbital nodes, the south pole (SP) and the ascending node (AN). Backgrounds in those two nodes were determined from USA’s periodic blank sky observations in the respective regions. All blank sky observations at each node were gathered, cut in the same manner as the XTE J1550–564 observations and then averaged in order to estimate the backgrounds at the SP and AN. See Table 4.3 for the background estimates in counts/second. The errors shown are the standard deviation of the average.

Once an estimation of the backgrounds in the regions of interest had been established, the light curves had that background subtracted for each of the three USA energy bands. Errors were determined by adding the error on the uncorrected light curve to the standard deviation of the background estimation in quadrature. When

necessary, light curves were corrected for both collimator response and ‘yoke obscuration.’⁵ Both of the corrections are available from `mktimeusa` as output for each second of an observation.

Once the corrected light curves in Figure 5.1 had been produced it was then possible to calculate the hardness ratio, which is simply the USA hard band divided by the USA soft band (HB/SB), in the bottom panel of Figure 5.1. Additionally, the hardness-intensity diagram (HID), Figure 5.2, was then found by plotting the total range as a function of the hardness ratio. HIDs and hardness ratios are used because of their sensitivity to changes in the X-ray spectrum.

4.5 Analyzing USA Data II: RMS Normalized Power Spectral Densities and Low-Frequency QPOs

This section will discuss the time series analysis of USA data. The most common tool X-ray astrophysicists use to study time series is the fast Fourier transform (FFT). FFTs are used to make PSDs, which allow weak periodic or quasi-periodic signals to be extracted from noisy data. PSDs can also help to disentangle multiple signals present in a single time series.

In general, PSDs are calculated from FFTs of time series. A time series, or finely binned light curve, is defined as

$$x(t_k) = \# \text{ of photons in interval } (t_k, t_k + \Delta t)$$

with $k = 1, 2, \dots, N$, $N = \#$ of bins, Δt is the bin width. This implies that t_k is the relative time in the series as defined by $t_k = (k - 1)\Delta t$. The Fourier amplitude, $a(f_j)$, is then defined in the standard way,

$$a(f_j) = \sum_{k=0}^{N-1} x(t_k) e^{-i2\pi f_j k \Delta t},$$

where f is the frequency of the the j th bin.

⁵Yoke obscuration is due to the instrument support structure, within which the USA detector is pointed by adjusting the pitch and yaw values, see Figure 3.3.

The work presented on XTE J1550–564 makes use of “rms” or fractional mean square variability of the PSD as defined by,

$$P_j \equiv \frac{2}{N_{\text{Photons}}^2} |a(f_j)|^2; j = 0, \dots, \frac{N}{2}$$

where N_{Photons} is total # of photons (van der Klis 1989a; Li and Muraki 2002; Focke 1998). This normalization is convenient because it gives a fractional measure of the variability in the time series. Further, the integral of any component in a PSD is equal to the fractional variability contained in that component.

The necessary PSDs to search for and track the behavior of LFQPOs in XTE J1550–564 were calculated using **specan**. The following bash shell script was used to submit the jobs to the SLAC batch farm.

```
for f1 in $datadir/U*.filt ; do
  base='basename $f1 .evt.filt' ;
  bsub -o $base.log -q medium specan -d \
  $base.dmp -c 1-14 -B geom:0.05:5210.0:0.05:0.03 \
  -n rms -l 8-64 -r 75-6000 -b 96e-6 $f1 ;
done
$
```

The **specan** code and its options are described in Appendix A and Appendix D. The important points, in this script used for the analysis of XTE J1550–564 data in the next chapter, are that the FFTs had 96 μs bins, their lengths were between 8–64 seconds, they were rms normalized and deadtime corrected. To learn about other features of **specan** see Appendix A.7. There are books available on the bash shell and the bsub command. The FFTs were averaged to make the final PSDs using **mergespec**. **Mergespec** is a program which appropriately handles the averaging of FFT output from **specan**. **Mergespec** documentation is given in Appendix E.

4.6 Fitting Quasi-Periodic Oscillations

After the PSDs have been calculated it is usually desirable to fit them. There are a variety of ways, throughout the literature, to fit PSDs (see for example Belloni et al. 2002). Because the main interest here was to track the strength (fractional

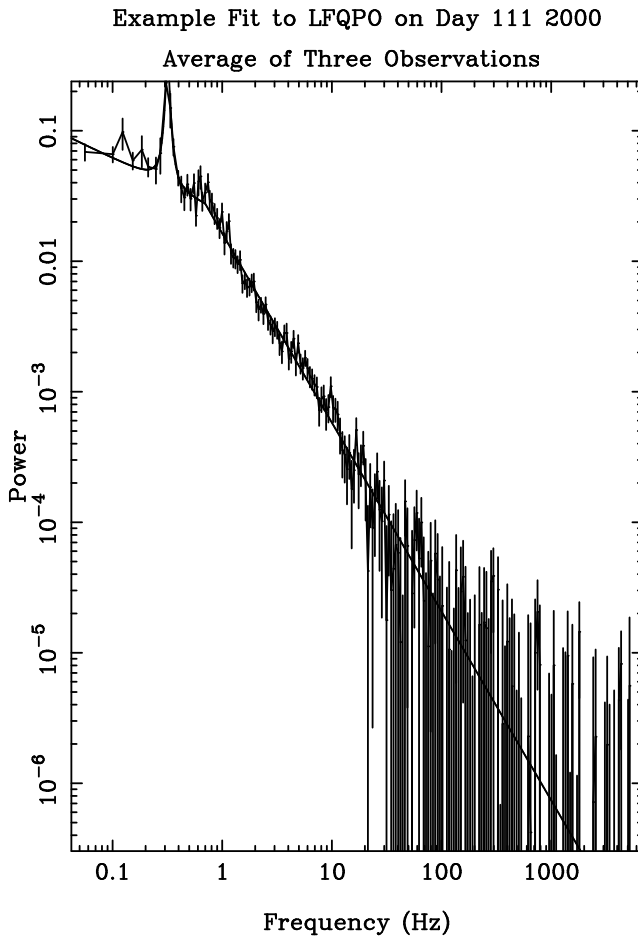


Figure 4.4: Low-hard state PSD with LFQPO fit. Line with error bars shows the PSD and the smooth curve shows the best fit.

variability) and frequency of low-frequency quasi-periodic oscillations (LFQPOs), the XTE J1550–564 PSDs were fit using an rms normalized Lorentzian function with either a power law or broken power law for the continuum power. An rms normalized Lorentzian is defined as,

$$L(f) = \frac{2}{\pi} \frac{R^2}{w + 4 \frac{(f-c)^2}{w}}$$

where, f is the frequency, w is the full width at half maximum, c is the centroid frequency, and R is the rms normalization

$$\mathbf{rms} = R = \sqrt{\frac{\pi N w}{2}}$$

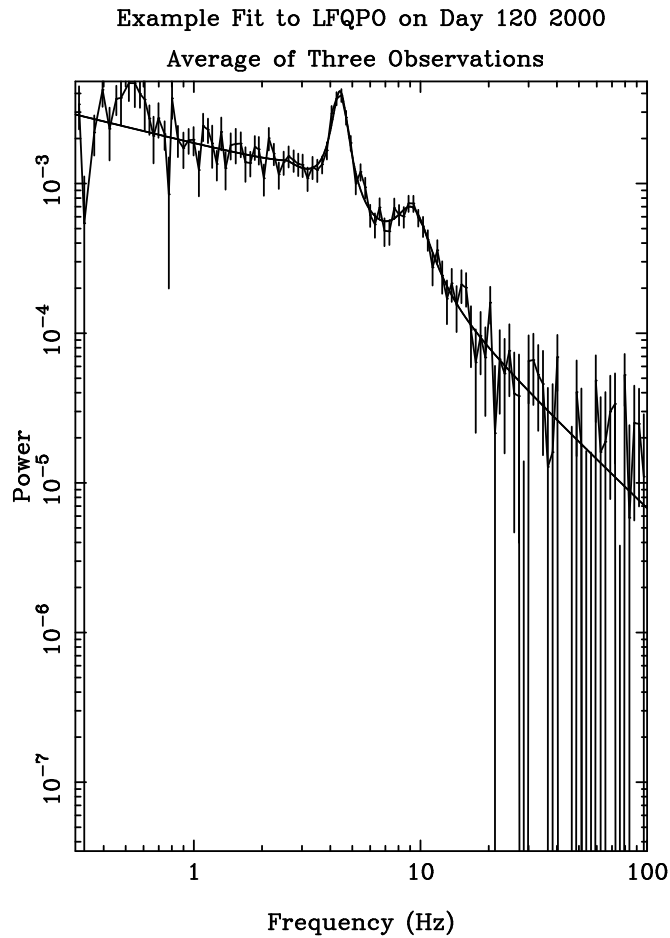


Figure 4.5: Intermediate state PSD with LFQPO fit. Line with error bars shows the PSD and the smooth curve shows the best fit.

if N is the peak power in the Lorentzian. The continuum was fit by a power law,

$$\begin{aligned}
 P(f) &= A_1 f^{\alpha_1} \quad \text{for } f < f_b, \\
 &= A_2 f^{\alpha_2} \quad \text{for } f \geq f_b,
 \end{aligned}
 \tag{4.1}$$

where A_1 and A_2 are constants, f_b is the break frequency of a broken power law and α_1 and α_2 are the power law indices before and after f_b , respectively. Equation 4.1 is for a broken power law. A standard power law may be obtained by setting $f_b = 0$ and A_1 to zero and then fitting.

Two examples of these FITS are shown in Figures 4.4 and 4.5. Figure 4.4 shows the PSD in the low-hard state (LS) as described in Chapter 2. and Figure 4.5 shows the intermediate state (IS). The difference in overall variability between the two states

is apparent as one of the state's distinguishing characteristics. The peak continuum power in Figure 4.4 is about 10^{-1} and in Figure 4.5 it is about 10^{-3} . This shows that there is less variability during the VHS/IS as compared to the LS.

Chapter 5

USA Observations of the Timing and Spectral Evolution of XTE J1550–564 During Its 2000 Outburst¹

5.1 Introduction

XTE J1550–564 was first observed in 1998 September by the All Sky Monitor (ASM) on board the *Rossi X-ray Timing Explorer* (RXTE) when it began an outburst lasting approximately 8 months (Smith 1998). XTE J1550–564 began a second outburst on 2000 April 2 (Masetti and Soria 2000), lasting approximately 2 months.

Recent optical observations of XTE J1550–564 have found the mass function to be

$$f(M) \equiv \frac{P_{sp} K_2}{2\pi G} = \frac{M_1^3 \sin^3 i}{(M_1 + M_2)^2} = 6.86 \pm 0.71 M_\odot \quad (5.1)$$

where M_1 is the mass of the compact object, M_2 is the mass of the companion star, P_{sp} is the spectrally determined orbital period of the binary system, K_2 is the observed radial velocity of the companion star, G is the gravitational constant, i is the orbital plane's angle of inclination to the line of sight (Orosz et al. 2001) (see Gelino 2001 for a derivation of Equation 5.1). The mass function is interesting because it sets the minimum for the mass of the compact object. The most likely mass of the

¹Most of this chapter has been published in its current form. There have been some additions to the chapter which were not published. See Reilly et al. 2001 for the published work.

compact object in XTE J1550–564 was determined to be $M \sim 10.56_{-0.88}^{+1.02} M_{\odot}$ (Orosz et al. 2001). This mass places the compact object well above the maximum mass for a stable neutron star and so provides compelling evidence that XTE J1550–564 contains a black hole. Optical and radio observations of the 2000 outburst show evidence of jet formation (Corbel et al. 2001; Jain et al. 2001).

Complex timing and spectral behavior has been observed by RXTE in XTE J1550–564 during its two full outbursts. This behavior includes detections of three classes of low-frequency quasi-periodic oscillations (< 20 Hz) (LFQPO) and several detections of high-frequency QPOs (> 100 Hz) (HFQPO) (Remillard et al. 2002; Miller et al. 2001; Kalemci et al. 2001). Further, color-color diagrams and hardness intensity diagrams of the 1998–1999 outburst showed separate spectral branches for each of the black hole states as well as correlations with quasi-periodic oscillations and other timing behavior (Homan et al. 2001).

During the 1998–1999 outburst, XTE J1550–564 exhibited all four (if the IS and VHS are counted together) identified black hole spectral states (Sobczak et al. 2000a; Homan et al. 2001). In the 2000 outburst the source never achieved the high state (HS), going from an initial low/hard state (LS) to an intermediate state (IS) or a very high state (VHS) and returning to a final LS (Miller et al. 2001). Although previous authors have made a distinction between the IS and VHS, recent work on XTE J1550–564 has suggested that the IS and VHS are actually the same state at different X-ray flux levels (Homan et al. 2001). Therefore, for the remainder of this paper we will refer to this state as the IS. The transition from the initial LS to the IS was made on 2000 April 26 (MJD 51660). The midpoint of transition from the IS to the final LS occurred on May 18 (MJD 51682) (Tomsick et al. 2001). The observations of (Tomsick et al. 2001) show a clear drop in the soft component and a hardening of the power law component, indicating a transition to the final LS, which was then followed by spectral evolution during the final LS.

In this chapter, X-ray observations of the 2000 outburst of XTE J1550–564 made by the USA Experiment are reported. Light curves and hardness ratios are presented. An LFQPO is tracked during the initial and late stages of the outburst.

5.2 Observations and Data Analysis

5.2.1 Light Curves and Hardness Ratios

The USA Experiment observed XTE J1550–564 at the rate of 2–8 times per day between 2000 April 14 (MJD 51648) and 2000 June 18 (MJD 51713). For the present investigation, 193 observations were used, from which we selected ~ 49 ks of data obtained in low-background regions. The data are time tagged, having $32 \mu\text{s}$ time resolution, and cover an energy range of approximately 1–17 keV in 16 pulse height analyzer (PHA) channels. In this work we do not make use of the lowest (channel 0) and highest (channel 15) PHA channel. The PHA channel 0 is excluded because it might contain false events due to noise in the detector electronics and PHA channel 15 is the overflow channel. See Figure 3.6 and especially Saz Parkinson 2003 for the details of the USA energy calibration. PHA channels 1–14 (~ 1 –16 keV) are referred to as the *total range*.

To create the light curves shown in Figure 5.1, a first order background subtraction was made by averaging blank sky observations and then subtracting these values from the count rate. To determine the total error, the standard deviation of the average in the background was added in quadrature to the error on the count rate. USA data were then corrected for obscuration by the instrument support structure and the collimator response. The overall average light curve (normalized to the USA Crab counting rate) for the total range is shown in panel (a) of Figure 5.1. The circles are RXTE/ASM daily averaged data used to give the complete outburst profile (USA observations did not cover the first few days of the outburst). The USA data points shown are an average of several USA observations. The number of observations averaged was dependent on the observation spacing and signal to noise ratio.

The spectral characteristics of the outburst were studied by dividing the USA data into two energy bands, USA PHA channels 1–3 and channels 4–14. These two bands correspond to 1–4 keV and 4–16 keV, respectively. For the remainder of this Chapter these bands will be referred to as the soft band count rate (SB) and the hard band count rate (HB). The motivation for choosing the specific energy ranges of the SB and HB came from properties of the hardness-intensity diagram (HID). During the outburst, XTE J1550–564 traces a cyclic pattern in the HID. Plots of count rates as a function of the total range (defined above) show this cyclical structure for individual channels in the range 4–14, but not for channels 1, 2 or 3.

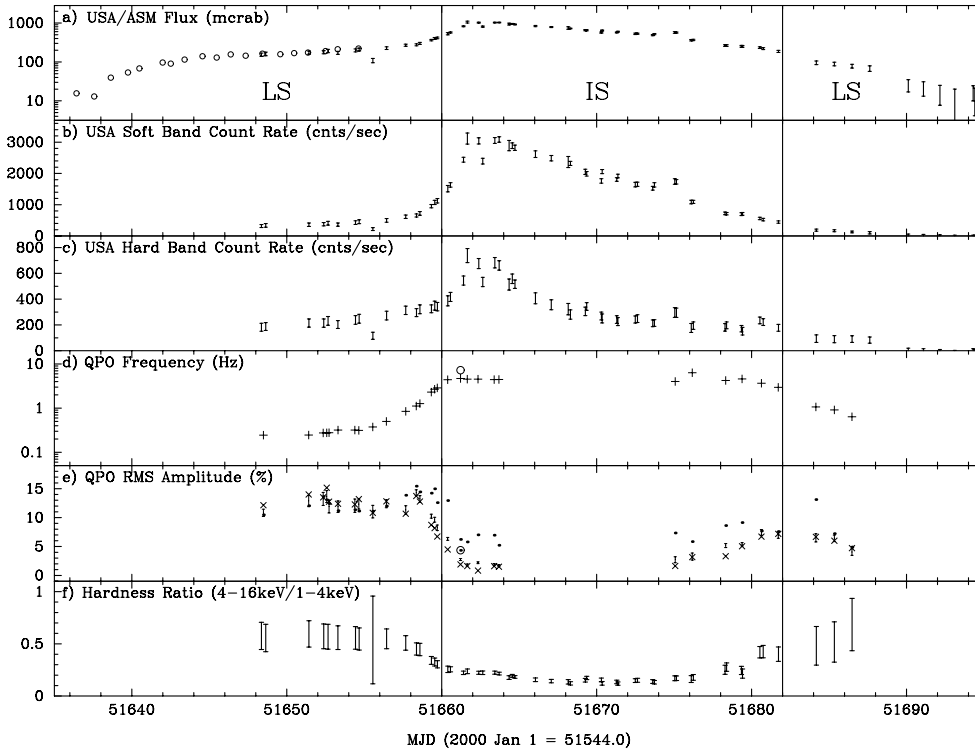


Figure 5.1: Time evolution of the SB, HB, USA total range and LFQPO parameters during the 2000 outburst of XTE J1550–564. The solid vertical lines show the time of transition between states. Panels: (a) USA/ASM Crab normalized fluxes for the outburst on a log scale. The circles are ASM daily averaged data taken before USA started observations. ASM error bars, not shown, are smaller than the circles. USA data are shown as error bars only. (b) USA Soft Band count rate (SB), ~ 1 –4 keV. (c) USA Hard Band count rate (HB), ~ 4 –16 keV. (d) LFQPO centroid frequency on a log scale. The plus signs show results for the total range 1–16 keV. The large unfilled circle shows the frequency of the anomalous HB QPO. Error bars, not shown, are smaller than the symbol size. (e) LFQPO percent rms amplitude. The total range 1–16 keV is represented by error bars only. Filled circles are the HB and the “X”s are the SB. The large unfilled circle marks the anomalous QPO. Error bars in the SB and HB are not shown, but are comparable to those on the total range. During the time between approximately MJD 51662 and MJD 51675, it was not possible to obtain reasonable fits to the data. If any LFQPOs are present during that time the rms amplitude is $< 1.7\%$, see Section 5.5.1 for details. (f) Hardness ratio (HB/SB).

Panels (b) and (c) of Figure 5.1 show the SB and HB as a function of time during the outburst. The bottom panel of Figure 5.1 shows the evolution of hardness ratio using these energy bands. The HID in Figure 5.2 shows how the hardness ratio evolves with total count rate during the outburst. The hardness ratio is plotted only for USA

data prior to MJD 51687, after which the signal to noise decreases to the point that the hardness ratio is not constrained. In Figure 5.2 and panel (f) of Figure 5.1, one point is shown for each point in panels (b) and (c) of Figure 5.1.

The design of the USA detector incorporated automatic gain stabilization hardware and frequent iron source energy calibrations were done while in orbit. We note that the USA channel to energy conversion varies slightly over the USA orbit; however, checks performed showed that this variation made no significant impact on the relevant features seen in the SB, HB, and hardness ratio. A further check of our spectral results was made by comparing our data to public RXTE/ASM data. Daily averaged ASM data were used to find the hardness ratio as a function of time and to make a HID. The ASM hardness ratio was calculated by dividing the sum of ASM B Band (3–5 keV) and C Band (5–12 keV) by A Band (1.5–3 keV). To try to emulate the ASM energy bands the USA PHA channels 3–11 (3–11.5 keV) were summed and divided by channel 2 (2–3 keV). The ASM data confirmed the hardness ratio observed with USA and the cyclic behavior in the HID, see Section 5.5 for a discussion of USA analysis checks.

5.2.2 Power Spectra: Low-Frequency QPOs

A low-frequency quasi-periodic oscillation (LFQPO) was ubiquitous during the rise of the outburst and during the decay of the outburst after the secondary maximum. In order to track the LFQPO evolution through the outburst, observations were grouped by day and frequently in sub-day groups (signal to noise ratio permitting).

Power spectra (see Nowak et al. 1999 and references therein) were calculated from these groups and averaged. The resultant power spectrum for each group containing a LFQPO was fit with a power law or broken power law and a Lorentzian for any observable QPO features. Fits were made in three energy bands: the total range, SB, and HB. In case of confusion by sub-harmonics, the strongest QPO feature was chosen as the primary LFQPO (see (Remillard et al. 2002)). In most cases no sub-harmonics were detectable. Panel (d) of Figure 5.1 shows how the centroid frequency of the LFQPO evolves during the outburst. The evolution of the rms amplitude for all three energy bands is shown in panel (e). Panels (d) and (e) show error bars calculated by allowing the χ^2 per degree of freedom (DOF) of the fit to vary by one. All error bars are given at the 68% confidence level.

5.3 Results

5.3.1 QPO Evolution and Correlation to State Changes

We observe LFQPOs between MJD 51648 and 51663 and between MJD 51675 and 51686 which vary in frequency between 0.24–7.19 Hz and 6.34–0.64 Hz, respectively. During the times of these detections the source is either in the LS or near the transition from one state to another. The LFQPO rms amplitude decreases rapidly at the state transition from the LS to the IS and then increases during the transition back to the LS, indicating that the mechanism for creating the LFQPO is suppressed in the IS. The LFQPO centroid frequency generally increases with increasing flux; the fractional rms amplitude is correlated with hardness ratio (see Figure 5.1). This correlation and others are discussed in greater detail in Chapter 6.

During the IS, significant detections of HFQPOs (249–278 Hz) were made by RXTE between MJD 51663 and 51675 (Miller et al. 2001). A 65 Hz QPO has been discovered by (Kalemci et al. 2001) at MJD 51684.8. These HFQPO detections occurred during the periods where USA observed the LFQPO to be weakening or not detectable at all. It is interesting to note that the HFQPOs were observed to decrease in significance as a function of time in the IS (Miller et al. 2001). We observe a decline in rms amplitude of the LFQPO near the LS/IS transition, which marks the approximate onset of the HFQPOs. Toward the end of the IS, near the IS/LS transition, the HFQPO weakens as the LFQPO once again becomes detectable. This trend continues in the last days of the outburst, when the LFQPO rms amplitude weakens and the 65 Hz QPO is detected.

These QPO features are qualitatively consistent with observations of XTE J1550–564 during the 1998–1999 outburst (Remillard et al. 2002), during which an “antagonism” between LFQPOs and HFQPOs was also observed. During that outburst, type “C”, as defined by Remillard et al. 2002, LFQPOs were observed when strong correlations were seen between the frequency and disk flux while the amplitude was observed to correlate with disk temperature (Remillard et al. 2002). These previous observations closely resemble what we see for the LFQPO observed during the 2000 outburst; thus we tentatively classify the LFQPO discussed here as a type C.²

At MJD 51661.21 an anomalous QPO was detectable exclusively in the HB, in

²Remillard et al. 2002 categorize the LFQPOs found by RXTE during the 1998–1999 outburst. There categories, A, B, C, etc., are defined by QPO percent rms, phase lags and other properties.

contrast to the primary LFQPO which appears in all energy ranges. In Figure 5.1 panel (d), this anomalous QPO is the highest frequency point and is marked with a large unfilled circle near MJD 51660. This QPO was detected between the primary LFQPO and its harmonic and has a frequency of $7.19_{-0.11}^{+0.12}$ Hz, whereas the primary LFQPO is seen at 4.71 ± 0.05 Hz and its harmonic is seen at $9.75_{-0.35}^{+0.4}$ Hz.

5.3.2 Spectral Evolution

From Figure 5.1 it is clear that the 2000 outburst of XTE J1550–564 does not follow the canonical fast rise, exponential decay (FRED) outburst as would have been expected prior to the RXTE era. Now, with many more examples of well-observed soft X-ray transient (SXT) outbursts, it has become clear that few outbursts look like pure FREDs, and that the outburst profile can be very different in different wavelengths, for example see Figure 2.8 for the optical and IR light curve profiles. Differences over slight changes in wavelength are seen by comparing the SB and HB light curves in Figure 5.1, panels (b) and (c), the two bands rise approximately in unison, but show very different behavior after the peak. With the exclusion of the secondary maximum the HB light curve shows a nearly symmetric outburst profile, while the SB rapidly rises, then decays approximately linearly. As is often observed in SXTs, the decay returns to its original path after the secondary maximum.

In the HID (Figure 5.2), we observe that the difference between the SB and HB light curves manifests itself as a cyclic structure that moves with time in a counter-clockwise direction. The HID shows a rapid drop in the hardness ratio as the source enters the IS and a rapid increase as the final LS is realized. This type of spectral structure, which has been seen in several other sources (Smith et al. 2002), is a consequence of the spectrum being harder during the rise than during the decline.

5.3.3 Multi-wavelength Correlations

In Figure 5.3 the lines numbered 1, 3, 4, 6, 7 and 8 represent observations made in other wavelengths. Lines 1 and 8 mark the approximate times of optical/IR maxima and lines 3 and 7 indicate significant radio detections made by ATCA while line 4 indicates ATCA radio observation having no significant flux. The radio signal at line 7 was found to have a slightly inverted spectrum (Corbel et al. 2001). Line 6 is the approximate time of an optical/IR minimum. (Optical/IR observations were

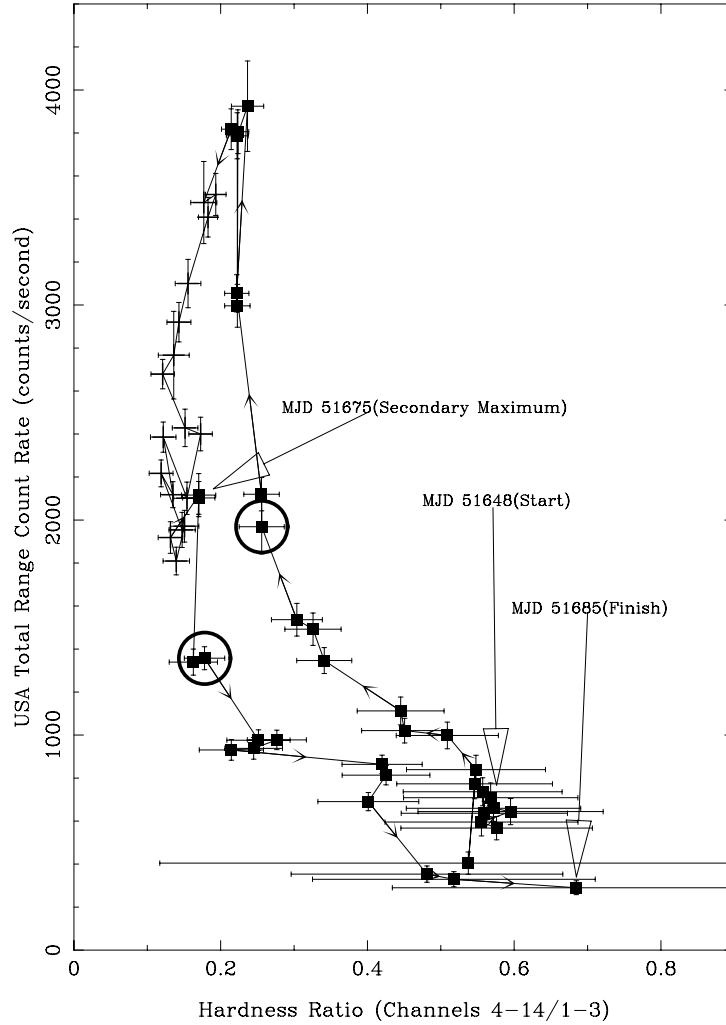


Figure 5.2: Hardness Intensity Diagram. Total Range Count Rate vs. Hardness Ratio (HB/SB). Squares are plotted on points in which the LFQPO was detected. Points at which no QPO detection was made only show error bars. The error bars shown are the standard deviation of the flux and the hardness ratio. Arrows plotted between points show the direction of time. The larger outlined arrows mark the start and stop times of USA observations and the time of the secondary maximum. Transitions between states have been marked with the bold circles.

made by YALO; for complete details on the radio and optical/IR observations see Corbel et al. 2001 and Jain et al. 2001). Radio observations by MOST (not shown) made during the initial LS show a detection of 8–15 mJy at 843 MHz (Corbel et al. 2001). This indicates that the radio emission prior to line 3 is more than a factor of

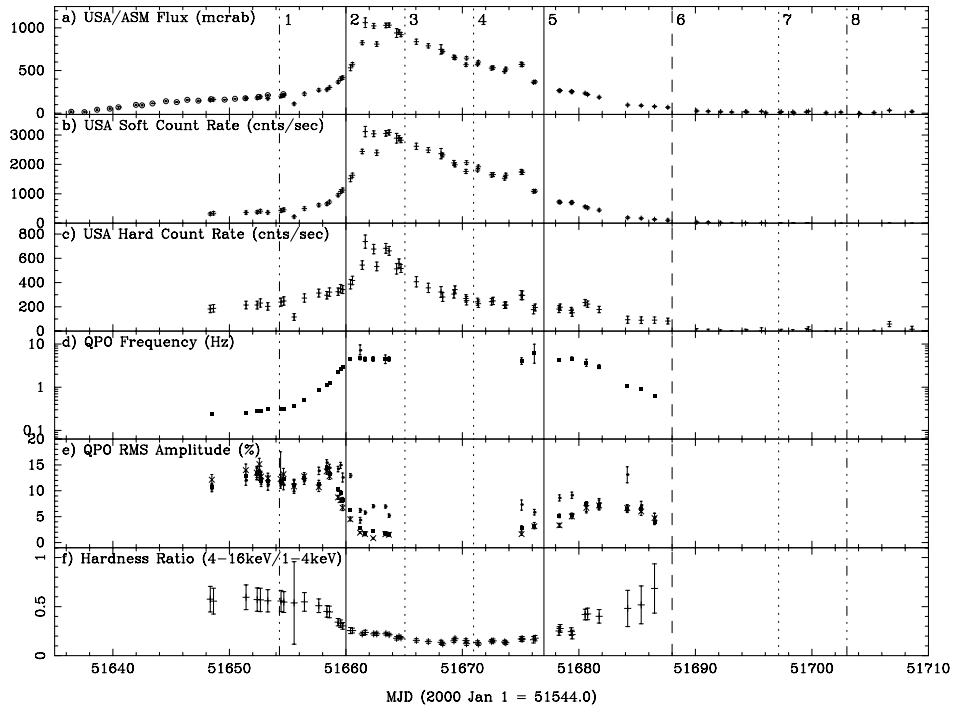


Figure 5.3: Time Evolution of XTE J1550–564 with Multi-wavelength Observations. (a) USA/ASM Crab normalized fluxes for the outburst. The circles are ASM daily averaged data taken before USA started observations. ASM error bars are shown but smaller than the circles. Pluses with error bars are USA data. (b) USA Soft Band count rate (SB), $\sim 1\text{--}4$ keV. (c) USA Hard Band count rate (HB), $\sim 4\text{--}16$ keV. (d) low-frequency quasi-periodic oscillation (LFQPO) centroid frequency plotted on a log scale. Pluses show the the frequency for the energy range $1\text{--}16$ keV. Filled circles are the HB and the “X”s are the SB. The high HB point seems to be a different LFQPO which does not show up in the SB or the HB+SB power spectra. (e) LFQPO percent rms amplitude. Symbols are the same as panel (d). During the time between approximately MJD 51662 and MJD 51675, it was not possible to obtain reasonable fits to the data. If any LFQPOs are present during that time their rms amplitude is $\lesssim 1.7\%$, see Section 5.5.1 for details. (f) Hardness ratio (HB/SB). Line 2 shows the transition between the initial LS and the IS. Line 5 shows the approximate beginning of the transition period between the IS and final LS. Lines 3, 4 and 7 are the times of ATCA observations. Lines 1 and 8 show optical maxima and line 6 shows an optical minima. The complete optical light curves for the 2000 outburst of XTE J1550–564 are shown in Figure 2.8.

50 stronger than at the time of the ATCA observation made at line 4 (Corbel et al. 2001). Note, lines 1, 6 and 8 are said to be the approximate times of the optical/IR extrema because the actual measurements show that the extrema occur at slightly different times (with a few days of each other) in each of the three bands, H, I and

V, observed (see Jain et al. 2001 for details).

These kinds of multi-wavelength studies are especially interesting in microquasars, where understanding jet production is limited and observations in different energies seem to allow some insights. The multi-wavelength observations, described above and shown in Figure 5.3, of XTE J1550–564 during the 2000 outburst have shown correlations between radio, optical, IR and X-rays. These observations have been compared with similar correlations seen in other black-hole candidates (BHCs), such as GX 339–4 (see Figure 2.7), and have led to the interpretation that the LS of BHCs is characterized by jets and the IS state is characterized by quenching of these jets and possibly relativistic ejections (in the state transition) (Corbel et al. 2001). According to the radio and optical/IR observations discussed here, the XTE J1550–564 2000 outburst only adds to these characterizations. Specifically, there is evidence for the presence of jets during the initial and final LS of the 2000 outburst (Corbel et al. 2001; Jain et al. 2001).

It is now generally thought that the LS, of microquasar outbursts, is distinguished by the presence of jets. Upon transition to the IS/VHS or HS, quenching of the jets/ejections occurs as is demonstrated by the sharply reduced radio signal. Here a link to the corona is proposed. Because the HB component is most likely a result of a hot Comptonizing corona, the rapid drop in the HB upon quenching of the radio is likely consistent with models which suggest a link between jets and the LS. Assuming, that outburst occur in a disk-instability model (DIM) fashion (Lasota 2001), then a scenario in which jet production is strongly dependent upon the hot corona can be imagined. At the beginning of an outburst the corona is large and the inner edge of the accretion disk is truncated at $> 100 R_{\text{Sch}}$. As the outburst begins, material rapidly flows in from an unstable accretion disk, there is perhaps a ‘splashing’ effect and maybe magnetic fields in the corona or accretion disk collimate this ‘splash’, which then leads to jets and ejections, this is the LS. Now as the DIM suggests the disk proceeds inward, becomes larger, increasing the flux of soft photons, which eventually cool the corona and inhibit the mechanism by which the jet is produced, thus quenching the jet. This is the IS/VHS or HS and may be commensurate with a mechanism of ‘physical suppression’ of jets in the soft states (Fender 2002).

The HB drop may be a further indication of jet quenching linked to high energy X-rays, (i.e. 20–100 keV BATSE data). (This is assuming that most SB photons are produced in the disk.) Additional support for these ideas comes from work linking

the formation of outflows to LFQPOs (Tagger and Pellat 1999) and to other work, see Chapter 6, linking the LFQPO to the corona, because the quenching of the radio signal occurs very near the time the LFQPO is no longer detectable. Specifically, it is noted, see Figure 5.3, that the weak radio detection (line 3) occurs while the SB is still very near its maximum and the HB has dropped from its maximum by a factor of ~ 2 and continues on a rapid decline. At the point of no significant radio detection (line 4), the HB has greatly reduced its rate of decrease. The return of the radio signal in the final LS suggests that the mechanism of jet production is related to but not dependent on HB photon production mechanism. In future outbursts, it would be helpful to obtain much more thorough radio coverage in order to pin down the nature of the relationship, if one exists, between the HB and jet quenching.

5.4 Discussion: Two-Flow Models

The different behavior of the HB and SB light curves, together with the lack of a strict correlation between the QPO frequency and source flux, suggest a scenario involving a two component accretion flow. Models invoking two *independent* accretion flows (*e.g.* a thin disk and a hot sub-Keplerian flow) have been described by (Chakrabarti and Titarchuk 1995) and (Smith et al. 2002), while (van der Klis 2001) presents a model where the two parameters are the instantaneous and time averaged values of a *single* quantity.

Whether the two accretion parameters are dependent or independent, there is most likely a transition radius at which the Keplerian disk is disrupted and forms an inner hot sub-Keplerian flow.³ This inner flow can be an advection-dominated accretion flow (Esin et al. 1997) or a postshock flow interior to the radius where two independent flows interact (Chakrabarti and Titarchuk 1995). This transition radius is a natural site to consider for the formation of low or high frequency QPOs. The relationship between the Keplerian orbital period and radius for a $10.0M_{\odot}$ black hole is $R \sim 109R_{\text{Sch}}P^{2/3}$, where R_{Sch} is the Schwarzschild radius ($R_{\text{Sch}} \sim 30.0$ km for a $10.0M_{\odot}$ black hole) and P is the orbital period in seconds. For small values of the transition radius, one can consider models where the high-frequency QPO is the Keplerian orbital period at the transition radius and the LFQPO is related to radial oscillations of the transition layer as described by (Titarchuk and Osherovich

³Chapter 6 will discuss why there should be this transition radius. The most compelling evidence comes from the disk instability model for SXT outburst (Lasota 2001).

1999). For large values of the transition radius, the LFQPO could be the Keplerian frequency, but then another explanation is required for the HFQPO which, at least in some instances, are seen simultaneously.

In order for a two flow model to explain the spectral characteristics described in Section 5.3.2, it should allow for spectral softening to occur while the overall source flux is dropping. For two independent flows, this type of spectral evolution occurs because changes in the radial flow may occur on a short (free-fall)⁴ timescale, while the effect of changes in the the disk accretion rate are delayed due to viscosity (Chakrabarti and Titarchuk 1995; Smith et al. 2002). A model of two independent flows was applied to GRS 1758–258 and 1E 1740.7–2942 by (Smith et al. 2002), both of which also showed spectral softening with decreasing flux. Using a dependent flow model (as described in van der Klis 2001), suggests that if the count rate is dominated by the disk accretion rate and the spectral hardness is related to the inner disk radius (which is determined by the time-averaged accretion rate), the same cyclic structure in the HID will result.

Recent ideas on the role of jets in microquasars suggest a link between the jet and the corona (see Fender 2002 and references therein) and may provide a theoretical basis for the observed association between the HB and the radio and optical/IR signals (Section 5.3.3). The LS is associated with a continuous radio-emitting outflow and the presence of the strong LFQPO. At the transition to the IS, discrete radio ejections seem to be common but the continuous jet ceases and the LFQPO mechanism is suppressed. This indicates that both the outflow and the LFQPO are characteristic of the LS and are related to the presence of a hot corona. The accretion-ejection instability model provides a mechanism where spiral density waves may be responsible for both the LFQPO and energizing the jet (Tagger and Pellat 1999).

Continued theoretical development and application to the body of observations of XTE J1550–564 may allow a final determination of the true LFQPO mechanism, the cause of the spectral state changes, and the means of jet production.

⁴Actually, free-fall is unlikely. Again refer to Chapter 6. All that is needed is a stable disk and another flow. The disk is assumed to be truncated. It is possible that free-fall occurs on short distance scales. Either way the presence of two flows (and possibly “three flows” if jets are also present) seems to be experimentally proven. The precise model is another question.

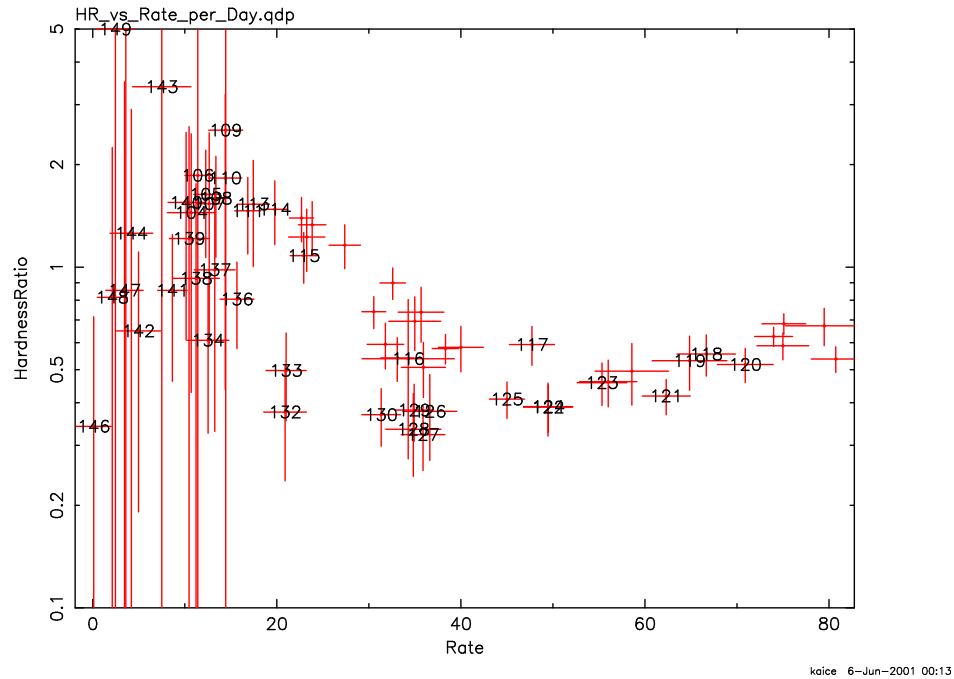


Figure 5.4: ASM Hardness Intensity Diagram. ASM Hardness Ratio Versus Total Rate. The hardness ratio is C Band Rate/A Band Rate and total rate is the sum of the A, B, and C bands. Time increases along the path of the increasing digits plotted on selected points. The axes in this figure are flipped with respect to Figure 5.2. The ASM A band is 1.5–3 keV, the ASM B band is 3–5 keV and the ASM C band is 5–12 keV.

5.5 Discussion of Analysis Checks Performed On USA XTE J1550–564 Observations

Because USA was a new experiment, it was prudent to perform several checks on the analysis presented in this chapter. In general, the USA science working group had confidence in low-frequency timing phenomena. This confidence was gained with the earlier LFQPO work done on XTE J1118+480, see Wood et al. 2000 for the XTE J1118+480 LFQPO data. The XTE 1550–564 data showed interesting spectral characteristics, which although observed in other sources, made it desirable to make checks and confirmations using other publicly available data. The steps taken to insure the correctness of the spectral and timing behavior observed in XTE J1550–564 are discussed in this section.

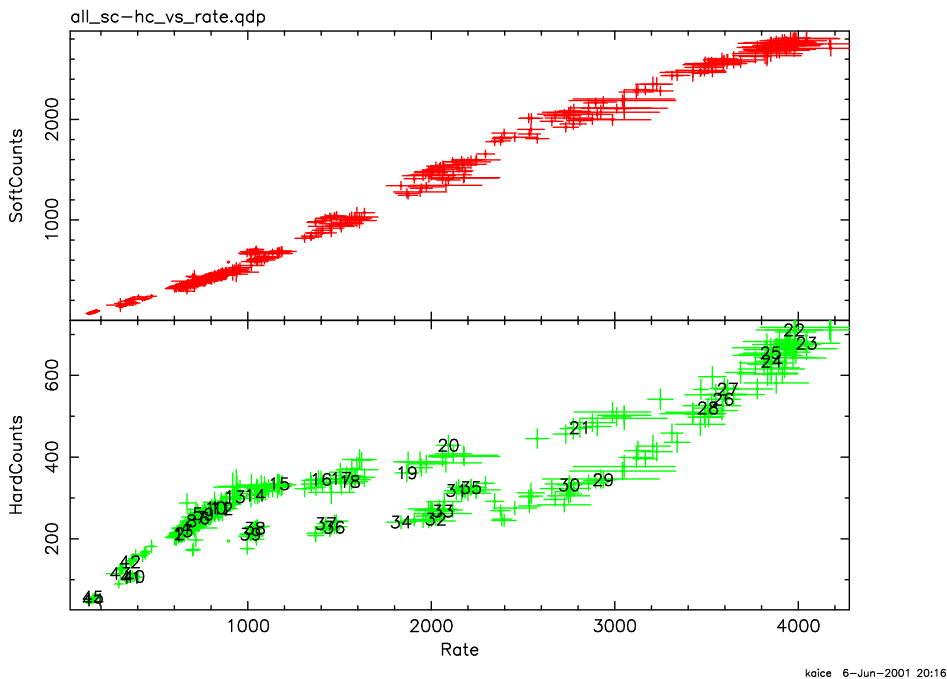


Figure 5.5: Top panel: USA Soft Band Count Rate Versus Total Range. Bottom panel: USA Hard Band Count Rate Versus Total Range. Time increases along the path of the increasing digits plotted on selected points.

First the work to test the veracity of the cyclic structure seen in Figure 5.2 is discussed. The most convincing confirmation is made by comparing Figure 5.4 to the bottom panel of Figure 5.5 and by comparing Figure 5.4 to Figure 5.2. On comparison it is seen that the cyclic structure exists in both the USA and ASM data. The curves are not expected to be exactly the same, because of the different energy acceptances and resolutions of the ASM and USA.

Figure 5.5 serves a second purpose. It is a demonstration of why the SB was chosen to be PHA channels 1–3 and HB was chosen to be PHA channels 4–14. In the top panel there is virtually no (within error bars) cyclic structure; it increases and decrease along the same path. The bottom panel shows clearly different behavior. When plots were made of all 14 PHA channels individually, PHA channels 1–3 looked like the top panel and all individual PHA channels between 4 and 14 looked like the bottom panel.

USA is known to have a gain which depends upon its orbital node. Correlations between the gain detector temperature indicate that gain fluctuations are result of

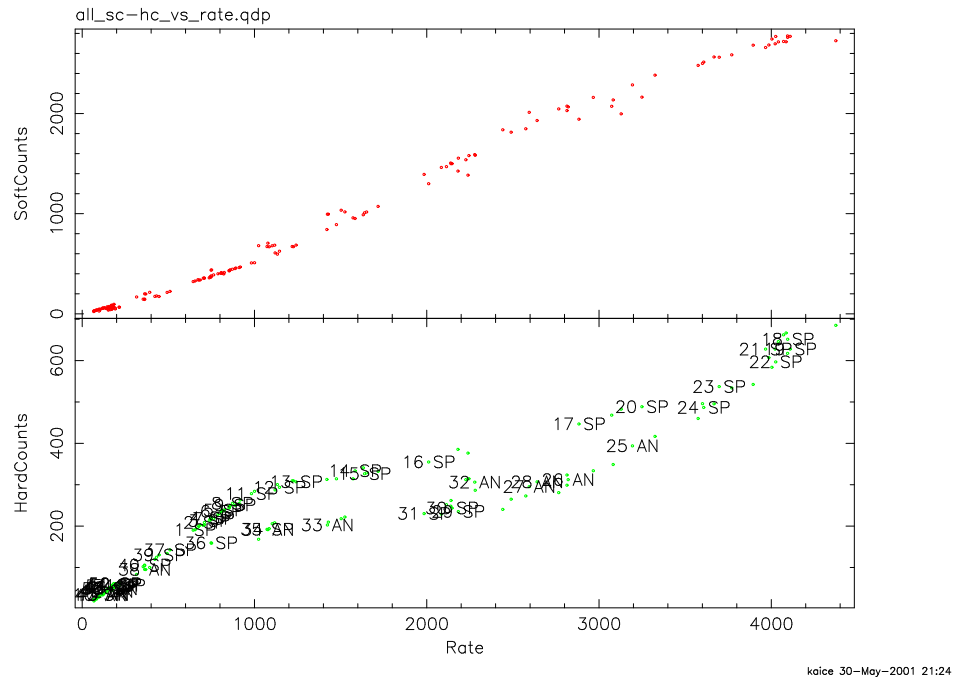


Figure 5.6: Top panel: USA Soft Band Count Rate versus Total Range with Ascending and South Pole Node Identifiers. Bottom panel: USA Hard Band Count Rate versus Total Range. No error bars are shown in this figure. Errors are identical to those shown in Figure 5.5. Time increases along the path of the increasing digits plotted on selected points. The labels AN and SP refer to observations taken on the ascending node and over the south pole, respectively.

thermal cycling in the instrument as it progresses through its orbit (Saz Parkinson 2003). This means that there is a small shift in the energy of a PHA channel as USA moves through its orbit (Saz Parkinson 2003). The XTE J1550–564 data were taken in two different orbital nodes, so it was necessary to make sure that gain changes were not the cause of the cyclic structure in Figure 5.2 and to make sure that these gain changes did not have a significant impact on the hardness ratios shown in Figure 5.1. In order to address the issue of gain changes on the cyclic structure, Figure 5.6 was made. Making use of the south pole (SP) and ascending node (AN) identifiers on the points and looking closely at the numbers in the figure it is clear that the results were not significantly affected by the orbital gain changes. Specifically, AN and SP observations which are closely spaced in time (relative to the outburst timescale) are also in close proximity in the figure. To address any concerns about the USA

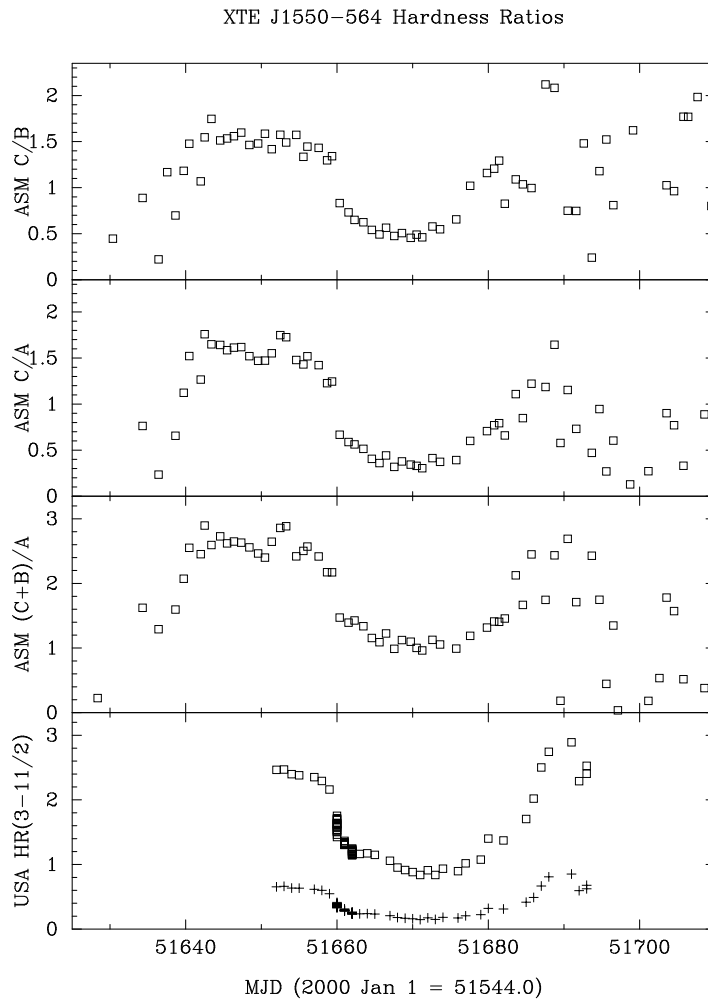


Figure 5.7: Comparison between ASM and USA hardness ratios. From the top panel to the next to the bottom panel: ASM C/B hardness ratio, ASM C/A hardness ratio, ASM (C+B)/A hardness ratio. Bottom panel: The squares represent the hardness ratio of USA PHA channels 3–11/2, which is $\sim 3\text{--}12\text{ keV}/2\text{--}3\text{ keV}$ and the pluses are the hardness ratio calculated from HB/SB. The squares in the bottom panel are close in energy range to the hardness ratio ASM (C+B)/A ($3\text{--}12\text{ keV}/1.5\text{--}3\text{ keV}$). Comparing these two hardness ratios shows no significant differences.

hardness ratios ASM data was once again used as a reference. Referring to Figure 5.7 and comparing the squares in the bottom panel to the ASM hardness ratio just above it shows no significant deviation. This serves as further evidence that the USA hardness ratios are correct.

Most of the discussion of the USA timing behavior was done in (Shabad 2000)

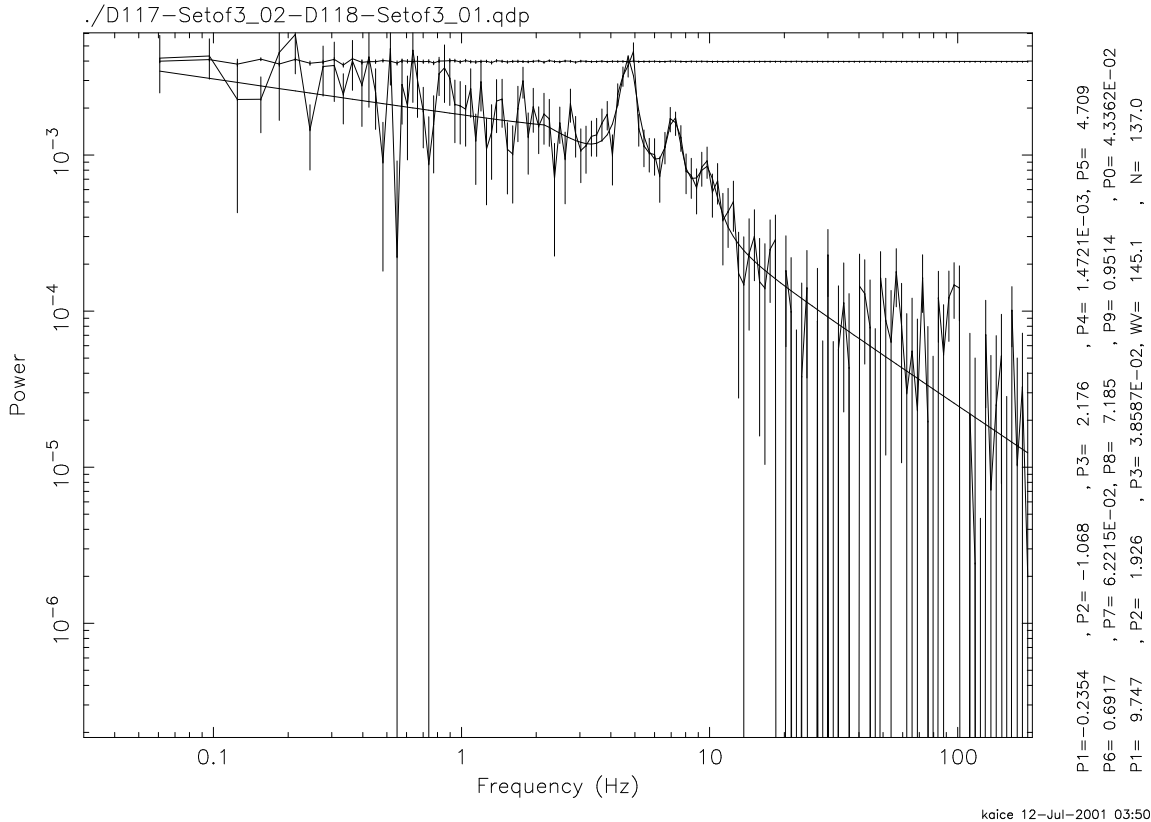
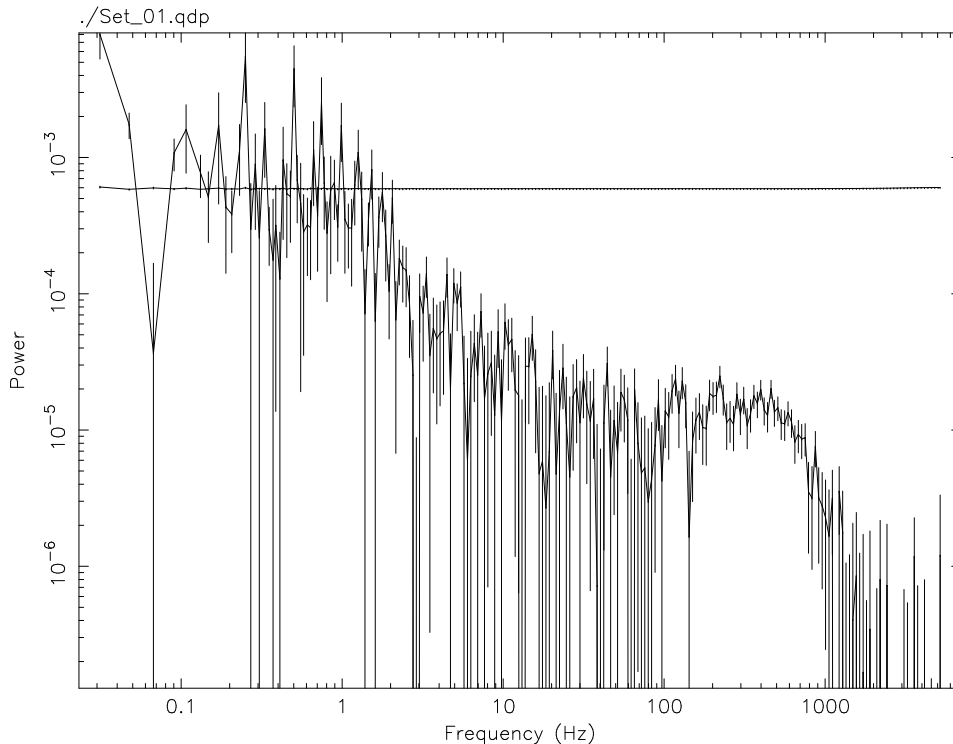


Figure 5.8: Detection of Anomalous LFQPO in USA Hard Band. The almost straight line is the USA deadtime correction which has already been subtracted from the PSD. The curve, a broken power law and three Lorentzians, is the best fit to the data. The central Lorentzian is not visible in the SB PSD and only marginally visible (a hint could be seen but it was not possible to fit) in the total range PSD. The first and third, from left to right, Lorentzians are the primary LFQPO and its harmonic, respectively.

and Section 3.8.1. Here some points related specifically to the timing behavior seen by USA in XTE J1550–564 are discussed. First it is interesting to see the fit to the anomalous LFQPO detection discussed earlier in this chapter. Figure 5.8 shows the fit to the HB PSD where the anomalous LFQPO was detected, it is the central Lorentzian peak in the spectrum. More details about this QPO are given in Section 5.3.1. Figure 5.14 is given for comparison as it shows a *typical* PSD in which an LFQPO detection was made.

Figures 5.9 to 5.13 show examples of PSDs during the IS in which no LFQPO was detected. The days in which no LFQPOs were detected came between Day 121



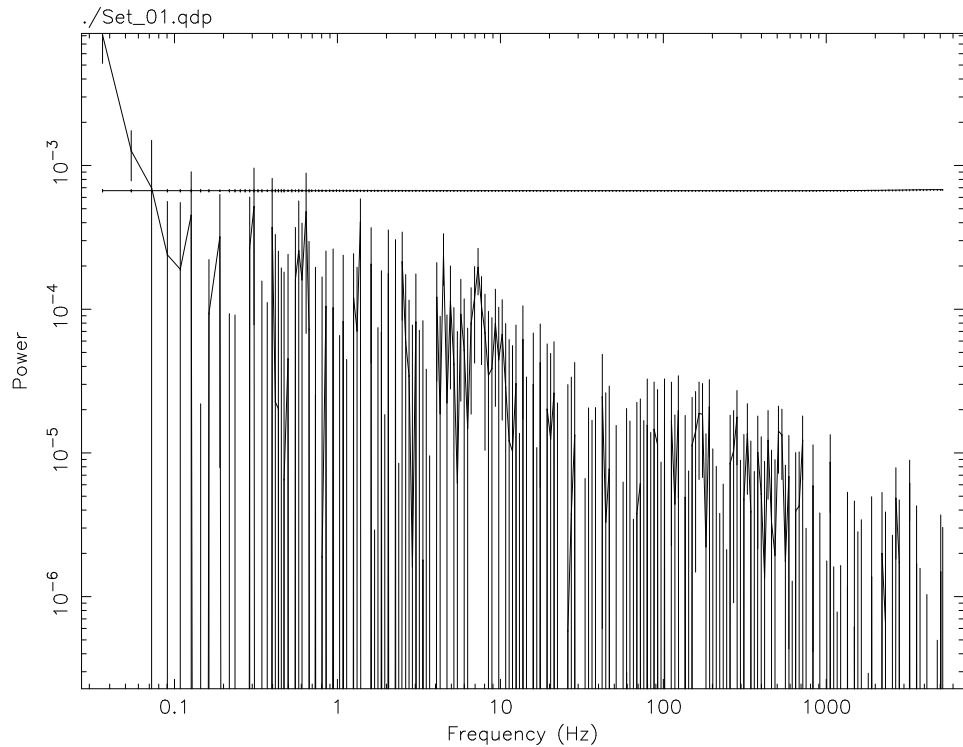
5-Jul-2001 16:55

Figure 5.9: Day 121 2000: LFQPO non-detection example. The almost straight line is the USA deadtime correction which has already been subtracted from the PSD. However, this plot is particularly interesting because there could to be two weak high-frequency QPOs, between 100 and 300 Hz, lost in EDIE.

of Year 2000 and Day 131 of Year 2000. These examples span this entire time range. As can easily be seen from these figures getting a fit to any of these PSDs would be difficult and it would be merely speculative to pick the position of a possible LFQPO in some of these PSDs. However, the PSD from Day 128, 2000, Figure 5.12, shows a possible LFQPO around 7 Hz (based on the trends of the LFQPO this is about the correct frequency). It was not possible to fit this LFQPO while varying all the fit parameters. However see Section 5.5.1 for how this observation was used to set an upper limit on the rms of LFQPOs, during the time in the IS, where no LFQPOs were explicitly detected.

It is worth pointing out several interesting features which are explicit in these PSDs, Figures 5.9 to 5.14.⁵ The first point to note is that the energy spectrum, corresponding to Figure 5.9, is among the softest during the outburst (possibly the

⁵Some of this discussion depends on on earlier chapters of this work, see Section 3.8.1.



5-Jul-2001 16:55

Figure 5.10: Day 123 2000: LFQPO non-detection example. The almost straight line is the USA deadtime correction which has already been subtracted from the PSD.

softest). Moving toward Day 132 the energy spectrum steadily hardens. The observation of a very soft source, such as SXTs during the IS/VHS and HS states, by USA results in a very asymmetric count rate spectrum. Generally, in SXTs, as the source hardens the count rate spectrum becomes less asymmetric. Thus, the distortion of the PSD due to EDIE is much more pronounced in Figure 5.9 than in Figure 5.14, which is exactly what should be expected. From Figure 5.9 the difficulties to USA's search for high-frequency variability are displayed, just as they were in Section 3.8.1 when looking at the USA XTE J1859+226 data. The large feature between 100–1000 Hz dominates the PSD at high frequencies. This makes it very difficult to determine if the two features in the 100–300 Hz range of Figure 5.9 are HFQPOs. It is possible that they are HFQPOs, because RXTE detected multiple HFQPOs in this frequency

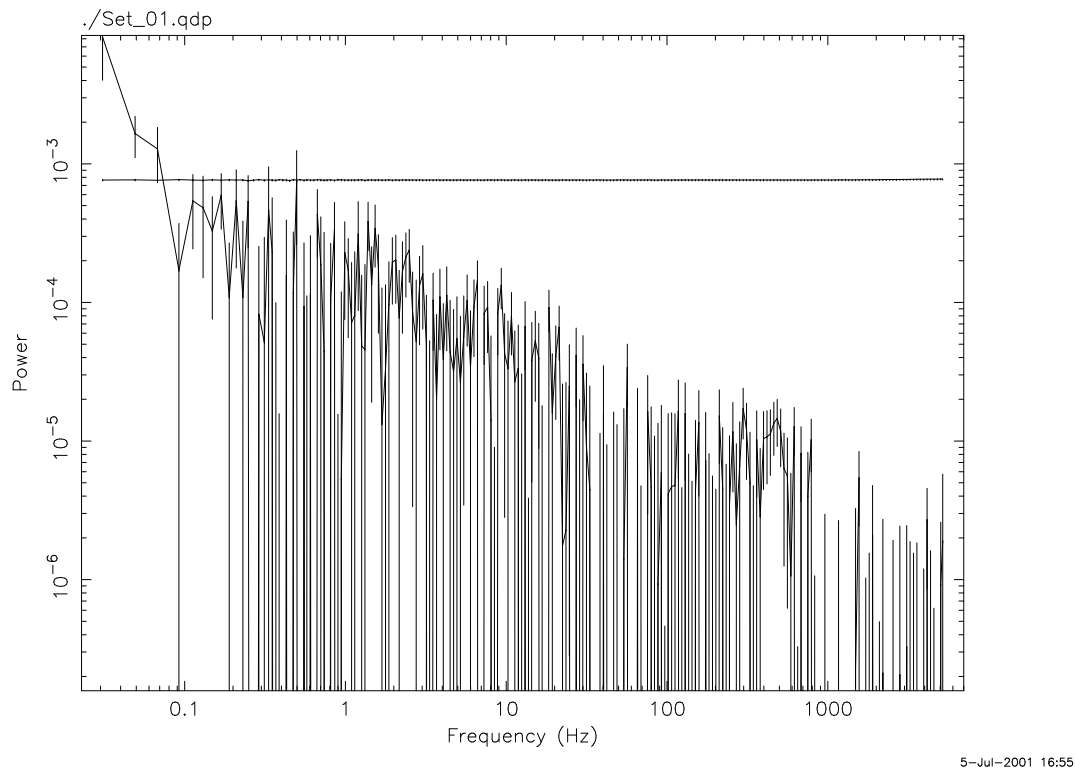


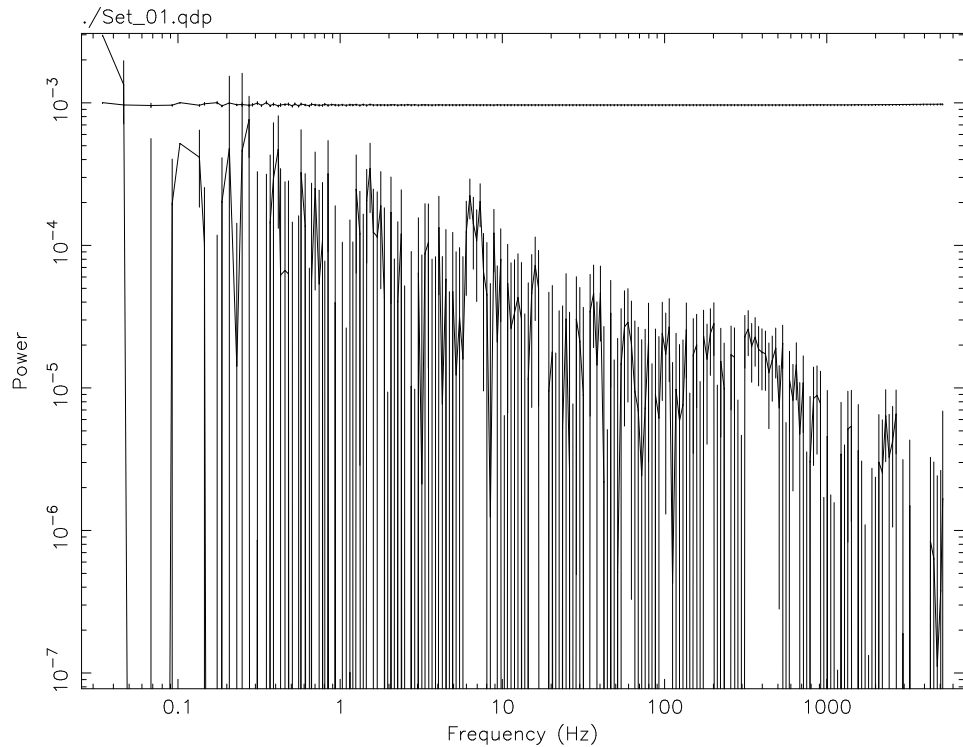
Figure 5.11: Day 125 2000: LFQPO non-detection example. The almost straight line is the USA deadtime correction which has already been subtracted from the PSD.

range and in approximately simultaneous observations of the 2000 outburst. Unfortunately, without a reliable way of subtracting off EDIE, it is not possible to know for sure if there are in fact HFQPOs present in Figure 5.9. An added difficulty is that HFQPOs are notoriously weak in SXTs.

5.5.1 Upper Limit on the RMS of ‘Undetected’ LFQPOs During the XTE J1550–564 Intermediate State

In this section an approximate answer is given to the following question: If LFQPOs are present, during the time in the IS, when USA⁶ is unable to make any LFQPO detection, then how strong might these LFQPOs be? The answer to this question

⁶It is pertinent that RXTE also does not see any LFQPOs during this time.



5-Jul-2001 16:55

Figure 5.12: Day 128 2000: LFQPO non-detection example. The almost straight line is the USA deadtime correction which has already been subtracted from the PSD. This is the strongest non-detection and it will be used to set an upper limit on the strength of the LFQPO during the IS of the outburst, where USA cannot make a true detection.

is not easily given, because the LFQPO appears to either be there or not. This is seen easily by comparing one of the weakest LFQPOs present in the data, shown in Figure 5.14, to the non-detection examples given in Figures 5.9– 5.13. Other detectable LFQPOs are considerably stronger than that shown in Figure 5.14.

The time during the IS, Day 121 to Day 131 2000, in which no LFQPOs were detected will be referred to as IS-non. The only days in which a possible LFQPO might be present are at the beginning and end of IS-non. See Figure 5.11 and Figure 5.12 around 6–8 Hz for a slight hint that an LFQPO might be present. These hints are in the generally expected, based on spectral data and the other LFQPOs, frequency range. In both figures the possible LFQPO peak height is about 2×10^{-4} , however the

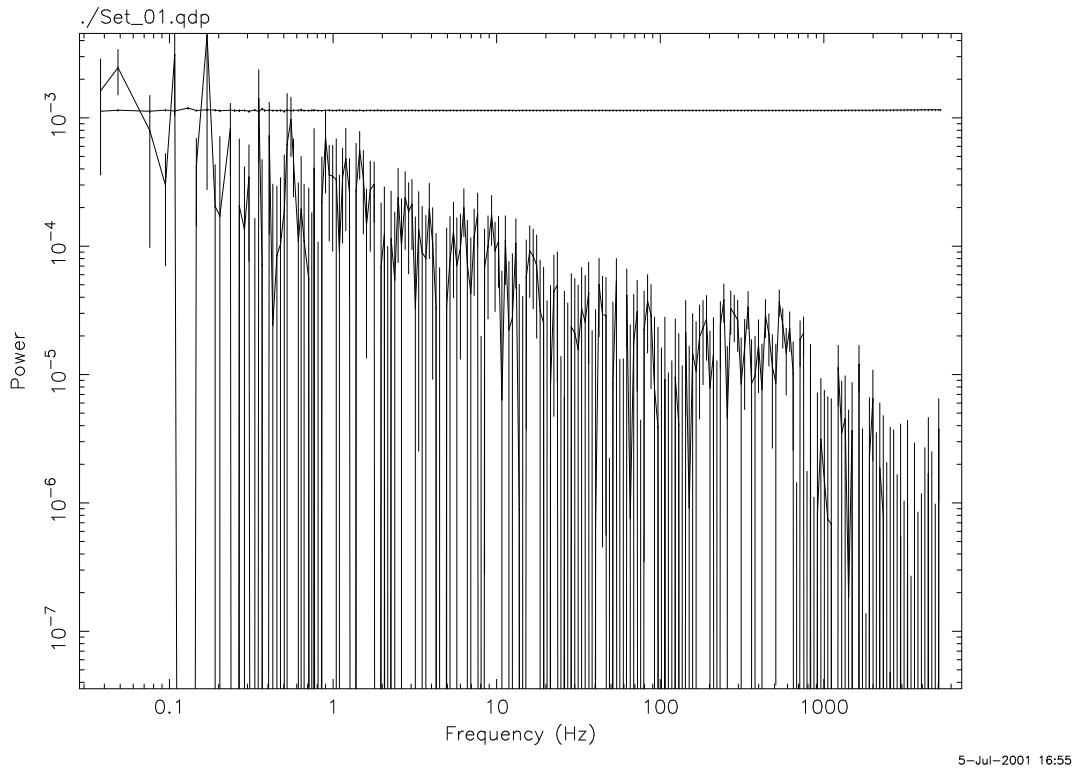
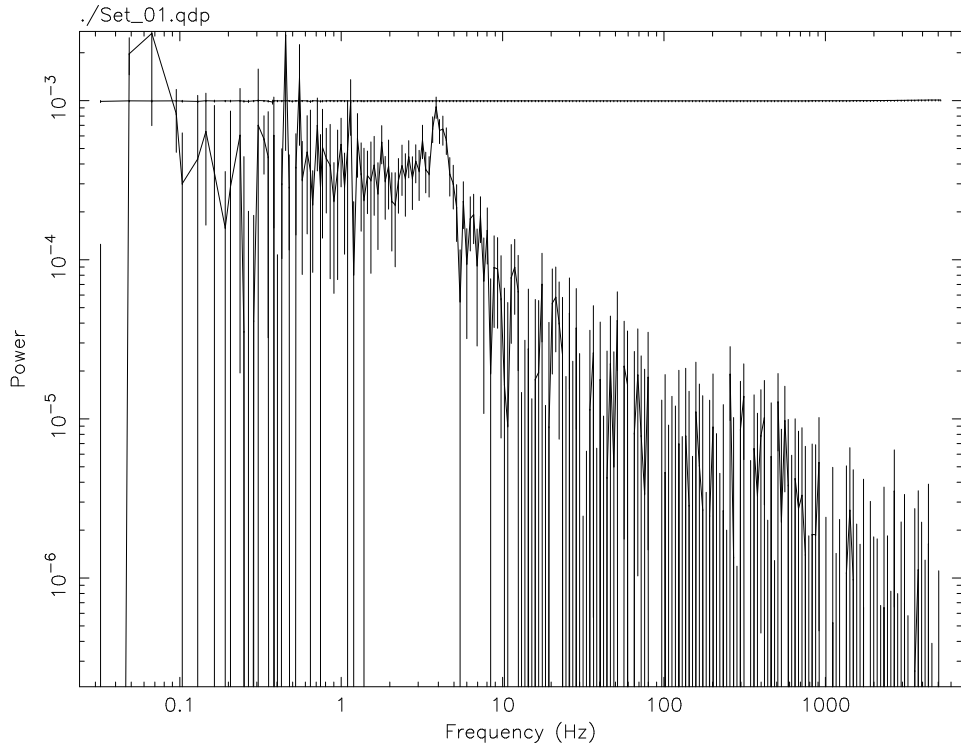


Figure 5.13: Day 130 2000: LFQPO non-detection example. The almost straight line is the USA deadtime correction which has already been subtracted from the PSD.

feature on Day 128 is broader. This will give it a greater area, indicating a larger rms.⁷ The Day 128 USA total range power spectra was used to generate the upper limit. There is no visible sign of any LFQPO in either of the SB or HB alone. It is noted that when the original LFQPO analysis was performed, the fits would not converge for these days. Many fits were attempted but under all conditions the parameters varied to unreasonable values and a fit could not be obtained.

In order to set the upper limit the Day 128 PSD was fit to a power law plus an rms normalized Lorentzian. The power law was allowed to vary first and then all of its parameters were frozen. Then the Lorentzian was fit. It was not possible to allow both features to vary simultaneously as was done with all other LFQPO detections.

⁷Generally, QPOs with higher Q are more significant, but this can be canceled by a small rms, see Equation 5.2.



5-Jul-2001 16:55

Figure 5.14: Day 132 2000: LFQPO detection. This figure is shown for comparison to the non-detection figures. Here there is a very strong, to the eye, LFQPO present, but the LFQPO is only slightly stronger than that shown in the non-detection figures, see text. The almost straight line is the USA deadtime correction which has already been subtracted from the PSD.

When the fit model used both the power law and the Lorentzian and all parameters were allowed to vary, a reasonable fit could not be obtained.

Fits were made to the PSD over the 1–25 Hz frequency range. The fit to a pure power law gave $\Gamma = 0.4245^{+0.24}_{-0.23}$ and a normalization of $A = (1.14^{+1.05}_{-0.64}) \times 10^{-4}$. The χ^2 per DOF for this fit was 0.95 for 64 degrees of freedom. When adding the Lorentzian, it was found to have a frequency of $\nu = 6.82^{+0.41}_{-0.41}$, and full width at half maximum of $w = 1.30^{+0.60}_{-0.62}$ and a fractional rms of $R = 0.017^{+0.003}_{-0.002}$. The χ^2 per DOF of this fit was 0.75 for 63 degrees of freedom. An f-test indicates that the Lorentzian is a necessary model component at the 82% confidence level. This is a weak requirement and it is rather dubious to add model components when the χ^2 per DOF is already less than one. This is considering that it was not possible to allow both components to vary

simultaneously.

This feature has only a slightly smaller rms than the weakest actual LFQPO detection. The difference is that this feature is more than three times as broad as the detectable LFQPO features. Thus, it is concluded that if there are in fact LFQPOs present during the IS-non, they are most likely broad features having an rms $< 1.7\%$. It is possible to calculate the statistical significance of broad features, such as QPOs, seen in PSDs. This significance, in terms of number of standard deviations above the noise floor, is given by

$$n_\sigma = \frac{1}{2} I r^2 \left(\frac{T}{\Delta\nu} \right)^{(1/2)} \quad (5.2)$$

where n_σ is the number of standard deviations, I is the mean intensity of the Fourier transformed source signal (counts per second), r is the fractional rms of the Lorentzian feature, T is the time series segment length, and $\Delta\nu$ is the Lorentzian full width at half maximum (van der Klis 1989b). Using Equation 5.2, the Lorentzian feature discussed above on Day 128 is a 1.2 (77%) sigma LFQPO detection. It is interesting to compare this with the example of a very weak LFQPO detection, Figure 5.14, on Day 132, which is 3.8 (99.99%) sigma above the PSD noise floor.⁸

⁸It may appear that if the Day 132 LFQPO was such a strong detection then the Day 128 LFQPO fit would be better, because the Day 132 LFQPO has only a slightly larger percent rms (≈ 1.8). However, as is clearly shown by Equation 5.2, very small changes in rms will cause the significance of a signal to decrease rapidly. This effect is discussed in van der Klis 1989b and references therein.

Chapter 6

The Acoustic Oscillation Model As a Mechanism for the Low-Frequency Quasi-Periodic Oscillations Observed in XTE J1550–564

6.1 Introduction

Quasi-periodic phenomena have been observed in white dwarf, neutron star and black hole candidate systems at frequencies of order tenths of hertz to kilohertz. In combination with spectral properties these timing properties can be used as probes of the overall accretion geometry of the systems in question. (The purpose is to answer questions such as: How close is the inner edge of the accretion disk, R_{inner} , to the last stable orbit? What are the dimensions of the accretion disk? How are accretion and jet formation related?) There are many puzzles posed by accretion in SXTs and concrete solutions seem to be a long way off, but there is an overwhelming amount of information to sift for clues. In this chapter the goal is to edge closer to understanding the LFQPO production in at least one system, XTE J1550–564.

In the previous chapter, USA observations during the 2000 outburst of XTE J1550–564 were discussed and are shown in Figures 5.1, 5.2, and 5.3 (see also Reilly et al. 2001). In order to motivate the content of this chapter some of the interesting aspects

of those observations are reiterated. Figure 5.1 hints at possibly interesting relationships between the LFQPO and the flux in the two USA energy bands. Specifically, the LFQPO tends to increase in frequency as the 1–16 keV flux increases, additionally there is an apparent relationship between the hardness ratio (HB/SB) and the rms amplitude of the LFQPO.

Another important result is that the HB and SB outburst profiles, shown in Figure 5.1, differ. The effect of this is readily apparent in Figure 5.2 where a cyclic¹ structure is seen. This type of structure in the HID is common in SXT's and is generally thought to be indicative of two accretion flows (See Smith et al. 2002 and van der Klis 2001 for possible explanations of two-flow accretion streams and their relation to structure in the HID). Two accretion flows are proposed because of the implied presence of two different timescales, one which governs the SB and another which governs the HB. Models explaining this HID structure often associate the SB with an α -like disk and use the viscous timescale within the disk to explain why its response to perturbations of the system (e.g. a change in the overall accretion rate, \dot{M}) takes weeks to months. Association of the HB with an inner Comptonizing medium is used to explain why perturbations are more rapidly apparent in the HB. This is because perturbations in the Comptonizing medium, often referred to as a corona or transition layer (TL), can propagate on timescales similar to free fall.

In this chapter a mechanism for the LFQPO is proposed. This mechanism is based on observational evidence for a strong dependence of the LFQPO on high energy flux. This dependence is seen in the 20–100 keV BATSE flux and the USA hardness ratio. The anti-correlation to the USA total range is also important, because it demonstrates that an increasing flux from the accretion disk diminishes the LFQPO mechanism. In the following sections, convincing evidence that the LFQPO is dependent upon the presence of a hot TL is given. The model proposed assumes that the LFQPO is generated in the hot TL.

The model explains the experimentally observed dependencies of the LFQPO on BATSE, HB and SB intensities by proposing that the LFQPO is generated by acoustic oscillations of the TL, thus the model will be referred to as the acoustic oscillation model (AOM). The AOM allows an approximate measure of the radius of the accretion disk inner edge, R_{inner} , throughout the XTE J1550–564 outburst. In fact the AOM allows a measure of the transition layer radius, R_{TL} . As a first order approximation,

¹Some authors describe this as spectral hysteresis, see Maccarone and Coppi 2002 for example.

Term	Energy Range	Instruments
soft flux	$\lesssim 20$ keV	USA (SB+HB), ASM, RXTE PCA
low energy flux	$\lesssim 20$ keV	USA (SB+HB), ASM, RXTE PCA
black body	$\lesssim 20$ keV	USA (SB+HB), ASM, RXTE PCA
hard flux	$\gtrsim 20$ keV	BATSE, HEXTE
high energy flux	$\gtrsim 20$ keV	BATSE, HEXTE

Table 6.1: Energy Band Term Definitions. The 20 keV value is chosen as an approximate dividing line between the bands.

R_{TL} and R_{inner} are set equal.² With this assumption the the AOM measurements of the outer radius of the TL, R_{TL} , are compared to the spectrally determined inner edge radius, R_{inner} . Finally, using the acoustically determined values of R_{TL} , an attempt to constrain HFQPO models is made. The results of this “test” of the HFQPO models are dubious at best, but interesting to think about. In the next section, some observational results are given which support the AOM.

6.2 Observational Evidence for the LFQPO Dependence on the Transition Layer

Observational evidence for the dependence of the LFQPO on the TL is the primary focus of this section. Here the existence of a TL is assumed. The dependence is established by looking at the energy dependence and, to a lesser extent, the phase lags of the LFQPO. Emphasis is placed on the LFQPO energy dependence because an energy dependence seems to be the easiest way to establish a connection to the TL. (Other correlations may be ignored for the time being.) This is because the most likely place for the production X-rays of more than a few keV is in the TL. The energy dependence will be established using the USA data presented in Chapter 5, the BATSE 20–100 keV flux, RXTE PCA and ASM data, see Figures 6.1, 6.2, 6.3, 6.4. The discussion presented in this chapter is based on results from both the 1998–1999 and 2000 outbursts of XTE J1550–564. Because several different energy ranges from several different instruments are discussed in the chapter, for its remainder the

²Assuming that the accretion disk inner edge and the outer boundary of the transition layer are coincident is an oversimplification. Most likely R_{TL} is larger than the radius of the inner edge of the accretion disk. However, there has been spectral work done which indicates that in many galactic black hole binaries the ratio of the radius of the accretion disk inner edge and R_{TL} is 0.8–0.9 (Poutanen 1998).

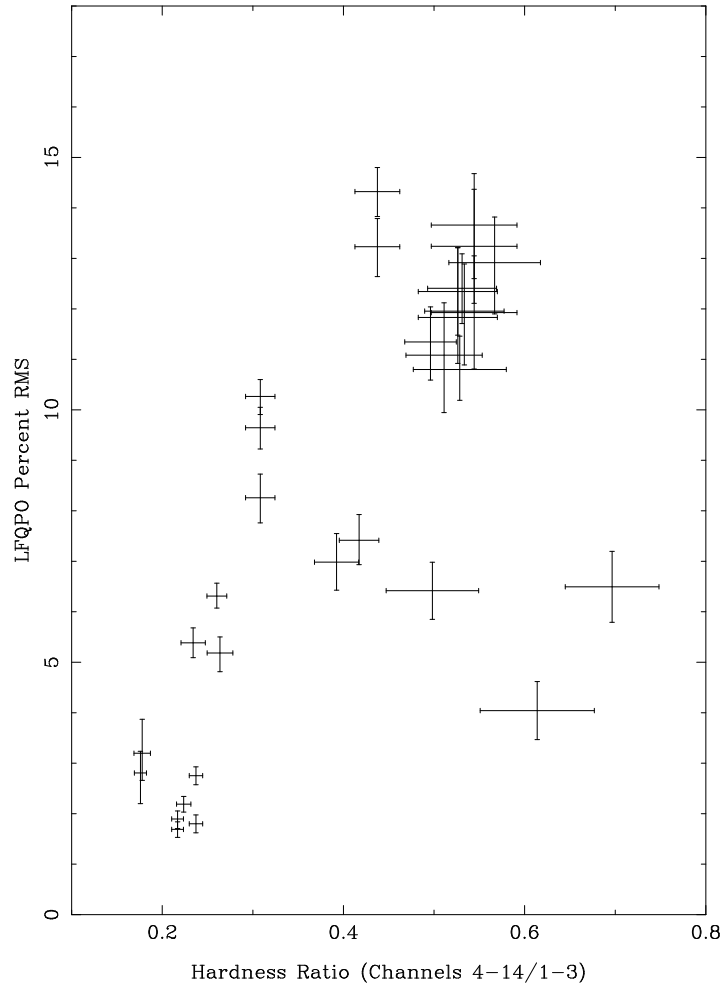


Figure 6.1: Plot of the LFQPO percent rms as a function of the USA hardness ratio. The data used in this plot are taken from the corresponding panels of Figure 5.1. The hardness ratio is HB/SB. The three outlying points at the lower right corner of the plot are discussed in the text.

definitions given in Table 6.1 will be used to avoid confusion. When it is necessary to refer to the two USA bands this will be done explicitly by using HB and SB.

The first indication, that the TL played a significant role in the production of the LFQPO, was given by the dependence of the LFQPO percent rms amplitude on the USA hardness ratio (HB/SB), see Figure 6.1. Aside from three points, the strength of the LFQPO is strongly correlated to the hardness ratio. The three outliers in Figure 6.1 might be explained in several ways. At the time those observations were made the source was known to be moving into quiescence. The transition into quiescence may considerably diminish the LFQPO mechanism. Also, the mass accretion

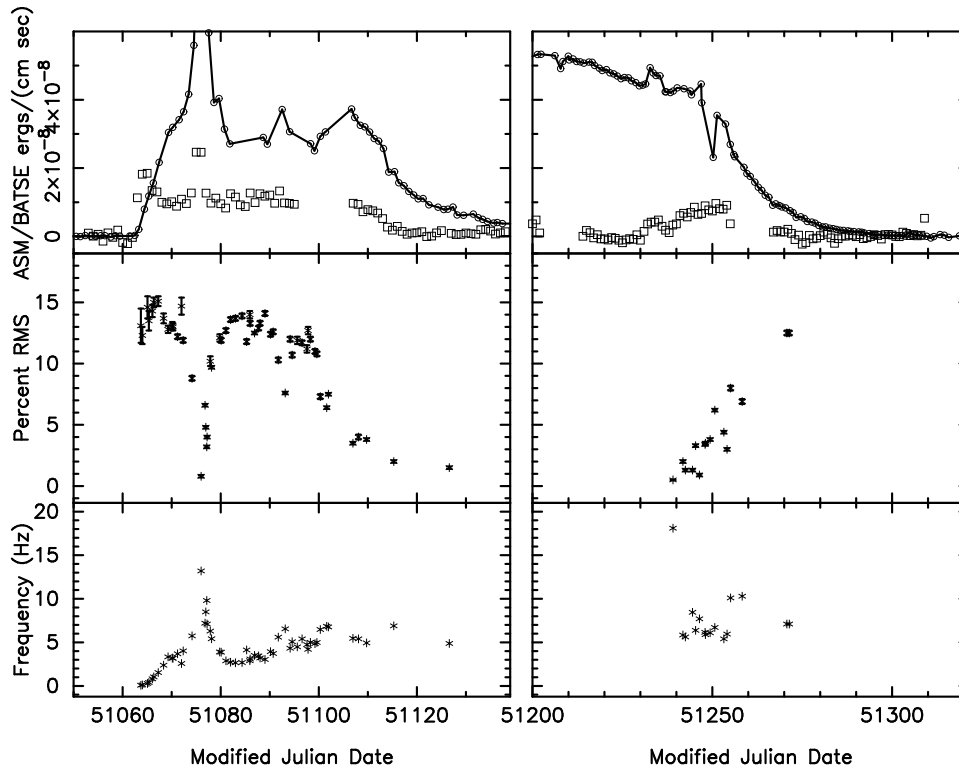


Figure 6.2: The ASM and BATSE fluxes, LFQPO percent rms and LFQPO frequency are plotted as a function of time during the 1998–1999 outburst. Top panel: The BATSE Flux, (20–100 keV) in $\text{ergs}/(\text{cm}^2\text{-sec})$, shown as boxes, and the ASM, 1.5–12 keV flux in $\text{ergs}/(\text{cm}^2\text{-sec})$, shown as a line with circles, plotted as a function of time. Center panel: The percent rms amplitude of LFQPO is plotted as a function of time. Bottom panel: LFQPO frequency is plotted as a function of time. The plot is split in order to emphasize the regions where the LFQPO is present. BATSE data is converted from count rate to flux as described on the BATSE web page. Errors on ASM and BATSE fluxes are on order of the symbol size. LFQPO rms and frequency errors are shown. If these errors are not visible it is because they are smaller than the symbol size. This figure indicates the LFQPO dependence on the BATSE flux.

in system was slowing considerably. This could limit ‘noise’ in the system which may be driving the LFQPO mechanism. A lower mass accretion rate certainly means less X-ray luminosity which may emphasize unknown systematics in detecting weak LFQPO signals. If, as is suggested in this chapter, the LFQPO is generated in a resonant cavity partially defined by the accretion disk edge at R_{TL} , then it is possible that a lower accretion rate implies a less well defined cavity. Another possibility is that the hardness ratio is simply not the ideal quantity to correlate with the LFQPO amplitude. The correlation is strong for the most part, so it is taken to indicate that

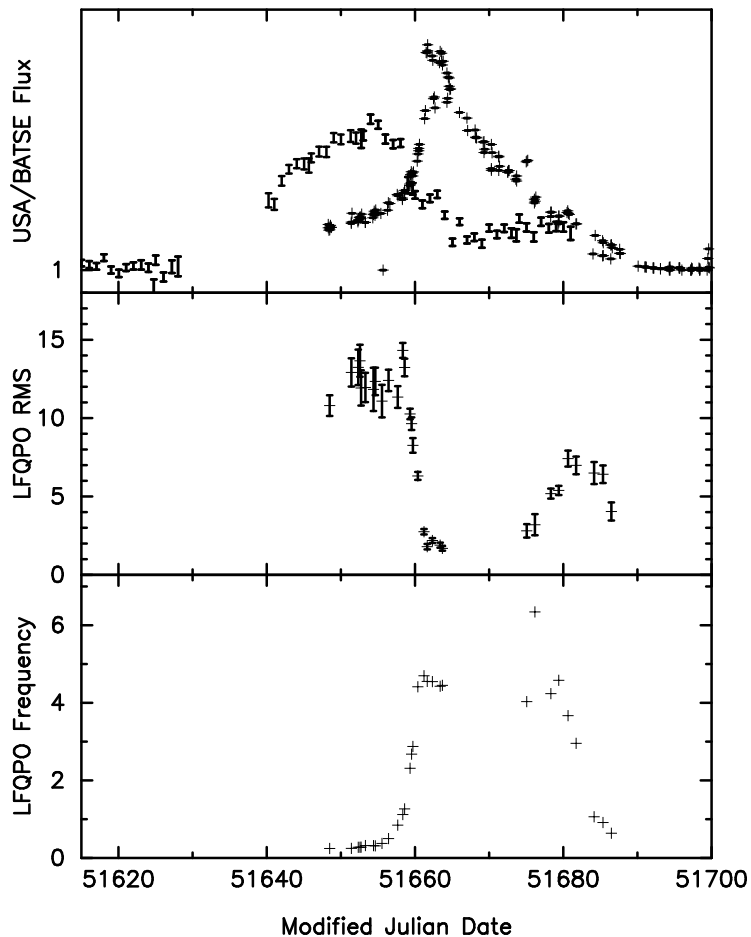


Figure 6.3: The USA and BATSE fluxes, LFQPO percent rms and LFQPO frequency are plotted as a function of time during the 2000 outburst. Top panel: The BATSE Flux, (20–100 keV) in $\text{ergs}/(\text{cm}^2\text{-sec})\times 10^8$, is represented by error bars only and the USA, 1–16 keV flux in $\text{ergs}/(\text{cm}^2\text{-sec})\times 10^8$, is shown as plus signs. Center panel: The percent RMS amplitude of the LFQPO is plotted as a function of time. Bottom panel: The LFQPO frequency is plotted as a function of time. BATSE data is converted from count rate to flux as described on the BATSE web page. USA count rates are converted to flux assuming a crab like spectrum. Error bars for USA data are dominated by systematics, because this assumption. Error bars on USA data are on order of a few percent. LFQPO rms errors are shown and centroid frequency errors are smaller than the symbol size. Error bars for BATSE are as shown. This figure indicates the LFQPO dependence on the BATSE flux.

a harder spectrum results, in general, in a stronger LFQPO.³ As a cautionary note:

³Other extensive spectral work using RXTE data has shown no *pure* correlations for any of the XTE J1550–564 LFQPO properties (Sobczak et al. 2000b; Rodriguez et al. 2002). There is always a roll-over or some other deviation away from what would be considered a true correlation.

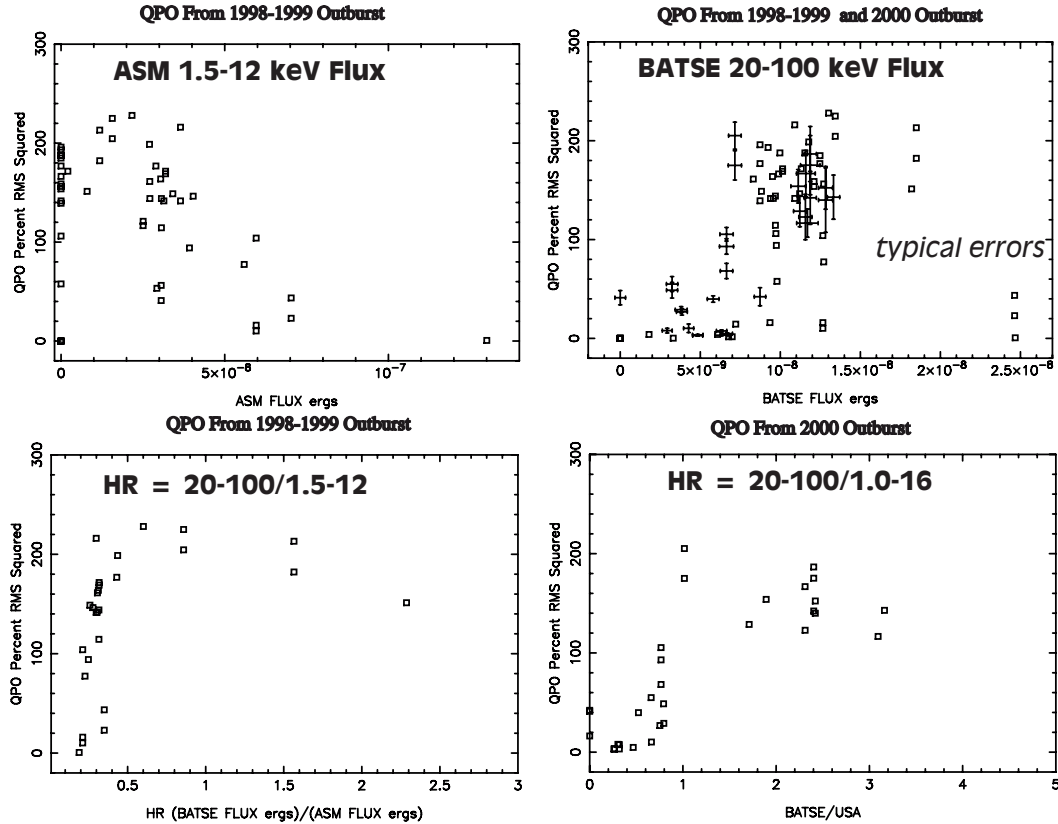


Figure 6.4: The LFQPO rms squared is plotted as a function of the ASM flux, the BATSE flux, the BATSE/ASM hardness ratio and the BATSE/USA hardness ratio. Top Left: The LFQPO percent rms amplitude squared from the 1998–1999 outburst is plotted as a function of ASM 1.5–12 keV flux in ergs/(cm²–sec). Top Right: The LFQPO percent rms amplitude squared from the 1998–1999 and 2000 outbursts is plotted as a function of BATSE 20–100 keV flux in ergs/(cm²–sec). Bottom Left: The LFQPO percent rms squared from 1998–1999 outburst is plotted as a function of the hardness ratio: (BATSE 20–100 keV ergs/(cm²–sec)/ASM 1.5–12 keV ergs/(cm²–sec)). Bottom Right: The LFQPO percent rms squared from 2000 outburst is plotted as a function of the hardness ratio: (BATSE 20–100 keV ergs/(cm²–sec)/USA 1–16 keV ergs/(cm²–sec)). Representative error bars are shown in the top right plot. Error bars are calculated as described in Figures 6.3 and 6.2. These plots demonstrate the LFQPO relation to spectral hardness. This figure is further evidence that the LFQPO strength has a correlation with a weaker disk emission and a stronger Compton component (i.e. TL).

Other instances of less than perfect correlations will arise in the following discussion. For now, it is not possible to speculate about all possible causes of such deviance. The point of this work is to establish a general trend. This trend is that the LFQPO is strong when the high energy flux is strong. A very simple model of the accretion

processes has been assumed and any deviation from it should be taken as tribute to the complexity of these systems and nature itself.⁴

A second potential sign of the TL's importance is the inferred relation of the LFQPO percent rms to its frequency. Specifically, as the frequency of the LFQPO increased, its strength decreased. This effect is readily seen during the rise to outburst in Figures 6.2 and 6.3. After MJD 51100 in Figure 6.2 the LFQPO rms declines while the frequency remains constant. This decline slightly precedes the decline in BATSE flux. It is interesting that the LFQPO frequency remains constant as does the ASM flux during this period. The LFQPO becomes undetectable around MJD 511300 as does the BATSE flux until about MJD 51240, when the LFQPO rms and BATSE flux increase. At this point the correlation between the LFQPO frequency and the soft band flux, as seen in the rise of the outburst, is not apparent. A very similar situation is seen in the 2000 outburst, Figure 6.3. During the rise to outburst, up to about MJD 51665, the rms and frequency show as strong correlation until the LFQPO becomes undetectable. Around MJD 51675 the BATSE flux slightly strengthens and the LFQPO returns, but the rms and frequency are no longer tightly correlated. It still may be possible to use the rms and frequency correlation which occurs during the rise of both outbursts in support of the LFQPO dependence on the TL.

Assuming an outburst mechanism like that described by the disk-instability model (DIM)⁵, it may be possible to understand the correlation during the rise to outburst and the lack of correlation during the decline in terms of the mass accretion rate and evolution of the accretion disk inner edge. If at the beginning of the outburst the disk is truncated at $> 100 R_{\text{Sch}}$, and, as the outburst evolves \dot{M} increases and R_{inner} moves toward the compact object throughout the rise to maximum, then this explains the decrease in LFQPO rms with the increase in frequency. The observation of increasing soft flux⁶ is a result of increasing black body flux from the growing accretion disk (i.e. R_{inner} is shrinking). As R_{inner} moves inward, R_{TL} must decrease and consequently cause an increase in LFQPO frequency, because of the decreasing size of the TL. As the TL decreases the LFQPO rms, assuming dependence on the TL,

⁴Maybe there is a rock in the stream.

⁵Note that others have interpreted outburst phenomena under similar conditions, see for example Fender 2001.

⁶Soft flux is basically thought to be due to a black body, the accretion disk, at a temperature less than a few keV. Here soft flux corresponds to SB and HB (i.e. the USA total range). However they are separate in relevance to the LFQPO, as is demonstrated by the USA hardness ratio. But, because the high energy flux, as defined in Table 6.1, has such a different role than the HB, they must be treated separately.

may be diminished in two ways. First, low energy photons from the disk will Compton cool the TL.⁷ Second, as the TL becomes smaller, acoustic oscillations within it will modulate a smaller flux. Thus, during the rise to outburst an explanation for the frequency rms correlation is readily available. During the decline of the outburst \dot{M} decreases significantly, possibly hindering the LFQPO mechanism and obscuring the correlation seen during the outburst rise. Specifically, as Compton cooling from the disk weakens, the TL is allowed to reestablish itself and is once again subject to modulations. However, the material in the TL should be significantly depleted compared to the time of the outburst onset. This will result in a smaller modulated flux from the TL. As the system returns to quiescence, the disk is expected to become unstable. This could result in a less well defined outer boundary of the TL.

Solid evidence for a dependence of the LFQPO on the TL comes from observations of both the 1998–1999 and 2000 outbursts. Figures 6.2 and 6.3 show that the LFQPO is only present while there is a detectable 20–100 keV BATSE flux. Generally the LFQPO rms increases with increasing BATSE flux. There may be in fact a cause and effect relationship, specifically, the absence of BATSE flux could explain the absence of the LFQPO. Because the likely cause of the 20–100 keV X-rays is the TL, these observations seem to soundly establish the dependence of the LFQPO on the TL. Plots of LFQPO percent rms squared as a function of the the ASM flux, BATSE/ASM hardness ratio, BATSE flux and the BATSE/USA hardness ratio, Figure 6.4, were made to confirm the LFQPO dependence on the flux in various energy bands. From Figure 6.4 it is clear that a strong dependence of the LFQPO on high energy flux exists for both outbursts. These results confirm the correlations previously observed by (Sobczak et al. 2000b) for the 1998–1999 outburst and establish a nearly identical pattern for the 2000 outburst.

From USA data collected during the 2000 outburst there is evidence that both the disk and TL photons are equally modulated. This is concluded from Figure 5.1, where the LFQPO rms amplitude is plotted in each of the three USA energy bands, total range, HB and SB. From the plot it is clear that the percent rms amplitudes are comparable in all three USA energy bands. Physically, this could indicate that as the TL resonates it also causes oscillations in the accretion disk.⁸

⁷This point may further be supported if a strong connection can be established between jet production and the TL. This is because (Corbel et al. 2001) found that the increased disk flux in the 2000 outburst of XTE J1550–564 seems to have had a role in quenching the jet. Perhaps a quenching (or cooling) of the TL is the cause of the quenching of the jet.

⁸The converse could also be true and may help with some of the more complicated phase lag

The lack of a significant difference of the LFQPO rms between the USA HB and SB is does not effect weaken the argument that the LFQPO is dependent on the TL. From RXTE observations and BATSE observations it is clear that the production of the LFQPO *is* contingent upon the existence of the TL or some other Comptonizing medium. It is known that for both outbursts the LFQPOs are only marginally detectable when the high energy flux is diminished, see Figure 6.4. The LFQPO is only observable while there is a significant BATSE flux. Sobczak et al. 2000b state this effect quantitatively, for the 1998–1999 outburst, where they find that the LFQPO is present only when a power law component contributes more than 20% of the 2–20 keV flux, see Section 6.3 for more details.

Finally, Remillard et al. 2002 report soft band phase lags in most observations of the primary LFQPO frequency. The harmonic phase lags often flip sign and the primary sometimes shows hard lags, but soft lags are most common. An interpretation of the soft phase lags is made by assuming that the LFQPO originates in the hard photons (i.e. the TL) and that some of those photons irradiate the disk, are down scattered and then observed at a slightly later time (corresponding time lags are of order milliseconds). See Figure 6.5 for the geometry of these phase lags.

6.3 RXTE Spectral Results from the 1998–1999 Outburst and the 2000 Outburst

RXTE spectral results from both the 1998–1999 outburst and 2000 outburst are supportive of the conclusions drawn in the previous section. Some of the keys points found by Sobczak et al. 2000b, Rodriguez et al. 2002 and Rodriguez et al. 2002 will be discussed. Based on their results, these authors have come to interpret the LFQPO dependence in a nearly identical manner to the interpretation presented in this work. However, Rodriguez et al. 2002 propose that the accretion ejection instability (AEI) model (Tagger and Pellat 1999) is responsible for the LFQPO production.⁹ Despite different LFQPO model proposals, the RXTE spectral results, presented by the aforementioned authors, provide important confirmation of ideas in this chapter.

As mentioned earlier, Sobczak et al. 2000b found that the LFQPO was only

behavior seen in XTE J1550–564 (Remillard et al. 2002).

⁹It would be interesting to develop a test which might distinguish between the AOM and the AEI.

present when the significance of the power law was above a certain level. This alone indicates that the LFQPO has a dependence on the TL. It is interesting that this result also holds for LFQPOs seen in GRO J1655–40, indicating the possibility of the same LFQPO mechanism in both sources. For both sources, Sobczak et al. 2000b find that the LFQPO frequency increases with increasing disk (black body) flux.

Rodriguez et al. 2002 state that their spectral results suggest “a strong coupling between the Compton medium and the modulation.” They find that the LFQPO frequency increases with decreases in the spectrally determined R_{inner} and decreases as R_{inner} increases. This agrees with the predicted behavior of the AOM. Even subtle changes seem to agree with the AOM. For example, during the 2000 outburst IS, the spectrally determined disk radius is found to hit a minimum just after MJD 51660 and to then slightly increase until about MJD 51665. Under the AOM this proves to be an extremely important observation. Looking closely at Figure 6.3, it can be seen that the LFQPO frequency follows this disk behavior exactly as would be suggested by the AOM. Specifically, the LFQPO frequency hits its maximum value just after MJD 51660 (the time of the inner disk edge minimum) and then has a trend of slightly decreasing frequencies, just prior to becoming undetectable by USA and RXTE. Interestingly, this is just as the spectrally determined disk inner edge stabilizes at a constant radius.

Although other possible LFQPO models have similar spectral dependencies and otherwise physical dependencies, the sum of results presented here and elsewhere lead to the same conclusions. Specifically, there is mounting evidence that the LFQPO seen in XTE J1550–564 and possibly other sources is generated in a TL and the frequency of the LFQPO is set by the radius of the accretion disk’s inner edge, R_{inner} , which helps to define the TL size, R_{TL} . So far the spectral work done here and elsewhere only serves to strengthen the case for the AOM as a possible mechanism for LFQPO production.

6.4 Theoretical and Observational Evidence for the Existence of a Transition Layer

The existence of a TL has strong observational and theoretical support and is now widely accepted as a part of the accretion physics in LMXBs. Some theoretical support is provided by the disk instability model (DIM) of SXT outbursts. Using the

DIM, it has been shown in numerical simulations that there must exist a truncated accretion disk which surrounds a TL or Corona in some form (Lasota 2001). If this geometry is not assumed, then the numerical simulations do not give the observed SXT outburst characteristics. Observational evidence of AGN and quiescent galactic black holes systems indicates a highly truncated accretion disk as is needed by the DIM, see for example Di Matteo et al. 2001.

There have been many proposed mechanisms for the formation of the TL inside of R_{inner} of the truncated accretion disk. One suggestion is that the TL is bounded and fueled by a shock at R_{TL} . The shock would give way to an inner post-shock region as defined in Chakrabarti and Titarchuk 1995. This post-shock region is what has so far been referred to as the TL. Other authors have questioned how such a shock might be formed in this region. It is in fact a subject of great controversy. Fortunately, the shock proposed by Chakrabarti and Titarchuk 1995 is only one mechanism by which a TL might be formed. Other models suggest that the accretion disk evaporates and, thus, fuels the TL. Models invoking this mechanism are more readily adapted to the DIM for outbursts and the ADAF-like models for accretion near the compact object. These models have a benefit which is compatible with the AOM. This benefit is that super-sonic flows are not necessary. Sub-sonic accretion flows are easily obtained from the various CDAF and ADIOS models. Numerical simulations of these accretion models contain sub-sonic accretion for a wide variety of parameters and show that stagnation points may be present (Igumenshchev and Narayan 2002; Abramowicz et al. 2002; Igumenshchev and Abramowicz 2000; Igumenshchev et al. 2000; Igumenshchev and Abramowicz 1999). These simulations indicate that there are natural boundary conditions, near the event horizon of black holes, which prevent the free-fall of accreting matter. The end result is a TL having inner and outer boundaries which create a cavity with the potential to resonate.

6.5 Acoustic Oscillation Model

The purpose of this section is to describe the AOM, review its assumptions and find the quantitative relationship between the LFQPO frequency and the R_{TL} . The AOM is based on acoustic oscillations of the hot accretion flow which is bound between the inner edge of the accretion disk and the compact object. This region is referred to as the TL. There are several assumptions made about the properties of the TL. The

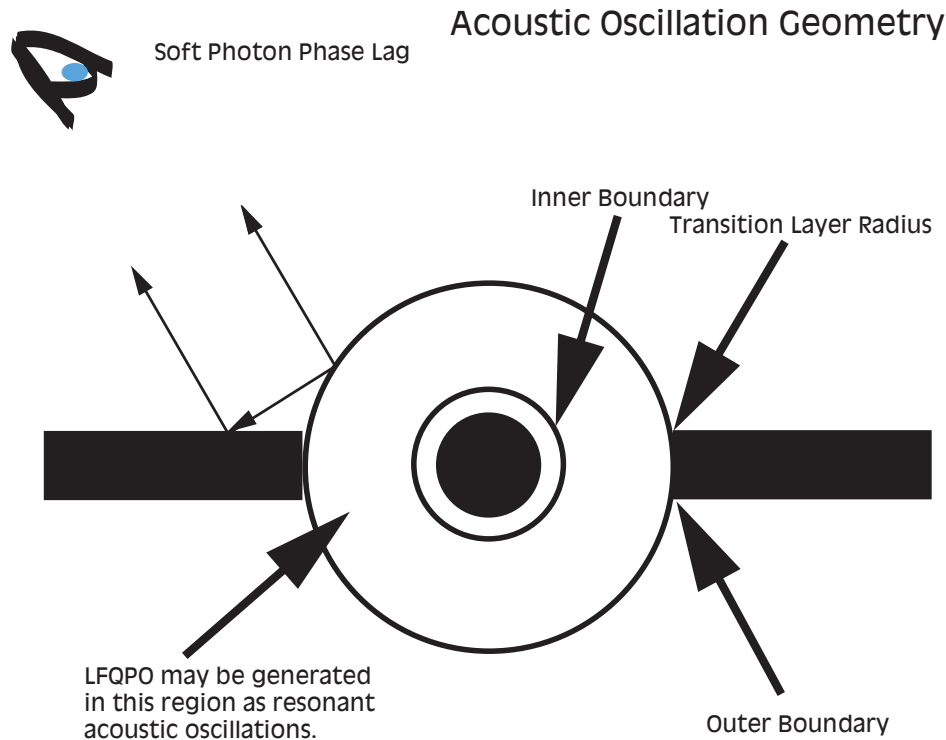


Figure 6.5: Diagram of the general accretion geometry assumed for the acoustic oscillation model. This figure shows a simplified view of the AOM accretion geometry. This geometry may be referred to as the sombrero geometry. Note how phase lags might occur in the AOM. The observer (top left) will see down scattered LFQPO photons from the disk just after those which take the direct path.

TL is isothermal throughout the outburst and its bulk motion is sub-sonic.¹⁰ We further assume that magnetic fields in the TL are negligible. Because the model is based on acoustic oscillations it is imperative that the accretion velocity in the TL be sub-sonic. This condition is satisfied under CDAF models and at radii larger than the sonic point in ADAF models (Igumenshchev and Narayan 2002; Igumenshchev and Abramowicz 1999; Chen et al. 1997). Sub-sonic accretion near the compact object is also possible in ADIOS models (Blandford and Begelman 1999).

Titarchuk et al. 2001 have shown that magneto-acoustic oscillations are readily generated as resonances (eigenfrequencies) of the TL. The authors do not discuss a specific mechanism for exciting the eigenfrequencies. However, a possible mechanism

¹⁰The assumption that the TL maintains constant temperature throughout the outburst is clearly objectionable. However, for practical purposes, it does simplify matters significantly. A more thorough test (than given in this chapter) of the AOM would involve using spectral fits to measure the temperature in the TL during all stages of the outbursts.

could be based on a noisy accretion flow at the inner disk edge, see Wood et al. 1992 and Wolff et al. 1991 and Osherovich and Titarchuk 1999 for examples of noise driven oscillations. Further, the means, by which the acoustic oscillations modulate the X-ray flux in the TL, are not clearly stated. It is proposed that the cavity will resonate acoustically and that these sound waves will cause a slight periodic change in the size of the cavity, causing the radius of the TL, R_{TL} , and possibly the radius of the accretion disk inner edge¹¹ to vary. This slight change in size could then result in modulation of photons from the TL. It is also possible that periodic compression and expansion of the gas in the TL, resulting in heating, cooling and density fluctuations, is the cause of modulation in the TL intensity.

For one possible geometrical description of the accretion processes involved in the AOM see Figure 6.5. A spherical or quasi-spherical region surrounding the compact object, having an inner boundary near the compact object and an outer boundary at the inner edge of the accretion disk, is shown. This region is the TL. The TL is defined by an outer boundary condition, C_{out} , located at $r_{\text{out}} = R_{\text{TL}}$, the position of the accretion disk inner edge, and an inner boundary condition, C_{in} , located at r_{in} , which is somewhat arbitrarily defined to be the photon bending radius of a Schwarzschild black hole (i.e. $r_{\text{in}} = 1.5 R_{\text{Sch}}$).¹² The value of r_{in} may need adjustment in the future.

Titarchuk et al. 2001 derive the magneto-acoustic oscillation eigenfrequencies for both stiff and free boundary conditions. The eigenfrequencies are found by solving the wave equation in cylindrical coordinates. Using the results of Titarchuk et al. 2001 the dependence of R_{TL} on the LFQPO frequency is determined. This result is now presented and derived in Section 6.7.¹³ Generally, the sound speed and the size of the TL may be used to determine the relationship between the LFQPO frequency, ν_{LFQPO} , and the size of the transition layer, R_{TL} . In Section 6.7 it is shown how the magneto-acoustic oscillation formula, derived by Titarchuk et al. 2001, is used to give

¹¹Again for simplicity, we assume that the inner edge of the accretion disk and R_{TL} are nearly the same, see footnote 2.

¹²If we were considering a source with a surface then r_{in} would be located at the radius of that surface.

¹³When originally considering the idea of acoustic oscillations as a mechanism for the LFQPO production, a formula giving $R_{\text{TL}}(\nu_{\text{LFQPO}})$ was derived by scaling. The size of the TL divided by the speed of sound gave the sound propagation time. Because XTE J1550–564 is a microquasar (and for other reasons) there are most likely magnetic fields present in the TL. Magnetic fields could have a 10–20 % effect on the TL size estimations. We wanted to make use of the already derived formulas for magneto-acoustic oscillations in Titarchuk et al. 2001. This was done for completeness and possible future work.

the relationship:

$$R_{\text{TL}} = 10^{-3} \left(\frac{kT_e}{1\text{keV}} \right)^{1/2} \frac{c}{2\pi\nu_{\text{LFQPO}}} + r_{\text{in}}. \quad (6.1)$$

where the sound speed is approximated as $s \approx 10^{-3} \left(\frac{kT_e}{1\text{keV}} \right)^{1/2} c$, with c being the speed of light (Frank et al. 2002), and kT_e is the temperature of the TL.

6.6 AOM Suggests Kerr Black Hole

From Equation 6.1 it is possible to estimate the size of the boundary region which produced the LFQPO in XTE J1550–564 and to calculate R_{TL} . Therefore it is possible to track the evolution of the accretion disk during the outbursts. The most recent mass estimate for XTE J1550–564 is $M \sim 10.56_{-0.88}^{+1.02} M_{\odot}$ (Orosz et al. 2002; Orosz et al. 2001). For simplicity we take $M \sim 10M_{\odot}$, which gives a Schwarzschild radius, R_{Sch} of ~ 30.0 km. Based on spectral data, from both XTE J1550–564 outbursts, showing a typical power law cut off of 30 keV, the TL is assumed to have a temperature of $kT_e \sim 70$ keV (Rodriguez et al. 2002; Sobczak et al. 2000a). Equation 6.1 indicates, based on LFQPO observations during the 2000 outburst, that R_{TL} evolves from $68 R_{\text{Sch}}$ to $3.7 R_{\text{Sch}}$, corresponding to the observed LFQPO frequencies between 0.2 Hz and 6 Hz, respectively. For the 1998–1999 outburst rise to maximum, it is determined that R_{TL} evolves from $166 R_{\text{Sch}}$ to $2.5 R_{\text{Sch}}$, corresponding to the observed LFQPO frequencies between 0.081 Hz and 13.2 Hz, respectively. Note that during the 1998–1999 outburst the highest frequency LFQPO was detected at 18.1 Hz, which indicates $R_{\text{TL}} \sim 2.2R_{\text{Sch}}$. Keplerian orbits with such small radii are only possible in Kerr black holes. For example, a black hole with specific angular momentum¹⁴ $a = J/M = 0.7$ (i.e. $a = 0.7 M$), where natural units ($c = G = 1$) are used, has:

$$R_H = 0.86 R_{\text{Sch}} \quad (6.2)$$

$$R_{\text{LSCO}} = 1.7 R_{\text{Sch}} \quad (6.3)$$

$$R_p = 1.0 R_{\text{Sch}} \quad (6.4)$$

where R_H , R_{LSCO} and R_p are the radius of the horizon, last stable circular orbit and photon bending, respectively. Thus, the radii suggested by the AOM may indicate a Kerr black hole (i.e. a black hole which is spinning). The radial evolution, as

¹⁴The value of 0.7 is based on work by Remillard et al. 2002.

determined by the AOM, is studied more closely in Section 6.8.

6.7 Derivation of the Transition Layer Radius as a Function of LFQPO Frequency in the Acoustic Oscillation Model

Magneto-acoustic resonances have been shown to readily occur in the TL (Titarchuk et al. 2001; Titarchuk and Wood 2002). The frequencies of these resonant magneto-acoustic oscillations were found to be

$$\nu_{MA} \approx [(\beta_s/\pi)^2 \nu_s^2 + (\beta_M/\pi)^2 \nu_M^2]^{1/2}, \quad (6.5)$$

where β_s and β_M are constants determined by the boundary conditions. For the case of pure acoustic oscillations $\beta_M = 0$ and, assuming Neumann boundary conditions, β_s is found to have a range of values:

$$0.6 \lesssim \beta_s \lesssim 1.22. \quad (6.6)$$

For simplicity β_s is approximated as one, $\beta = \beta_s = 1$. The acoustic and magnetic frequencies, ν_s and ν_M are given by

$$\nu_\alpha = [(\alpha + 2)/4]A^{1/2}/(r_{out}^{(\alpha+2)/2} - r_{in}^{(\alpha+2)/2}), \quad (6.7)$$

where $\alpha = 0$ gives the acoustic frequency, $\nu_0 = \nu_s$, and $\alpha = 6$ gives the magnetic dipole frequency, $\nu_6 = \nu_M$. The values and physical significance of these constants are derived from the specific boundary conditions used, see Titarchuk et al. 2001 for the detailed derivation. The constant A is proportional to the square of the acoustic velocity or Alfvén velocity for the acoustic or magnetic case, respectively. The variables r_{out} and r_{in} represent the radii at the outer and inner boundaries, respectively, of the TL. For the case of pure acoustic oscillations in the TL,

$$\nu_s = s/2(r_{out} - r_{in}) = s/2L \quad (6.8)$$

where s is the speed of sound in the TL and $L \equiv r_{out} - r_{in}$. This gives

$$\nu = \nu_{MA} \approx \frac{s}{2\pi L}, \quad (6.9)$$

for the acoustic oscillation frequency in the TL.

In order to use Equation 6.9 to estimate the size of the TL, the speed of sound, s , must be found in terms of the TL temperature. In general, a perturbation will propagate through the medium at a rate of s which is of the same order as the mean thermal velocity of ions in the medium (Frank et al. 2002). Assuming a fully ionized gas of hydrogen, the internal thermal energy per unit mass is $\epsilon = \frac{3kT}{4m_H}$, where k is Boltzmann's constant, T is the temperature, $m_H = 0.938 \times 10^6 \frac{\text{keV}}{c^2}$ is the mass of hydrogen and c is the speed of light. Plugging in m_H gives a good approximation for s :

$$s \approx 10^{-3} \left(\frac{kT_e}{1\text{keV}} \right)^{1/2} c, \quad (6.10)$$

where TL electron temperature, T_e , has been substituted for T . Again based on spectral fitting of RXTE data an approximate value for the temperature of the TL, in XTE J1550-564 is $kT_e \approx 70$ keV. From Equation 6.10 the sound speed in the TL is $s \approx 2.51 \times 10^8$ cm/sec.

The sound speed and size of the TL may now be used to determine the dependence of the R_{TL} on ν_{LFQPO} . Combining Equation 6.9 and $L = r_{out} - r_{in}$ gives

$$R_{\text{TL}} = 10^{-3} \left(\frac{kT_e}{1\text{keV}} \right)^{1/2} \frac{c}{2\pi\nu_{\text{LFQPO}}} + r_{in}, \quad (6.11)$$

where it has been assumed that $R_{\text{TL}} = r_{out}$ and $\nu_{\text{LFQPO}} = \nu$.

6.8 Cross Checks of Radii Predicted by Acoustic Oscillations

In this section radii determined by the AOM will be compared to those determined through spectral fitting. This comparison is intended to serve as a check for the viability of the AOM as a model for LFQPOs. Further, the comparison of the spectrally determined R_{inner} to the AOM determined R_{TL} acts as an independent check of the AOM.

The distance to XTE J1550–564 has recently been determined to be ~ 5.3 kpc and its inclination to the line of sight has been determined to be 73.1° (Orosz et al. 2002). With these newly measured parameters and the spectral data of Sobczak et al. 2000a, it is possible to determine R_{TL} . Based on the observed luminosity, Sobczak et al. 2000a were able to find an uncorrected value for the radius of the accretion disk inner edge, R^* . The uncorrected radius is related to the actual radius through the disk inclination and the distance to the source according to:

$$R_{\text{TL}} = \frac{R^*}{\sqrt{\cos i}} \frac{D}{6 \text{ kpc}} \quad (6.12)$$

where $D = 5.3$ kpc is the distance to XTE J1550–564, $i = 73.1^\circ$ is the inclination angle and R^* is the spectrally measured, but uncorrected, inner disk radius. Although, the spectrally determined radii are not likely to be exact, they will give an idea about the plausibility of the AOM determined radii.

See Figures 6.6, 6.7, 6.8, 6.9, and 6.10 for a comparison between the AOM determined radii and the spectrally determined radii. These figures were generated by using Equation 6.1 to convert the LFQPO frequencies into the corresponding R_{TL} . For the 1998–1999 outburst the spectral data were matched to the LFQPO observations and these spectral radii were converted using Equation 6.12. Figures 6.6 and 6.7 plot the LFQPO frequency as a function of the spectrally determined and AOM determined R_{TL} . These two figures plot AOM data from the 1998–1999 and 2000 outbursts, but spectral radii are plotted for the 1998–1999 outburst only.¹⁵ Figure 6.8 uses 1998–1999 outburst data to plot the spectral radii as a function of the AOM radii. Figures 6.9 and 6.10 use 1998–1999 outburst data to plot the ratio of AOM radii to spectral radii as a function of the LFQPO frequency.

In Figure 6.6 there is general agreement, especially in the overall trend (note the uppermost circle and error bar around 18 Hz), aside from a few outlying points, between the two sets of radii. Several of the outlying spectral points (i.e. the ones which are not in agreement with the AOM points) are at radii less than $1 R_{\text{Sch}}$. At low LFQPO frequencies, < 1 Hz, there are four points at less than two R_{Sch} which do not agree with the AOM radii. These outlying spectral measurements are discussed by Sobczak et al. 2000a. They note that these points are likely to be spurious for various reasons, including a weak black body component at the times of those measurements. If the black body component is very weak it is difficult to constrain

¹⁵Spectrally determined radii for the 2000 outburst were not available at the time of writing.

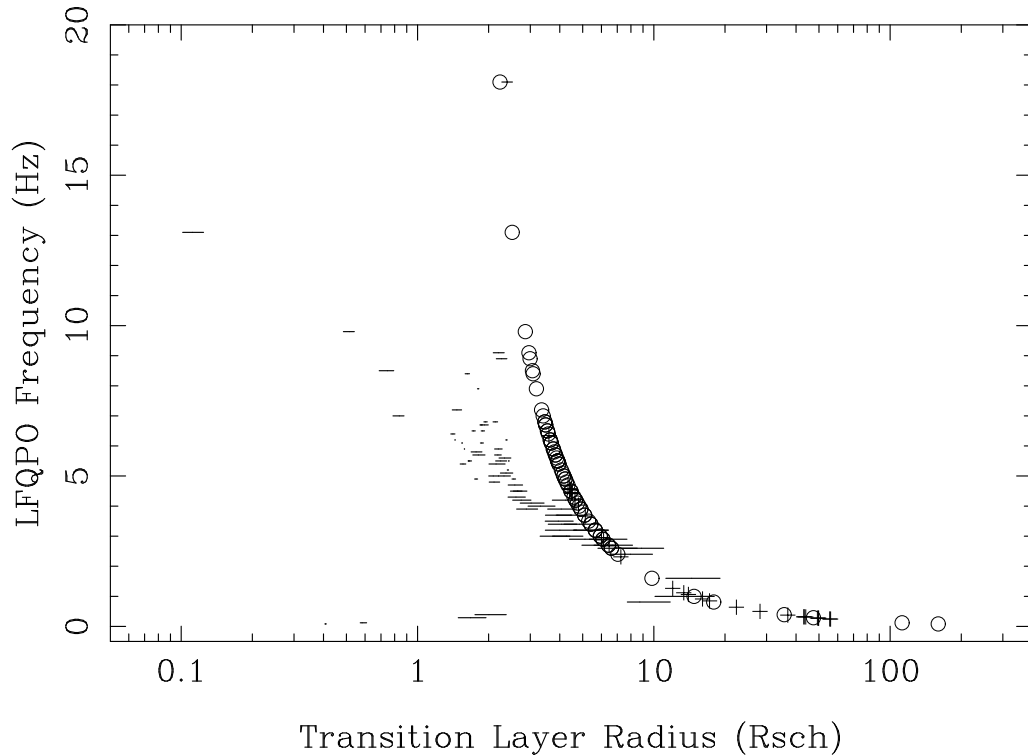


Figure 6.6: The LFQPO frequency is plotted as a function of the AOM radii and the spectrally determined radii. The error bars (horizontal lines) show the LFQPO frequency as a function of R_{TL} as determined by (Sobczak et al. 2000a) and corrected using Equation 6.12. The circles and plus signs (difficult to see as they fall in the same general area as the circles) mark the AOM radii as determined from the observed LFQPO frequencies for the 1998–1999 and 2000 outbursts, respectively. The AOM radii were calculated assuming a TL temperature of 70 keV. The errors on the AOM determined radii are not shown. These errors are dominated by a systematic uncertainty in the TL temperature. Based on a possible range of TL temperatures, the systematic uncertainty is estimated to be about 25%. There is an additional error due to the uncertainty of the inner boundary point which would cause an overall shift in the AOM radii.

the size of the accretion disk. Further, any points predicting a radius of less than $1 R_{\text{Sch}}$ must be wrong for physical reasons. In light of these uncertainties, Figure 6.6 shows reasonably good agreement between the AOM radii and the spectral radii.

Figure 6.7 shows the same data as Figure 6.6 with a $2 R_{\text{Sch}}$ shift applied to the spectral data. The shift is possibly justified because it changes the unphysical values of spectral radii (i.e. those with values less than $1 R_{\text{Sch}}$) to physical values. Some of the

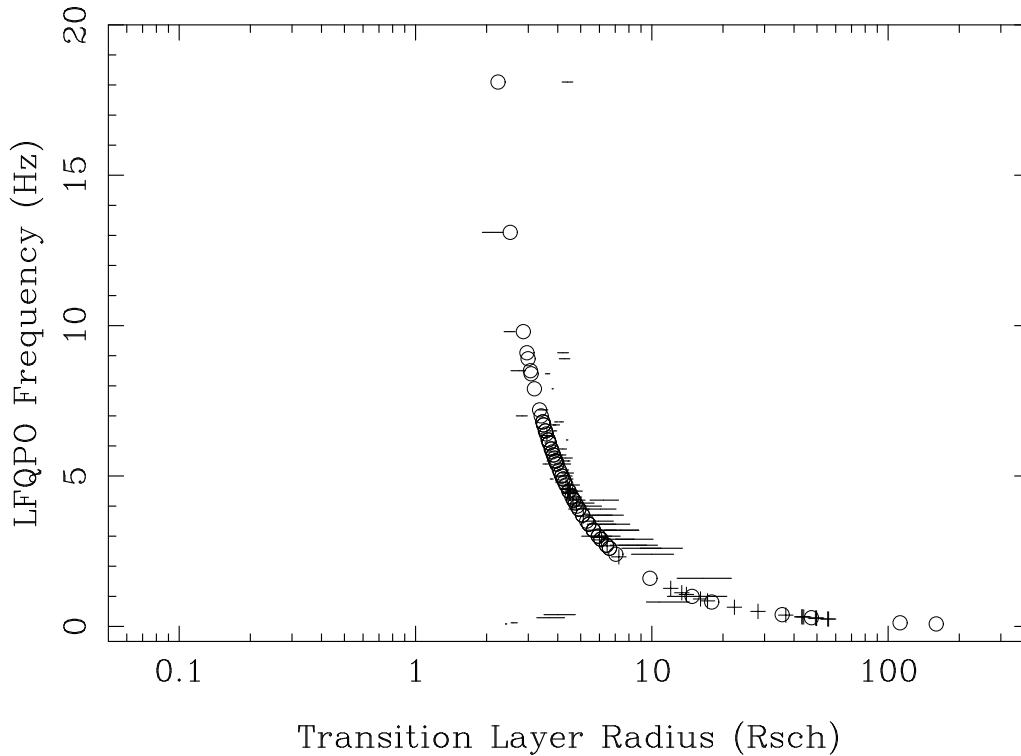


Figure 6.7: The LFAQPO frequency is plotted as a function of the AOM radii and the spectrally determined radii plus $2.0 R_{\text{Sch}}$. Other than an overall shift of $2.0 R_{\text{Sch}}$ applied to the spectral radii, this plot is identical to Figure 6.6. This $2.0 R_{\text{Sch}}$ radii shift is arbitrary but possibly reasonable, because many of the spectrally determined radii are less than $1 R_{\text{Sch}}$. This plot may not be of much scientific use, but is interesting nonetheless.

obviously incorrect spectral radii are most likely a sign that the spectral models used to fit the RXTE data were incomplete or incorrect with respect to the actual physics of the system (the basic spectral model was a power law with a black body component) (Sobczak et al. 2000a). This seems reasonable because more physically detailed spectral studies have shown that the accretion disk may never reach last stable orbit or might only be there for a short time, see Section 6.2 for a discussion. This possibility is actually supported by other spectral work, on the 1998–1999 outburst of XTE J1550–564, showing that the accretion disk only moves in to a few R_{Sch} , never reaching the last stable circular orbit (Wilson and Done 2001).¹⁶ Thus, a shift in the spectral data

¹⁶The spectral work of Wilson and Done 2001 was not used here, because they did not determine a radius for each observation of the outburst.

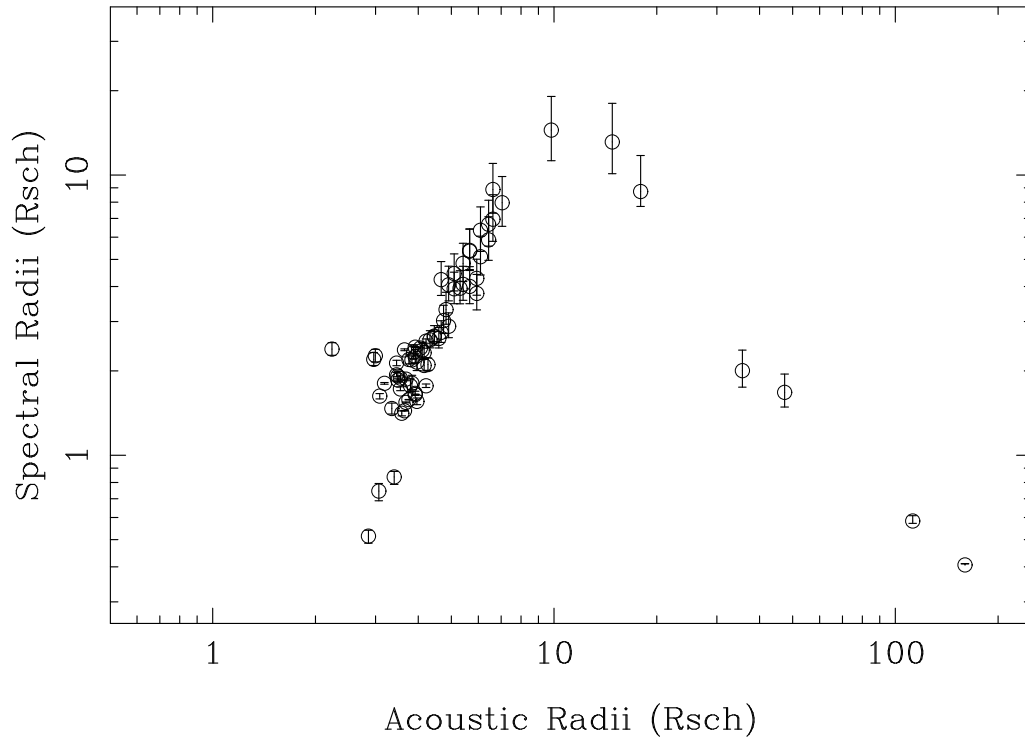


Figure 6.8: The AOM determined radii are plotted against the spectrally determined radii for the 1998–1999 outburst. This plot allows a more direct comparison between the two sets of radii.

may not be entirely out of order.

Figures 6.8, 6.9 and 6.10 provide results similar to those shown in Figures 6.6 and 6.7. These figures show the AOM determined radii versus the the spectrally determined radii, the ratio of AOM radii to spectral radii as a function of LFQPO frequency and the ratio of AOM radii to spectral radii plus $2.0 R_{\text{Sch}}$ (as in Figure 6.10) as a function of LFQPO frequency, respectively. These plots were only made for the 1998–1999 outburst. Again, there is generally good agreement between the two sets of radii. Perfect agreement would be seen as a slope of one in Figure 6.8 and a ratio of one at all frequencies in Figures 6.9 and 6.10. Notice how close to one the ratio is in Figure 6.10. As in the earlier figures, the majority of outlying points are influenced by spectral systematics as previously discussed. The purpose of these figures is to make a direct comparison between the AOM radii and the spectral radii. Figure 6.7 and 6.6 can be used to make this comparison, but are more useful for seeing the

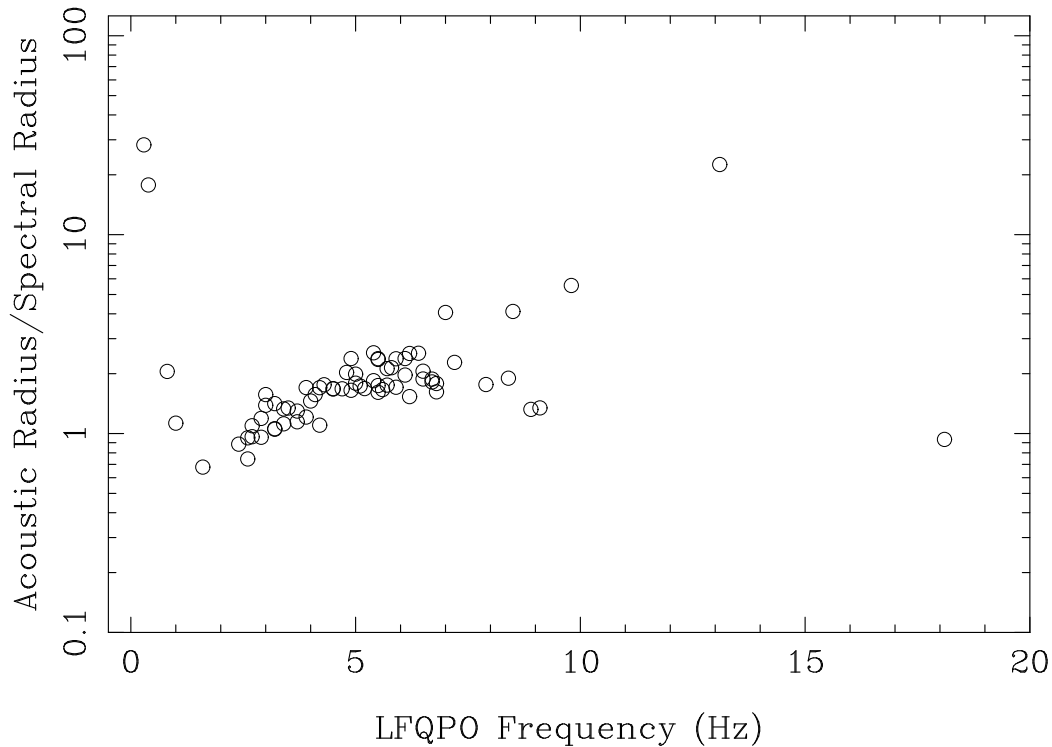


Figure 6.9: The ratio of the AOM radii to the spectral radii is plotted as a function of the LFQPO frequency for the 1998–1999 outburst. This plot allows a more direct comparison between the two sets of radii.

overall trend of the radii during the outbursts.

The acoustically determined radii agree well with the spectral fits and their consequent radii. Considering the possible uncertainties in both methods for predicting the radii, the AOM does seem to be, even in its current rough form, a plausible mechanism for the LFQPO seen in XTE J1550–564. The next step for improvement is to use RXTE data, from both outbursts, for spectral fits to a model which will give a direct measure of the TL temperature. This would help tremendously as there is every reason to suspect the temperature of the TL to change throughout the outburst. The ideal spectral model would also allow the independent extraction of R_{TL} for each observation.

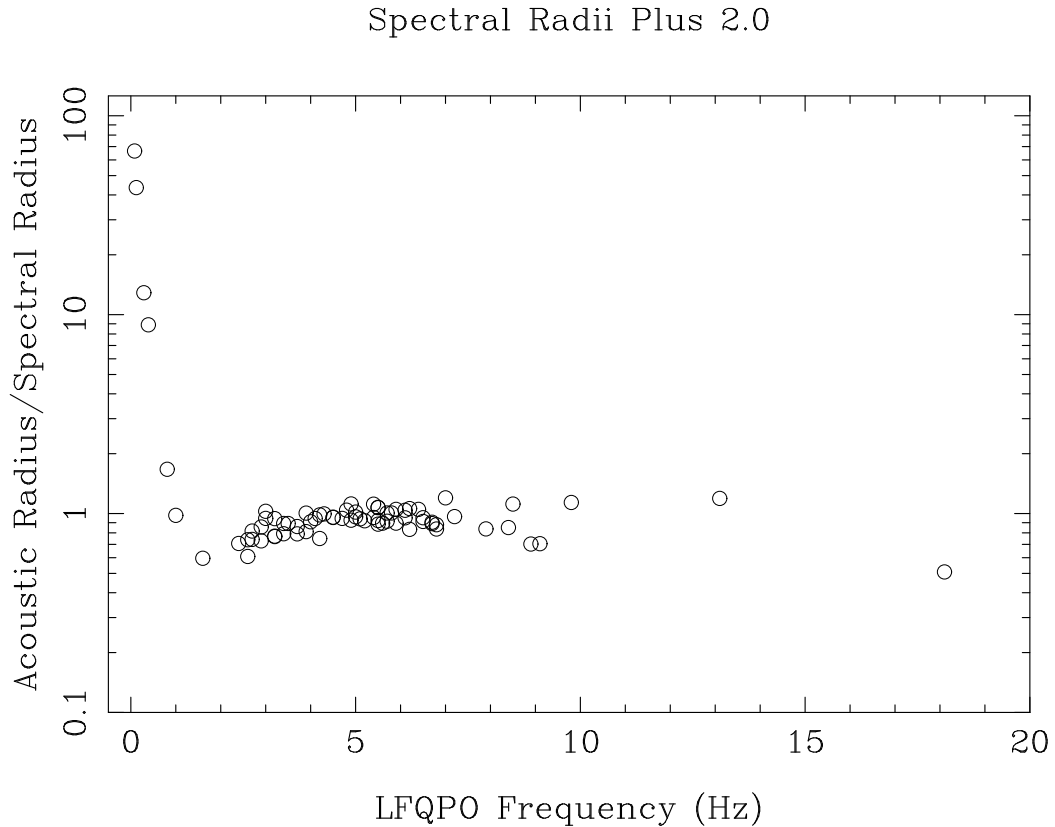


Figure 6.10: The ratio of the AOM radii to the spectral radii plus $2.0 R_{\text{Sch}}$ is plotted as a function of the LFQPO frequency for the 1998–1999 outburst. The same shift is applied here as was applied in Figure 6.7. This plot allows a more direct comparison between the two sets of radii.

6.9 High-Frequency Quasi-Periodic Oscillations

In general, acoustic oscillations cannot directly account for HFQPOs. However, the AOM is compatible with most HFQPO models, because AOM LFQPOs are a result of oscillations in the TL and most HFQPO models assume that the oscillations occur in the accretion disk. This allows for many HFQPO models to coexist with the AOM. Additionally, if LFQPOs can be firmly linked to acoustic oscillations, then it may provide a unique way for discriminating between the various HFQPO mechanisms. Specifically, if R_{TL} (really R_{inner} , but they are assumed equal) can be established via the AOM, then the HFQPO models can be distinguished by their radial dependence. See Figure 6.11 for how this distinction might be made. Because there is much controversy over which mechanism causes the HFQPOs, it would be a significant advantage for the AOM if it could provide an independent means for checking the

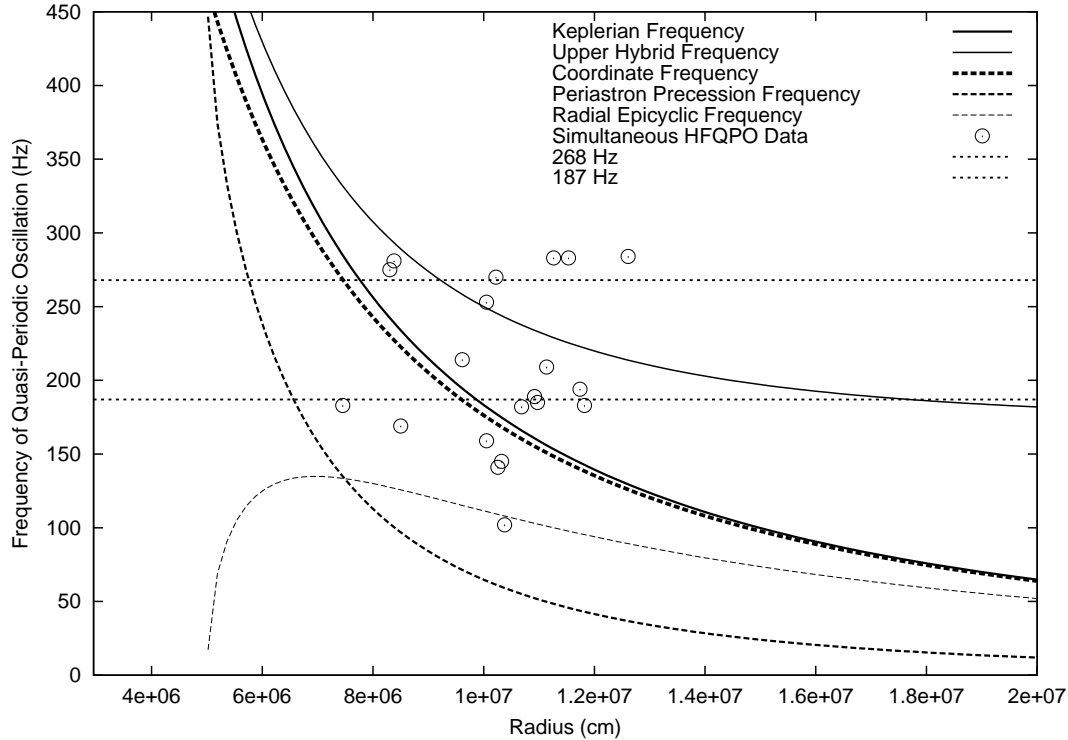


Figure 6.11: The frequency of HFQPOs, which are observed simultaneously with an LFQPO during the 1998–1999 outburst, are plotted as a function of the AOM determined radius, R_{TL} . HFQPO points are plotted with curves from HFQPO models. The lines and points are as described in the top right corner of the figure. Frequencies of the two-oscillator model (see text) are represented by solid lines and frequencies of the relativistic precession model are shown as dashed lines. Theoretical curves are made assuming a $10 M_{\odot}$ black hole with spin $a = 0.7$. The horizontal lines at 268 Hz and 187 Hz represent the HFQPOs observed during the 2000 outburst, in the IS, at times when no LFQPO was observed. The uncertainty in the position of these horizontal lines is about 5%. Error bars on the HFQPO frequencies are on the order of the size of the plotting symbol. However, errors on the radii are of order 25%. Systematic uncertainties in the temperature dominate these radial errors.

HFQPO mechanism.

The accretion geometry required by the AOM is compatible with virtually any HFQPO mechanism. For example, the HFQPO could be due to Keplerian frequencies of orbits at R_{TL} .¹⁷ There could be coupling between the LFQPO modes and the Keplerian HFQPO modes, such that during certain states the different QPOs are more prominent. It is also possible that diskoseismic modes creating HFQPOs (Nowak and

¹⁷It is possible that the Keplerian frequencies could be due to orbits inside R_{TL} , because the accretion disk probably penetrates the TL somewhat. This would leave a region of overlap.

Wagoner 1991) are present with the acoustic modes. Lense-Thirring models (Stella et al. 1999) are another possibility. The dripping handrail (Young and Scargle 1996) is a model which could produce HFQPOs and is well suited to the assumption that the acoustic oscillations are noise driven. All of these possibilities are allowable within the framework of the AOM. For future work it is important to incorporate magnetic fields in the accretion flow (i.e. magneto-acoustic oscillations), see Titarchuk and Wood 2002 for how magneto-acoustic oscillations might be used with HFQPO models.

During the 1998–1999 outburst there were multiple observations of simultaneously occurring LFQPO–HFQPO ‘pairs’ (Remillard et al. 2002). For all such observations, the AOM was used to predict the approximate radius of the accretion disk inner edge. These radii were then used to make a plot of the HFQPO frequency as a function of radius. In Figure 6.11, the HFQPO associated with the LFQPO is plotted at the radius implied by the AOM. Plotted with these data are the theoretical curves for the two-oscillator model (Titarchuk et al. 1999) and the relativistic precession model (Stella et al. 1999).

The two-oscillator model was developed for neutron stars, but may be applicable black holes if the TL is allowed to rotate. The high frequencies of the model are the Keplerian frequency and the upper hybrid frequency, a radial mode of the Coriolis force due to the rotating TL,

$$\nu_K = \left(\frac{GM}{R^3} \right)^{1/2} \quad (6.13)$$

$$\nu_h = \left(\nu_K^2 + (\Omega/\pi)^2 \right)^{1/2}, \quad (6.14)$$

respectively. In the relativistic precession model, the relevant frequencies are the coordinate (Keplerian) frequency,

$$\nu_\phi = \pm M^{1/2} r^{-3/2} \left[2\pi \left(1 \pm aM^{1/2} r^{-3/2} \right) \right]^{-1}, \quad (6.15)$$

the radial epicyclic frequency,

$$\nu_r^2 = \nu_\phi^2 \left(1 - 6Mr^{-1} \pm 8aM^{1/2} r^{-3/2} - 3a^2 r^{-2} \right), \quad (6.16)$$

and the Lense-Thirring (periastron) precession frequency,

$$\nu_{per} = \nu_\phi - \nu_r. \quad (6.17)$$

See Figure 6.11 for plots of these five curves and how they compare to the observed HFQPO frequencies.

Based on Figure 6.11, it cannot be determined which of either of the two HFQPO models is correct. According to the uncertainties in the radii, given by the AOM, neither of the two HFQPO models are inconsistent with the data. However, from Figure 6.11 it is hoped that several points are conveyed. The plot shows how the AOM may be used as a tool for differentiating between various HFQPO models. The next point is related to the horizontal lines on the plot at 268 Hz and 187 Hz. These lines are important because HFQPOs in a ratio of 3:2 have been noticed in other sources and it has been suggested that HFQPOs group around frequencies in that ratio (Remillard et al. 2002). This grouping could be a result of natural frequencies in the relativistic precession model. From the figure, it is not clear that this grouping is present. The HFQPO data appears to be inconsistent with the 3:2 ratio. With respect to distinguishing between different HFQPO models, the uncertainties in the AOM radii are just too great to perform any conclusive tests. With such large uncertainties, any model could be consistent with the data.

6.10 Other Viable Low-Frequency Quasi-Periodic Oscillations Models

There are several other models in the literature that provide an LFQPO mechanism. For completeness some of these models are mentioned with references. The Accretion-Ejection Instability (AEI) model proposes that LFQPOs are generated by differentially rotating spirals in the accretion disk (Tagger and Pellat 1999). Another LFQPO model is based on the Lense-Thirring precession of a warped accretion disk, the Bardeen-Petterson effect (Shirakawa and Lai 2002). Finally, there are models which rely on the TL, as does the AOM, for the LFQPO mechanism. These last models assume that the LFQPO is result of eddies in the inner ADAF or CDAF (Igumenshchev et al. 1996). For future work it is important to compare the theoretical predictions of each of these models, including the AOM, to LFQPO observations.

6.11 Summary of AOM and Future Work

Evidence that the LFQPOs observed in both the 1998–1999 and 2000 outbursts of XTE J1550–564 are strongly dependent on a high energy photon flux has been presented. If the assumption is made that high energy photons are produced in the TL, then the dependence of the LFQPO on the high energy flux implies a dependence on the TL. The AOM is a model which satisfies this dependence and is supported by the appearance of negative phase lags in most of the LFQPOs detected during the 1998–1999 outburst of XTE J1550–564. Phase lag data for LFQPOs in the 2000 outburst is not yet available.

The AOM has a several attractive features. It gives estimates of the location of the inner edge of the accretion disk. These estimates may be more reasonable than some of those obtained through spectral fitting. The geometry of the AOM allows the inclusion of most HFQPO models. This is because most HFQPO models involve disk oscillations and the AOM involves TL oscillations. Both mechanisms may occur simultaneously.

There is a great deal of work which still needs to be done in order to test the AOM. The first step is to get spectral fits for all observed LFQPO observations with the goal of more accurately determining kT_e . The present work only estimates kT_e based on power law cut offs and assumes that kT_e is constant during all times of the outburst. The latter assumption is almost certainly incorrect, but large variations in kT_e will not destroy the plausibility of the AOM. Accurately determining how kT_e evolves through the outburst should allow a more accurate determination of how R_{TL} evolves.

If the spectral fits of the data are made to physical models, then it is possible that more accurate spectral radii, than given by Sobczak et al. 2000a; Rodriguez et al. 2002, will be found. Then it will be possible to compare these more accurate spectral radii to the more accurate AOM radii. This could prove to be a very convincing test of the AOM. Using physical models for spectral fitting would then allow interesting LFQPO spectral correlation studies to be done for the 1998–1999 outburst and the 2000 outburst. Earlier spectral studies were done by (Sobczak et al. 2000b; Rodriguez et al. 2002) using only simple spectral models for the outbursts (a power law plus a black body).

The next step might be to look at other sources, such as XTE J1859+226, where

similar spectral and timing behavior has been observed. LFQPO and spectral behavior similar to that observed in XTE J1550–564 has also been seen in XTE J1859+226 (Swank et al. 2002). XTE J1859+226 has demonstrated cyclic behavior in the HID and similar flux dependence of the LFQPO.

The AOM is closely tied to a specific outburst scenario and accretion geometry, both of which shape the TL and accretion disk evolution during the outburst. A very interesting test would be to use numerical simulations, such as the DIM, of the outbursts (assuming they could be made to accurately reproduce the XTE J1550–564 outbursts) and to then calculate the acoustic resonances of the TL. These calculation would be based on the density of the gas in the TL, size of the accretion disk and other physical properties of the system as given by the numerical simulations for the entire outburst process. A simulation of the modulated flux might be obtained. This might then make it possible to re-create the LFQPO frequency and rms and potentially the complex phase lag behavior.

There may be some LFQPO properties which the AOM cannot address. These include the different types of LFQPOs seen in XTE J1550–564 and the phase lag flips. It may be some time before it is possible to adequately address these questions.

Chapter 7

Discussion & Conclusions

The primary focus of this dissertation was X-ray observations of the SXT and micro-quasar XTE J1550–564. Observations made by the USA experiment were emphasized, although observations made by the ASM, RXTE and BATSE were also discussed. SXTs are a class of LMXBs exhibiting occasional outbursts. During an outburst, SXTs can increase their luminosity by two orders of magnitude or more. These outbursts may be observed throughout the electromagnetic spectrum (e.g. X-ray, optical, radio, etc.) (van Paradijs and McClintock 1995).

SXT outbursts are of great interest because they allow the study of LMXBs under a wide range of accretion rates and conditions. SXT outbursts are key to developing a complete understanding of accretion physics in LMXBs and provide insights to the accretion processes of active galactic nuclei (AGN), which are thought to contain super-massive, $M \sim 10^6\text{--}10^{10} M_{\odot}$ (M_{\odot} = solar mass), central compact objects (Meyer-Hofmeister and Meyer 2001). Among SXTs, the majority contain central compact objects dynamically determined to have masses in excess of $\sim 3 M_{\odot}$. Often the central objects of SXTs and AGN are referred to as black holes because $\sim 3 M_{\odot}$ is the greatest stellar mass for which hydrostatic equilibrium is possible, assuming reasonable equations of state (Longair 1994). However, the direct detection of a black hole, such as confirmation of an event horizon at the Schwarzschild radius, $R_{Sch} = \frac{2GM}{c^2}$, has not yet been made. Finally, LMXBs and SXTs provide a unique opportunity to test General Relativity and to probe fundamental physics under conditions not terrestrially attainable.

In this work, a detailed discussion of the USA experiment was given prior to delving deeply into the X-ray timing and spectral observations of XTE J1550–564.

The collection and analysis of USA data were discussed extensively. Obstacles encountered by the USA mission were reviewed and when possible the solutions were discussed. It was noted that there remain two outstanding issues to be ameliorated before USA data can be analyzed to its fullest potential. The first of these issues is the full implementation of GPS corrections to the USA time stamps. The second is the development of a robust correction to EDIE. An EDIE correction methodology was presented; however, in order to extract weak signals in the range of 100–1000 Hz, a more detailed understanding of EDIE is required. The EDIE correction method presented should work well in the extraction of strong signals in the PSD, but may not work well with weak signals. Also presented was work toward the construction, filtering and analysis of USA time series. Tools created for the purpose of automating the USA data analysis stream were described and examples of their usage were given. A more robust tool for the automated generation of background and instrument corrected light curves still needs implementation. After addressing the experiment, attention was turned to the USA observations of XTE J1550–564.

In 2000 April, the ASM detected the onset of an X-ray outburst in the source XTE J1550–564. Shortly thereafter, USA began collecting the observations presented in this work. Here the timing and spectral observations of XTE J1550–564, during its 2000 outburst, were reported. A low-frequency quasi-periodic oscillation (LFQPO) with a centroid frequency that tends to increase with increasing flux and a fractional rms amplitude which is correlated with the hardness ratio was observed. Several high-frequency quasi-periodic oscillations (HFQPOs) were detected by the *Rossi X-ray Timing Explorer* (RXTE), during periods where the LFQPO is seen to be weakening or not detectable at all. The evolution of the USA hardness ratio (4–16 keV/1–4 keV) with time and source flux was examined. The hardness-intensity diagram (HID) showed a counterclockwise cyclical movement that possibly indicates the presence of two independent accretion flows: a geometrically thin, optically thick accretion disk and a hot sub-Keplerian flow.

In addition to the correlation of the LFQPO percent rms amplitude with the USA hardness ratio, also observed was an approximate anti-correlation in the LFQPO percent rms amplitude squared with low energy photons from the RXTE All Sky Monitor (ASM) and USA data, and an approximate correlation with high energy (20–100 keV) photons from the Burst And Transient Source Experiment (BATSE). Comparisons of LFQPO observations made by USA during the 2000 outburst with

LFQPO observations made by RXTE during the 1998–1999 outburst show similar behavior.

Based on the cumulative evidence obtained from USA, RXTE and BATSE observations of the two major XTE J1550–564 outbursts, the LFQPO was found to be dependent upon a hot Comptonizing medium, the transition layer (TL), which is bounded near the compact object by a surface or event horizon, and bounded at R_{TL} , by a truncated accretion disk (Titarchuk et al. 1999). The TL defines a resonant cavity driven by random perturbations in the accretion flow. The TL resonance was interpreted as a mechanism for the LFQPO and the eigenfrequencies were assumed to be the LFQPO frequencies, ν_{LFQPO} .

The LFQPO energy and frequency dependencies are explained by assuming an outburst scenario in which the inner edge of the accretion disk changes position as transitions are made between the five spectral and timing states (low/hard, high/soft, and intermediate or very high) typical of SXT outbursts. Current understanding of SXT outbursts suggests that this disk behavior is reasonable. For example, the disk instability model, which is widely thought to be, at least qualitatively, an accurate description of SXT outbursts, assumes a disk truncated at $\gtrsim 1000 R_{Sch}$ during quiescence, which moves in toward the compact object during the rise to the outburst maximum (Lasota 2001). The spectral properties of each outburst state are due to varying relative contributions from the TL and the accretion disk. These contributions are modeled by a power law and a black body, respectively.

As the source moves from state to state, it is expected that the LFQPO energy and frequency characteristics will change. The observation that the LFQPO is weak or not observable during the high and very high states is explained by the transition layer growing smaller and being subjected to severe Compton cooling (i.e. inverse Comptonization) as the disk moves in and brightens. The observation of ν_{LFQPO} increasing during the outburst rise and decreasing during decline is explained by the changing size of the transition layer ($\nu_{LFQPO} \propto 1/(\text{size of transition layer})$). Based on this ‘acoustic oscillation model’ (AOM) it is found that, during the USA observations of the 2000 outburst rise to maximum, the inner edge of the accretion disk evolves from $68 R_{Sch}$ to $3.7 R_{Sch}$, corresponding to the observed LFQPO frequencies between 0.2 Hz and 6 Hz, respectively. For the 1998–1999 outburst rise to maximum, it is determined that the inner edge evolves from $166 R_{Sch}$ to $2.5 R_{Sch}$, corresponding to the observed LFQPO frequencies between 0.081 Hz and 13.2 Hz, respectively.

The AOM predicted radii were compared with spectrally determined radii and it was found that, within uncertainties, the two are consistent. However, the uncertainties are large, indicating that more work needs to be done in constraining the input parameters to the AOM. The two greatest uncertainties come from the TL temperature and the location of the inner boundary point. Even with these unknowns, the preliminary results of the AOM indicate that it may be a useful tool in determining the location of the accretion disk inner edge. Knowledge of the accretion disk inner edge can be extremely helpful in testing the veracity of proposed models for the production of HFQPOs. Because many these models rely on General Relativistic effects, their corroboration or falsification may provide insight into the theory of General Relativity.

The LFQPO observed by USA had distinctive properties leading to the proposal of the AOM as the LFQPO mechanism. However there are many interesting conclusion which can be drawn without imposing a particular LFQPO model for XTE J1550–564. For example, it is possible to say that the LFQPO frequency is regulated by the accretion rate through the disk. Further, without making any assumptions about the geometry, it is found that that LFQPO is dependent upon the existence of a Comptonizing medium. When the flux of high energy photons, as reflected in the spectral power law, becomes weak the LFQPO disappears. This statement is true of both XTE J1550–564 outbursts.

Despite the small successes of the AOM, open consideration should be given to other possible models. Future work should consist of applying the various LFQPO models available and comparing the results. It is not likely that any one QPO model will describe the complexity of timing behavior seen in all SXTs. Most QPO models cannot explain the simultaneously occurring QPOs (HFQPOs and LFQPOs). It could be the case that multiple mechanisms are at work. Perhaps resonances in the TL cause some QPOs and resonances or warping in the accretion disk cause others. Such a scenario might require two models. Due to the complexity of these systems it is difficult to believe that there is not some ‘chaotic’ behavior present, thus dynamical models such as the dripping handrail (DHR) (Young and Scargle 1996) should also be considered. The DHR model is interesting because, unlike most other QPO models, it provides a mechanism for X-ray flux modulation and it has the potential for both LFQPOs and HFQPOs.

Most of the conclusions presented here and throughout this work are not very

definitive, especially in the area of theoretical models describing specific processes (i.e. QPOs, outburst profiles, etc.). This is a reflection on the nature of the field at this time. In high energy astrophysics and particle astrophysics, just enough is known such that there are many more questions than answers. For example, there are multiple models for the same processes in X-ray sources and it is extremely difficult to determine which are correct. The only choice is to continually improve the experimental apparatus. This is not to say that progress has not been made, there is an understanding now which did not exist even 10 years ago. Only a few decades ago, the plausibility of release of gravitational potential energy as fuel for X-ray luminous objects was questioned. Now accretion powered X-ray binaries are almost taken for granted. The theory of accretion power has withstood the scrutiny of of years of observations by ever improving experiments. Many more theories have been proposed and eventually disproved. Others still are left in question due to experimental limitations. Ultimately, understanding astrophysical processes is a matter of increasing the resolution of our microscope.¹

¹This may not in fact be the ultimate case. It may be possible that the ultimate case is the realization of our inability to truly understand anything.

Appendix A

USA Data Analysis Tools

A.1 Introduction

The sections of this appendix discuss, roughly in the order of use as described in Chapter 4, the USA specific tools for data collection and analysis. Many tools are described in detail here, however, the reader is referred to the appropriate references when complete details are not given.

A.2 `usaview`: Observation Scheduling

`Usaview`'s original functionality and modifications, making it a valuable long term planning tool for the USA mission, will be discussed in this section.

From the start of the USA mission, 1999 February 23, until about 2000 May 18, source planning software was not conducive to long term scheduling. It was difficult to plan observations such that the object of interest was in an optimally viewable region of the sky (i.e. the time of year when a source can be given the longest possible observation time in a low background region of the orbit and is within USA's restricted field of view). As was discussed earlier in this work the USA experiment faced several restrictions which limited the total time of source observability. The polar orbit of ARGOS, because of Earth's radiation belts, was one such restriction.

Orbital constraints on observation length were known before the launch of ARGOS/USA. After launch there were some unexpected problems which restricted the USA observing ability. The problem, most relevant to long term scheduling of observations, was the thermal cycling due to heat shield damage. The USA detectors

would become hot when at small angles with respect to the Sun. The thermal cycling resulted in a self-imposed restrictions on the range of yaw values, for a definition of yaw see Figure 3.3. The yaw restrictions were designed to prevent the instrument from being stuck or locked, for a prolonged period, in a position that might leave USA vulnerable to the Sun and in danger of suffering irreparable damage and ending the experiment.

After significant experience had been gained in the analysis of in orbit USA data, several other issues, related to observation scheduling and strategy, became apparent. There were two primary issues to be addressed. The first was to insure that all high intensity sources were observed in a high telemetry rate mode. The second was to insure that observations were scheduled, though they were short, in closely spaced bunches over periods of days weeks or months. The problem with using low telemetry rate modes to observe intense sources is that the one second memory buffers become filled before the end of a second. The result is a ‘gap’ containing no data at the end of the second. The problem with not closely spacing observations is that they cannot be combined to extract weak transient signals. By scheduling enough observations closely together, it is possible that they be combined allowing an increase in the signal to noise. These two issues came up in the midst of fixing pointing issues and generally getting the experiment debugged.

The significance of these problems was realize after data analysis began on the 1999 outburst of XTE J1859+226. During the outburst, most observations were performed in USA’s mode 1. This is a low telemetry rate mode and because XTE J1859+226 was a bright source nearly all of the mode 1 observations of XTE J1859+226 are riddled with data gaps at the ends of seconds.¹ Additionally, observations of the outburst were spaced sporadically and infrequently. The combined effect of these issues was to deeply hinder the search for high frequency variability in XTE J1859+226. The search for high frequency variability being one of the major goals of X-ray astrophysics led to a re-evaluation of the USA observing strategy.² Once these issues were brought to light, every effort was made to use mode 2 for high rate sources and to make more continuous observations of sources. However, sometimes scientific goals which required more sporadic observations were pursued.³ For more information about the

¹Section A.4.1 discusses gaps in USA data. See also Shabad 2000 for a discussion of gaps in USA data.

²EDIE was another problem with high frequency variability, but better statistics would have definitely helped in the case of XTE J1859+226.

³One example in monitoring AGN over periods of months (Giebels et al. 2002).

USA observations of XTE J1859+226 see (Shabad 2000) and Section 3.8.1.

Given the above set of observational restrictions and the mission goal, which was to obtain large data sets on a small number of sources, it was necessary to make plans for at least a year out into the mission (to at least 2001 May). In particular it was necessary to insure that large data sets were accumulated and that, when needed, observations were spaced closely together in time. This strategy was applied to a small number of scientifically relevant sources. This left a clear objective for observation scheduling. A program was designed that would give the most *continuous observations* of single sources in the low background regions over the remaining period of the USA lifetime. Prior to this time, sporadic observations of a variety of the sources were made in order to insure that the instrument was operating correctly and to obtain a broad sampling of sources by the USA experiment. It was hoped that this observing strategy, in the first phase of the experiment, would allow USA to observe a wide variety of sources, establish a solid base of science data and deepen the understanding of the instrument.

With this shift in priority, it was realized that the means to make long term projections, for the optimal observability of multiple sources, did not exist. This made it difficult to satisfy and balance the observational needs of everyone in the collaboration. The reason for this difficulty was the lack of a way to determine, day by day, what sources would be observable for months on end. The easiest and most expeditious means to ameliorate this difficulty was to modify the **usaview** program.

Prior to making modifications, **usaview** was only able to determine the observability of one object for one Modified Julian Date (MJD). **Usaview** required the user to type in source coordinates and MJDs for every source on every day of interest. Once modifications were made **usaview** was able to read a list of all sources of interest to the USA collaboration and a time range (the next year for example). **Usaview** would then give out the sections of that time range for which a source was optimally observable.

Specifically, **usaview** was modified such that it could be given a range of days for a source. For each of the the days in the range, **usaview** would print out whether an observation was BAD, GOOD, or OPTIMAL, depending on the constraints. The labeling of BAD, GOOD, or OPTIMAL was dependent upon a combination of the length of the observation, if any obscuration from the yoke would occur and if the yaw angle was placing the detector in a dangerous position relative to the Sun.

At the time of these modifications it was desirable to have observability for all sources which might be relevant to the USA mission. This information was obtained by using an awk script to run **usaview** for all such sources. The awk script, `usaview.awk`, read the file `SourceCoordinates.ltx`, which contained the RA and DEC of all sources of interest to the USA mission. `Usaview.awk` then generated a script which would run **usaview** for all of these sources and then generate an output file containing entries with a rating for all days in the range. Once done, the ranges of observability and their rating were extracted by hand from the output files of individual sources.

Tables were made for both GOOD and OPTIMAL observation times. The GOOD dates always contained the OPTIMAL dates. The USA observations after 2000 May were based on a table similar to Table A.1, which represents the good observing dates for a few of the USA sources. In addition to the information contained in Table A.1, **usaview** was also able to determine the observation length and the node (ascending or descending) of observation.

The directory `kaice/cvs_base_home/Notebook/ObsOutFiles` in the SLAC group `ek cvs` repository contains all significant results used in scheduling USA observations. Scripts, data products and other relevant files are all contained there.

A.3 Intermediate Steps

Once the sources to be observed were decided upon and the data were collected, several intermediate steps were required before using **dat2fits** to obtain FITS files and begin analysis. There has already been a thorough write up on most of the USA data stream (from satellite data recorder to the ARGOS/USA data archive at NRL), see USA SWG 2001b. A brief overview is given here for completeness. In the next section, significant attention will be given to **dat2fits** and time construction.

ARGOS/USA data are stored in a data recorder on the ARGOS satellite. When a ground station is passed a wideband data link is opened and the contents of the ARGOS data recorder are dumped to the ground station. This wideband data contains the data from all experiments onboard ARGOS. The wideband data are split, at Kirtland Airforce Base, into files for the individual experiments (these are in a specialized file format, made specifically for Boeing, called EXPD). The code **wide2dat** is used to convert the USA wideband files into a dat format. These dat files comprise the USA level 0 database. The data in the dat files may be accessed in a few different

RA (deg)	DEC (deg)	Source	Begin	End	Begin	End	USA
244.98	-15.64	ScOX-1	4 27 2000	6 17 2000	9 2 2000	10 21 2000	0 <i>k:secs</i>
251.45	-45.61	GX 340+0	5 11 2000	10 21 2000			13.8 <i>k:secs</i>
256.44	-36.42	GX 349+2	5 13 2000	10 29 2000			183.1 <i>k:secs</i>
274.01	-14.04	GX 17+2	5 27 2000	7 15 2000	10 3 2000	11 20 2000	26.0 <i>k:secs</i>
270.29	-15.08	GX 5-1	5 23 2000	7 12 2000	9 28 2000	11 16 2000	28.6 <i>k:secs</i> 4
326.17	+38.32	Cyg X-2	7 9 2000	9 8 2000	11 23 2000	1 22 2001	278.6 <i>k:secs</i>
243.18	-52.42	4U 1608-522	5 5 2000	10 10 2000			0 <i>k:secs</i>
094.28	+09.14	4U 0614+09 ^a	4 22 2000	5 25 2000	11 22 2000	1 8 2001	6.2 <i>k:secs</i>
262.99	-33.83	4U 1728-34	5 19 2000	7 28 2000	8 28 2000	11 5 2000	0 <i>k:secs</i>
270.38	-20.53	GX 9+1	5 24 2000	7 16 2000	9 25 2000	11 15 2000	13.0 <i>k:secs</i>
262.93	-16.96	GX 9+9	5 16 2000	7 6 2000	9 20 2000	11 8 2000	21.8 <i>k:secs</i>
273.63	-17.16	GX 13+1	5 27 2000	7 17 2000	9 30 2000	11 19 2000	16.7 <i>k:secs</i>
253.80	-40.03	GRO 1655-40	5 11 2000	10 25 2000			0 <i>k:secs</i>
288.23	+10.88	GRS 1915+105	6 6 2000	7 23 2000	10 24 2000	12 9 2000	108.1 <i>k:secs</i>
169.54	+48.04	XTE J1118+480	6 5 2000	8 18 2000	1 29 2001	4 14 2001	17.0 <i>k:secs</i>
237.75	-56.48	XTE J1550-564	5 1 2000	10 3 2000			0 <i>k:secs</i>
248.50	-47.48	X1630-472	5 8 2000	10 18 2000			93.1 <i>k:secs</i>
255.71	-48.79	GX 339-4	5 16 2000	10 25 2000			2.8 <i>k:secs</i>
270.30	-25.74	GRS 1758-258	5 25 2000	7 21 2000	9 19 2000	11 14 2000	17.2 <i>k:secs</i>

Table A.1: Example Table of Source Observability. The two date (month day year) ranges are for GOOD observations. The last column, labeled USA, is a tally of the total number of USA observing seconds accumulated on a given source before 2000 May.

^aAlso observable from 4 11 2001 to 4 20 2001

ways. **Dumptelem** can be used to dump the contents of a dat file. **Dat2fits** may be used directly on the dat files to create FITS files. The best way is to have the level 0 archive (the dat files) converted into the time-ordered level 1 archive and to then access the level 1 archive via **picktelemII**. **PicktelemII** allows the user to access a variety of data products and to convert the observations into FITS files via **dat2fits**.

A.4 dat2fits: USA Data Unpacking and the Construction of GPS Time Stamps

A.4.1 Introduction to dat2fits

Dat2fits is an over 7000 line, not including external library functions, C code, which allows users to extract data from the level 0 and level 1 archives. The primary purpose of **dat2fits** is to create FITS files for individual observations. This involves unpacking of data in the level 0 or 1 archive. **Dat2fits** must handle a variety of tasks before writing a FITS file. These tasks include the extraction of housekeeping information, checks for data quality, the derivation of useful quantities to be written to housekeeping FITS files, alignment of event data with housekeeping data⁴ and the construction of GPS times. This last task is discussed in the following sections.

The **dat2fits** code has been the project of several people over many years. The code was inherited by this author with several significant tasks to be completed. These tasks involved all functionality of **dat2fits** mentioned above. Several issues were of primary concern. The most significant of these was the proper construction of event times. Initially, there were major bugs in time construction. Other issues included the addition of header key words to allow compliance with FITS standards, addition of good time interval tables, restructuring of the code for better organization and readability, and performing periodic maintenance and modification.

The FITS files made by **dat2fits** follow standard format as described in FITS documentation, see Hanisch et al. 2001. There are a wide variety of tools already available to process data in the FITS format. The main sweet of FITS tools are known as FTOOLS. One of the primary jobs of **dat2fits** is to write FITS files in a format that can be used easily with the FTOOLS. USA FITS files come in three

⁴For some USA event modes housekeeping data are not packed in the frame to which it belongs. For modes 1 and 3 housekeeping data are packed in the frame after the event data and for modes 2 and 4 the housekeeping data are packed in the frame before the event data.

forms: event, spectral and housekeeping. All observations, event and spectral, have an accompanying housekeeping file. The first data table in all FITS files is an image table. This table is always empty for USA observations. USA event and spectral files contain two tables following the image table. In event files the second table contains an entry for each event detected. Each event is associated with a GPS time stamp, a PHA channel identification, a detector identification and a layer identification. The third table is a good time interval (gti) table and contains an entry for each second of data collected. Each entry in the gti table contains a start time and a stop time. The gti start time is the beginning of a second of data collection and the stop time is either when the second has finished or earlier if the memory buffer fills before the second is finished. In spectral files the second table contains an entry for every 10 ms of observation. Each entry contains the number of events, in each of the 48 PHA channels, during the 10 ms span. Each event is grouped according to detector 0 or 1 and the sum of the two detectors. No layer identification is available in spectral mode. The third table in spectral mode is also a gti table. The spectral gti table contains only one entry. The start time of the entry is the observation start time and the stop time is the observation stop time.

USA FITS are labeled according to the following naming convention:

- USA_Yyyyy_Dddd_HHMMSS_Dddd_HHMMSS_M#.evt.fits,
- USA_Yyyyy_Dddd_HHMMSS_Dddd_HHMMSS_M5.spc.fits,
- and USA_Yyyyy_Dddd_HHMMSS_Dddd_HHMMSS_M#.hkp.fits,

for event, spectral and housekeeping files, respectively. The yyyy stands for the year, the first ddd and HHMMSS combination is the start day of the year, hour, minute and second. The second is the stop time. The # is replaced by a digit, 1–5, which represents the mode of the event observation.

A.4.2 GPS Time Construction in `dat2fits`

The fundamental problem of time reconstruction in USA data is the determination of which second of data a photon actually belongs. To understand the meaning of this statement, it is necessary to explain the manner in which USA data buffers are created, events are written to memory, and how time stamps are given. This

explanation serves as the subject for this section. The next section is reserved for difficulties which arise when events are not sorted into their correct second.

The simplest example will be used as a starting point for the explanation of how times tags are constructed. Each photon in the USA level 0 or 1 archive has several pieces of information associated with it. This information includes the PHA channel, detector identification, layer identification and timing information. A full description in painstaking detail of how events are stored and USA buffers are written can be found in USA SWG 1996. Here a simple model is relied upon in order to explain more the pertinent issues of time construction.

The timing information given to each event includes frame ticks and time ticks. The frame tick counter is a simple counter which advances from 0 to 3 and then rolls over to 0. The frame tick counter is incremented upon reinitialization of the time tick counter, this occurs every second. The time tick counter keeps track of the number of microseconds passed since the moment in which events may be written to a frame. A frame may be thought of as a memory buffer which holds one second of events. The time ticks give knowledge as to what microsecond since the beginning of a frame did a particular photon get detected. The time tick counter advances from 0 to 999999. Each frame is given a GPS time stamp, specifically, each frame is stamped with a GPS week and a GPS number of seconds, with microsecond resolution, since the beginning of that week. The GPS frame stamp gives USA its microsecond resolution in absolute times.

Once the timing information has been extracted, event times, *etime*, are constructed according to the following formula:

$$\begin{aligned} \text{etime} = & (\text{GPS week}) \times 7.0 \times 86400.0 \\ & + (\text{GPS seconds}) + (\text{time ticks}) \times 10^{-6} - \text{TIMEOFFSET}. \end{aligned} \quad (\text{A.1})$$

where GPS week, GPS seconds and time ticks are as described above and

$$\text{TIMEOFFSET} = 536544000.0$$

or the number of seconds between 1980 January 6 and 1997 January 6. TIMEOFFSET was subtracted from the USA event times in order to keep greater timing resolution and to save on disk space. In order to construct GPS times from USA times the

following equation is used:

$$\text{GPS seconds} = \text{etime} + \text{TIMEOFFSET}. \quad (\text{A.2})$$

If unix time or UTC seconds are wanted then use:

$$\text{UTC} = \text{etime} + \text{TIMEOFFSET} + \text{GPSOFFSET}. \quad (\text{A.3})$$

where

$$\text{GPSOFFSET} = 315964800.0$$

or the number of seconds between 1970 January 1 and 1980 January 6. UTC time is time given in the number of seconds since midnight 1970 January 1. GPS time is given in seconds since midnight 1980 January 6. The times in USA FITS files are defined as seconds since 1997 January 6.

It may have been noticed that the frame tick counter was not used in any way in the above formulae for calculating USA event times. This is because under ideal conditions the frame tick counter would be superfluous. Photons belonging to a particular GPS week and GPS second would always be written to the frame (or relative second) which they belong. This brings back the fundamental problem of constructing USA event times. In general it cannot be expected that an event will be stored in the appropriate frame. It is often the case that photons will be written to the following or preceding frame to which they actually belong. The frame ticks are the only way of knowing to which frame an event actually belongs. Thus, frame ticks provide the only means of avoiding out of order events (OOEs) in USA time series. Event “sorting” using frames ticks is the subject of the next section.

A.4.3 Difficulties in USA Time Construction: Out of Order Events (OOEs)

One of the most challenging task handled by **dat2fits** is the construction of photon arrival times in the event modes (modes 1–4).⁵ The reason for difficulties is that there are a variety of ways in which photon arrival times can be “mislabeled” due to being written to an earlier or later frame. If the event’s frame tick is not monitored, then the event will be given an incorrect time in the FITS file and will appear to be out

⁵Time construction in mode 5 is much easier because every event is not given a time stamp.

of order in the time series. There are ~ 50 permutations by which an event can be “mis-labeled” and cause an OOE in the time series.

As was discussed previously, frame ticks keep track of the current frame number and they advance from 0 to 3. Each second frame ticks are incremented by one. When 3 is reached the next increment returns the frame tick counter to 0. A simple picture of how USA events get stored in frame buffers can be made by representing each event by its corresponding frame tick. The case of ideal conditions, in which all events are placed in the correct frame, is used as a starting point. If the symbol `||` represents a frame boundary and numbers are the frame ticks associated with events, then 5 seconds of an ideal USA data stream would look something like:

```
||0000000000||1111111111||2222222222||3333333333||0000000000|| ...
```

The key point to notice is that within a set of frame boundaries all of the events have the same frame tick, showing that they belong to that frame. This means that the time stamps for all of these events are given by Equation A.1 with no further thought.

In practice the ideal case is rarely ever seen. Due to imperfect timing between detection of an event, reading an event, writing an event and building frame buffers, events are often stored in an incorrect frame. Other problems may cause events, Logbook dumps or corrupt frames or lost frames, to be written to adjacent frames or even frames more than a single second away. Here are some examples of data streams that might cause OOE. The first three are the most common and the last two show how further complications might come up if a frame happens to be missing.

```
||0000000000000001||1111111111111112||22222222222222222222|| ...
```

```
||0000000000000000||0111111111111111||11222222222222222223|| ...
```

```
||0000000000000000||0011111111111111||1222222222222222233|| ...
```

```
||0000000000000000||Missing Frame||122222222222222223|| ...
```

```
||0000000000000000||Missing Frame||022222222222222223|| ...
```

This is not an exhaustive list of all possible permutations. This list is further complicated by GPS initializations, the first frame of an observation, data corruption, etc. When `dat2fits` was first inherited, $> 50\%$ FITS files had OOE. After all OOE

scenarios were accounted for the number of FITS files containing OOE's was reduced to $\sim 0.3\%$. Inspection of these remaining OOE's indicates that they are most likely not fixable and are due to data corruption.

A.4.4 Other Timing Anomalies in USA Data

There are some remaining timing anomalies in USA data. The most significant is the GPS drift between GPS initializations. This problem is still being addressed. There are also problems concerning the presence of same time events (STEs) and data gaps at the beginnings and ends of frames. See Shabad 2000 for a discussion of STEs and data gaps.

A.5 `usabckgnd`: Calculating Background Files

For details on `usabckgnd` see Saz Parkinson 2003.⁶ Briefly, `usabckgnd` is the USA tool which estimates the backgrounds for any given observation. It is necessary to run `usabckgnd` prior to running `mktimeusa` and cutting the data. `Mktimeusa` also cuts the background files and, in the future, background subtracted light curves could be made as standard output from `mktimeusa`.

A.6 What MkTimeUSA (`mktimeusa`) Does

A.6.1 `mktimeusa`: Construction of Good Time Intervals

The `mktimeusa` Perl script feeds the appropriate arguments to and executes the MkTimeUSA program and a variety of FTOOLS on an entire directory of USA event observations. The directory must contain an event file, a housekeeping file and a background file (created by `usabckgnd`) for each observation. The files should have the suffixes `evt.fits`, `hkp.fits` and `bck.fits`, respectively. (`Mktimeusa` does not currently handle spectral mode data.)

The MkTimeUSA C++ code generates a set of good time intervals (gtis) for an observation. These gtis are based on housekeeping and event data. Once these gtis are created, FTOOLS are used to plot key data in postscript files, cut out regions

⁶The USA background model and `usabckgnd` have been jointly developed by Pablo Saz Parkinson at SLAC and Mike Wolff at NRL.

of bad data as delimited by the MkTimeUSA gtis and merge the MkTimeUSA gtis with the gtis contained in the original event FITS files. The end product is a .filt file which contains only good data, the original gti table and gti table corresponding to the merging of the original gti table and the MkTimeUSA generated gtis.

A.6.2 MkTimeUSA Cutting Criteria

The gtis generated by MkTimeUSA and used to filter USA event data are based on simple criteria. These criteria include high voltage, pointing offset, angle to Earth's limb, data length and backgrounds. More extensive discussion of these criteria and how they might be changed is given in Section A.6.4. One of the most useful background cutting criteria is soft electrons. An example of how MkTimeUSA uses soft electrons to make background cuts is shown in Figure 4.1 and discussed in Section 4.3. Now a discussion of how to run **mktimeusa** is given.

A.6.3 How to Run mktimeusa

The general command for running **mktimeusa** is

```
mktimeusa your_data_dir output_dir bsub=[0 | 1] (nospacesaround=''),
```

where `your_data_dir` is the path to the un-cut FITS file directory and `output_dir` is the path to the output directory, `output_dir` can be `./`, and `bsub` is for batch jobs (SLAC). Full paths are not necessary but they are safer. At SLAC try not to use “/a paths,” use “/nfs paths” instead.

If you want to use the **mktimeusa** default cuts then all you need is a directory containing your data. Then type

```
mktimeusa your_data_dir output_dir bsub=0
```

This is assuming that the job will be run in non batch mode. The `output_dir` need not exist although it can.

If you want to use your own cuts then you must first create `output_dir` and copy `$USARoot/scripts/mktimeusa.in` to `output_dir`

```
cp $USARoot/scripts/mktimeusa.in output_dir
```

Make any desired changes to the arguments in `mktimeusa.in` and then issue the following command:

```
mktimeusa your_data_dir output_dir bsub=0.
```

Many files will be created in the directory in which the **mktimeusa** job is started. So **mktimeusa** should always be run from an empty directory and only one **mktimeusa** job should be run in a single directory. If more than one **mktimeusa** job is run in a directory it will cause problems. This is especially true when running in batch mode. In batch mode no files are moved to the `output_dir`. All output files are created in the directory where the user starts the job. When all batch jobs are finished the user should execute, from the **mktimeusa** working directory, the command

```
sh cleanup.sh
```

and this will put all of the files where they belong.

A.6.4 MkTimeUSA Argument Descriptions

Here is a description of the cut parameters used in MkTimeUSA. The default input for these values is shown in `mktimeusa.in`, located in `$USARoot/scripts`. The default parameter values are likely to change in the future, as USA backgrounds and anomalies are understood in more detail.

MinimumHV This is the minimum acceptable high voltage in the chamber. If a section of data has a high voltage less than **MinimumHV** then it will be cut out.

PoleRatioMultiplier is multiplied by the **RatioMultiplier** (defined below). Because the polar regions are expected to have higher electron rates, this parameter is used to make the soft electron cut less sensitive in those regions.⁷ In order for data to be excluded using this parameter, the current seconds top layer highest PHA channel must have a rate higher than the user input for parameter **BackgroundCounts**, see below.

MaximumOffset is the maximum allowable offset (in degrees) from directly pointing at the source. Note the offset is given in the HKP file as calculated using the `goodunroll` routine from `usalib` in the USA cvs repository.

⁷Soft electron cuts are discussed in Section 4.3.

MinimumOffset is the minimum allowable offset (in degrees) from directly pointing at the source. This quantity is intended for use in finding the off source segments in an observation. Normally this parameter is set to zero, however setting it to some other appropriately chosen value will allow the user to extract background data at the beginning and end of standard USA pointing observations and from off source pointing during raster scans and pings.

MinimumLimbAngle is the minimum allowable angle (in degrees) between the pointing direction of USA and Earth's limb. The current default value of 5.0° appears to work very well. Changing this parameter to smaller values will tend to contaminate an observation with X-rays coming off of Earth's limb.

RatioMultiplier is a constant which multiplies the ratio of the highest top layer PHA channel to the highest bottom layer PHA channel.⁸ The ratio determined by the actual efficiencies in the two layers is 0.85. This value was found to be much too restrictive, so the ratio in MkTimeUSA is set to 1.5, which is also found to be very restrictive. So RatioMultiplier is used to tune the ratio between the two layers. Large values of this parameter will allow regions with high rates of soft electrons to remain in the data. In order for data to be excluded using this parameter, the current seconds top layer highest PHA channel must have a rate higher than the user input for parameter BackgroundCounts, see below.

FracAboveBckgnd is the acceptable fraction of veto counts above a calculated low point. MkTimeUSA goes through each observation and determines the minimum background veto level. This minimum is indicative of the actual background minimum during the observation. Using FracAboveBckgnd MkTimeUSA cuts out regions where *any* veto rate, for 1 second, is greater than $(1 + \text{FracAboveBckgnd}) \times (\text{The minimum calculated background})$.

MaximumCh15Diff is another parameter for handling the soft electrons in a slightly different way. This parameter simply sets a limit on the acceptable difference between the top and bottom layers in the highest PHA channel. Greater differences allow more soft electrons.

TimeBeforeOnSource is the number of seconds after pointing at the source (i.e. the offset is $< \text{MaximumOffset}$) to begin considering the data as good. This is mainly used to avoid the rate spike that occurs in USA observations just after slewing from blank sky onto the source. This is a very flexible parameter and might be used to

⁸The highest PHA channel number depends on the mode, see Chapter 3 for a description of USA modes.

avoid other problems.

NbinsAVG is the number of one second bins to average when deriving quantities to be used in cutting (e.g. the minimum perimeter veto rate). This value sets the number of bins to average when determining the minimum calculated background. In most cases, increasing the number of bins averaged will increase the calculated minimum background.

MinDataLength sets the minimum number of contiguous seconds of good data, as determined by `MkTimeUSA`, for a segment of data to be kept. If `MinDataLength` is 4 and a files longest uninterrupted segment of data is 3 seconds, then no good data will be obtained from that file.

TimeBeforeOffSource is the opposite of `TimeBeforeOnSource`. This is the number of seconds prior to the last event frame stop to stop considering data as good. The last event frame stop is the last stop time in the original `gti` table produced by `dat2fits`.

MinimumYawAngle is self descriptive. This is a parameter used to cut out data collected while the detector was heavily shaded by the yoke. When yoke obscuration is very large it is difficult to accurately correct the counting rate.

MinPVtoTCVRatio is the minimum ratio of perimeter veto counts to total coincident veto counts. This is another way of cutting out regions containing large amounts of soft electrons. A value of 0.58 should cut out most soft electron regions.

RateMultiplier is multiplied by the average number of counts in highest PHA channel of the top layer (layer 1 channel 15 or channel 7). If the current second has a count rate greater than this product then the current second is excluded. In order for data to be excluded using this parameter, the current seconds top layer highest PHA channel must have a rate higher than the user input for parameter `BackgroundCounts`, see below. For better worse this quantity will exclude regions in which the count rate spikes. Making this number very large will include data spikes if they exist. Care should be taken with this parameter, because it could cut out real X-ray bursts.

PoleMaxCh15DiffMultiplier is multiplied by **MaximumCh15Diff** in order to account for higher occurrence of soft electrons at the poles. The parameter is very similar to the `PoleRatioMultiplier`.

BackgroundCounts is a user defined background rate for the highest energy channel in the upper layer or for the sum of all PHA channels depending on the implementation (both tests are made against this parameter and are compatible in the

code). The default value is 1.0. If one wishes to exclude bursts or potential false bursts from their data, then they should set this value very small and the RateMultiplier to a reasonable value (based on fluctuations in the data not a result of ‘bursts;’ this may require some trial and error). If one wishes to include possible bursts then this value should be set small or large (a large value will virtually guarantee that data spikes will be kept) and the RateMultiplier should be made large. This parameter is also compared to the total rate in both layers of the detector. In this case it is possible to set this value as an absolute minimum count rate in both layers. This would be done by setting other background related cuts to an insensitive extreme (allowing most data to be kept) and then setting the BackgroundCounts value to some desired minimum value. For example, if this procedure is followed and BackgroundCounts is set to 100 then any second of data with a count rate less than 100 will be excluded. Other cuts are possible while BackgroundCounts (i.e. cuts on soft electrons) is set to greater than a few, but it may not be possible to exclude bursts with such values. Be careful to not set BackgroundCounts too high in order to keep data spikes, because you may lose data based on the minimum count rate criterion. High RateMultiplier values are best for the inclusion of data spikes.

A.6.5 MkTimeUSA Output

The primary output of **mktimeusa** is a filtered event and background file. For each observation these files are located in a subdirectory of the output directory called **FILT**. Each filtered event file is given the suffix **.filt**. The filtered files contain only data from observation segments passing the user specified criteria for good data. The criteria used are either the defaults contained in the MkTimeUSA code or they are set in a file called **mktimeusa.in** which should be located in the desired output directory (see above).

If the user wants to know more about what **mktimeusa** does, they may look in the **SH** subdirectory. This directory contains a shell script for each observation. Here all commands executed to give the data products can be seen. The output of these commands is stored in a file in the **LOG** subdirectory. There should be one log file for each **evt.fits** file. The vast majority of this output represents each time a second of data is *lost* due to cuts. In general, each time a second is lost a line is printed out. The first three characters on this line are either HKP or EVT. HKP indicates that the second was lost to some quantity in the HKP data (i.e. the offset). EVT

indicates something derived from the event data (i.e. highest PHA channel count rate difference) caused the second to be lost. The log files are critical in understanding what **mktimeusa** does. *If ever it seems that the data filtering is not correct then the first place to look for a problem is the **LOG** directory!*

In the subdirectories **EVTps** and **HKPps** **mktimeusa** gives multiple plots on one second intervals for each observation. For the event data three postscript files are generated: evt1.ps evt2.ps and evt3.ps are the suffixes. The first file shows data after cuts are made and contains a plot of the total count rate, yoke corrected total count rate, collimator response and the pointing offset versus time. The second file contains the same plots as the first except it shows the unfiltered data. The third event postscript file plots derived quantities used to make selections of good data from the unfiltered event data. These derived quantities are the highest PHA channel difference and ratio, and the total (all channels summed) difference and ratio between layer 0 and layer 1.

In the **HKPps** subdirectory there are six postscript files for each observation: similarly hkp1–6.ps are the suffixes. The plots in these files cover all times for which there are data given in the housekeeping files. All quantities are plotted with respect to time. The first file contains the detector 1 layer 0 count rate, detector 1 layer 1 count rate, the total coincident veto and the detector 1 perimeter veto. The second file contains the detector 1 layer 0 coincident veto, detector 1 layer 1 coincident veto, the sae pitch steps and the collimator response. The third file contains the ratio of the perimeter veto to the total coincident veto, the yaw, the pointing offset and the limb angle. The fourth file contains the longitude of ARGOS, the latitude of ARGOS, the detector 1 electronic plate temperature and the detector 1 back plate temperature. The fifth file contains the pointing RA, the pointing DEC, detector 1 high voltage for layer 0 and the detector 1 high voltage for layer 1. The sixth file contains the ARGOS eci x position, eci y position, eci z position and the USA telemetry mode.

The general purpose of the plots is to give the user a quick way of checking that their cuts are reasonable. When **MkTimeUSA** is run, several directories are created within **output_dir** and the output files, including plots, are placed in their appropriate directory. The user should always have a look at the plots to make sure the cuts are as expected. When done, most of the files generated by **mktimeusa** may be deleted.

In addition to the postscript files contained in **EVTps** and **HKPps** there is the subdirectory **QDP_files**. Within this directory one will find QDP command files

(.pco) and data files (.qdp) for each of the postscript plots. These files may be used to regenerate and toy with any of the postscript plots made. Further, all of the data and some derived parameters are there in an easily accessible ASCII format.

In the output directory there is a **PHA** directory with a .pha file for each observation. The .pha files contain the normalized uncorrected energy spectrum for good data in each of the observations.

The **STAT** directory contains .stat files, which contain a variety of information including count rates by channel and layer. However, the variety of information is so wide that the entire next section (see Section A.6.6) has been dedicated to the content of .stat files.

Two less important subdirectories are **EDIE** and **TIME**. In **EDIE** are .edie files that contain differential energy spectra, as described in Section 3.8.1, of each observation.⁹ These EDIE files might someday be useful for correcting or adding to the understanding of the distortion in USA PSDs. All files related to the good time interval construction are stored for each observation in the **TIME** directory. Clever use of FTOOLS and these time files make it possible to re-filter data without re-running **mktimeusa**. This might occur if it is necessary to regenerate the FITS files but have identical data cuts to a previous set of filtered FITS files.

Finally there are three log files created in the top level of the output directory. The file logfile.log summarizes some of the outcome of **mktimeusa**. The files ObsLengthLog.log and ObsLengthLogRaw.log give the total length of each observation before filtering. They both contain the same information except that ObsLengthLog.log matches an observation name with the observation length and does a tally of unfiltered observation time. If there is a need for the number of remaining or good seconds then the following command can be use in the **STAT** directory:

$$\text{zcat *.stat.gz | grep -v HKP | wc -l.} \quad (\text{A.4})$$

The output of this command may be compared to the ObsLengthLog.log times to find how much of the original data remained after cutting.

⁹A modification to these differential spectra should be made to make them more useful. They should be done for one PHA channel at a time, not for all PHA channels simultaneously.

A.6.6 STAT File Contents

Perhaps the most useful output, other than the .flt file, is the file associated with each observation having the suffix .stat. These files contain a variety of information about all seconds in an observation which passed the cuts. Here are the column headings for the stat files:

```
1:HKPtime 2:EVTtime 3:BCKtime
4:Lyr0Chn0Rate 5:Lyr1Chn0Rate
6:Lyr0Chn1Rate 7:Lyr1Chn1Rate
8:Lyr0Chn2Rate 9:Lyr1Chn2Rate
10:Lyr0Chn3Rate 11:Lyr1Chn3Rate
12:Lyr0Chn4Rate 13:Lyr1Chn4Rate
14:Lyr0Chn5Rate 15:Lyr1Chn5Rate
16:Lyr0Chn6Rate 17:Lyr1Chn6Rate
18:Lyr0Chn7Rate 19:Lyr1Chn7Rate
20:Lyr0Chn8Rate 21:Lyr1Chn8Rate
22:Lyr0Chn9Rate 23:Lyr1Chn9Rate
24:Lyr0Chn10Rate 25:Lyr1Chn10Rate
26:Lyr0Chn11Rate 27:Lyr1Chn11Rate
28:Lyr0Chn12Rate 29:Lyr1Chn12Rate
30:Lyr0Chn13Rate 31:Lyr1Chn13Rate
32:Lyr0Chn14Rate 33:Lyr1Chn14Rate
34:Lyr0Chn15Rate 35:Lyr1Chn15Rate
36:TotalRate 37:ArgosLat 38:ArgosLong
39:Sae_Yaw 40:YawDeg 41:YokeObs
42:YokeCorrectedRate 43:det_1_pv
44:d1_ep_temp 45:d1_bp_temp
46:d1_l1_cv 47:d1_l2_cv 48:d1_tot_cv
49:CollimatorResponse 50:PointingOffset
51:limb_angle 52:Node
53:Lyr0Chn0Bck 54:Lyr1Chn0Bck
55:Lyr0Chn1Bck 56:Lyr1Chn1Bck
57:Lyr0Chn2Bck 58:Lyr1Chn2Bck
59:Lyr0Chn3Bck 60:Lyr1Chn3Bck
61:Lyr0Chn4Bck 62:Lyr1Chn4Bck
```

63:Lyr0Chn5Bck 64:Lyr1Chn5Bck
65:Lyr0Chn6Bck 66:Lyr1Chn6Bck
67:Lyr0Chn7Bck 68:Lyr1Chn7Bck
69:Lyr0Chn8Bck 70:Lyr1Chn8Bck
71:Lyr0Chn9Bck 72:Lyr1Chn9Bck
73:Lyr0Chn10Bck 74:Lyr1Chn10Bck
75:Lyr0Chn11Bck 76:Lyr1Chn11Bck
77:Lyr0Chn12Bck 78:Lyr1Chn12Bck
79:Lyr0Chn13Bck 80:Lyr1Chn13Bck
81:Lyr0Chn14Bck 82:Lyr1Chn14Bck
83:Lyr0Chn15Bck 84:Lyr1Chn15Bck

Column 52: Node indicates on which orbital segment the observation took place. The Node code is as follows: +2, North Pole; +1, Ascending Node; -1, Descending Node; -2, South Pole.

Anything may be added to this file if it is derivable from what is contained in the housekeeping and event files.

A.6.7 Future Development of USA Data Cuts

The current set of default parameters work well on some sources, but there are still sets to be developed. There should be at least three standard sets of parameters. One set would match the event data to the exact orbital locations of data used to develop the background model. Another set would allow the use to keep the maximum amount of data useful for timing studies (i.e. PSDs). The third to select of parameters would be developed to select for off source pointing, these cuts would be useful in refining the background model. It may be necessary to develop a database of parameters for specific sources.

There are many other tasks would could be performed by **mktimeusa**. At this time the most useful would be the creation of background corrected count rates. Currently, .stat files contain uncorrected count rates. In the future .stat files should contain corrected count rates.

A.7 **GUfft** and **specan**: Fast Fourier Transforms on USA Data

The proper calculation of PSDs¹⁰ using USA data has been a primary issue of the USA group for several years. Initial work done to understand USA PSDs and the USA detector deadtime is given in Shabad 2000. Initially IDL codes were developed in order to calculate PSDs from USA time series. These IDL codes were capable of handling many of the USA time series anomalies (Shabad 2000). In this work, some attention has already been given to these anomalies, see Section A.4.1. In general, these anomalies can be described as data gaps, same time events (STEs) and out of order events (OOEs). The greatest problems in time series analysis are data gaps, which occur at the beginning and end of seconds, and EDIE.

As the work presented in Shabad 2000, Section A.4.1 and Section 3.8.1 progressed, the understanding of USA time series became increasingly refined. Earlier knowledge was passed down and new things were learned. After the launch of USA and the commencement of data collection, new problems in the use of USA time series for PSD calculations had to be addressed. Additionally, it became clear that the original IDL codes used for calculating PSDs were not versatile enough. The inflight data needed be handled with greater flexibility. Features were not easily added to the original codes. The IDL codes were converted into a C code which was more expandable.

This C code became known, humorously, as **GUfft** or Grand Unified FFT, because it accounted for all of the known USA data glitches, used USA observation good time interval (gti) tables and allowed the user to make energy selected time series and then calculate PSDs. Further the code could easily combine PSDs calculated from large numbers of observations. After some time it was found that **GUfft** was not sufficiently expandable and there were procedures that were not handled in the best way possible. Two such procedures were the subtraction of deadtime and the use of only powers of two in the determination of the time series length. Limited two lengths which could only be expressed as a power of two made it impossible to use the greatest percentage of the data. In certain observations **GUfft** would lose as much as 50% of data because of frame gaps. Additionally, **GUfft** provided only Leahy normalized PSDs. Other normalizations were not available and cross-spectra

¹⁰The mathematical definition of a PSD is given in Section 4.5. That section also presents the specific type of PSD normalization used in the analysis of USA XTE J1550–564 data. Here the focus is given to the tools used to calculate PSDs for USA time series.

could not be calculated.

For these reasons it was necessary to write a new code for calculating PSDs from USA time series. This new code is called **specan**.¹¹ The **specan** software was a great step forward for USA data analysis because it calculated PSDs using variable length time series. This ability is extremely useful with USA data, because USA observations are generally short, less than 20 minutes, and are subject to frequent data gaps, possibly occurring every second as a result of frame filling.

A.7.1 Description of **specan**

Specan has multiple options which allow the user to calculate PSDs by multiple methods. For a list of all available command line switches and options, see Section D. **Specan** provides all standard options, such as setting the size of frequencies bins in the final PSD, making energy selected time series, and choosing a normalization for the PSD. It is possible to have the PSD linearly or geometrically binned. The user may decide whether or not to have the USA deadtime, as in Equation 3.4 and Shabad 2000, subtracted from the PSD. Windowing functions other than the standard square window may also be applied to the time series. There are other USA specific options available; however, the quality giving **specan** its uniqueness is that the user does not need to settle on a single length for the time series. A range of lengths may be given and **specan** will decide the length of each time series. These lengths are chosen to make the most efficient possible use of the data. **Specan's** use of variable length data segments is discussed in the following section.

specan Uses a Novel Binning Technique¹²

Typically, when calculating the PSD through use of the periodogram, several (time binned) light curves covering non-overlapping time ranges (segments) are formed and the squared moduli of their discrete Fourier transforms (DFTs) are averaged. The averaging is usually carried out across both time and frequency. That is, a set of frequency ranges (frequency bins) is decided upon, and all DFT power estimates

¹¹The primary credit for writing **specan** goes to Warren Focke. He wrote the code (and re-wrote some of what I tried to write). My main contributions to **specan** were in design, knowledge of how to handle the various data gaps and testing.

¹²This section was primarily written by Warren Focke and is included for completeness. W. Focke was the best person to write about the binning which **specan** uses, because it was his idea and he wrote the **specan** code.

from each segment which fall within a given frequency bin are averaged to form an overall power estimate for that frequency bin. This process is described more fully in van der Klis 1989a.

A variation of the usual method, just described, is used in **specan**. The difference is that, in the usual case, all of the light curves have the same length and time and frequency bin width, while those restrictions are relaxed here (in the current implementation, the time bins are all the same width, but this is not necessary, and may be changed in the future). This results in slightly more bookkeeping during the calculation, since the differing lengths of the segments result in frequency spacings between the individual DFT power estimates which are not constant across segments, so that each segment contributes a different number of power estimates to each frequency bin; thus in addition to running sums of power (for the average) and power squared (for the variance), one must keep a running sum of the number of estimates in each frequency bin.

This method may be applied to estimating the cross-spectral phase shifts and coherence, as well as the periodogram.

Segment lengths are often chosen to be 2^i (i an integer), for speed of calculation, since efficient routines to calculate the DFT of such sequences are widely available and widely known. This restriction can result in inefficient use of the data – up to half of the data can be unused, and loss of a quarter of the data is likely if segment lengths are chosen to be a constant power of 2. With the use of the binning technique described here and more versatile DFT libraries, almost all of the data can be used while retaining high computational speed. The DFT can be calculated rapidly for sequences whose length is a product of powers of small integers (where the definition of “rapidly” depends on the definition of “small”), not just powers of 2. We use a routine which finds the largest number of the form $2^i 3^j 5^k$ ($i, j,$ and k integers), which is not larger than the maximum segment length available. The worst-case efficiency for this scheme is for maximum segment lengths of length 7 and 14, where 1/7 of the data are lost. The scheme is more efficient for longer segments, in practice over 99% of the data are used.

A.8 Fitting Tools etc.

The fitting in tool used for work done in this dissertation was the Quick and Dandy Plotter (QDP). QDP makes use of the Levenberg-Marquardt technique for minimization.

Appendix B

Summary of USA Observations

Summary of USA Observations

NAME	CLASS	COMPACT OBJECT	EXPOSURE (ks)
Mkn 421	AGN	AGN	306.1
3C273	AGN	AGN	120.4
1es1959+650	AGN	AGN	59.0
Mkn 501	AGN	AGN	58.5
1es2344+514	AGN	AGN	26.8
NGC 1275	AGN	AGN	14.5
H1426+427	AGN	AGN	13.8
BL Lac	AGN	AGN	13.0
PKS2005-489	AGN	AGN	12.1
2EG1224+2155	AGN	AGN	10.1
1es1741+196	AGN	AGN	9.8
MK 501	AGN	AGN	6.0
1Zw187	AGN	AGN	5.9
PG 1448+273	AGN	AGN	1.5
TOTAL			657.5
Cyg X-1	HMXB	BH	728.6
XTE J1118+480	LMXB	BH	332.8
GRS 1915+105	HMXB	BH	292.0
XTE J1859+226	LMXB	BH	135.6
Cyg X-3	BHC	BH	116.4
XTE J1550-564	LMXB	BH	94.3

Summary of USA Observations Continued

X1630-472	LMXB	BH	90.9
SAXJ1819-25	LMXB	BH	21.0
GRS 1758-258	LMXB	BH	16.0
X1957+115	LMXB	BH	6.2
GX 339-4	BHC	BH	2.9
TOTAL			1836.7
X0142+614	AXP	NS	247.7
E 2259+586 SNR	AXP	NS	205.1
1E 1048.1-5937	AXP	NS	119.5
1E 1841-045	AXP	NS	80.5
1RXSJ170849.0-400910	AXP	NS	63.0
RX J0720.4-3125	AXP	NS	52.1
TOTAL			767.9
Crab Pulsar	PSR	NS	603.5
X1820-30 (NGC 6624)	PSR	NS	226.3
PSR 1509-58	PSR	NS	203.8
PSR B0540-69	PSR	NS	93.2
SAX J0635+0533	PSR	NS	57.0
PSR 1821-24	PSR	NS	52.6
PSR 1937+21	PSR	NS	10.1
SAX J1452-59 mon	PSR	NS	9.8
TOTAL			1256.3
Cyg X-2	LMXB	NS	357.3
Cir X-1	LMXB	NS?	234.5
EXO 0748-676	LMXB	NS	231.5
4U 0614+09	LMXB	NS	225.3
GX 349+2 (Sco X-2)	LMXB	NS	222.6
Rapid Burster (X1730-333)	LMXB	NS	184.0
Aql X-1	LMXB	NS	152.4
GX 354-0	LMXB	NS	150.4
X1636-536	LMXB	NS	139.1
Sco X-1	LMXB	NS	117.0
X1254-690	LMXB	NS	93.9
GX 340+0	LMXB	NS	78.4

Summary of USA Observations Continued

X1735-444	LMXB	NS	68.2
GX 5-1	LMXB	NS	64.1
GX 17+2	LMXB	NS	59.4
Ser X-1	LMXB	NS	53.0
GX 3+1	LMXB	NS	46.2
X1624-490 (Big Dipper)	LMXB	NS	31.3
EXO 1745-248	LMXB	NS	30.4
X1659-298 (X1658-298)	LMXB	NS	28.2
GX 9+9	LMXB	NS	24.7
KS1731-260	LMXB	NS	22.4
X1608-522	LMXB	NS	22.2
GX 13+1 mon	LMXB	NS	20.6
GX 9+1 mon	LMXB	NS	12.2
GX 331-1	LMXB	NS	11.5
SAX J1712.6-3739	LMXB	NS	2.5
1H 1556-605	LMXB	NS	0.4
TOTAL			2683.7
SMC X-1	XPSR	NS	314.2
Cen X-3	XPSR	NS	211.0
LMC X-4	XPSR	NS	170.2
X0115+634	XPSR	NS	128.1
X1145-616	XPSR	NS	105.9
Her X-1	XPSR	NS	95.6
Vela X-1	XPSR	NS	86.0
GX 1+4	XPSR	NS	65.2
X1627-673	XPSR	NS	46.7
X1942+274	XPSR	NS	35.4
X1657-415	XPSR	NS	23.6
GX 301-2	XPSR	NS	11.2
1SAX J1452.8-5949	XPSR	NS	8.1
MX 0836-429	XPSR	NS	0.8
TOTAL			1302.0

Summary of USA Observations Continued

X1700-377	HMXB	NS/BH	32.1
Cas A	SNR	SNR	209.2
EX Hya	CV	WD	41.2
AM Her	CV	WD	30.1
BL Hyi	CV	WD	19.1
AN UMa	CV	WD	7.7
TV Col	CV	WD	6.3
V834 Cen	CV	WD	6.2
V2301 Oph	CV	WD	4.5
BG CMi	CV	WD	4.3
EP Dra	CV	WD	3.9
GK Per	CV	WD	2.4
VV Pup	CV	WD	2.4
TOTAL			128.1
Bckgnd *	BKG		189.1
Earth	BKG		4.2
Unknown (Pointing Cal)	CAL		88.4
TOTAL			281.7
GRAND TOTAL			9155.2

Table B.1: Accounting of the observations made during the lifetime of the USA experiment. The first column gives the source name, the second tells the source class, the third tells the type of compact object and the fourth gives the approximated actual exposure time. The different acronyms are active galactic nuclei (AGN), high-mass X-ray binary (HMXB), low-mass X-ray binary (LMXB), black hole candidate (BHC), anomalous X-ray pulsar (AXP), rotation powered pulsar (PSR), accretion powered pulsar (XPSR), cataclysmic variable (CV), background (BKG), calibration (CAL), white dwarf (WD), neutron star (NS), supernova remnant (SNR) and black hole (BH).

Appendix C

Example usaview Output for XTE J1550–564

```
%> usaview -r 2451838 2451847 237.75 -56.48 XTE1550-564  
XTE1550-564 237.750 -56.480
```

Source yaw is 8.3 deg

** Source yaw is on the potentially dangerous sun side

Yoke obscuration will reduce count rate to 100.00 % of full value

Sun Angle = 52.303

RAAN = 239.6, yaw_a = 8.3, pitch_a = 56.1

Visible on AN side from lat -69.7 to 53.9 deg.

RADN = 59.6, yaw_d = 8.3, pitch_d = -123.9

Visible on DN side from lat 0.0 to 0.0 deg.

XTE1550-564 IS observable on JD 2451838.000000. ii = 1

lat_a -69.657791 to 53.912209 lat_d 0.000000 to 0.000000

Minutes in Low-Background Region and Not Behind Yoke(Yaw>-32.0):

XTE1550-564 GOOD on JD 2451838.000000. ii = 1 ASC

GOOD Date: 10/20/2000

GOOD Ascending for 17.500000 minutes.

TIMEa On Descending for 0.000000 minutes.

XTE1550-564 OPTIMAL on JD 2451838.000000. ii = 1 ASC

OPTIMAL Date: 10/20/2000
OPTIMAL Ascending for 17.500000 minutes.
XTE1550-564 IS observable on JD 2451840.000000. ii = 2
lat_a -69.614687 to 53.955313 lat_d 0.000000 to 0.000000
Minutes in Low-Background Region and Not Behind Yoke(Yaw>-32.0):
XTE1550-564 GOOD on JD 2451840.000000. ii = 2 ASC
GOOD Date: 10/22/2000
GOOD Ascending for 17.500000 minutes.
TIMEa On Descending for 0.000000 minutes.
XTE1550-564 OPTIMAL on JD 2451840.000000. ii = 2 ASC
OPTIMAL Date: 10/22/2000
OPTIMAL Ascending for 17.500000 minutes.
XTE1550-564 IS observable on JD 2451841.000000. ii = 3
lat_a -69.603679 to 53.966321 lat_d 0.000000 to 0.000000
Minutes in Low-Background Region and Not Behind Yoke(Yaw>-32.0):
XTE1550-564 GOOD on JD 2451841.000000. ii = 3 ASC
GOOD Date: 10/24/2000
GOOD Ascending for 17.500000 minutes.
TIMEa On Descending for 0.000000 minutes.
XTE1550-564 OPTIMAL on JD 2451841.000000. ii = 3 ASC
OPTIMAL Date: 10/24/2000
OPTIMAL Ascending for 17.500000 minutes.
XTE1550-564 is NOT observable on JD 2451842.000000, yaw angle 10.471311.
XTE1550-564 is NOT observable on JD 2451843.000000, yaw angle 11.014343.
XTE1550-564 is NOT observable on JD 2451844.000000, yaw angle 11.557269.
XTE1550-564 is NOT observable on JD 2451845.000000, yaw angle 12.099978.
XTE1550-564 is NOT observable on JD 2451846.000000, yaw angle 12.642357.

Appendix D

specan: Functionality and Command Line Options

specan: Do Power Spectra and Cross Spectra for USA

Usage:

specan [options] file ...

You must supply at least one of -o or -d, and at least one input file.

Options: (NI = not implemented)

-B, --freqbin: Allows different types of frequency binning to be performed.

Syntax: 'binning_type:option[:...]'

Current types are:

linear: Constant width.

options: low_edge:high_edge:width (all in Hz)

geom: Constant fractional width, but not less than an absolute minimum.

options: low_edge:high_edge:geom_width:minimum_width

All in Hz, except geom_width, which is a ratio.

-I, --intervalfile: Dump each unbinned interval to a file. (NI)

- N, --dont-subtract: Do not subtract the Poisson noise floor from the spectra.
- W, --window: Use a window[press, harris] or multitapers[mccoy].
 Syntax: 'win_type[:options...]'
 Current types are:
 c1whole: A family of multitapers designed to have spectral leakage with an f^{-6} asymptotic falloff.
 options: ntapers, the number of tapers to use. An integer.
 hann: The hann window. No options.
 square: No window. No options. This is the default.
 trigprolate: Sinusoidal approximations to the DPSS tapers.
 options: ntapers, the number of tapers to use.
 Must be one of (2, 4, 5, 7).
- b, --timebin: Light curve time bin size, in seconds.
 Must be one of (32, 96, 960) * $1e^{-6}$.
- c --channels: Energy channel ranges.
 Syntax 'a-b,c-d,...' Limits are inclusive.
 A single value may be used instead of a range.
 The PSD is calculated for each band.
 If more than one range is given then cross spectra are calculated for all bands but the first relative to the first (unless it's suppressed with -x).
- d, --dumpfile: Dump files are intermediate output files used when running parallel jobs.
 They contain all information necessary to combine results from two runs of the program as if they had been a single run. Their format and contents are intentionally undocumented.
 mergespec is used to perform the combination.
- f, --use-frames: Use the second delimiters instead of the merged gti table.
- h, --help: Print this message.

-l, --length: Minimum and maximum length of data to transform at once.

Syntax 'min-max' or a single value, in seconds.

Data segments longer than max will be broken up into the longest pieces that fit within the limits. Some data may be discarded.

-i, --interactive: Stay in python interpreter.

-n, --normalization: Normalization used for the power spectra.

Current values:

raw: This is $|a_j|^2$, where a_j is defined by eq. (2.4a) in [vdk].

ratesquared: As raw, but each interval is divided by its length squared.

leahy: Expected value for white noise is 2.0. Eq. (2.8) in [vdk].

rms: Fractional mean squared variability per Hz. The square root of the integral of a feature is its RMS normalization.

-o, --outfile: Output files contain analyzable output data like average power or phase lag. They are currently QDP files, although QDP might have trouble reading them if they have too many columns.

Current columns are:

Frequency (Hz) The average frequency of all estimates in each bin.

for each energy band:

Power N, Error (various) The PSD and its 1-sigma error.

for each energy band:

Noise N, Error (same as above) The average estimated noise floor

for the PSD and its 1-sigma error.

for each energy band but the first:

Phase N:1 (rad) The phase of the cross spectrum relative to the first band.

for each energy band but the first:

UnCoh N:1 (unitless) The coherence relative to the first

band. Uncorrected. This is eq. (6.51) in [bp], NOT eq. (2) in [vn].

for each energy band but the first:

CorCoh N:1 (unitless) The coherence relative to the first band. Corrected for noise as in eq. (8) in [vn].

-p, --plot: Plot the spectra as they come up. (NI)

-r, --rate: Set minimum and maximum rate limits.

Syntax: 'min-max' or a single value (this would probably be silly), in counts/s.

This is applied after length cuts but before spectral cuts.

-s, --sort: Sort files with out-of-order events, instead of rejecting them.

-x, --no-cross-spectrum: Don't calculate the cross spectrum.

Input files are expected to be filtered USA event files. They can be gzipped.

[bp] Bendat & Piersol 2000, "Random Data", Wiley, ISBN 0-471-31733-0

[harris] Harris, F. 1978, Proceeding of the IEEE, 66,1:51

[mccoy] McCoy, E. et al. 1998, IEEE Trans. on Signal Processing, 46,3:655

[press] Press, W. H. et al. 1992, "Numerical Recipies" section 13.4, Cambridge University Press, second edition.

[vdk] van der Klis, M. 1989 Proc. NATO Advanced Study Institute "Timing Neutron Stars", Cesme, Turkey, NATO ASI Series C, Vol. 262, p. 27. also EXOSAT preprint #81.

[vn] Vaughan & Nowak 1997, ApJ 474:L43

Appendix E

mergespec Command Line Options

Usage: mergespec [options] file ...

Options:

-d, --dumpfile: Output results in a dump file.

Syntax: -d filename

The resulting file will closely resemble those produced by specan -d.

-h, --help: Print this message.

-o, --outfile: Output results in an output file.

Syntax: -o filename

The resulting file will closely resemble those produced by specan -o.

Input files are expected to be dump files as made by specan -d.

Bibliography

- Abramowicz, M. A., I. V. Igumenshchev, E. Quataert, and R. Narayan (2002, February). On the Radial Structure of Radiatively Inefficient Accretion Flows with Convection. *ApJ* 565, 1101–1106.
- Balbus, S. A. and J. F. Hawley (1991, July). A powerful Local Shear Instability in Weakly Magnetized disks. I - Linear Analysis. II - Nonlinear Evolution. *ApJ* 376, 214–233.
- Balbus, S. A. and J. F. Hawley (2002, July). On the Nature of Angular Momentum Transport in Nonradiative Accretion Flows. *ApJ* 573, 749–753.
- Balbus, S. A., J. F. Hawley, and J. M. Stone (1996, August). Nonlinear Stability, Hydrodynamical Turbulence, and Transport in Disks. *ApJ* 467, 76.
- Belloni, T., D. Psaltis, and M. van der Klis (2002, June). A Unified Description of the Timing Features of Accreting X-Ray Binaries. *ApJ* 572, 392–406.
- Binney, J. and M. Merrifield (1998). *Galactic Astronomy*. New Jersey: Princeton University Press.
- Blandford, R. D. and M. C. Begelman (1999, February). On the Fate of Gas Accreting at a Low Rate on to a Black Hole. *MNRAS* 303, L1–L5.
- Bondi, H. (1952). On Spherically Symmetrical Accretion. *MNRAS* 112, 195.
- Bradt, H. V., A. M. Levine, R. A. Remillard, and D. A. Smith (2000). Transients Observed with the RXTE All-Sky Monitor. In *Rossi2000: Astrophysics with the Rossi X-ray Timing Explorer*, pp. E114.
- Chaisson, E. and S. McMillan (2002). *Astronomy Today*. Prentice Hall.
- Chakrabarti, S. and L. G. Titarchuk (1995, December). Spectral Properties of Accretion Disks Around Galactic and Extragalactic Black Holes. *ApJ* 455, 623.
- Charles, P. A. and F. D. Seward (1995). *Exploring the X-ray Universe*. Cambridge, Great Britain: Cambridge University Press.
- Chen, X., M. A. Abramowicz, and J. Lasota (1997, February). Advection-Dominated Accretion: Global Transonic Solutions. *ApJ* 476, 61.

- Corbel, S., R. P. Fender, A. K. Tzioumis, M. Nowak, V. McIntyre, P. Durouchoux, and R. Sood (2000, July). Coupling of the x-ray and radio emission in the black hole candidate and compact jet source gx 339-4. *AAP* 359, 251–268.
- Corbel, S., P. Kaaret, R. K. Jain, C. D. Bailyn, R. P. Fender, J. A. Tomsick, E. Kalemci, V. McIntyre, D. Campbell-Wilson, J. M. Miller, and M. L. McCollough (2001, June). X-Ray States and Radio Emission in the Black Hole Candidate XTE J1550-564. *ApJ* 554, 43–48.
- Di Matteo, T., C. L. Carilli, and A. C. Fabian (2001, February). Limits on the Accretion Rates onto Massive Black Holes in Nearby Galaxies. *ApJ* 547, 731–739.
- Done, C. (2002, March). Accretion Flows in X-ray Binaries. *Philosophical Transactions of the Royal Society (Series A: Mathematical, Physical, and Engineering Sciences)* 251, 3246–3259.
- Dorman, B. and K. A. Arnaud (2001). Redesign and Reimplementation of XSPEC. In *ASP Conf. Ser. 238: Astronomical Data Analysis Software and Systems X*, Volume 10, pp. 415.
- Encyclopedia.com (2002). X-ray Astronomy. Information obtained from the website encyclopedia.com <http://www.encyclopedia.com/html/x/xrayastr.asp>.
- Esin, A. A., J. E. McClintock, and R. Narayan (1997, November). Advection-Dominated Accretion and the Spectral States of Black Hole X-Ray Binaries: Application to Nova MUSCAE 1991. *ApJ* 489, 865.
- Fender, R. (2002). Relativistic Outflows from X-ray Binaries ('Microquasars'). In *Relativistic Flows in Astrophysics*, pp. 101.
- Fender, R. P. (2001, March). Powerful Jets from Black Hole X-Ray Binaries in Low/Hard X-Ray States. *MNRAS* 322, 31–42.
- Focke, W. B. (1998). *X-Ray Timing Properties of Cygnus X-1 and Cygnus X-2*. Ph. D. thesis, University of Maryland, Colleg Park.
- Frank, J., A. King, and D. Raine (2002). *Accretion Power in Astrophysics, Third Edition*. New York: Cambridge University Press.
- Garcia, M. R., J. E. McClintock, R. Narayan, P. Callanan, D. Barret, and S. S. Murray (2001, May). New Evidence for Black Hole Event Horizons from Chandra. *ApJL* 553, L47–L50.
- Gelino, D. M. (2001). *Modeling Infrared Ellipsoidal Variations: Determining the Masses of Black Holes in Soft X-Ray Transients*. Ph. D. thesis, New Mexico State University.

- Giebels, B., E. D. Bloom, W. Focke, G. Godfrey, G. Madejski, K. T. Reilly, P. M. S. Parkinson, G. Shabad, R. M. Bandyopadhyay, G. G. Fritz, P. Hertz, M. P. Kowalski, M. N. Lovellette, P. S. Ray, M. T. Wolff, K. S. Wood, D. J. Yentis, and J. D. Scargle (2002, June). Observation of X-Ray Variability in the BL Lacertae Object 1ES 1959+65. *ApJ* 571, 763–770.
- Godfrey, D. G. (2002). Personal Communication.
- Godfrey, G. (2001). *Gary Godfrey's Report on EDIE*. From USA Internal Documentation. See USA private page at <http://xweb.nrl.navy.mil/usa/index.html>.
- Hanisch, R. J., A. Farris, E. W. Greisen, W. D. Pence, B. M. Schlesinger, P. J. Teuben, R. W. Thompson, and A. Warnock (2001, September). Definition of the Flexible Image Transport System (FITS). *AAP* 376, 359–380.
- Hawley, J. F. and S. A. Balbus (1991, July). A Powerful Local Shear Instability in Weakly Magnetized Disks. II. Nonlinear Evolution. *ApJ* 376, 223.
- Hjellming, R. M. and K. J. Johnston (1988, May). Radio Emission from Conical Jets Associated with X-Ray Binaries. *ApJ* 328, 600–609.
- Homan, J., R. Wijnands, M. van der Klis, T. Belloni, J. van Paradijs, M. Klein-Wolt, R. Fender, and M. Méndez (2001, February). Correlated X-Ray Spectral and Timing Behavior of the Black Hole Candidate XTE J1550-564: A New Interpretation of Black Hole States. *APJS* 132, 377–402.
- Igumenshchev, I. V. and M. A. Abramowicz (1999, February). Rotating Accretion Flows Around Black Holes: Convection and Variability. *MNRAS* 303, 309–320.
- Igumenshchev, I. V. and M. A. Abramowicz (2000, October). Two-Dimensional Models of Hydrodynamical Accretion Flows into Black Holes. *APJS* 130, 463–484.
- Igumenshchev, I. V., M. A. Abramowicz, and R. Narayan (2000, July). Numerical Simulations of Convective Accretion Flows in Three Dimensions. *ApJL* 537, L27–L30.
- Igumenshchev, I. V., X. Chen, and M. A. Abramowicz (1996, January). Accretion Discs Around Black Holes: Two-Dimensional, Advection-Cooled Flows. *MNRAS* 278, 236–250.
- Igumenshchev, I. V. and R. Narayan (2002, February). Three-Dimensional Magnetohydrodynamic Simulations of Spherical Accretion. *ApJ* 566, 137–147.
- Jain, R. K., C. D. Bailyn, J. A. Orosz, J. E. McClintock, and R. A. Remillard (2001, June). Multiwavelength Observations of the Black Hole Candidate XTE J1550-564 during the 2000 Outburst. *ApJL* 554, L181–L184.

- Jernigan, J. G., R. I. Klein, and J. Arons (2000, February). Discovery of Kilohertz Fluctuations in Centaurus X-3: Evidence for Photon Bubble Oscillations (PBO) and Turbulence in a High-Mass X-Ray Binary Pulsar. *ApJ* 530, 875–889.
- Kalemci, E., J. A. Tomsick, R. E. Rothschild, K. Pottschmidt, and P. Kaaret (2001, May). The X-ray Variability and Quasi-Periodic Oscillations in XTE J1550-564 During the Decay of the 2000 Outburst. In *American Astronomical Society Meeting*, Volume 198, pp. 1002.
- Larson, R. B. (1995, January). Star Formation in Groups. *MNRAS* 272, 213–220.
- Lasota, J.-P. (2001, June). The Disc Instability Model of Dwarf Novae and Low-Mass X-Ray Binary Transients. *New Astronomy Review* 45, 449–508.
- Li, T. P. and Y. Muraki (2002, October). Power Spectra of X-Ray Binaries. *ApJ* 578, 374–384.
- Longair, M. S. (1994). *High Energy Astrophysics, Second Edition, Volume 2*. Cambridge, UK: Cambridge University Press.
- Maccarone, T. and P. Coppi (2002). Hysteresis in X-ray Transient Spectral Transitions. *Bulletin of the American Physical Society* 47(2), S11.010.
- Masetti, N. and R. Soria (2000, April). XTE J1550-564. *IAUCIRC* 7399, 2.
- Meyer-Hofmeister, E. and F. Meyer (2001, December). The Change from Accretion via a Thin Disk to a Coronal Flow: Dependence on the Viscosity of the Hot Gas. *AAP* 380, 739–744.
- Miller, J. M., R. Wijnands, J. Homan, T. Belloni, D. Pooley, S. Corbel, C. Kouveliotou, M. van der Klis, and W. H. G. Lewin (2001, December). High-Frequency Quasi-Periodic Oscillations in the 2000 Outburst of the Galactic Microquasar XTE J1550-564. *ApJ* 563, 928–933.
- Narayan, R. and J. S. Heyl (2002, August). On the Lack of Type I X-Ray Bursts in Black Hole X-Ray Binaries: Evidence for the Event Horizon? *ApJL* 574, L139–L142.
- Narayan, R., R. Manadevan, and E. Quataert (1998). Advection-Dominated Accretion Around Black Holes. In M. A. Abramowicz and G. Björnsson and J. E. Pringle (Ed.), *Theory of Black Hole Accretion Discs*. (Cambridge University).
- Nowak, M. A., B. A. Vaughan, J. Wilms, J. B. Dove, and M. C. Begelman (1999). *Rossi X-ray Timing Explorer* Observation of Cygnus X-1. II. Timing Analysis. *ApJ* 510, 874.
- Nowak, M. A. and R. V. Wagoner (1991, September). Diskoseismology: Probing Accretion Disks. I - Trapped Adiabatic Oscillations. *ApJ* 378, 656–664.

- Orosz, J. A., P. J. Groot, M. van der Klis, J. E. McClintock, M. R. Garcia, P. Zhao, R. K. Jain, C. D. Bailyn, and R. A. Remillard (2002, April). Dynamical Evidence for a Black Hole in the Microquasar XTE J1550-564. *ApJ* 568, 845–861.
- Orosz, J. A., M. van der Klis, J. E. McClintock, R. K. Jain, C. D. Bailyn, and R. A. Remillard (2001, May). Dynamical Evidence for a Black Hole in the Microquasar XTE J1550-564. *The Astronomer's Telegram*, #70 70, 1+.
- Osherovich, V. and L. Titarchuk (1999, September). Interpretation of ~ 35 HZ QPO in the Atoll Source 4U 1702-42 as a Low Branch of the Keplerian Oscillations under the Influence of the Coriolis Force. *ApJL* 523, L73–L76.
- Poutanen, J. (1998). Accretion Disc–Corona Models. In M. A. Abramowicz and G. Björnsson and J. E. Pringle (Ed.), *Theory of Black Hole Accretion Discs*. (Cambridge University).
- Quataert, E. and A. Gruzinov (2000, August). Convection-Dominated Accretion Flows. *ApJ* 539, 809–814.
- Ray, P. S., K. S. Wood, G. Fritz, P. Hertz, M. Kowalski, W. N. Johnson, M. N. Lovellette, M. T. Wolff, D. Yentis, R. M. Bandyopadhyay, E. D. Bloom, B. Giebels, G. Godfrey, K. Reilly, P. Saz Parkinson, G. Shabad, P. Michelson, M. Roberts, D. A. Leahy, L. Cominsky, J. Scargle, J. Beall, D. Chakrabarty, and Y. Kim (2001). The USA X-ray Timing Experiment. In G. Malaguti, G. Palumbo, and N. White (Eds.), *X-ray Astronomy 1999 – Stellar Endpoints, AGN, and the Diffuse Background*, Volume 599 of *AIP Conference Proceedings*, Melville, New York, pp. 336. AIP.
- Reilly, K. T., E. D. Bloom, W. Focke, B. Giebels, G. Godfrey, P. M. Saz Parkinson, a. G. Shabad, P. S. Ray, R. M. Bandyopadhyay, K. S. Wood, M. T. Wolff, G. G. Fritz, P. Hertz, M. P. Kowalski, M. N. Lovellette, a. D. J. Yentis, and a. D. Scargle (2001, November). USA Experiment Observation of Spectral and Timing Evolution During the 2000 Outburst of XTE J1550-564. *ApJL* 561, L183–L186.
- Remillard, R., M. Munro, J. McClintock, and J. Orosz (2002, April). Evidence for Harmonic Relationships in the High Frequency QPOs of XTEJ1550-564 and GROJ1655-40. In *American Physical Society: High Energy Astrophysics Division: APR02*, pp. 17076.
- Remillard, R. A., G. J. Sobczak, M. P. Munro, and J. E. McClintock (2002, January). Characterizing the Quasi-periodic Oscillation Behavior of the X-Ray Nova XTE J1550-564. *ApJ* 564, 962–973.
- Rodriguez, J., S. Corbel, E. Kalemci, and J. Tomsick (2002, March). RXTE Observations of XTE J1550-564 During its 2000 Outburst. In *Proceedings of the XXII Moriond*

- Astrophysics Meeting "The Gamma Ray Universe"*, pp. 5341–5346.
- Rodriguez, J., S. Corbel, E. Kalemci, J. A. Tomsick, and M. Tagger (2002, July). Evolution of a Low Frequency QPO During the 2000 Outburst of XTE J1550-564. In *Proceedings of the 4th Microquasar Workshop, 2002*, pp. 7649–7653. The Center for Space Physics: Kolkata.
- Saz Parkinson, P. M. (2003). *Timing and Spectral Studies of the Peculiar X-Ray Binary Circinus X-1*. Ph. D. thesis, Stanford Universtiy.
- Shabad, G. (2000). *Detection of High-Frequency Variability in a Black Hole Transient With USA*. Ph. D. thesis, Stanford Universtiy.
- Shakura, N. I. and R. A. Sunyaev (1973). Black Holes in Binary Systems. Observational Appearance. *AAP 24*, 337–355.
- Shirakawa, A. and D. Lai (2002, January). Precession of Magnetically Driven Warped Disks and Low-Frequency Quasi-periodic Oscillations in Low-Mass X-Ray Binaries. *ApJ 564*, 361–368.
- Smith, D. A. (1998, September). XTE J1550-564. *IAUCIRC 7008*, 1+.
- Smith, D. M., W. A. Heindl, and J. H. Swank (2002, April). Two Different Long-Term Behaviors in Black Hole Candidates: Evidence for Two Accretion Flows? *ApJ 569*, 362–380.
- Sobczak, G. J., J. E. McClintock, R. A. Remillard, W. Cui, A. M. Levine, E. H. Morgan, J. A. Orosz, and C. D. Bailyn (2000a, December). Complete RXTE Spectral Observations of the Black Hole X-ray Nova XTE J1550-564. *ApJ 544*, 993–1015.
- Sobczak, G. J., J. E. McClintock, R. A. Remillard, W. Cui, A. M. Levine, E. H. Morgan, J. A. Orosz, and C. D. Bailyn (2000b, March). Correlations Between Low-Frequency Quasi-periodic Oscillations and Spectral Parameters in XTE J1550-564 and GRO J1655-40. *ApJ 531*, 537–545.
- Stella, L., M. Vietri, and S. M. Morsink (1999, October). Correlations in the Quasi-periodic Oscillation Frequencies of Low-Mass X-Ray Binaries and the Relativistic Precession Model. *ApJL 524*, L63–L66.
- Swank, J., C. Markwardt, and W. Focke (2002, April). Spectral and Temporal Evolution of XTE J1859+226. In *American Physical Society: High Energy Astrophysics Division: APR02*, pp. 17077.
- Tagger, M. and R. Pellat (1999, September). An Accretion-Ejection Instability in Magnetized Disks. *AAP 349*, 1003–1016.

- Titarchuk, L. and V. Osherovich (1999, June). Correlations between Kilohertz Quasi-periodic Oscillations and Low-Frequency Features Attributed to Radial Oscillations and Diffusive Propagation in the Viscous Boundary Layer around a Neutron Star. *ApJL* 518, L95–L98.
- Titarchuk, L., V. Osherovich, and S. Kuznetsov (1999, November). Timing Spectroscopy of Quasi-Periodic Oscillations in the Low-Mass X-Ray Neutron Star Binaries. *ApJL* 525, L129–L132.
- Titarchuk, L. and K. Wood (2002, September). On the Low and High Frequency Correlation in Quasi-periodic Oscillations among White Dwarf, Neutron Star, and Black Hole Binaries. *ApJL* 577, L23–LL26.
- Titarchuk, L. G., C. F. Bradshaw, and K. S. Wood (2001, October). B-Field Determination from Magnetoacoustic Oscillations in Kilohertz Quasi-periodic Oscillation Neutron Star Binaries: Theory and Observations. *ApJL* 560, L55–LL58.
- Tomsick, J. A., S. . Corbel, and P. Kaaret (2001, December). X-Ray Observations of XTE J1550-564 during the Decay of the 2000 Outburst. I. Chandra and RXTE Energy Spectra. *ApJ* 563, 229–238.
- Tucker, W. (2002). Timeline: 40 Years of X-ray Astronomy. Harvard-Smithsonian Center for Astrophysics.
- USA SWG (1996). *USA Detector Interface*. From USA Internal Documentation. See USA private page at <http://xweb.nrl.navy.mil/usa/index.html>.
- USA SWG (2001a). *Summary of Pointing Epochs*. From USA Internal Documentation. See USA Calibration Info page at <http://xweb.nrl.navy.mil/usa/index.html>.
- USA SWG (2001b). *USA Data Analysis System.doc*. From USA Internal Documentation. See USA cvs repository under the USA/doc directory.
- USA SWG (2001c). *USA Mission Critical Events Summary*. From USA Internal Documentation. See USA Calibration Info page at <http://xweb.nrl.navy.mil/usa/index.html>.
- van der Klis, M. (1989a). Fourier Techniques in X-Ray Timing. In H. Ogleman and E. P. J. van den Heuval (Eds.), *Timing Neutron Stars*, pp. 27.
- van der Klis, M. (1989b). Quasi-Periodic Oscillations and Noise in Low-Mass X-Ray Binaries. *araa* 27, 517–553.
- van der Klis, M. (2001, November). A Possible Explanation for the “Parallel Tracks” Phenomenon in Low-Mass X-Ray Binaries. *ApJ* 561, 943–949.

- van Paradijs, J. and J. E. McClintock (1995). Optical and Ultraviolet Observations of X-Ray Binaries. In W. H. G. Lewin, J. van Paradijs, and E. P. J. van den Heuvel (Eds.), *X-ray Binaries*. (Cambridge University).
- Verbunt, F. and E. P. J. van den Heuvel (1995). Formation and Evolution of Neutron Stars and Black Holes in Binaries. In W. H. G. Lewin, J. van Paradis, and E. P. J. van den Heuval (Eds.), *X-Ray Binaries*, pp. 457.
- Wen, H. C. (1997). *10 Microsecond Time Resolution Studies of Cygnus X-1*. Ph. D. thesis, Stanford Universtiy.
- White, N. E., F. Nagase, and A. N. Parmar (1995). The Properties of X-Ray Binaries. In W. H. G. Lewin, J. van Paradis, and E. P. J. van den Heuval (Eds.), *X-Ray Binaries*, pp. 1.
- Wilson, C. D. and C. Done (2001, July). Mapping the Inner Accretion Disc of the Galactic Black Hole XTE J1550-564 Through its Rise to Outburst. *MNRAS* 325, 167.
- Wolff, M. T., K. S. Wood, and J. N. Imamura (1991, July). Noise-Driven Radiative Shocks - A New Model for the Optical Quasi-Periodic Oscillations of the AM Herculis Objects. *ApJL* 375, L31–L34.
- Wood, K. S., G. Fritz, P. Hertz, W. N. Johnson, M. P. Kowalski, M. N. Lovellette, M. T. Wolff, D. J. Yentis, E. Bloom, L. Cominsky, et al. (1994). The USA Experiment on the ARGOS Satellite: A Low Cost Instrument for Timing X-ray Binaries. In *EUUV, X-Ray, and Gamma-Ray Instrumentation for Astronomy V*, Volume 2280 of *SPIE Proceedings*, pp. 19.
- Wood, K. S., J. N. Imamura, and M. T. Wolff (1992, October). Noise-Driven Radiative Shocks. II - Further Implications for the Quasi-Periodic Oscillations of the AM Herculis Objects. *ApJ* 398, 593–601.
- Wood, K. S., J. F. Meekins, D. J. Yentis, H. W. Smathers, D. P. McNutt, R. D. Bleach, H. Friedman, E. T. Byram, T. A. Chubb, and M. Meidav (1984, December). The HEAO A-1 X-Ray Source Catalog. *APJS* 56, 507–649.
- Wood, K. S., P. S. Ray, R. M. Bandyopadhyay, M. T. Wolff, G. Fritz, P. Hertz, M. P. Kowalski, M. N. Lovellette, D. Yentis, E. D. Bloom, B. Giebels, G. Godfrey, K. Reilly, P. Saz Parkinson, G. Shabad, and J. Scargle (2000, November). USA Experiment and RXTE Observations of a Variable Low-Frequency Quasi-periodic Oscillation in XTE J1118+480. *ApJL* 544, L45–L48.
- Young, K. and J. D. Scargle (1996, September). The Dripping Handrail Model: Transient Chaos in Accretion Systems. *ApJ* 468, 617.

Yuan, F., S. Markoff, and H. Falcke (2002, March). A Jet-ADAF model for Sgr A*.
AAP 383, 854–863.

Zac (2002). <http://www.astro.keele.ac.uk/zac/rochelob.html>.